

ÉCOLE DOCTORALE DE PHYSIQUE ET CHIMIE PHYSIQUE

Institut Pluridisciplinaire Hubert Curien

THÈSE

présentée par :

Alexandre AUBIN

soutenue le : 28 septembre 2015

pour obtenir le grade de : **Docteur de l'université de Strasbourg**

Discipline/Spécialité : Physique des particules

**Recherche de paternaire pour
le quark top dans l'expérience CMS**

CERN-THESIS-2015-290
28/09/2015



THÈSE dirigée par :

Mme. Caroline COLLARD Université de Strasbourg

RAPPORTEURS :

M. Pascal PRALAVORIO Centre de Physique des Particules de Marseille
M. Dirk ZERWAS Université de Paris Sud

AUTRES MEMBRES DU JURY :

M. Eric CHABERT Université de Strasbourg
M. Filip MOORTGAT CERN
M. Jerome BAUDOT Université de Strasbourg

UNIVERSITÉ DE STRASBOURG

THÈSE

pour l'obtention du diplôme de

DOCTEUR DE L'UNIVERSITÉ DE STRASBOURG

spécialité : physique des particules

présentée par

Alexandre AUBIN

**Recherche de partenaire pour le quark top
dans l'expérience CMS**

présentée le 28 septembre 2015 devant la commission d'examen composée de

Mme. Caroline COLLARD,	directrice de thèse
M. Eric CHABERT,	co-encadrant
M. Pascal PRALAVORIO,	rapporteur
M. Dirk ZERWAS,	rapporteur
M. Jerome BAUDOT,	examineur
M. Filip MOORTGAT,	examineur

To Megyn, Nicolas and Jérémie

*« Given enough time,
Hydrogen begins to wonder
Where it came from,
And where it is going... »*

Edward R. Harrison

*« Out of the cradle onto dry land
Here it is standing:
Atoms with consciousness;
Matter with curiosity.*

*Stands at the sea,
Wonders at wondering:
I... A universe of atoms,
An atom in the universe. »*

Richard P. Feynman

Acknowledgements

What a privilege it has been, through these three years, to have been working on the search for new physics in the CMS collaboration! I can't think of many other projects which are as fantastic and tremendous from a scientific and human point of view as the LHC. I still remember being a teenager and reading or hearing at the television about the construction and science behind this adventure, but I couldn't even imagine being able to contribute to it. This has truly been an honor to add my stone to this project. There are a lot of people I am grateful for, though I probably can't cite everybody without making a list longer than the CMS collaboration authors :P - so please forgive me if you don't find your name here.

I must of course start by my mom, which raised me and transmitted me values such as respect, patience and generosity. She always gave me freedom and support in my academic choices. Thanks also to my sister and brother, who had to endure my younger-self >:P, and with whom I remember having many small discussions on math, physics and biology with them, which help developed in me a passion for science.

I do not resist to mention some of the greatest teachers I had through my school years: B. Tritsch in high school for his intense philosophy courses; J-J. Fleck in prep. school for his amazing physics courses, and because he convinced me to pursue research; P. Colin who became my personal Yoda when it comes to computer science; A-S. Cordan and Y. Leroy for their courses on quantum physics and scientific computing, and the internship in their lab; and B. Fuks for its excellent lecture on the theory of the Standard Model.

I want to give warm thanks to my two supervisors, who are truly among the best supervisors one can wish to have: Caroline, for her communicative cheerfulness, her support, encouragements and for always making sure the work is recognized - and Eric, for his implication, his rigor and calm that became a model, and the many thought-provoking discussions we had together, many of which were supposed to be « just five minutes » :). Both of them provided me with continuous, crucial feedbacks to raise me to the top and make me progress on all the aspects of the thesis - a big thank you for everything you taught me and helped me to accomplish!

Thanks also to Michael, who have been my officemate for more than two years and with

ACKNOWLEDGEMENTS

whom I had many professional and unprofessional discussions, allowing me to step back from my own work and not becoming crazy about it :). I owe him big time for his support in the very last month of the thesis writing. Congratulations on your astonishing imitation of Abu from Aladdin ! I will certainly miss the people of the CMS group at the IPHC, in particular the legendary *c'est pas facile* of Jeremy (Jean-Remy :D), the unswerving generosity of Jean-Eric, the weekly attempt of Xavier to achieve world domination, the ambiguous and witty puns of Pierre and Thierry, the enthusiasm of Nicolas, the serenity of Jean-Laurent, the spicy political anecdotes of Jean-Marie, the italianism of Lorenzo and the enigmatism of Kirill, as well as Daniel, Anne-Catherine and all the other people of the lab. A little thought for the previous PhD students, Adam and Christophe, to whom I wish the best, and to the system administrators that take care of our sacred ui5, ui6 and ui8. It has also been a pleasure to work with other people from the CMS collaboration, in particular Lara, Michael, Verena, Adrien, and the SUSY and *b*-tagging conveners.

I want to thank my friends from the ENSPS - Nol, Vincent, ToKamaK, Erwin, to name a few, the buddies from Hackstub - J-C, Zirst, Michael, Karchnu, Elie, Regis, Léo, and many others, the IRC folks - Mut, Fae, Hayate and angenoir, and the other PhD students of the lab - Hugo, Damien, Dominique and Pierre, among others.

Let me finish with a few special friends. Megyn, the Bright Star, who gave me a reason to hold on when I needed it the most. I get so much enthusiast about everything in life each time I talk to you. I owe you a Tardis for all of that - so let me just a few years to figure out how to build one :). And Nico and Jérémie, who have been changing my perception of life from the very beginning I've known them and have been making me discover new things on a daily basis without realizing it. You guys actually kept reminding me through this thesis why I decided to do research in the first place instead of taking it as routine work. I owe so much to the three of you.

Contents

Acknowledgements	v
Introduction	1
1 The Standard Model of particle physics and beyond	5
1.1 Fields and symmetries	6
1.1.1 Quantum field theory	6
1.1.2 Noether's theorem and gauge symmetries	8
1.2 The Standard Model of particle physics	10
1.2.1 The electroweak sector	11
1.2.2 The strong interaction	16
1.2.3 The success of the Standard Model	17
1.3 Shortcomings of the Standard Model	20
1.3.1 The hierarchy problem	20
1.3.2 Dark matter	22
1.3.3 Other open questions and criticism	23
1.4 Theories beyond the Standard Model	24
1.4.1 Zoology of Standard Model extensions	24
1.4.2 Supersymmetry	28
2 The Compact Muon Solenoid experiment at the LHC	35
2.1 The Large Hadron Collider	36
2.1.1 Scientific context and challenges	36
2.1.2 Beam injection, control and acceleration	37
2.1.3 Physics of pp collisions	39
2.1.4 LHC timeline and roadmap	42

2.2	The Compact Muon Solenoid experiment	43
2.2.1	The CMS detector	44
2.2.2	Trigger system	52
2.2.3	Object and event reconstruction	54
2.3	Collisions and detector simulations	62
2.3.1	Monte-Carlo generation of the hard scattering	63
2.3.2	Hadronization	64
2.3.3	Detector simulation	64
3	<i>b</i>-tagging techniques and validation in CMS	67
3.1	Topology of <i>b</i> jets and tagging algorithms	68
3.1.1	Properties of <i>B</i> hadrons and topology of <i>b</i> jets	68
3.1.2	<i>b</i> jets discriminating quantities and objects	70
3.1.3	<i>b</i> -tagging algorithms	74
3.2	<i>b</i> -tagging validation in the CMS collaboration	79
3.2.1	Context and validation method	80
3.2.2	Sample size and impact on performance estimation	80
3.2.3	Validation of the new jet size parameter for the Run II	82
3.2.4	Validation of new default pile-up rate for validation samples	83
3.2.5	Validation of the premixing technique for pile-up simulation	87
3.2.6	Studies of high pile-up scenario for Phase 2	89
4	Search for stop pair production at $\sqrt{s} = 8$ TeV	95
4.1	Context and phenomenology	97
4.1.1	Theoretical context and constraints	97
4.1.2	Phenomenology and signature	100
4.2	Analysis strategy and overview	106
4.3	Monte-Carlo generation and datasets	107
4.4	Objects and events selection	108
4.4.1	Trigger	108
4.4.2	Leptons	108
4.4.3	Jets and missing transverse energy	112

4.4.4	Events preselection	113
4.5	Signal region design and optimisation	114
4.5.1	Discriminating variables	117
4.5.2	Figure of merit and sensitivity estimation	125
4.5.3	Cut-based signal regions	128
4.5.4	BDT-based signal regions	130
4.6	Background estimation	132
4.6.1	Overview	132
4.6.2	Background normalization in the M_T -peak region	134
4.6.3	M_T -tail correction in the 0 b -tag region	135
4.6.4	Control of the $t\bar{t} \rightarrow \ell\ell$ component and second lepton veto	139
4.6.5	Control of variables at preselection level	141
4.6.6	Background prediction in the signal regions	143
4.7	Systematic uncertainties	144
4.7.1	Systematic uncertainties on the background	144
4.7.2	Systematic uncertainties on the signal	146
4.8	Signal contamination handling	147
4.9	Results and interpretation	149
4.9.1	Results and limits for the cut-based and BDT approaches	149
4.9.2	Combination with the search in two lepton channel	153
4.9.3	Comparison of polarization scenarios	153
4.9.4	Examination of an individual event and discussion	154
4.9.5	Comparison with other direct stop pair production searches	156
4.10	Perspectives	159
4.10.1	W -tagging in the high Δm regime	159
4.10.2	Sensitivity estimation for the Run II	166
	Conclusion	169
	Bibliography	173

Introduction

« It all has to do with habit. Mom has learned that people cannot fly. Thomas (the baby) has not. He still isn't certain what you can and cannot do in this world... [...] To children, the world and everything in it is new, something that gives rise to astonishment. [...] A philosopher never gets quite used to the world. To him or her, the world continues to seem a bit unreasonable – bewildering, even enigmatic... "Ladies and gentlemen," they yell, "we are floating in space!" »

Jostien Gaarder, *Sophie's world*

The philosophical and scientific approaches share a common fundamental element, which is to question the world around us instead of taking it for granted. When we gaze at the world, we see the clouds, the forests and the mountains, the architecture of the buildings in a city, the people sitting on the grass and chatting, the stars and the moon in the night sky. We experience the warm feeling of the sunshine, the wind against the skin, or the tone of a piano. As much as we can get amazed by all these objects and phenomena around us, we may also ask a myriad of questions about them. What are these bright dots in the sky and where do they come from? What is it that differentiate a tree from a rock? What is consciousness and how comes that a particular sequence of notes on a piano is able to affect it? And what does it all mean for our existence?

Among all these questions, the nature of the fundamental bricks composing everything we see is a fascinating and captivating interrogation for the human mind. What are the principles and laws guiding their organization? How can we learn about them? And will we ever be able to understand Nature for what it really is? Physics attempt to answer part of these questions using the scientific method. The first theories seeking to describe the fundamental bricks date back to the Classical Greece when Aristotle proposed that everything is made of a combination of the four elements earth, water, air and fire. Humanity has since well progressed in this understanding, with the discovery of the basic structure of the atoms by Thomson and Rutherford at the end of the 19th century. In the early 20th century, fundamental physics encountered an extraordinary change of paradigm with, on one hand, the discovery of quantum mechanics, describing the remarkable and unexpected properties of Nature at short distances, and on the other hand, the discovery

of special and general relativity, revealing the relations between energy, mass, space, time and gravitation.

Modern particle physics arised from the development of quantum field theory during the 20th century, effectively combining the understanding of the quantum world with classical field theory and special relativity. Around 1920 came the first formulation of quantum electrodynamics which turned out to yield quite reliable predictions. In parallel, during the middle of the century, many experiments investigated the properties of mesons and baryons, which eventually led to the discovery of quarks and quantum chromodynamic. Finally, around 1965, the Higgs mechanism was proposed as a way to explain the short range of the weak interaction and unify it with electromagnetism. Together, these elements helped to build the modern Standard Model of particle physics which has since been recognized to be one of the most successful scientific theory in the history of sciences.

After the discovery of the top quark in 1995 at the Tevatron by the CDF and D0 experiments, and the discovery of the tau neutrino in 2000 at Fermilab, the only missing piece of the Standard Model was an evidence for the existence of the Higgs boson. This evidence has been brought in 2012 by the ATLAS and CMS experiments, which claimed the discovery of a Standard Model-like Higgs boson with a mass around 125 GeV. Nevertheless, scientists have reasons to believe that the Standard Model is not the end of the story, despite its stunning success. As much as we have progressed in our understanding of the fundamental bricks of the Universe, many puzzles arose with it. In particular, we do not yet understand why the electroweak scale should be many orders of magnitude lower than the Planck scale, a puzzle known as the hierarchy problem. Furthermore, the existence of dark matter, a type of matter which seems to interact essentially through gravitation, is now a well established fact in modern cosmology, but its nature is not explained by the Standard Model of particle physics.

Many extensions of the Standard Model have been proposed to answer these various shortcomings. Among them, supersymmetry is a theory that add a new space-time symmetry relating fermions to bosons. Its theoretical success comes from its ability to answer many questions left by the Standard Model. In particular, the fermion-boson symmetry implicitly prevents the corrections to the Higgs mass from being too large, and in turn solves the hierarchy problem. Moreover, in many scenarios, supersymmetry predicts the existence of new stable, neutral and massive particles that could shed light on the dark matter problem.

The search for supersymmetry and other theories beyond the Standard Model (BSM) is currently part of the scientific program of the Large Hadron Collider (LHC). The LHC

program is a fantastic technical and human enterprise on which thousands of scientists and engineers are working. The LHC apparatus is a ring of several kilometers in radius designed to produce proton-proton collisions at an energy of 14 TeV in the center of mass, which are then recorded by four main experiments along the ring. At these energies, one may expect the production of yet unknown particles predicted by BSM theories and, by studying the particular experimental signature they would lead to, try to put them in evidence.

In the context of this thesis, we are looking for a signature essentially motivated by the so-called natural supersymmetry, in which no extensive fine-tuning of the parameters of the theory is needed to explain the observed value of the Higgs mass. The naturalness argument indicates that the scalar top quark (or stop), the superpartner of the top, should have a mass below around 1 TeV, and higgsinos-like neutralinos, which would be dark matter candidates, should be below around 500 GeV. The existence of such particles can be probed at the LHC, and their discovery would be a spectacular breakthrough for particle physics. The core of this thesis therefore relates to a search for stop pair production at the LHC, with a decay chain involving a neutralino being a dark matter candidate and leaving a characteristic signature of missing energy. The search is performed using the collisions recorded by the Compact Muon Solenoid (CMS) experiment during the first run of the LHC, with a center of mass energy of 8 TeV.

The thesis is organized as followed. In the first chapter, we go through a brief discussion of the key principles behind quantum field theory and the foundations of the Standard Model. Then, the shortcomings of the Standard Model are discussed, to finally introduce supersymmetry and in particular the Minimal Supersymmetric Standard Model. The second chapter discusses the experimental setup comprising the Large Hadron Collider and the Compact Muon Solenoid detector. In this chapter, we also introduce the techniques used to reconstruct and analyze the collisions. The third chapter describes in more detail the technique known as *b*-tagging which aims to identify jets originating from bottom (*b*) quarks. This technique is of particular importance for many Standard Model analyses and new physics searches involving top quarks, Higgs bosons or bottom quarks in general. In this regard, the work during this thesis consisted in the validation of the algorithms. This document highlights in particular the work that has been done in the context of the preparation of the Run II of the LHC, and the upgrades of the CMS detector.

Finally, the fourth chapter concentrates on the search for stop pair production with an experimental signature composed of one lepton, four jets, and missing energy. After discussing the phenomenology and signature of this search, the document presents the different contributions that were developed during this thesis. A focus is made on the design of a second lepton veto to reject one of the main background of the analysis.

After this, the design and optimization of the cut-based signal regions of the analysis are presented. The different aspects of the background estimation are discussed and in particular, the correction of the tail of the discriminating M_T variable, keystone of the analysis. Moreover, a problem of signal contamination has been identified in the control regions and we present how the background estimation is corrected during the interpretation of the results. After presenting the conclusions of the analysis, we go through prospective studies, first to investigate the use of W -tagging in the region with high difference between the stop and neutralino masses, and secondly to investigate the sensitivity of the analysis at the beginning of the Run II.

Chapter 1

The Standard Model of particle physics and beyond

« It's like when you're a kid. The first time they tell you that the world's turning and you just can't quite believe it 'cause everything looks like it's standing still.. I can feel it: the turn of the Earth. The ground beneath our feet is spinning at 1,000 miles an hour and the entire planet is hurtling around the sun at 67,000 miles an hour, and I can feel it. We're falling through space, you and me, clinging to the skin of this tiny little world. »

The Ninth Doctor

Contents

1.1	Fields and symmetries	6
1.1.1	Quantum field theory	6
1.1.2	Noether's theorem and gauge symmetries	8
1.2	The Standard Model of particle physics	10
1.2.1	The electroweak sector	11
1.2.2	The strong interaction	16
1.2.3	The success of the Standard Model	17
1.3	Shortcomings of the Standard Model	20
1.3.1	The hierarchy problem	20
1.3.2	Dark matter	22
1.3.3	Other open questions and criticism	23
1.4	Theories beyond the Standard Model	24
1.4.1	Zoology of Standard Model extensions	24
1.4.2	Supersymmetry	28

In this chapter, we go through the key points of modern particle physics. In [Section 1.1](#), we recall the main idea of quantum field theory and the relation between gauge symmetries and interactions. In [Section 1.2](#), we present the Standard Model of particles physics with a particular attention given to the spontaneous electroweak symmetry breaking via the Higgs mechanism. Then, [Section 1.3](#) discusses the shortcomings of the Standard Model with a particular focus on the hierarchy problem and dark matter. Finally, [Section 1.4](#) describes some of the theories beyond the Standard Model that attempt to address these shortcomings, and in particular supersymmetry.

1.1 Fields and symmetries

1.1.1 Quantum field theory

Before building the Standard Model, let's first introduce the fundamental objects that are used to build a particle physics theory, namely quantum fields. The concept of fields corresponds to degrees of freedom at each point of space-time. Originally used to describe electrodynamics, this concept was later found to suit well the description of many-particle systems with relativistic interactions, something that classical mechanics was not able to achieve.

Quantum field theory [[1](#), [2](#)] applies the idea of quantum mechanics to fields, by treating the field ϕ as an operator subject to commutation relations analogous to those of quantum mechanics algebra. The quantum field can then be expressed as a Fourier sum of quanta creation and quanta annihilation operators. In such a theory, a particle is a quanta of the field and can be seen as excitations (or ripples) on this field, much like a plane wave. Quantum field theory also introduces the important concept of virtual particles, which does not have any classical correspondence. Virtual particles can be interpreted as disturbances, or energy transiting through the field. A simple illustration is to consider two electrons being repelled, which is understood as coming from the exchange of virtual photons. Virtual particles are not observable *per se*, but are a crucial element in the understanding of particle physics phenomena and in the computations of physical observables such as process cross sections or masses.

The behavior of fields can be described using the powerful and concise Lagrangian formalism which introduces a quantity called the Lagrangian density (referred later as simply the Lagrangian):

$$\mathcal{L}(\phi, \partial_\mu \phi) = T(\phi, \partial_\mu \phi) - V(\phi, \partial_\mu \phi) \tag{1.1}$$

where the terms T and V describe respectively the kinetics and potential of the field ϕ . The least action principle states that one can obtain the equation of motion of a system by requiring that the action, defined from the Lagrangian as

$$\mathcal{S} \equiv \int_V \mathcal{L}(\phi, \partial_\mu \phi) d^4x, \quad (1.2)$$

is stationary with respect to an infinitesimal variation $\phi \rightarrow \phi + \delta\phi$. This principle yields the Euler-Lagrange equation:

$$\frac{\partial \mathcal{L}}{\partial \phi} - \partial_\mu \left(\frac{\partial \mathcal{L}}{\partial (\partial_\mu \phi)} \right) = 0 \quad (1.3)$$

which can be solved to obtain the equations of motion. This is why the Lagrangian is a core element, as it summarizes all the dynamic of the fields and can be used to derive the laws of Nature.

Fields with spin zero, also called scalar fields are usually noted ϕ . For a free complex scalar field with mass m , the dynamic is described by Klein-Gordon's Lagrangian:

$$\mathcal{L}_{\text{free scalar}} = \partial_\mu \phi \partial^\mu \phi - m^2 \phi^\dagger \phi. \quad (1.4)$$

Fields with spin one-half, also called fermionic fields, are described using a spinor usually noted ψ and are ruled by Dirac's Lagrangian:

$$\mathcal{L}_{\text{free fermion}} = \bar{\psi}(i\gamma^\mu \partial_\mu - m)\psi \quad \text{with} \quad \bar{\psi} = \psi^\dagger \gamma^0 \quad (1.5)$$

where γ^μ are the Dirac matrices. Finally, free fields with spin one are called vector fields, usually denoted A_μ , and are described by Maxwell's Lagrangian:

$$\mathcal{L}_{\text{free vector}} = -\frac{1}{4} F_{\mu\nu} F^{\mu\nu} \quad \text{with} \quad F_{\mu\nu} = \partial_\mu A_\nu - \partial_\nu A_\mu. \quad (1.6)$$

It is also possible to describe fields with spin three half or two, but these are beyond the scope of this document.

The structure of the Lagrangian \mathcal{L} can be easily analyzed knowing that a term with the form $\phi^\dagger \phi$ (or $\bar{\psi} \psi$) corresponds to a mass term for the field ϕ , and a term with the form $k \cdot \phi_1 \phi_2 \phi_3$ corresponds to an interaction between the fields $\phi_{i=1,2,3}$ with strength k . It is convenient to represent such an interaction using Feynman diagrams which provide a graphical and intuitive understanding of what is going on. The Feynman diagram corresponding to the term $k \cdot \phi_1 \phi_2 \phi_3$ is sketched on [Figure 1.1](#). In a sense, the goal of a particle physicist can be seen as using particles as a mean to understand which fields

exist, what their properties are and how they couple with each other.

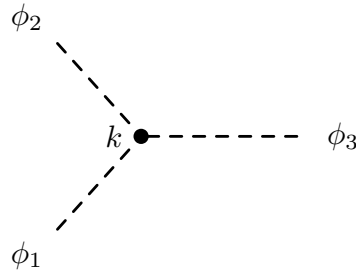


Figure 1.1: Example of vertex corresponding to the Lagrangian term $k \cdot \phi_1 \phi_2 \phi_3$.

1.1.2 Noether's theorem and gauge symmetries

A big part of the theoretical work in particle physics is related to the studies of the symmetries of the Lagrangian. One of the most remarkable theorem in physics is called the Noether theorem [3], stating that for every transformation of the space-time coordinates and fields that let the Lagrangian invariant, there are two quantities called current and charge which are conserved. This is a very powerful theorem as it creates a direct link between symmetries and the laws of Nature. Using this theorem on space-time symmetries, one can deduce for instance the conservation of energy-momentum from invariance of the Lagrangian according to space-time translations.

A particular interest goes into studying internal symmetries of the field, called gauge symmetries. Gauge transformations are transformations built from a gauge group and acting on the fields. They take the form:

$$\psi(x^\mu) \rightarrow U(x^\mu)\psi(x^\mu) \tag{1.7}$$

where U is an element of the group. If U does not depend on x^μ , the gauge is said to be global, while if it does depend on x^μ , the gauge is said to be local.

One of the most striking example of application of gauge symmetry is the emergence of quantum electrodynamics from the group $U(1)$. Let's start from the Dirac Lagrangian describing massive, non-interacting electrons with the field ψ_e ,

$$\mathcal{L} = \bar{\psi}_e(i\rlap{\not{\partial}} - m)\psi_e \quad \text{with} \quad \rlap{\not{\partial}} \equiv \gamma^\mu \partial_\mu. \tag{1.8}$$

We consider a $U(1)$ transformation,

$$\psi_e(x^\mu) \rightarrow e^{i \cdot q_e \cdot \theta(x^\mu)}\psi_e(x^\mu), \tag{1.9}$$

where we introduce q_e a constant, and θ parametrizing the transformation.

One easily finds that \mathcal{L} is invariant under global transformation (i.e. considering $\partial_\mu\theta = 0$) but not under local transformation. If we step back a little, we realize that the transformation from Equation (1.9) can be seen as a change in the phase of the field ψ_e . A global invariance corresponds to being able to offset the phase of the field in the same way across all the universe without changing the laws of physics. However, from the principle of locality, we know that what happens somewhere in the universe doesn't immediately affects a distant place. In a similar manner, the motivation to require local gauge invariance is that we should be able to vary continuously the offset on the phase of the field ψ_e across space-time without changing the laws of physics.

Local gauge invariance can be obtained by introducing a vector field A_μ which transforms according to

$$A_\mu \rightarrow A_\mu + \frac{1}{g}\partial_\mu\theta, \quad (1.10)$$

where g is an arbitrary constant we may call coupling constant, and replacing the derivative ∂ in the Lagrangian of Equation (1.8) by a covariant derivative \mathcal{D} :

$$\mathcal{D} \equiv \partial - i \cdot q_e g \cdot \gamma^\mu A_\mu \quad (1.11)$$

The Lagrangian becomes, after expansion,

$$\mathcal{L} = \underbrace{i\bar{\psi}_e\gamma^\mu\partial_\mu\psi_e}_{\psi_e \text{ kinetic}} - \underbrace{m\bar{\psi}_e\psi_e}_{\psi_e \text{ mass}} - \underbrace{iq_e g\bar{\psi}_e\gamma^\mu A_\mu\psi_e}_{\psi_e \leftrightarrow A_\mu \text{ interaction}} - \underbrace{\frac{1}{4}F_{\mu\nu}F^{\mu\nu}}_{A_\mu \text{ kinetic}}, \quad (1.12)$$

where the kinetic term of A_μ was added, with

$$F_{\mu\nu} \equiv \frac{i}{g}[D_\mu, D_\nu] = \partial_\mu A_\nu - \partial_\nu A_\mu. \quad (1.13)$$

There are now two kinetic terms, a mass term and an interaction term with strength $q_e g$ between ψ_e , the electron field, and A_μ , identified as the photon field. The constant q_e is interpreted as the electron charge, and g is the coupling constant of the interaction. To summarize, imposing a local gauge symmetry has led to introduce interaction between the two fields and the theory we obtained corresponds to quantum electrodynamics (QED).

This remarkable result was generalized to non-abelian groups $SU(n)$ by Yang and Mills [4]. In the Yang-Mills theory, fields are associated to a representation in $SU(n)$, which determines how they transform [5]. Fields either belong to the trivial (or singlet) representation which are left unaffected by the gauge transformation, or to the fundamental

representation in which they transform according to

$$\psi(x^\mu) \rightarrow e^{i \cdot t_k \theta^k(x^\mu)} \psi(x^\mu), \quad (1.14)$$

where θ^k are arbitrary values and t_k are the $n^2 - 1$ generators of $SU(n)$ satisfying the Lie algebra commutation relations. To get an invariance with respect to this transformation, one is forced to introduce $n^2 - 1$ vector gauge bosons A_μ^k which belong to the adjoint representation of $SU(n)$. The covariant derivative for the fields in the fundamental representation becomes

$$D\!\!\!/ = \not{\partial} - i \cdot g \cdot \gamma^\mu t_k A_\mu^k. \quad (1.15)$$

An important feature of non-abelian groups is that additional terms appear because the matrices t_k do not commute, and correspond to interaction terms between the gauge bosons A_μ^k .

1.2 The Standard Model of particle physics

The Standard Model [6, 7] reflects our current understanding of particle physics. It is a quantum field theory constructed with the following ingredients:

- the fermionic fields and their properties ;
- the gauge symmetries corresponding to interactions ;
- one scalar field called the Higgs field.

The Standard Model includes two interactions: electroweak and strong. The electroweak sector corresponds to the gauge group $U(1)_Y \times SU(2)_L$ where Y and L stand for weak hypercharge and weak isospin. A notable property of this interaction is how it affects differently left-handed fermions from right-handed ones. This interaction is spontaneously broken by the Higgs field, leading to the known electromagnetism $U(1)_Q$. The gauge group describing the strong interaction is $SU(3)_C$, where C stands for color. This is an unbroken symmetry with $3^2 - 1 = 8$ associated gauge bosons. The symmetries of the Standard Model can be summarized under this form:

$$\underbrace{SU(3)_C}_{\text{strong}} \times \underbrace{SU(2)_L \times U(1)_Y}_{\text{electroweak}} \xrightarrow[\text{mechanism}]{\text{Higgs}} \underbrace{SU(3)_C}_{\text{strong}} \times \underbrace{U(1)_Q}_{\text{electromagnetism}}. \quad (1.16)$$

The fermionic fields of the Standard Model are categorized according to their properties: quarks are fields that carry both electroweak charges and colors, whereas leptons

1 st gen.	2 nd gen.	3 rd gen.	$SU(3)_C$	$SU(2)_L$	$U(1)_Y$
Q_L^1	Q_L^2	Q_L^3	3	2	1/3
U_R^1	U_R^2	U_R^3	3	1	4/3
D_R^1	D_R^2	D_R^3	3	1	-2/3
Λ_L^1	Λ_L^2	Λ_L^3	1	2	-1
E_R^1	E_R^2	E_R^3	1	1	-2

Table 1.1: Fundamental fermionic fields of the Standard Model and their representations in the different gauge groups.

carry only electroweak charges. Fermions are initially massless and acquire a mass via the electroweak symmetry breaking. They are grouped into three families, or generations, sharing the same charges and representations as shown on [Table 1.1](#). While it is common to write directly the left-handed fermions with lowercase letters, let us write them for the moment with uppercase letters to emphasize that these flavour states are not necessarily the mass states. Similarly, it is common to explicitly write the fields Q_L and Λ_L as $SU(2)$ doublets involving the right-handed counterparts of the left-handed fermions U_R , D_R and E_R . However, we decide here to not introduce any psychological bias in the writing to show how these $SU(2)$ components can naturally be identified after the electroweak symmetry breaking.

1.2.1 The electroweak sector

From the way gauge bosons behave with respect to a gauge transformation, as seen in [Equation \(1.10\)](#), it can be deduced that a gauge boson can not be massive as the corresponding term would break gauge invariance:

$$m^2 A_\mu A^\mu \neq m^2 \left(A_\mu + \frac{1}{g} \partial_\mu \theta \right) \left(A^\mu + \frac{1}{g} \partial^\mu \theta \right). \quad (1.17)$$

Following this remark, one of the big challenge of particle physics around the 50's was to understand why the weak interaction was short-range whereas the electromagnetic interaction is infinite-range. To be able to describe an interaction with range $\mathcal{O}(d)$, one would need a massive mediator with a mass $m \sim d^{-1}$. Attempting to describe the weak interaction with an $SU(2)_L$ gauge symmetry alone therefore proved unsuccessful.

Nevertheless, a remarkable property of some physical systems is how their symmetry can be spontaneously broken. To understand this, a straightforward experience is to place a pen perpendicular to a table. This system exhibits an invariance by rotation around the axis of the pen. However, it is in an unstable configuration and as soon as the pen is released, micro-fluctuations makes it fall in one particular direction. Despite the fact

that the set of all possible outcomes is symmetric by rotation, the fact that only one of this outcome can be realized at a time breaks the cylindrical symmetry of the system.

The keystone of the Standard Model is the successful application of this idea to the electroweak symmetry $U(1)_Y \times SU(2)_L$ to obtain massive gauge bosons and massive fermions, via a spontaneous breaking of this symmetry introduced by R. Brout, F. Englert [8] and P. Higgs [9].

Spontaneous breaking of the electroweak symmetry

In this subsection, we propose to describe explicitly how the introduction of the Higgs field leads to the spontaneous breaking of the electroweak symmetry [10]. Let's introduce a complex scalar ϕ , which has a charge +1 under $U(1)_Y$, and is a doublet under $SU(2)_L$ and a singlet under $SU(3)_C$. As a $SU(2)_L$ doublet, ϕ may be written:

$$\phi = \begin{pmatrix} \phi_1 \\ \phi_2 \end{pmatrix} = \frac{1}{\sqrt{2}} \begin{pmatrix} h_1 \cdot e^{i\theta_1} \\ h_2 \cdot e^{i\theta_2} \end{pmatrix}. \quad (1.18)$$

According to Equation (1.1), the Lagrangian of ϕ can be written with the kinetic part on one hand, and potential on the other hand:

$$\mathcal{L} = D_\mu \phi D^\mu \phi - V(\phi), \quad \text{with} \quad V(\phi) = \mu^2 |\phi|^2 + \lambda |\phi|^4. \quad (1.19)$$

The key point here is to choose the right shape for the potential V . For $\mu^2 < 0$ and $\lambda > 0$, one gets a non-trivial shape sketched on Figure 1.2, with a degenerated minima for $V(\phi)$ satisfying

$$|\phi| = \sqrt{\phi^\dagger \phi} = \frac{v}{\sqrt{2}}, \quad \text{with} \quad v \equiv \sqrt{\frac{-\mu^2}{\lambda}}. \quad (1.20)$$

Because the symmetry is local, we may perform different isospin rotations for different values of x^μ and define the unitary gauge such that $h_1 = \theta_1 = \theta_2 = 0$ and $h_2(x^\mu) = v + h(x^\mu)$ with $h = 0$ in the vacuum. v therefore corresponds to the vacuum expectation value of the Higgs field, and h to a longitudinal excitation of the field, as summarized on Figure 1.2. Note that even though this choice is arbitrary, one may work with h_1 instead of h_2 and still obtain a consistent picture at the end. In our case, ϕ takes the form

$$\phi = \begin{pmatrix} \phi_1 \\ \phi_2 \end{pmatrix} = \frac{1}{\sqrt{2}} \begin{pmatrix} 0 \\ v + h \end{pmatrix}. \quad (1.21)$$

To understand how this field impacts the physics of $SU(2)_L \times U(1)_Y$, let us look at

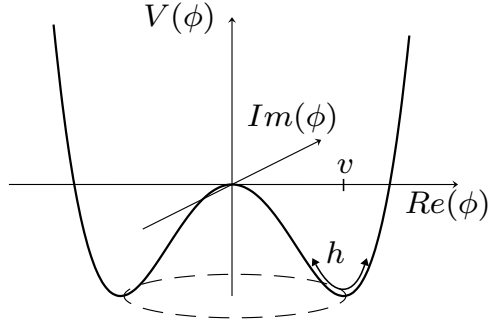


Figure 1.2: Representation of the Higgs potential with $\mu^2 < 0$ and $\lambda > 0$. The factor $1/\sqrt{2}$ is omitted for clarity.

the covariant derivative. We note $W^{i=1,2,3}$ and B the gauge bosons and g_W and g_B the coupling constants associated to $SU(2)_L$ and $U(1)_Y$ respectively. The covariant derivative writes

$$\begin{aligned} D_\mu \phi &= \partial_\mu \phi - ig_B B_\mu \phi - ig_W t_a W_\mu^a \phi \\ &= \partial_\mu \phi - i \begin{pmatrix} g_W W_\mu^3 + g_B B_\mu & g_W (W_\mu^1 - iW_\mu^2) \\ g_W (W_\mu^1 + iW_\mu^2) & -g_W W_\mu^3 + g_B B_\mu \end{pmatrix} \phi. \end{aligned} \quad (1.22)$$

This covariant derivative can be rewritten under the form

$$D_\mu \phi = \partial_\mu \phi - i \begin{pmatrix} \frac{g_W^2 - g_B^2}{g_{WB}} Z_\mu + \frac{2g_W g_B}{g_{WB}} A_\mu & g_W W_\mu^- \\ g_W W_\mu^+ & -g_{WB} Z_\mu \end{pmatrix} \phi, \quad (1.23)$$

where we introduced the following notation which will become convenient:

$$\begin{aligned} g_{WB} &\equiv \sqrt{g_W^2 + g_B^2} \\ W^\pm &\equiv W^1 \pm iW^2 \\ \begin{pmatrix} Z \\ A \end{pmatrix} &\equiv \frac{1}{g_{WB}} \begin{pmatrix} g_W & -g_B \\ g_B & g_W \end{pmatrix} \begin{pmatrix} W^3 \\ B \end{pmatrix}. \end{aligned} \quad (1.24)$$

Expanding the kinetic term of ϕ , one find the following terms appearing:

$$\begin{aligned} D_\mu \phi D^\mu \phi &= \underbrace{\frac{1}{2} \partial_\mu \phi \partial^\mu \phi}_{h \text{ kinetic}} + \underbrace{\left(\frac{v^2 g_W^2}{2}\right) W_\mu W^\mu}_{\text{massive } W^\pm} + \underbrace{\left(\frac{v^2 g_{WB}^2}{2}\right) Z_\mu Z^\mu}_{\text{massive } Z} + \underbrace{(0) A_\mu A^\mu}_{\text{massless } A_\mu} \\ &+ \underbrace{(vg_W) h W_\mu W^\mu}_{hWW \text{ interaction}} + \underbrace{(vg_{WB}) h Z_\mu Z^\mu}_{hZZ \text{ interaction}} + \underbrace{\left(\frac{g_W^2}{2}\right) hh W_\mu W^\mu}_{hhWW \text{ interaction}} + \underbrace{\left(\frac{g_{WB}^2}{2}\right) hh Z_\mu Z^\mu}_{hhZZ \text{ interaction}}. \end{aligned} \quad (1.25)$$

And the potential term yields, up to a constant,

$$V(\phi) = \underbrace{(\mu^2)hh}_{h \text{ mass}} + \underbrace{(\lambda v)hhh}_{hhh \text{ interaction}} + \underbrace{\left(\frac{\lambda}{4}\right)hhhh}_{hhh \text{ interaction}} . \quad (1.26)$$

Introducing the $SU(2)$ doublet ϕ with the right properties therefore lead to two things. First, the prediction of a scalar, observable boson h which is called the Higgs boson and is a radial excitation of the Higgs field. Second, new terms in the Lagrangian that break the invariance under $SU(2)_L \times U(1)_Y$, namely the mass terms of W and Z bosons which are the mass eigenstates of the W^i and B bosons. This can be summarized by saying that the breaking of the symmetry leads to four massless Goldstone bosons, one for each degree of freedom of the Higgs field. Three of them are absorbed by the W^i and B bosons leading to the massive W^\pm and Z , while the last degree of freedom leads to the massive Higgs boson h .

We find that the Lagrangian is now invariant under a symmetry $U(1)_Q$ with $Q \equiv Y + L^3$ which is identified as the electromagnetic interaction, and whose gauge boson is the massless A_μ which is identified as the photon. With respect to electromagnetism, right-handed quarks U_R and D_R get charges equal to $2/3$ and $-1/3$, and right-handed leptons E_R get charges equal to -1 . The components of Λ_L under $SU(2)_L$, $\Lambda_L = (\lambda_{+L}, \lambda_{-L})$, have electromagnetic charges equal to 0 and -1 . Since λ_{-L} now transforms the same way than E_R under $SU(3)_C \times U(1)_Y$, we are tempted to simply call it E_L . The same observation goes for the components of the left-handed quarks Q_L which we are tempted to call U_L and D_L .

Fermions masses and mass eigenstates

Since we introduced a new field ϕ , we may introduce also new terms in the Lagrangian corresponding to couplings between the scalar field ϕ and the fermion fields, so-called Yukawa couplings. Such terms can exist provided that they respect the symmetry of the Lagrangian. For instance, terms of the form ϕ -quark-lepton can *not* be introduced as they would break the $SU(3)_C$ invariance. However, we can introduce terms of the form $E_R^i \phi^\dagger \Lambda_L^j$. Notice how i is not necessarily equal to j , meaning that there can be mixing

between two different generations. All the terms for leptons can be written with the form:

$$\begin{aligned}\mathcal{L}_{\text{Yukawa}} &= -\sum_{i,j}(y^{ij}\bar{E}_R^i\phi^\dagger\Lambda_L^j + \text{h.c.}) && \text{with } \Lambda_L = \begin{pmatrix} N_L \\ E_L \end{pmatrix} \text{ under } SU(2) \\ &= -\frac{v+h}{\sqrt{2}}\sum_{i,j}(y^{ij}\bar{E}_R^iE_L^j + \text{h.c.})\end{aligned}\quad (1.27)$$

where h.c. is the Hermitian conjugate. The matrix y^{ij} is not necessarily diagonal. However we can redefine the flavor eigenstates Λ_L and E_R^i such that y^{ij} is diagonal. Let's label these eigenstates (e, μ, τ) . We simply obtain:

$$\begin{aligned}-\mathcal{L}_{\text{Yukawa}} &= \left(\frac{y_e v}{\sqrt{2}}\right) \cdot \bar{e}_R e_L + \left(\frac{y_\mu v}{\sqrt{2}}\right) \cdot \bar{\mu}_R \mu_L + \left(\frac{y_\tau v}{\sqrt{2}}\right) \cdot \bar{\tau}_R \tau_L \\ &\quad + \left(\frac{y_e}{\sqrt{2}}\right) \cdot h \bar{e}_R e_L + \left(\frac{y_\mu}{\sqrt{2}}\right) \cdot h \bar{\mu}_R \mu_L + \left(\frac{y_\tau}{\sqrt{2}}\right) \cdot h \bar{\tau}_R \tau_L \\ &\quad + \text{h.c.}\end{aligned}\quad (1.28)$$

The first line shows how the vacuum expectation value v leads to mixing between the *a priori* unrelated e_L and e_R fields. We may simply summarize the situation by saying that the field $e \equiv (e_R, e_L)$ obtains a mass term $\frac{y_e v}{\sqrt{2}} \bar{e} e$. Additionally, on the second line, the field e couples to the Higgs boson with strength $\frac{y_e}{\sqrt{2}}$. The remaining component of the Λ_L^i are relabelled $(\nu_{e,L}, \nu_{\mu,L}, \nu_{\tau,L})$ and remain massless as they don't have any ν_R counterpart to mix with. It should also be noticed how these mass terms for fermions are different from those of the gauge bosons. The masses of gauge bosons are directly determined by the electroweak coupling constants and Higgs field expectation value while the fermion masses are related to new free parameters y .

The situation for quarks is analogous to leptons, with the exception that both components of Q_L have a right-handed fermion to mix with. A complication appears, as it is not possible to simultaneously diagonalize the Yukawa matrices of the up-type quarks and down-type quarks. We therefore only diagonalize the up-type matrix and label the new flavor and mass eigenstates with (u, s, t) . For the down-type quarks, relabelled with (d, c, b) , there remain off-diagonal elements which mix the different flavor eigenstates, necessary to describe the data and corresponding to the so-called CKM matrix.

Table 1.2 summarizes the observable fermions after breaking the electroweak symmetry and their associated charges.

1 st gen.	2 nd gen.	3 rd gen.	$SU(3)_C$	$U(1)_Q$
u	s	t	$\mathbf{3}$	$2/3$
d	c	b	$\mathbf{3}$	$-1/3$
$\nu_{e,L}$	$\nu_{\mu,L}$	$\nu_{\tau,L}$	$\mathbf{1}$	0
e	μ	τ	$\mathbf{1}$	-1

Table 1.2: Observable fermionic fields after breaking of the electroweak symmetry by the Higgs field, and their representations under $SU(3)_C \times U(1)_Q$.

1.2.2 The strong interaction

The group $SU(3)$ corresponds to the strong interaction which affects quarks. The associated gauge bosons are called the gluons and the charge is called color, which is at the origin of the name quantum chromodynamic (QCD), in analogy to quantum electrodynamic. As $SU(3)$ is a non-abelian group, the gluons are also carrying color and interact with each other. The adjective *strong* relates to the value of the coupling constant, being larger than the weak interaction by a factor $\mathcal{O}(100)$ at the QCD scale which is $\mathcal{O}(200 \text{ MeV})$. The Lagrangian writes:

$$\mathcal{L}_{\text{QCD}} = \bar{\psi}(i\not{D} - m)\psi - \frac{1}{4}G_{\mu\nu}^a G_a^{\mu\nu}, \quad (1.29)$$

with the gluonic field tensors $G_{\mu\nu}^a$ equal to

$$G_{\mu\nu}^a = \partial_\mu A_\nu^a - \partial_\nu A_\mu^a + gf_{abc}A_\mu^b A_\nu^c. \quad (1.30)$$

$SU(3)$ is unbroken and therefore its associated gauge bosons, the gluons, are massless. Because of this, one could conclude that the range of the strong interaction is infinite just like electromagnetism is. However, the strong coupling constant α_S tends to zero at high-energies and to infinity at low energies. This leads to the two following key, and rather counterintuitive, features of the strong interaction.

At high energies, i.e. short distances, two colored particles are not much affected by each other presence, a phenomenon referred to as asymptotic freedom [11]. In comparison, if one would consider the analogous situation in electromagnetism, two charged particles close to each other feel important attraction or repulsion and are therefore not free. In this regime, α_S is small and a reasonably good understanding and predictions can be obtained from perturbative QCD.

At low energies, i.e. long distances, the intensity of the interaction grows. As a consequence, to split a hadron into individual quarks, the system needs energy up to a point where this energy will be converted into new colored particles coming out of vacuum,

and will form new hadrons. This leads to the concept of confinement and explains why it is not possible to observe free quarks or gluons in nature [12]. Interestingly, confinement is a property which is still not completely demonstrated from a mathematical point of view. Moreover, confinement results in hadrons, such as the proton, having a structure that cannot be computed analytically from perturbative QCD: one must instead rely on experimental measurements.

In the context of high energy physics, confinement translates into the production of jets of hadrons when quarks or gluons are produced in collisions. Jet physics is therefore a crucial aspect when reconstructing an event in a particle collider.

In the previous section, we have seen how the particle masses arise from the introduction of the Higgs field breaking the symmetry. It is remarkable to notice that the masses of hadrons, which ultimately composes everyday matter, come essentially from the kinetic and binding energy holding the quarks, and not from the quark masses themselves. This is related to the fact that, in a simple model with two quarks u and d , the mass term of the quarks, $m\bar{q}q = m(\bar{q}_Lq_R + \bar{q}_Rq_L)$, breaks the $SU(2)_L \times SU(2)_R$ invariance of the QCD Lagrangian, down to an isospin symmetry $SU(2)_V$.

1.2.3 The success of the Standard Model

Let us now briefly review the success of the Standard Model. It includes 19 free parameters: nine fermion masses, one scalar mass, three coupling parameters, four quark mixing matrix parameters, the Higgs vacuum expectation value and the strong CP-violating phase.

The physical observables such as the cross-section associated to a given process can be predicted following a perturbative development. For instance, the observation of the process $e^+e^- \rightarrow \mu^+\mu^-$ in a theory containing only a $U(1)_Q$ interaction is given by the superimposition of all possible processes leading to the final state as represented on [Figure 1.3](#). A given observable can be computed at leading-order (LO) by considering only the first diagram in the development or next-to-leading-order (NLO) and so on with increasing accuracy. For instance on [Figure 1.3](#), if α characterize the strength of the $ee\gamma$ and $\mu\mu\gamma$ vertices, then the LO diagrams corresponds to terms proportional to α^2 while NLO diagrams corresponds to terms proportional to α^4 . As one consider higher orders diagrams, one may start to be sensitive to other parts of the Lagrangian. For instance, if we now include QCD in the previous example, and consider higher order diagrams, we will eventually have diagrams containing gluon loops or top loops. This makes virtually any observable sensitive, to some extent, to all Nature's Lagrangian. Therefore, precise

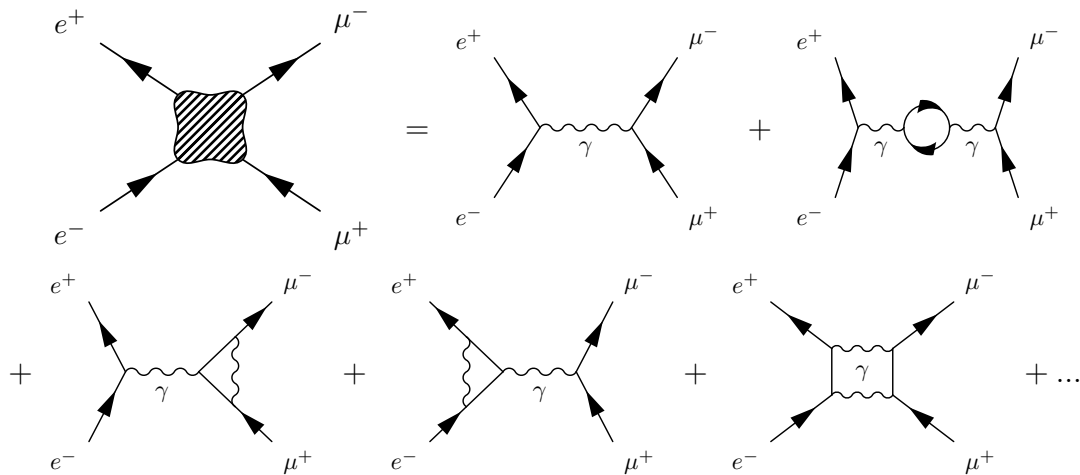


Figure 1.3: Illustration of the process $e^+e^- \rightarrow \mu^+\mu^-$ in a model with only electrons and muons coupling to a photon.

measurements of observables allow to check the consistency of the theory, and any significant deviation between theory and experiment could be interpreted as caused by a missing piece in the theory.

In this perspective, the parameters and the consistency of the Standard Model have been extensively measured and tested in several experiments, in particular at the LEP collider [13], the Belle and BaBar experiments [14], and at the Tevatron collider [15]. In 2012, the CMS and ATLAS experiments at the LHC discovered the last remaining particle of the Standard Model, the Higgs Boson with a mass $m_h \sim 125$ GeV [16, 17]. The mass spectrum of the particles of the Standard Model is summarized on Figure 1.4 and shows a clear hierarchy between the different fermion generations.

Figure 1.5 shows the result of a global fit of the electroweak Standard Model observables [18]. In such a procedure, the observables are fitted simultaneously according to the model, using as input the experimental measurements. After the fit, the resulting values for each observable (O_{fit}) are compared to the experimental measurement ($O_{\text{meas.}}$). The difference is finally compared to the experimental uncertainty ($\sigma_{\text{meas.}}$). This allows to have a global test of the consistency of the model, as any significant deviation between the predicted and measured values would indicate a flaw. The results shows that the theory is quite consistent, as no deviation larger than 3σ is found.

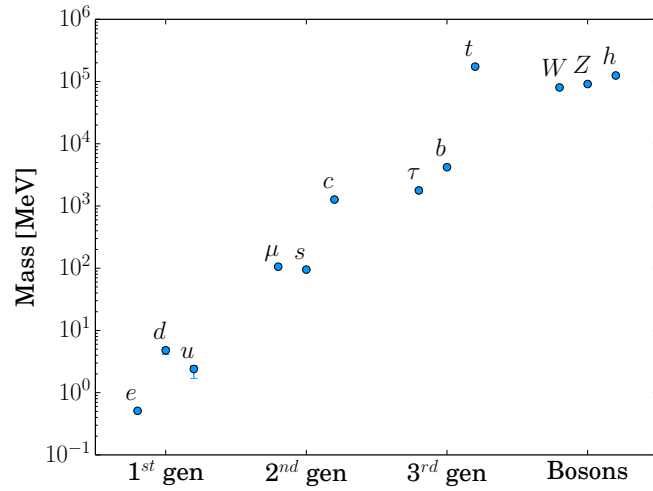


Figure 1.4: Masses of the fermions and bosons of the Standard Model. The photon γ , gluon g and neutrinos ν_ℓ are not represented as they are massless in the context of the Standard Model.

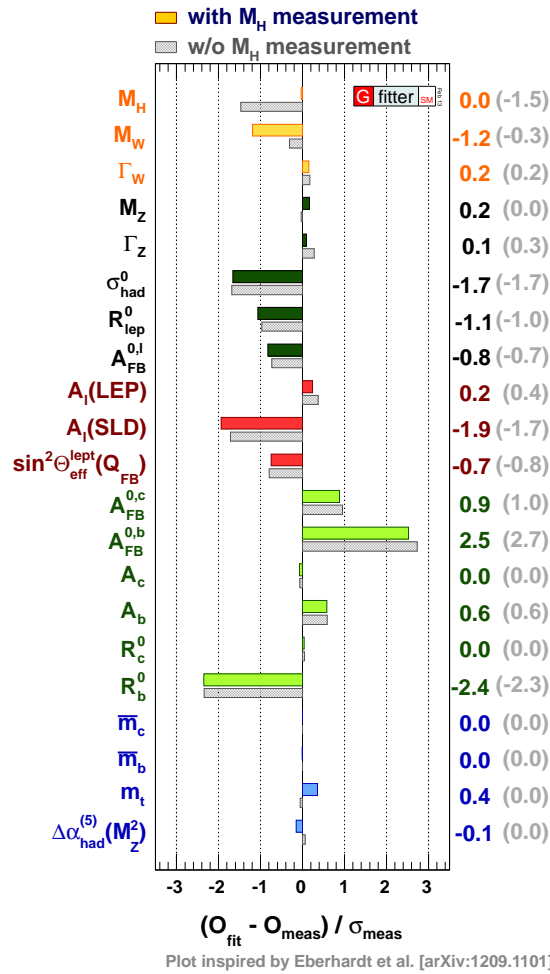


Figure 1.5: Global fit of observables of the electroweak Standard Model [18].

1.3 Shortcomings of the Standard Model

Despite its success, the Standard Model contains theoretical open questions and unexplained experimental facts. For these reasons, it is considered as incomplete or as an effective theory valid only up to an upper bound in energy. In this section, we focus especially on the hierarchy problem and dark matter as they will be the most relevant one in the context of this document, and discuss briefly other open questions.

1.3.1 The hierarchy problem

The hierarchy problem is related to the radiative corrections of the Higgs boson mass. To have a complete understanding of the problem, let's first look at the case of the mass of fermions and gauge bosons before looking at the Higgs [19].

To compute a physical observable in a quantum field theory, one needs to integrate over all possible quantum corrections related to this parameter. In the case of the cross-section of a process, this means considering all loops and diagrams with the same initial and final states. For the mass of a particle, one is interested in diagrams that contribute to the propagator. An example of diagram contributing to the propagator of the electron is given in Figure 1.6. We may express the observable mass m_e of the electron as the sum of the bare mass m_e^0 , that is to say the actual parameter one writes in the Lagrangian, and Δm_e representing the contributions from the quantum corrections:

$$m_e^2 = m_e^{02} + \Delta m_e^2. \quad (1.31)$$

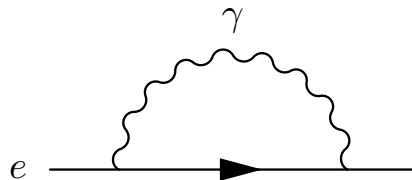


Figure 1.6: Example of contribution to the electron propagator.

In effective theories, the computation of quantum corrections is done with respect to an energy cutoff Λ , representing the scale at which new physics is expected to play a significant role. In the case of Figure 1.6, this means that we shall integrate over all momentum inside the loop, up to the scale Λ . For instance, if one considers electrodynamics

as an effective theory of the electroweak symmetry, at one-loop level, the correction is given by:

$$\Delta m_e \simeq \frac{\alpha}{4\pi} m_e^0 \ln \left(\frac{\Lambda}{m_e^0} \right). \quad (1.32)$$

With $\Lambda = \Lambda_{\text{electroweak}} = \mathcal{O}(100 \text{ GeV})$, we find that $\frac{\Delta m_e}{m_e} \sim 20\%$. It is a relatively small correction, in the sense that it is not surprising to have a mass for the electron that is $\mathcal{O}(1 \text{ MeV}) \ll \Lambda_{\text{electroweak}}$. The most important feature in Equation (1.32) is the fact that Δm_e is proportional to m_e^0 and not Λ as it means that the mass will not skyrocket as Λ grows.

There is a remarkable and more general property behind this term, which is that a gauge invariant Lagrangian cannot generate corrections that break the symmetry. In the case of electrodynamics with a massive electron, the mass term is already breaking the chiral symmetry $U(1)_L \times U(1)_R$, but because this is a so-called soft-breaking term (i.e. from spontaneous symmetry breaking), the property should still hold in the limit where $m_e^0 \rightarrow 0$. Therefore the correction cannot be proportional to Λ but only to m_e , by dimensional analysis. It is common to refer to this by saying that chiral symmetry protects the mass of fermions from diverging. The same fact is observed for gauge bosons masses in the case of the electroweak symmetry breaking by the Higgs field: here, the gauge bosons are protected by the gauge invariance.

Regarding the mass of the Higgs boson, the Standard Model does not include any mechanism that prevents the mass of a scalar boson from diverging. The actual computation for the correction from a fermion loop gives:

$$\Delta m_h^2 \propto G_F m_f^2 \Lambda^2, \quad (1.33)$$

which diverges with Λ . If one believes that the Standard Model is valid up to the Planck scale, where gravity is expected to play a significant role, then the observable Higgs mass can be written as

$$m_h^2 \simeq m_h^{02} + \kappa \cdot m_{\text{Planck}}^2 \quad (1.34)$$

where κ is a function of the Standard Model parameters. The three quantities m_h^0 , κ , and m_{Planck} are *a priori* unrelated to each other from the point of view of the theory. Hence, unless the parameters of the Standard Model conspire with each other and are *fine-tuned* at twenty decimal places, there is no reason to expect that $m_h \ll m_{\text{Planck}}$. However, we observe that $m_h \sim \mathcal{O}(10^2 \text{ GeV}) \ll m_{\text{Planck}} \sim \mathcal{O}(10^{19} \text{ GeV})$, which is not natural. This is referred to as the hierarchy problem, as from these considerations there is no reason to expect such a large hierarchy between the electroweak scale and the Planck scale.

1.3.2 Dark matter

Dark matter is one of the greatest mystery in current cosmology and fundamental physics. The first observation leading to the dark matter hypothesis came from the measurement of rotation curves of galaxies [20]. These curves showed the evolution of the orbital velocity of stars inside galaxies as function of their distance to the galactic center. One can predict such curves by inferring the galaxy's mass repartition from models and spectrometry, and applying Newton's law of gravitation. The observed curves are well-described for the central region of the galaxy but then instead of decreasing with distance as predicted, were found to stay approximately constant.

This observation suggested that there is a halo of invisible matter around galaxies, interacting gravitationally but not electromagnetically with the rest of the matter, hence the denomination of *dark* matter. Further experimental measurements provided indirect evidences for the existence of such dark matter [21]. Among them, the technique of gravitational lensing allows to infer the distribution of the mass inside a galaxy or a cluster from the bending of the light emitted by an object further in the background. Nowadays, dark matter is part of the standard model of cosmology as there are many astrophysical and cosmological phenomena which cannot be described without it, and has been found to represent $\mathcal{O}(80\%)$ of the matter content of the universe.

However the nature of dark matter is still unknown and it has not been directly observed. Dark matter candidates must be gravitationally interacting, not be short-lived and must not be baryonic. Last but not least, it must also be cold, meaning that it must have low kinetic energy, which rules out neutrinos as dark matter candidates [22]. It is now commonly admitted that there is no suitable candidate for it in the Standard Model.

If one assumes that dark matter is made of a single particle X thermally produced in the early universe, then it is possible, using the Boltzmann equation, to compute the relic density Ω_X [21, 23, 24]. This relic density is proportional to m_X^2/g_X^4 where m_X is the mass of the dark matter particle and g_X is the coupling constant in the co-annihilation process $XX \leftrightarrow f\bar{f}$. It is remarkable to note that taking $\Omega_X = \mathcal{O}(0.1)$ from cosmological observations and $g_X \sim 0.6$ from the weak interaction, we expect $m_X = \mathcal{O}(100 \text{ GeV})$. This encourages physicists to look for weakly interacting massive particles (or WIMPs) which are predicted by many models beyond the Standard Model.

1.3.3 Other open questions and criticism

Other open questions or unexplained facts strengthen the belief that the Standard Model is not the final theory.

- **Dark energy** - The standard model of cosmology, so-called Λ CDM model, contains a non-zero cosmological constant Λ . The cosmological constant is initially an additional authorized term in Einstein's equation which relates space-time curvature to energy-momentum. Such term is necessary to explain the observed accelerated expansion of the universe from the study of the redshift of supernovas. The cosmological constant can be interpreted as vacuum energy, often referred to as dark energy. Despite the fact that this is in principle in agreement with quantum field theory which predicts vacuum energy from quantum fluctuations, there is a complete mismatch, of $\mathcal{O}(10^{120})$, between the small measured value of Λ and its prediction by quantum field theory [25]. This is often called the vacuum catastrophe or the worst prediction in the history of physics. A big challenge of current physics therefore consists in understanding the nature of dark energy and the reason why it is so small compared to predictions.
- **Matter-antimatter asymmetry** - It is a well established fact that the baryonic content of the Universe is made of matter. Because matter and antimatter should have been produced in equal proportion during the big bang, there must be sources of asymmetry that led to a state dominated by matter. Sakharov [26] established a set of conditions that would induce such an asymmetry. Among them is the violation of the symmetries C (charge) and CP (charge-parity). The Standard Model with massless neutrinos contains two sources of CP-violation originating from the CKM matrix and the CP-violating phase in the QCD sector. So far however, these sources are not important enough to explain the magnitude of the baryon asymmetry [27].
- **Neutrino masses** - It has been measured by experiments that neutrinos can oscillate from one flavor to another. This indicates that neutrinos should be massive and have different flavor states than mass states much like down-type quarks and the CKM matrix. The problem of neutrinos being massive is itself not so much a problem as it is possible to introduce right-handed neutrinos in the field content of the Standard Model. However the exact mechanism depends on whether neutrinos are Dirac or Majorana fermions. The main source of interrogation is to understand why neutrinos have such a small mass compared to the other fermions.
- **Strong CP problem** - As introduced before, there is a term allowed in the QCD Lagrangian that introduces CP-violation via a phase θ . The value of this parameter

has been so far found to be very close to zero despite lack of theoretical arguments for it not to be of the order of 1. This situation is similar to the hierarchy problem for which we can expect that a hidden mechanism protects this phase to be too different from zero.

- **Quantum gravity description** - Gravitation is currently not described by the Standard Model. The underlying problem, which is to know how to unify general relativity with quantum field theory, is one of the biggest problem of modern physics. If it exists, the gauge boson associated to gravitation would need to have a spin equal to 2. It is however not known if and how such a theory would be renormalizable as it leads to uncancellable divergences.
- **Forces unification** - Several times in the history of physics, phenomenons have been understood to have a common structure and been unified. The simple name electromagnetism has in its etymology a clear reference to electrodynamic and magnetism. It is therefore natural for physicists to look for possibilities of unification, in our case regarding the electroweak and strong interaction, and ultimately with gravitation.
- **Free parameters and arbitrary field content** - Finally, there are conceptual interrogations about the fact that the quarks have such different masses, in particular regarding the top quark as it is the heaviest known particle. The same kind of conceptual interrogations goes about the number of fermion families: is there any fundamental reason to have three families instead of one, two, or an infinity of them? More generally, there are numerous facts about the Standard Model parameters and field content that feel arbitrary and may hide an underlying, more fundamental pattern.

1.4 Theories beyond the Standard Model

1.4.1 Zoology of Standard Model extensions

Since a few decades, extensions to the Standard Model have been proposed and studied with the aim to address its shortcomings. One can attempt to categorize them as function of the fundamental ingredients they add to the theory, either additional symmetries, space-time dimensions or field content.

Additional or extended symmetries

One of the possibility to extend the Standard Model is to look at symmetries. There are different kind of symmetries that can be considered, which do not impact the theory the same way, namely space-time symmetries or gauge symmetries. The only possible extension of space-time symmetries is supersymmetry which is discussed later in a dedicated section. For the moment, let us focus on additional or extended gauge symmetries.

It is possible to think about gauge groups which include the Standard Model group, $SU(3) \times SU(2) \times U(1)$ to create Grand Unification Theories (GUT) in which the coupling constants are unified. Such groups are also motivated because they naturally introduce a symmetry between leptons and quarks as one can think of when looking at the pattern of the Standard Model.

The most simple group one can find is $SU(5)$ [28] which would be a broken symmetry at low energy just as the electroweak symmetry is. Rotations in the $SU(5)$ space can mix the quark and lepton fields which led to a prediction of proton decay incompatible with experimental measurements. Grand-unification with $SU(5)$ is now mostly abandoned but remains an idea studied for larger groups such as $SO(10)$.

On another side, driven this time by the strong CP problem, an idea introduced in 1977 [29] consists in introducing a new global $U(1)$ symmetry with a new scalar field which breaks this symmetry, and ends up with a strong CP phase being naturally zero. This theory predicts a new particle, the axion, which turns out to be a good dark matter candidate. Axions would have masses lower than $\mathcal{O}(1 \text{ eV})$ while still satisfying the criterion to be cold dark matter candidates. In particular, axions are predicted to form a Bose-Einstein condensate, which offers an opportunity to distinguish them from other dark matter candidates such as WIMPs [30].

Additional dimensions

The second possibility is to add extra space-time dimensions. While everyday's life is only composed of 3+1 (space and time) dimensions, theoretical mechanisms can explain why additional dimensions are not noticeable at our scale. The extra dimensions are usually considered to be space-like dimensions, as an additional time-like dimension would break causality. Extra dimensions theories are of particular interest to unify interactions with gravitation and answering the hierarchy problem.

A first idea is to consider extra dimensions that are compactified such that they are not noticeable at macroscopic scales. An useful analogy to understand the compactification

concept is to consider that, for instance, a guitar string seen from very far looks like a one-dimensional object, whereas if one looks at it closely, it exhibits a second periodic dimension around the string axis because of its thickness. When adding such compactified, periodic dimension, one must therefore state the radius of this dimension, defining the compactification scale.

Large extra dimensions (ADD) [31] theories are based on the idea that the Standard Model interactions take place only in the four well-known dimensions and gravity would be allowed to travel extra, compactified dimensions. As a consequence, at large distances, gravity would be diluted while at low distances (i.e. high energies) the Standard Model interactions and gravitation would have coupling constants that are of the same order. A phenomenological consequence is that microscopic black holes could be produced in high-energy collisions provided that the collision probe distances lower than the Schwarzschild radius. Alternatively, universal extra dimensions (UED) [33] theories assume that all interactions may travel through the extra dimensions. Phenomenologically, one would observe in that case a discrete mass spectra for the Standard Model particles corresponding to excitations along the compactified dimensions.

An other idea, found in Randall-Sundrum scenarios (RS) [32], considers a five dimensions universe made of two four-dimension branes separated by an extremely warped fifth dimension. One of the brane corresponds to the Standard Model physics while the other brane would correspond to the realm of gravity. The distance separating the two branes is directly linked to the difference of energy scales between the Standard Model sector and the gravitation sector. A phenomenological prediction of these models is the production of graviton excitations at the TeV scale.

Additional or modified field content

A third possibility is to introduce new ad-hoc fields or modify existing ones to address the shortcomings of the Standard Model.

One of the most obvious idea one can come up with is to postulate a fourth family of fermions. However, there are tight constraints on the existence of such a fourth family, such as limits on the number of neutrinos with a mass lower than $m_Z/2$ from measurements of the branching ratio $\text{BR}(Z \rightarrow \text{invisible})$ [34].

Focusing on the problem of neutrino masses, some theories are being investigated, predicting the existence of sterile neutrinos or right-handed neutrinos [35]. Such neutrinos are expected to be heavy and would then be good dark matter candidates, and in some cases would explain why left-handed neutrinos have such a low mass, for instance in the

context of the See-Saw mechanism [36].

Alternatively, focusing exclusively on the dark matter problem, it has been proposed that dark matter is not made of just one, but several kind of particles regrouped in the concept of an hidden sector. There are several possibilities to describe the link between the Standard Model and this hidden sector, for instance by assuming that the Higgs boson relates the two sectors, or by introducing a new $U(1)_H$ gauge group whose gauge boson would be a “dark” photon [37].

Finally, one elegant idea to try to explain the lightness of the Higgs boson is to consider it as a composite object [38, 39]. This idea is inspired from QCD where light scalars are encountered and do not exhibit a naturalness problem. Pions for example, in the massless quark limit, are massless Goldstone bosons coming from the breaking of the chiral symmetry by the QCD vacuum, composed of the chiral condensate $\langle \bar{q}_L q_R \rangle$. However in practice, chiral symmetry is not exact as the quarks are massive, and thus pions are only pseudo-Goldstone boson and get a mass - though they are still protected from being heavy by the approximate chiral symmetry. This idea can be applied to the Higgs, which would be a Goldstone boson of a new strongly-interacting sector above the weak scale, and would solve the hierarchy problem. Phenomenologically, different signatures exist depending on the exact model considered, but can involve different couplings to gauge bosons compared to the Standard Model, and the existence of new particles such as top partners.

The anthropic principle

Finally, one of the alternative to theories beyond the Standard Model is to simply accept the Standard Model as it is. This is strongly related to Einstein’s interrogation regarding whether or not Nature had any choice at the creation of the universe. It can be argued that most of the shortcomings of the Standard Model are related to gravitation and cosmology and might simply be unsolvable at scales accessible by particle physics experiments. The most important remaining issues are related to fine-tuning in the hierarchy problem and the arbitrariness of the other parameters of the theory.

The anthropic principle states that when studying the universe, it should be taken into account that it allows for conscious life to exist. It might be that our universe is simply one realization of universe among many others in what would be called a multiverse. What appears to be fine-tuning would in fact be equivalent to natural selection at the scale of the multiverse where the observed universes can only be the ones allowing conscious life [40, 41].

This view is however controversial, as it is not clear at this point what kind of testable prediction such an idea can provide. It nevertheless remains a legitimate hypothesis and questions the place and origin of the universe. A more extensive and interesting discussion can be found in [42].

1.4.2 Supersymmetry

General idea and motivations

Here, we propose to have a dedicated look at the idea of supersymmetry. Supersymmetry (SUSY), emerged around the 70's. At this time, Gol'fand and Likhtman, two russian mathematicians, were working with the space-time symmetries of the Poincaré group. The usual space-time symmetries, i.e. translations, boosts and rotations, are all bosonic symmetries. They noticed that another type of space-time symmetry with fermionic (i.e. spin 1/2) generators could also exist [43]. Such a symmetry Q , the supersymmetry, would therefore relate the different representations of the Lorentz group, namely fermions (f) and bosons (b):

$$\begin{aligned} Q|f\rangle &\rightarrow |b\rangle \\ Q|b\rangle &\rightarrow |f\rangle. \end{aligned} \tag{1.35}$$

Q is therefore a non-trivial extension of the Poincaré algebra. This is an important consideration: it has been demonstrated by Coleman and Mandula [44] that the only possible symmetries of Nature are the Poincaré symmetry and the gauge symmetries. Nevertheless, Haag, Lopuszanski and Sohnius later relaxed this theorem [45] by noticing that another type of symmetry is possible and precisely corresponds to supersymmetry [46, 47].

Here, we have introduced Q as a *global* symmetry, i.e. a transformation that does not depend on space-time, and is therefore not a gauge symmetry. However, a remarkable feature in SUSY is that trying to gauge Q , meaning making the transformation space-time dependent, yields a description of gravitation called supergravity (SUGRA). Supersymmetry also provides a link with string theory which is a candidate for the « theory of everything ».

To each fermionic degree of freedom is therefore associated a boson with same quantum numbers (apart from spin), and similarly to each boson is associated a fermion. The particle associated to another one by SUSY is called its superpartner, and can be put together in a superfield. To ensure the consistency of the theory, superpartners of vector

bosons have spin 1/2 and superpartners of fermions have spin 0. SUSY alone predicts that a particle and its superpartner should have the same mass. However this cannot be the case in practice as no such thing has been observed by experiments, meaning that supersymmetry must be a broken symmetry.

There are several mechanisms that are candidates to spontaneously break SUSY. Some are based on a gravity mediated supersymmetry breaking (such as minimal SUGRA), others involve a gauge mediated mechanism (GMSB), and another possibility is to have an anomaly mediated breaking (AMSB). Since the exact mechanism is unknown at the moment, one solution is to simply add a $\mathcal{L}_{\text{soft}}$ component to the Lagrangian, that includes all allowed terms and corresponding new parameters.

One of the main motivations for supersymmetry is to provide a mechanism that protects the mass of scalar bosons, thus answering the hierarchy problem. In the case of the Higgs boson, one can show that if the superpartners have equal masses, then the quadratic divergences introduced in Equation (1.33) cancel each other and it becomes natural for the Higgs boson to have a mass much lower than the Planck scale. If SUSY is only softly broken (i.e. broken spontaneously), as for chiral and gauge symmetries, then the boson-fermion symmetry still prevents to have a quadratic divergence. Instead, we are left with a mild logarithmic divergence:

$$\Delta m_h^2 \propto (m_f^2 - m_b^2) \ln \left(\frac{\Lambda}{m_b} \right). \quad (1.36)$$

But this alone does not solve everything. If the mass of the superpartners are too high, then the difference $(m_f^2 - m_b^2)$ is large and we are left with $\Delta m_h \gg m_h$. Therefore, we would need to reintroduce a certain level of fine-tuning in the parameters of the theory for the corrections to cancel each others, and we want to avoid that in order to keep the theory natural. Hence, the naturalness of SUSY is strongly related to the mass of the superpartners, and can be used as an indication for experimental searches. This is in particular true for the mass of the partners of the top quark, the Higgs, the gauge bosons as these sectors lead to the largest corrections.

The MSSM

The most studied realization of supersymmetry is the Minimal Supersymmetric Standard Model (MSSM). It corresponds to adding the minimum number of fields to the Standard Model for it to become supersymmetric [47, 48, 49]. Since the MSSM breaks SUSY with ad-hoc terms, it is to be seen as an effective theory up to $\Lambda_{\text{SUSY breaking}}$, i.e. a few TeV for low-scale SUSY.

Flavor eigenstates			Mass eigenstates		
1 st gen.	2 nd gen.	3 rd gen.	1 st gen.	2 nd gen.	3 rd gen.
\tilde{u}_L	\tilde{s}_L	\tilde{t}_L	"	"	\tilde{t}_1
\tilde{u}_R	\tilde{s}_R	\tilde{t}_R	"	"	\tilde{t}_2
\tilde{d}_L	\tilde{c}_L	\tilde{b}_L	"	"	\tilde{b}_1
\tilde{d}_R	\tilde{c}_R	\tilde{b}_R	"	"	\tilde{b}_2
$\tilde{\nu}_e$	$\tilde{\nu}_\mu$	$\tilde{\nu}_\tau$	"	"	"
\tilde{e}_L	$\tilde{\mu}_L$	$\tilde{\tau}_L$	"	"	$\tilde{\tau}_1$
\tilde{e}_R	$\tilde{\mu}_R$	$\tilde{\tau}_R$	"	"	$\tilde{\tau}_2$
→					
Higgs sector	Electroweak sector	Strong sector	Charginos and neutralinos	Strong sector	
$\tilde{h}_u^0, \tilde{h}_u^+$	\tilde{B}	$\tilde{g}_{1..8}$	$\tilde{\chi}_{1,2}^\pm$	"	
$\tilde{h}_d^0, \tilde{h}_d^-$	$\tilde{W}_{1,2,3}$		$\tilde{\chi}_{1,2,3,4}^0$		

Table 1.3: Superpartners of the fermions and bosons of the Standard Model, categorized according to flavor eigenstates (on the left) and mass eigenstates (on the right). A symbol " indicates that the mass eigenstate is identical to the flavor eigenstate.

At each fermion and gauge boson is therefore associated a superpartner called sfermion and gaugino. It should be stressed once again that left-handed and right-handed fermions are different fermions. Hence, there are for example two selectrons, one associated to each chirality of the electron. These are usually noted \tilde{e}_R and \tilde{e}_L to associate them easily with their fermion partner, even though they are spinless. Regarding the Higgs sector, it is necessary to add not only a superpartner called higgsino, but a second Higgs $SU(2)$ doublet to avoid a gauge anomaly.

As shown in the case of the Standard Model, the mass eigenstates are not necessarily the flavor eigenstates. This is also true in the MSSM, especially because of the SUSY breaking terms, and is an important consideration for the phenomenology. The introduction of a second Higgs $SU(2)$ doublet leads to four additional physical Higgs states noted H^0 , A and H^\pm . In the supersymmetric sector, mass eigenstates are formed by the combinations of the higgsinos and electroweak gauginos and are called charginos $\tilde{\chi}^\pm$ and neutralinos $\tilde{\chi}^0$. For the fermions, mixing terms are authorized in $\mathcal{L}_{\text{soft}}$ between the left and right-handed superpartners and are especially important for the phenomenology of the third generation. The mass eigenstates can be determined by diagonalizing the mass matrices. The resulting particles spectrum is given on [Table 1.3](#).

We introduce a quantum number called R-parity defined as:

$$R = (-1)^{2S+3B+L} \tag{1.37}$$

where S is the spin, B the baryon number, and L is the lepton number. R is equal to 1 for the particles of the Standard Model and -1 for their superpartners. If it is conserved, supersymmetric particles can only be pair-produced and only decay into an odd number of supersymmetric particles. In particular, this means that the lightest supersymmetric particle (LSP) is stable as its decay would violate the R -parity. The important consequence is that it provides a good candidate for dark matter, if the LSP is neutral.

The construction of the MSSM leads to the introduction of more than 100 additional parameters compared to the Standard Model, with more than 50 coming from $\mathcal{L}_{\text{soft}}$. Dealing with such a large number of parameters is quite inconvenient in terms of phenomenological and experimental analysis. The phenomenological MSSM (pMSSM) reduces this number of parameters by assuming that there is no new source of CP violation, that the lightest neutralino $\tilde{\chi}_1^0$ is the LSP, and other assumptions on the sfermion masses, trilinear couplings and flavor violation. This reduces the number of new parameters to 19, namely:

- the higgsino mass parameter μ and pseudo-scalar Higgs mass m_A ;
- the ratio of the Higgs vacuum expectation values, $\tan \beta \equiv v_2/v_1$ (with $0 \leq \beta \leq \frac{\pi}{2}$) ;
- the soft gaugino masses M_1 , M_2 and M_3 , corresponding respectively¹ to the bino \tilde{B} , wino \tilde{W} and gluino \tilde{g} masses ;
- the first and second generation sfermion masses $\tilde{m}_{\tilde{q}}$, $\tilde{m}_{\tilde{u}}$, $\tilde{m}_{\tilde{d}}$, $\tilde{m}_{\tilde{l}}$ and $\tilde{m}_{\tilde{e}}$;
- the third generation sfermion masses $\tilde{m}_{\tilde{Q}}$, $\tilde{m}_{\tilde{t}}$, $\tilde{m}_{\tilde{b}}$, $\tilde{m}_{\tilde{L}}$ and $\tilde{m}_{\tilde{\tau}}$;
- the trilinear couplings A_t , A_b and A_τ .

Note that we wrote \tilde{m} instead of simply m to highlight that these masses comes from the SUSY breaking Lagrangian $\mathcal{L}_{\text{soft}}$ and not from the electroweak symmetry breaking. One can go one step further and reduce this number of parameters to 5 in the case of the constrained MSSM, noted cMSSM (or mSUGRA), by assuming that at grand unification scale, all the scalar particles have the same breaking mass m_0 , all gauginos have the same breaking mass $m_{1/2}$, and all the trilinear couplings are equal to A_0 . The remaining two parameters are $\tan \beta$ and the sign of μ . Although the assumptions of the pMSSM and cMSSM can be seen as arbitrary, one can also simply take them as guidance to reduce the parameter space in the context of phenomenology and experimental studies.

¹One can notice that the index in $M_{1,2,3}$ refers to the gauge groups $U(1)$, $SU(2)$ and $SU(3)$, which makes it easier to remember which gaugino it refers to.

Phenomenology of the chargino, neutralino and stop sector

To get a better and concrete idea of the phenomenology of the chargino, neutralino and stop sector, which is of interest in this document, let's write down explicitly the mass matrices in the context of the MSSM and briefly discuss their implications. By mass matrices, we refer to the same kind of matrices that arose when we described the electroweak symmetry breaking in Section 1.2.1 and which led to the introduction of the physical states W^\pm , Z and γ .

The chargino sector arises from the mixing between the winos \tilde{W}_i and charged higgsinos \tilde{h}^\pm . In the $(\tilde{W}^\pm, \tilde{h}^\pm)$ basis, the mass matrix is

$$\mathcal{M}_{\tilde{\chi}^\pm} = \begin{pmatrix} M_2 & \sqrt{2}m_W \sin \beta \\ \sqrt{2}m_W \cos \beta & -\mu \end{pmatrix} \quad (1.38)$$

and the mass of the charginos $\tilde{\chi}_{1,2}^\pm$ are obtained by diagonalizing this matrix. The chargino sector is therefore only described by M_2 , β and μ . For very large values of $\tan \beta$, it is straightforward to see that the mass of the charginos tends to M_2 and μ .

The neutralino sector arises from mixing between the bino \tilde{B} , the wino \tilde{W}^3 and the two neutral higgsinos \tilde{h}_1^0 and \tilde{h}_2^0 . In the corresponding basis, $(\tilde{B}, \tilde{W}^3, \tilde{h}_1^0, \tilde{h}_2^0)$, the mass matrix is

$$\mathcal{M}_{\tilde{\chi}^0} = \begin{pmatrix} M_1 & 0 & -m_Z \cos \beta \sin \theta_W & m_Z \sin \beta \sin \theta_W \\ 0 & M_2 & m_Z \cos \beta \cos \theta_W & -m_Z \sin \beta \cos \theta_W \\ -m_Z \cos \beta \sin \theta_W & m_Z \cos \beta \sin \theta_W & 0 & \mu \\ m_Z \sin \beta \sin \theta_W & -m_Z \sin \beta \cos \theta_W & \mu & 0 \end{pmatrix} \quad (1.39)$$

where θ_W is the weak mixing angle. The neutralino masses therefore only depend on M_1 , M_2 , β and μ . For example, for M_1 and $M_2 \gg \mu$, the two lightest neutralinos are essentially higgsino-like.

Finally, in the stop sector, \tilde{t}_L and \tilde{t}_R are not necessarily the mass eigenstates, noted \tilde{t}_1 and \tilde{t}_2 . They are determined from the mass matrix

$$\mathcal{M}_{\tilde{t}} = \begin{pmatrix} \tilde{m}_{\tilde{t}_L}^2 + m_t^2 + m_Z^2 \left(\frac{1}{2} - \frac{2}{3} \sin^2 \theta_W \right) \cos 2\beta & m_t (A_t + \mu \cot \beta) \\ m_t (A_t + \mu \cot \beta) & \tilde{m}_{\tilde{t}_R}^2 + m_t^2 + \frac{2}{3} m_Z^2 \sin^2 \theta_W \cos 2\beta \end{pmatrix} \quad (1.40)$$

where A_t characterizes the trilinear coupling appearing in $\mathcal{L}_{\text{soft}}$ and $\tilde{m}_{\tilde{t}_{L,R}}$ are the soft stop masses. The mixing between \tilde{t}_L and \tilde{t}_R is characterized by the off-diagonal terms and it is usually convenient to introduce the stop mixing parameter $X_t \equiv (A_t + \mu \cot \beta)$.

Experimental strategies and status of search for natural SUSY

The naturalness argument for supersymmetry can be used to derive limits on the mass of the sparticles. According to [50], the following conditions should be satisfied for SUSY to be natural :

- $|\mu| < 150 - 200$ GeV
- $m_{\tilde{t}_{L,R}}, m_{\tilde{b}_L} < 1 - 1.5$ TeV
- $m_{\tilde{g}} < 3 - 4$ TeV
- $m_{\tilde{B}}, m_{\tilde{W}} < 2 - 3$ TeV
- $m_A < |\mu| \tan \beta$
- 1st and 2nd generation sfermions masses $< 10 - 50$ TeV

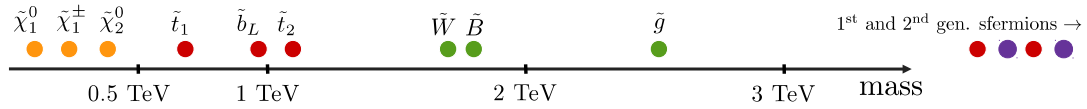


Figure 1.7: Example of natural SUSY mass spectra with first neutralinos and chargino being mainly higgsinos.

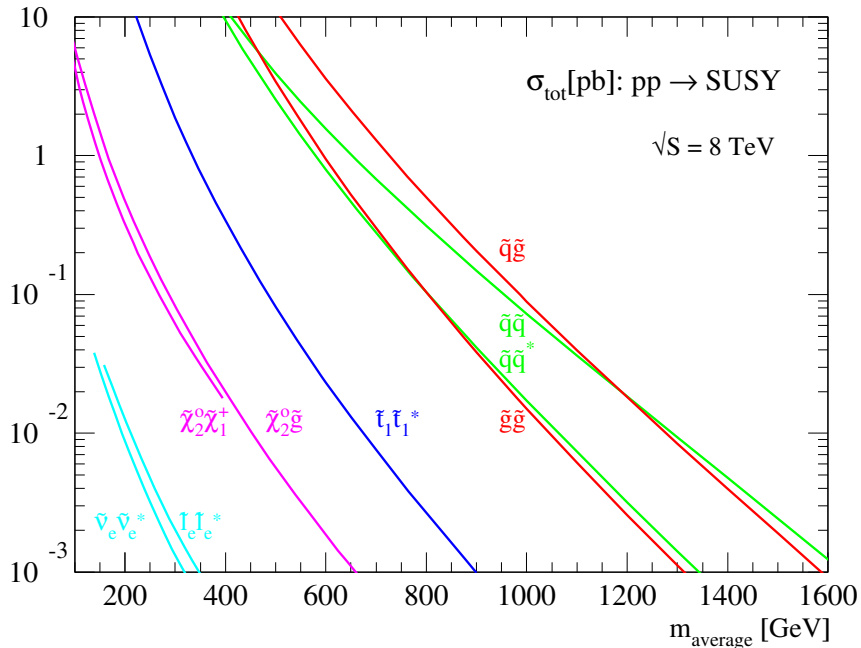


Figure 1.8: Cross section for supersymmetric particles production for proton-proton collisions at $\sqrt{s} = 8$ TeV, as function of the mass of the particle.

An example of such a natural SUSY spectra is represented on [Figure 1.7](#). Let us now discuss the different approaches one can consider when experimentally searching for natural supersymmetry. [Figure 1.8](#) presents the evolution of the cross section as function of the mass of the particle, for several processes at a pp collider such as the LHC, with a center of mass energy $\sqrt{s} = 8$ TeV. In a pp collider, we naturally expect the direct production of coloured particles such as gluino and squarks to be easier compared to direct production of electroweakinos and sleptons which involve the weak interaction.

Three main strategies are therefore used at the LHC to search for natural supersymmetry. The first one is to look for gluino production. In models with a neutralino LSP, gluinos are expected to decay to the neutralino via quarks, experimentally corresponding to a large number of jets in the event, and energy escaping detection as they are carried by neutralinos. The Run I of the LHC have made it possible to exclude gluino masses up to 1 – 1.4 TeV depending on the exact decay considered [[53](#), [54](#)].

A second approach is look for electroweakinos production. As it is motivated for electroweakinos to have a mass of only a few hundred GeV, it is worth looking for such processes despite their relatively low cross-sections. The topology of the decay chain may vary a lot depending on the mass gaps between the sparticles and the possibility to decay via sleptons. One of the processes typically looked for is the production of $\tilde{\chi}_1^\pm \tilde{\chi}_2^0$. If no decay via sleptons is possible, then $\tilde{\chi}_1^\pm$ decays to $W \tilde{\chi}_1^0$ and $\tilde{\chi}_2^0$ decays to $Z \tilde{\chi}_1^0$ or $h \tilde{\chi}_1^0$. Using the Run I of the LHC, it has been possible to exclude masses for these particles up to 275 GeV (CMS) or 425 GeV (ATLAS) [[55](#), [56](#)].

Finally, one may look for direct third generation squark direct production, and in particular direct stop pair production which is the focus of this document. The cross-section of such process is typically two orders of magnitude lower than direct gluinos production, but is relevant given the importance of light stops to preserve naturalness.

Chapter 2

The Compact Muon Solenoid experiment at the LHC

*« Tracked you down with this. This is my timey-
wimey detector. It goes ding when there's stuff! »*

The Tenth Doctor

Contents

2.1	The Large Hadron Collider	36
2.1.1	Scientific context and challenges	36
2.1.2	Beam injection, control and acceleration	37
2.1.3	Physics of pp collisions	39
2.1.4	LHC timeline and roadmap	42
2.2	The Compact Muon Solenoid experiment	43
2.2.1	The CMS detector	44
2.2.2	Trigger system	52
2.2.3	Object and event reconstruction	54
2.3	Collisions and detector simulations	62
2.3.1	Monte-Carlo generation of the hard scattering	63
2.3.2	Hadronization	64
2.3.3	Detector simulation	64

In this chapter, we introduce the Large Hadron Collider (LHC) and the Compact Muon Solenoid Experiment (CMS). In [Section 2.1](#), we present the LHC apparatus, its scientific motivation and the physics of proton-proton collisions. In [Section 2.2](#), we describe the CMS experiment by describing the layout and technologies used for each subdetectors, as well as their performances. We will also go through the main techniques used to reconstruct the objects produced in the collisions. Finally in [Section 2.3](#), we describe the principles behind the production of Monte-Carlo events, in particular the Monte-Carlo generation of collisions, the hadronization and the detector simulation.

2.1 The Large Hadron Collider

2.1.1 Scientific context and challenges

There are several approaches one can follow to search for new physics. For instance, using measurements of observables and exploiting the fact described in [Section 1.2.3](#) that observables are impacted through loops by the entire Nature's Lagrangian, it is possible to infer information or limits regarding yet-unknown physics. Historically, this has been proved to be successful, for instance to predict the mass of the top quark from electroweak measurements, in particular the W and Z bosons mass [\[57\]](#). Similarly, a smoking-gun for some supersymmetric models is the enhancement of the branching ratio $\text{BR}(B_s \rightarrow \mu^+ \mu^-)$ [\[58\]](#). However, despite the fact this approach provides valuable information, it can be criticized as only providing indirect evidences and not a clear window to new phenomena. Moreover, the statistics and detector resolution required to increase the accuracy of the prediction grow drastically.

Another approach, probably the most attractive and informative, is the direct production and observation of new phenomena. One often forgotten fact is that new physics might not appear at high energies but at low energies instead. This is motivated for instance by axions theories and some hidden sector theories which predict particles with sub-eV masses or rare interactions [\[59, 60\]](#). Nevertheless, it is more common to assume that new physics will show up at high energies. To probe higher energies, particle colliders have been built with increasing center of mass energies (\sqrt{s}) during the last decades. Two famous ones are the Large Electron-Positron (LEP) collider [\[13\]](#) and the Tevatron collider [\[15\]](#). The LEP was an e^+e^- collider which operated at a maximum of $\sqrt{s} \approx 200$ GeV at CERN in the 1990's and allowed precise measurements of the electroweak Z and W bosons and tested the robustness of the Standard Model. The Tevatron was a $p\bar{p}$ collider which operated at a maximum $\sqrt{s} \approx 2$ TeV at Fermilab until 2011 and led to the discov-

ery of the top quark and first measurements of its properties. Nowadays, the only high energy collider in operation is the Large Hadron Collider.

The LHC [61] is a circular hadron collider built at CERN, near Geneva. One of its physics goals is the production of high-energy proton-proton (pp) collisions to uncover the mechanism of electroweak symmetry breaking, to test the validity of the Standard Model, and more generally to explore physics around $0.1 \sim 10$ TeV. It is also capable of producing heavy ions (PbPb) collisions or proton-ion collision (pPb) in order to study quark matter at high temperature, and in particular the properties of quark-gluon plasma. The rest of this document will focus on pp collisions.

The LHC collider has been built in the same tunnel as the LEP. The beam energy at the LEP was largely limited by the energy loss from synchrotron radiation. This loss is proportional to $E^4/(m^4r^2)$ with E and m being the energy and mass of the particle, and r the radius of the tunnel. As m_p is $\mathcal{O}(1000)$ times larger than m_e , it is easier to maintain the energy of a rotating proton beam than an electron/positron one. Consequently, using protons is preferred in the context of reaching the highest possible energy, justifying this choice for the LHC. We will see however, in Section 2.1.3, how proton collisions are more challenging from the point of view of the reconstruction and analysis due to their internal structure.

2.1.2 Beam injection, control and acceleration

The creation and first acceleration of the proton beam work as follow. Protons are initially obtained by heating low-pressure H_2 gas which produces $H^+(=p)$ and e^- , by isolating the protons using high voltages. The protons are fed to an acceleration chain made of different rings which use radiofrequency cavities to create an acceleration gradient. At the end of the chain, in the Super Proton Synchrotron (SPS), the beam acquires an energy of 450 GeV before being injected in the LHC ring. The LHC ring is a tunnel of 27 kilometers built between 50 and 200 m underground. The project is designed to accelerate the proton beam up to 7 TeV per beam, corresponding to a center of mass energy $\sqrt{s} = 14$ TeV. Four main experiments are installed along the ring, at each collision point. Two of them, ATLAS and CMS, are general-purpose experiments while ALICE focuses on heavy-ion collisions, and LHCb studies the properties of B and C -hadrons and CP -violation. Figure 2.1 presents an overview and the general layout of the machine.

One of the biggest challenges of the LHC is the design and operation of magnets powerful enough to bend the trajectory of the protons at such high energies. To do so, superconducting magnets made of a niobium-titanium alloy produce a magnetic field of

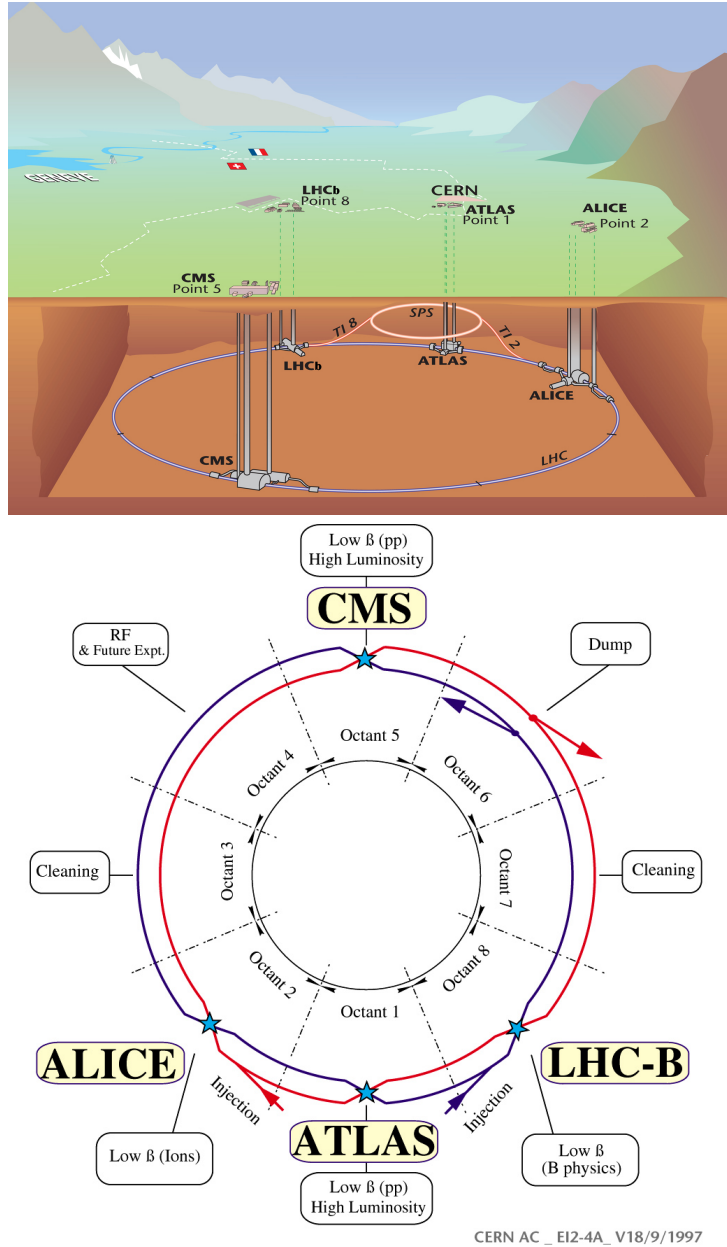


Figure 2.1: On the top, sketch of the underground installation showing the SPS, the injection tunnels, the LHC, as well as the four experiments. On the bottom, layout of the LHC ring. The installation is divided in eight octants, with some of them dedicated to collisions but also injection, acceleration (RF) and beam dump.

up to 8.33 T. The operating temperature of such magnets is only a few Kelvins: at the LHC, they are required to be cooled using a complex system of superfluid ^4He at 1.9 K. It is remarkable to note that this temperature is actually cooler than the cosmic microwave background at around 2.7 K.

Operating superconducting magnets requires a good control and understanding of quenches. A magnet quench occurs when a part of the superconducting material loses its superconducting property and starts to heat because of Joule effect. Because the

critical temperature is usually low, this can create a chain reaction as the heat spreads. Quenches are not such unusual events, and the LHC employs a sophisticated system to detect them and protect the magnetic system by automatically dumping the beam, mitigating the effect of the quench and extracting the energy stored inside the magnet [62]. However, defects in the protection system or more generally in the electrical and mechanical apparatus can have dramatic impact as the energy can easily damage the machine if improperly released. In 2008, a faulty electrical interconnection between two magnets led to an electrical arc that punctured the cryogenic fluid enclosure and vaporized a fraction of the fluid, causing important damages to the installation [63].

The pipes of the LHC consist of about 1200 dipole magnets represented on [Figure 2.2](#), each 15 m long, whose role are to bend the proton beam. In addition, about 400 quadrupole magnets are used to squeeze the beam. Higher multipolar magnets are also used to prevent and correct instabilities of the beam. The effective bending radius, created from the 17.6 km of dipoles, is $r \approx 2.8$ km, to be compared to the radius of the full apparatus being about 4.3 km.

Each beam is organized in bunches of protons separated by a time interval of 50 or 25 ns depending on the machine configuration. Each bunch is made of about 10^{11} protons. The LHC uses radio frequency cavities to increase the energy of the beam by about 0.5 MeV per rotation, or 5.4 GeV per second. At 7 TeV per beam with 25 ns between bunches, the total energy of the beam is about 360 MJ and the energy stored in the magnet system is about 600 MJ, roughly corresponding to the energy of a lightning bolt. The beams collide at four different points along the ring, corresponding to the four main experiments.

2.1.3 Physics of pp collisions

When considering a single pp collision, it must be kept in mind that protons are composite objects made of three valence quarks in a sea of virtual quarks and gluons called partons. A parton in the proton only carries a fraction of the total proton momentum. In quantum chromodynamic, the structure of the proton can not easily be derived from first principles. Instead, we rely on the parton distribution functions (PDF), determined from experiment, which characterizes the probability to find a parton with a fraction of momentum x , depending on the nature of the parton. Two examples of PDF are given on [Figure 2.3](#). The shape of these distributions implies that, in a collision, the center of mass energy of the two incoming partons is generally much lower than the beam energy. Each incoming parton may also radiate partons right before the interaction, a process called initial state radiation (ISR), leading to additional jets in the event. Similarly, radiations from quarks or gluons in the final state are called final state radiation (FSR). Finally, the remaining partons

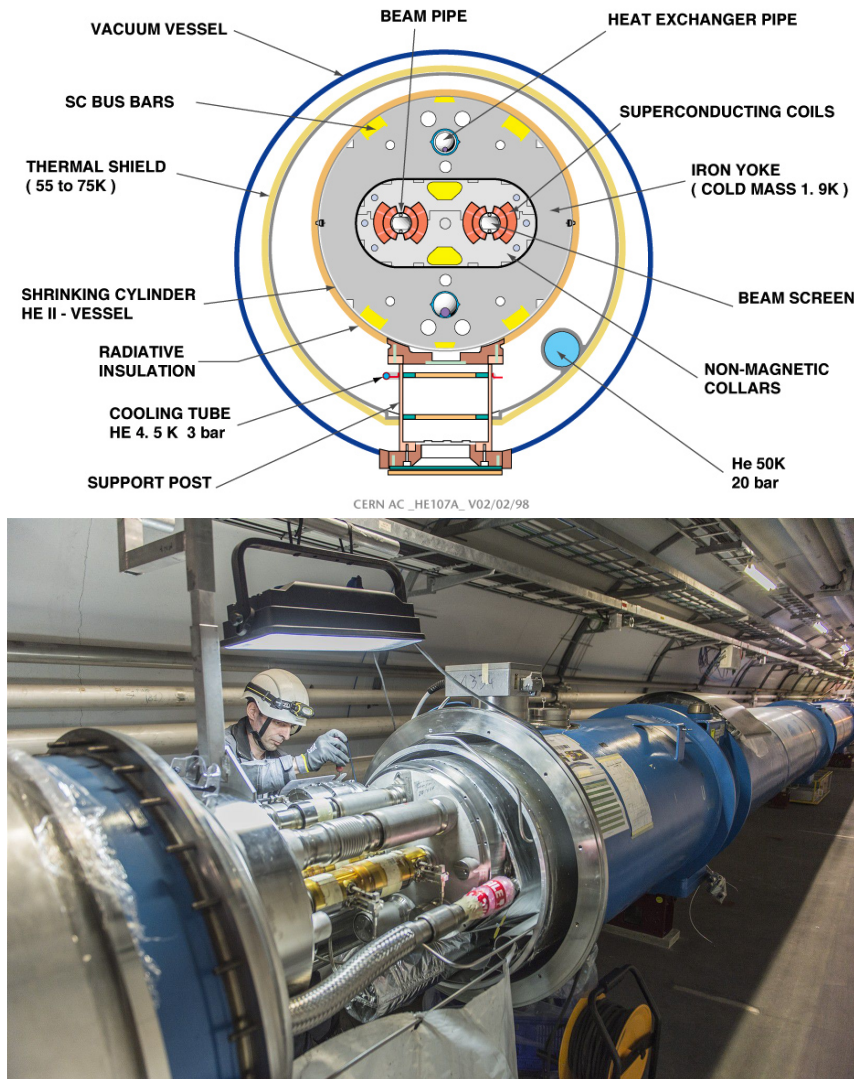


Figure 2.2: On the top, cross-section of a cryodipole of the LHC showing the magnet coils around the two beam pipes, and the cooling system [61]. On the bottom, technician working on an interconnection between two LHC sections (credits: Anna Pantelia, CERN).

from the protons may interact with each other in what is called the underlying event, and produce high-energy forward jets, almost collinear to the beam axis. pp collisions are therefore complex processes, as summarized in Figure 2.4, due to the composite nature of the proton and the fact that the partons are colored objects.

In the context of the LHC, the number of pp collisions happening per unit of time is proportional to the instantaneous luminosity $L_{inst.}$,

$$L_{inst.} = \frac{n_p^2 n_b f}{4\pi\sigma_x\sigma_y} \quad (2.1)$$

where n_p is the number of proton per bunch, n_b is the number of bunches, f is the revolu-

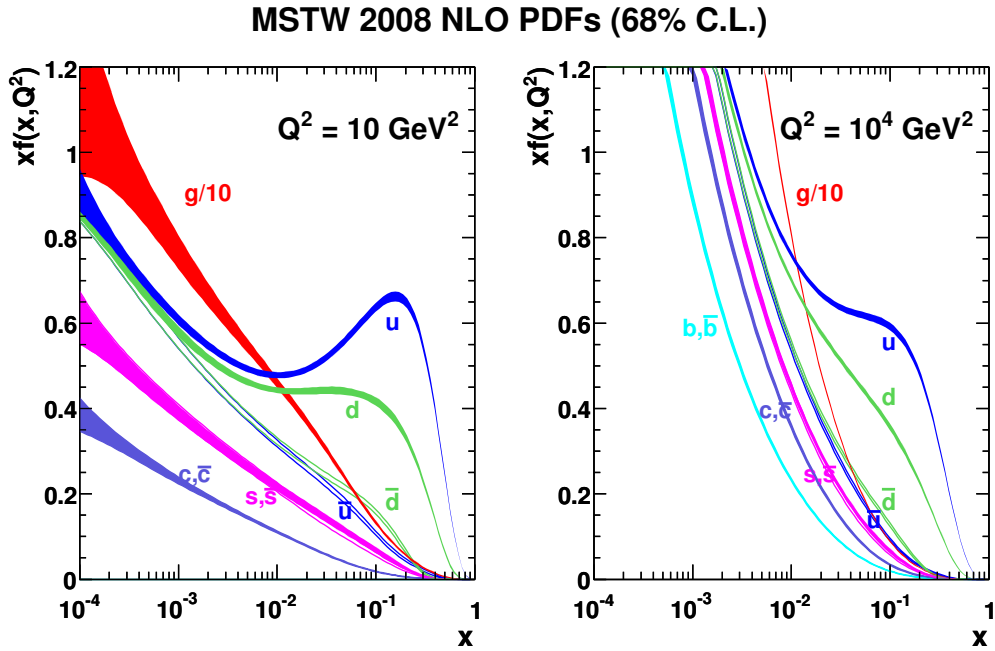


Figure 2.3: Example of PDFs for two different energy scales Q , provided by the MSTW group [64]. At lower energies, one clearly distinguish the large fraction of momentum x carried by u and d valence quarks while other species are only present in the parton sea and less probable as their mass increases. As Q^2 grows, the probability to probe sea partons increases.

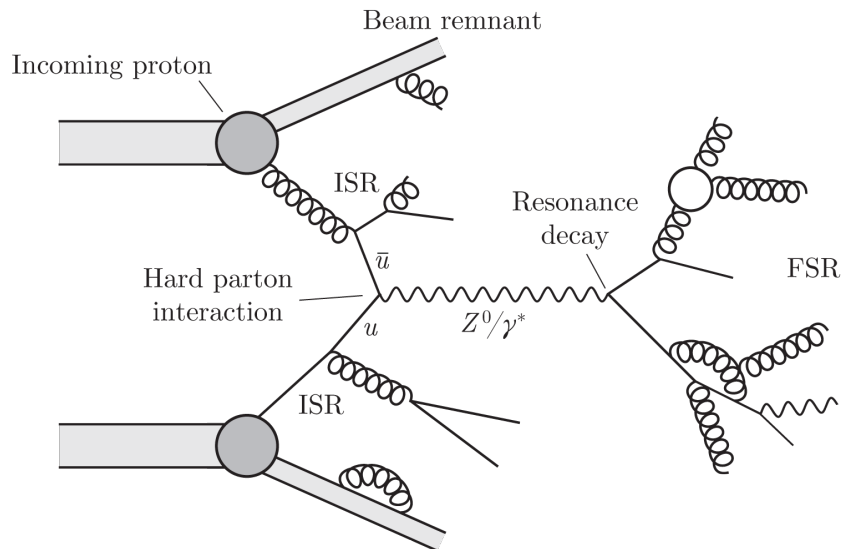


Figure 2.4: Feynman diagram showing the complexity of a single proton-proton collision. Two partons from the incoming protons participate to the hard scattering leading to a Z/γ^* resonance which decays into two quarks. In both the initial and final states, the colored particles may radiate gluons (or a gluon may split into a quark pair), leading to initial and final state radiations.

tion frequency and σ_x and σ_y are the transverse beam size. The two general purpose experiments, ATLAS and CMS, are designed for a typical luminosity $L_{\text{inst.}} = 10^{34} \text{ cm}^{-2}\text{s}^{-1} = 10 \text{ nb}^{-1}/\text{s}$. For a given process, one can compute n the number of expected events per unit of time:

$$n = L_{\text{inst.}} \times \sigma_{\text{process}} \quad (2.2)$$

where σ_{process} is the cross-section of the process considered. Later, we may refer to the integrated luminosity $L_{\text{integr.}}$ over a defined period of data-taking, which relates to N , the total number of expected events during that time:

$$N = L_{\text{integr.}} \times \sigma_{\text{process}} \quad (2.3)$$

Figure 2.5 shows the evolution of the cross section of different processes such as W , Z , top or Higgs production as function of \sqrt{s} . The total inelastic cross section is about 60 mb. At an instantaneous luminosity of $10 \text{ nb}^{-1}/\text{s}$ and with a bunch crossing every 25 ns, this corresponds to an average of 15 inelastic interactions per bunch crossing. This is what is behind the notion of pile-up: one event, or bunch crossing, contains $\mathcal{O}(10 - 30)$ interactions with generally at most one of interest, e.g. the production of a W or Z boson.

The concept of pile-up have crucial implications for the study of pp collisions: the additional inelastic hadron collisions naturally produce jets of particles, which pollute the environment of each event, affecting the number of hits in the tracking detectors and the energy measurement in calorimeters. It is thus needed to develop methods to mitigate the effect of pile-up.

2.1.4 LHC timeline and roadmap

Table 2.1 presents the timeline and roadmap of the LHC. Because of the incident that happened in 2008, the machine had to be repaired and collisions could only be provided at energies $\sqrt{s} = 7$ and 8 TeV during the Run I, while waiting for consolidations of the machine. An integrated luminosity of respectively 5 and 20 fb^{-1} was recorded at these energies. During 2015 and until the end of 2018, the LHC is expected to work at 13 or 14 TeV and to provide about 100 fb^{-1} of integrated luminosity. After the run III, foreseen to take place from 2021 and to the end of 2023, the LHC is expected to be upgraded, which would be the start of the high-luminosity LHC (HL-LHC) program. During this period, the LHC will still operate at 14 TeV but with an instantaneous luminosity around 100 nb^{-1}/s corresponding to a pile-up around 150. To be able to sustain such conditions, the LHC experiments will need to be significantly upgraded.

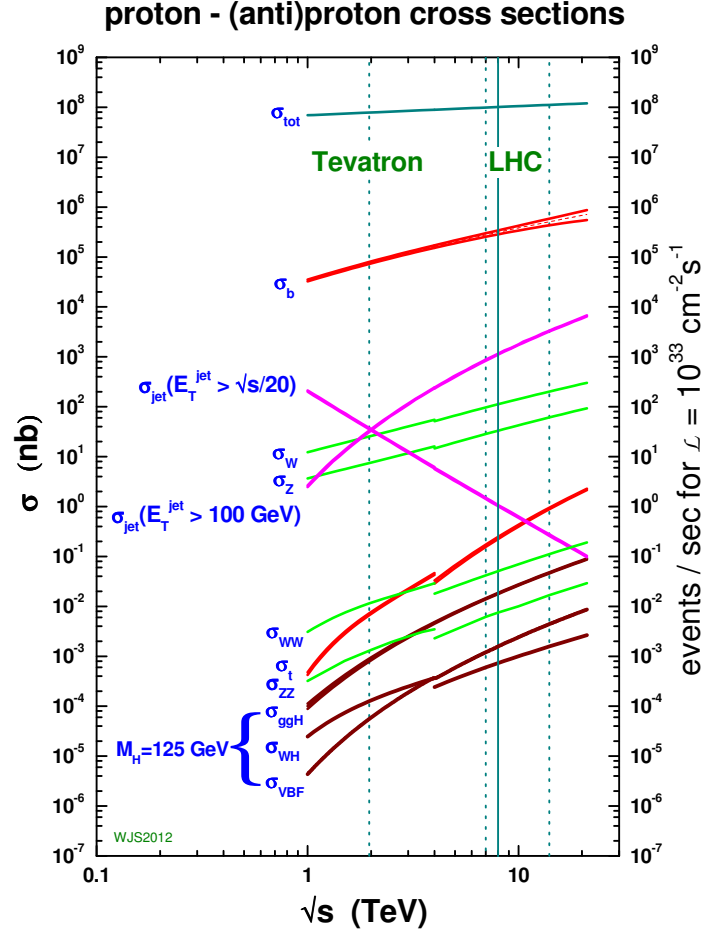


Figure 2.5: Evolution of the cross sections of typical processes for $p\bar{p}/pp$ collisions as function of \sqrt{s} . Two vertical lines corresponds to the center of mass energy of the Tevatron ($\sqrt{s} \approx 2$ TeV) and the LHC ($\sqrt{s} = 7, 8$ and 14 TeV) [65].

2.2 The Compact Muon Solenoid experiment

The Compact Muon Experiment experiment is one of the four experiments installed at the collision points of the LHC. It is a general purpose experiment, though mostly dedicated to the study of pp collisions, in particular to test the validity of the Standard Model at the TeV scale, to understand the electroweak symmetry breaking, and to search for new physics. From this perspective, CMS is in scientific cooperation and competition with ATLAS, the other general purpose experiment. In the context of the search for new physics, having two experiments independently studying the same phenomena is stimulating but also crucial to have robust claims. It is indeed highly desirable from a scientific point of view to be able to cross-check any possible discovery by one experiment with another independent experiment.

	Period	\sqrt{s} (TeV)	\langle Pile-up \rangle	$L_{inst.}$ (nb $^{-1}$ /s)	$L_{integr.}$ (fb $^{-1}$)
Phase 0, Run I	2010-12	7-8	20	6-7	5+20
Phase 1, Run II	2015-18	13-14	40	15	100
Phase 1, Run III	2021-23	14	60	20-30	300
Phase 2 (HL-LHC)	2027	14	130-200	100	3000

Table 2.1: Timeline and roadmap of the LHC (as of July 2015).

So far, the CMS experiment, through the analysis of the Run I data at $\sqrt{s} = 7$ and 8 TeV, allowed significant improvements on the precision measurements of the Standard Model, in particular in the top sector, and complemented the measurements of ALICE on heavy-ions and LHCb on flavor physics. In July 2012, CMS and ATLAS claimed evidence for a Standard Model-like Higgs boson at a mass around 125 GeV [16, 17].

In the following subsections, the CMS detector is first introduced generally before inspecting each subsystems individually. Then follows the presentation of the trigger system that aims to select which collisions to record. Finally, it is explained how the physics objects can be reconstructed from the information recorded by the detector.

2.2.1 The CMS detector

Physics motivations and detector overview

The CMS detector [66] is an instrument that answer the fantastic challenges posed by the LHC machine while providing good measurements for physics purpose. The subsystems of the detector must indeed have a time response of the order of 25 ns, corresponding to the design bunch crossing frequency, and to be synchronized with each other. The detector must also allow the physicists to disentangle between the several collisions occurring at each bunch-crossing by being able to reconstruct the collision vertices with good precision. Last but not least, the quantity of data per event is such that all events cannot be recorded. The detector must then decide in real time which events to keep, and which to reject from a fast analysis of each event.

Among all the physics signatures CMS was designed to look for, the discovery and study of a light ($\mathcal{O}(125$ GeV)) Higgs boson in the channels $h \rightarrow \gamma\gamma$ and $h \rightarrow ZZ \rightarrow 4\ell$ requires good resolution on the photons, electrons and muons energy-momentum. Furthermore, from the perspective of final states involving dark matter candidates, one must be able to measure the energy escaping detection. This requires an hermetic coverage of the detector around the interaction point.

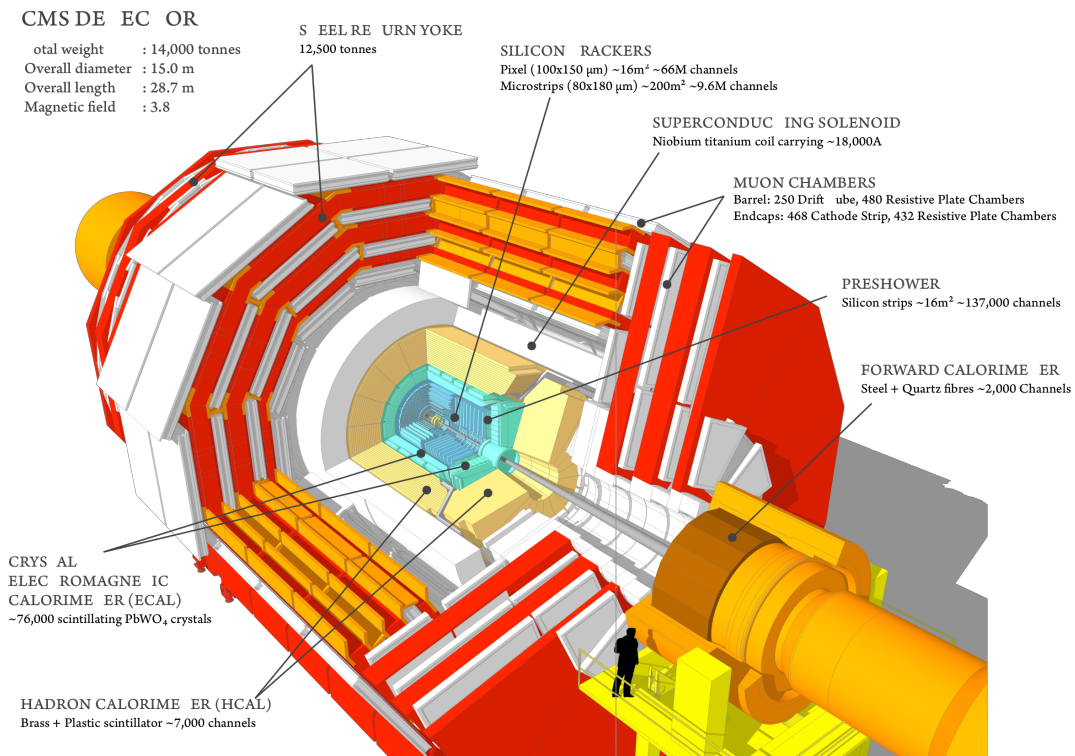


Figure 2.6: Overview of the CMS detector.

The CMS detector is a quasi-hermetic, cylinder-shaped detector consisting of several complementary layers¹ as represented on Figure 2.6. The CMS design is centered around a superconducting magnet delivering a field of 3.8 T using the same technology than the LHC, a niobium-titanium alloy. The strong magnetic field allows to bend the trajectory of charged particles, allowing a measurement of their momentum with an accuracy inversely proportional to the value of the field. Near the interaction point, the tracker system is dedicated to the detection of hits left by charged particles. It is a fully silicon system composed of pixel detector layers and microstrip layers. Beyond the tracker, the electromagnetic calorimeter measures the energy of photons and electrons using scintillation crystals. The next layer, the hadronic calorimeter, aims to measure the energy carried by hadrons produced in the collisions. It is a scintillator made of brass and plastic sandwich. Finally, the muon system uses three different gas-based technologies to record the hits of muons. Figure 2.7 shows a photograph of the detector during its assembly.

The coordinate system (x, y, z) of CMS, represented on Figure 2.8, is defined such that x is directed to the center of the LHC, y points toward the sky and z is collinear to the beam axis. As the detector exhibits a cylindrical symmetry, it is convenient to work

¹While this structure is found in three of the four main experiments at the LHC, other structures exist in particle physics detectors, for instance the LHCb detector and AMS detector are composed of successive transversal layers.

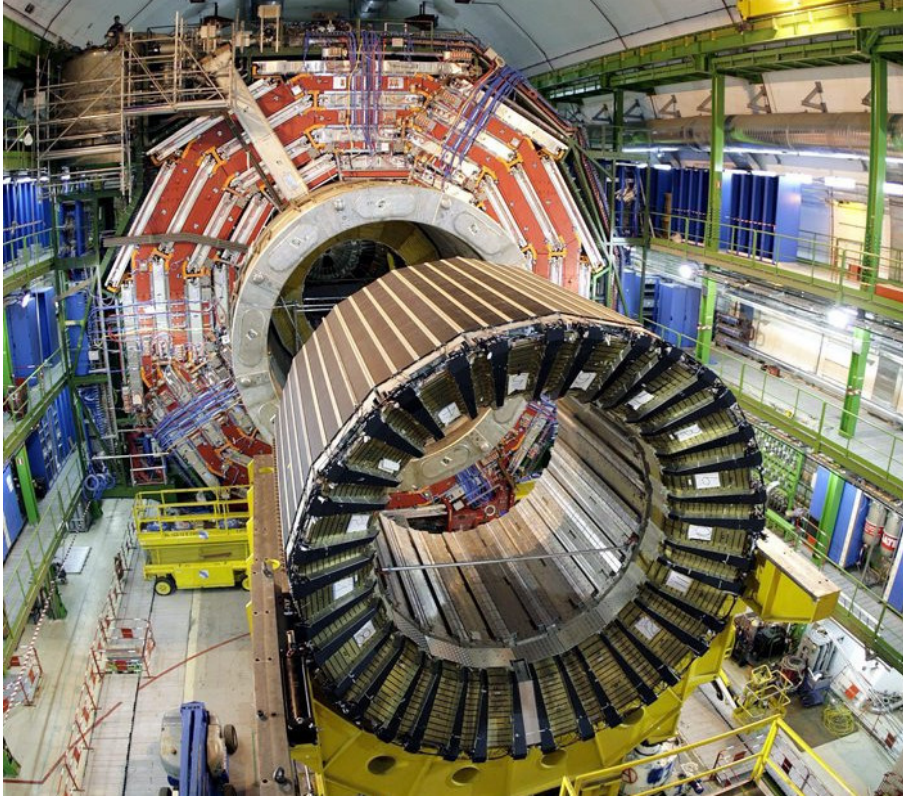


Figure 2.7: Photography of the CMS detector, showing some of the muon system, the magnet and the return yoke, and the HCAL barrel during assembly.

with the azimuthal angle ϕ between the momentum \vec{p} of a particle and the x axis in the transverse plane. The projection of \vec{p} in the transverse plane is called \vec{p}_T . Additionally, the pseudo-rapidity η is defined as:

$$\eta \equiv -\ln\left(\tan\frac{\theta}{2}\right) \quad (2.4)$$

where θ is the polar angle with respect to the z axis. η is equal to 0 for particles produced in the transverse plane, about 0.88 for $\theta = \pi/4$ and tends to ∞ in the limit where the particle is produced along the beam axis. More qualitatively, we refer to low η values ($|\eta| < 1.5$) as the central or barrel region, while high η values ($|\eta| > 1.5$) are referred to as forward or endcap region. In the plane (ϕ, η) , we define the distance between two directions as $\Delta R \equiv \sqrt{\Delta\phi^2 + \Delta\eta^2}$.

Tracking system

The tracker is the subdetector closest to the interaction point. Its goal is to reconstruct hits left by charged particles to estimate their direction and momentum, and to identify not only the primary interaction vertices, but also secondary vertices found in, for ex-

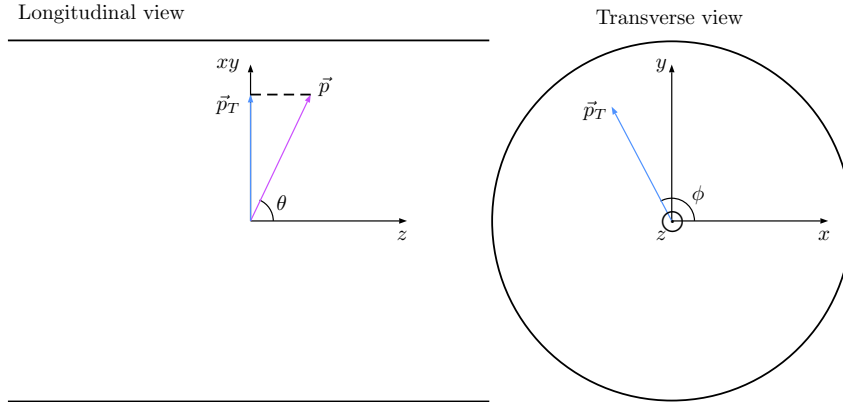


Figure 2.8: Coordinate system of CMS represented in the longitudinal plane (on the left) and in the transverse plane (on the right).

ample, jets from the hadronization of b quarks. This requires a precision on the vertex position to less than one millimeter.

While achieving this level of accuracy, the tracking system must also be able to handle the conditions of the LHC. At nominal conditions, it can be estimated that about 1000 charged particles are produced per bunch crossing. This roughly corresponds to a hit rate of 1 MHz/mm² at 4 cm of the interaction point and 3 kHz/mm² at 115 cm. To not be overwhelmed (i.e. have a low occupancy), the detector must therefore have a high granularity. Moreover, the electronics should resist and be reliable with respect to the high-level of radiations. Last but not least, the overall quantity of material involved should be as small as possible to not alter the trajectory of the particle and the measurement of the energy in the calorimeters cells. The chosen technology is a fully silicon-based detector as it is at the same time compact and accurate. However, for optimum performances, these silicon sensors must operate at around -15°C , which requires a cooling system.

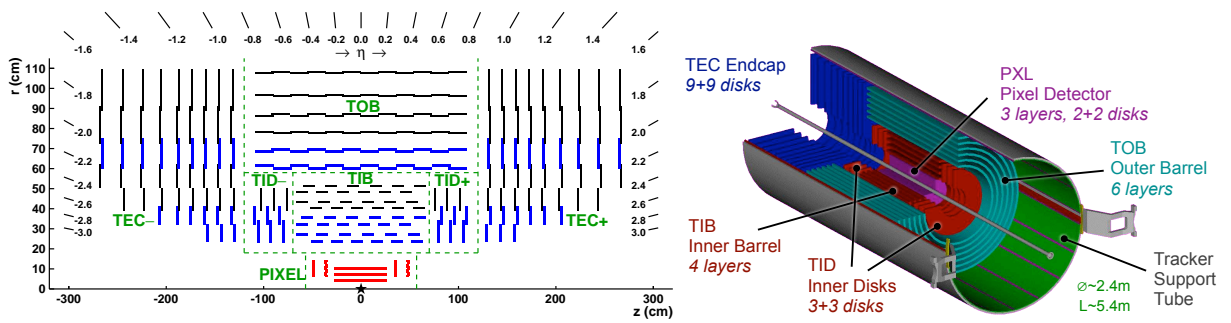


Figure 2.9: Layout of the tracker system. On the left, red lines represent pixels, blue lines represent double-sided strips modules and black lines represent single-sided strips modules. On the right, a 3D representation of the tracking system is presented. The pixel is represented in magenta and the different parts of the strips system are represented in red, teal and blue.

The tracker system is made of several sensors arranged in layers, in turn arranged in modules, as represented in [Figure 2.9](#). At the center, the pixel module uses silicon pixel sensors of $100 \times 150 \mu\text{m}^2$, providing a resolution on the position of hits around $10 \mu\text{m}$ in the transverse plane and $20 \mu\text{m}$ in z . The barrel module is composed of three layers long of 53 cm in the region $r < 10 \text{ cm}$, supplemented by two disk layers placed at $|z| \approx 35$ and 45 cm to cover the forward region. In total, the pixel detector contains 66 million pixels covering about 16 m^2 .

The rest of the tracker system is based on silicon microstrips with a pitch (equal to the strip width plus the space between strips) ranging from 80 to $205 \mu\text{m}$ and length ranging from 10 to 25 cm . The resolution of these sensors on the hit position ranges from 23 to $52 \mu\text{m}$ in the transverse plane and from 230 to $530 \mu\text{m}$ along z . This strip tracker is divided in two barrel subdetectors, the tracker inner barrel (TIB) and outer barrel (TOB), supplemented by two endcap modules, the tracker inner disks (TID) and tracker endcaps (TEC). The strips tracker contains 9.6 million strips and cover almost 200 m^2 of surface. Overall, the system has a length of 5.6 m and a radius of 1.1 m and covers up to $|\eta| \approx 2.5$.

Electromagnetic calorimeter

The role of the electromagnetic calorimeter (ECAL) is to measure the energy of incoming electrons and photons. The specifications of this subdetector are particularly oriented by the search for the Higgs boson in the $h \rightarrow \gamma\gamma$ channel. The resolution on the invariant mass of the diphoton system depends directly on the energy and angular resolution of the photons. This part of the detector is of course also crucial for all processes involving electrons, such as Z and W .

The technology adopted for the ECAL is lead tungstate crystals (PbWO_4). Lead tungstate is a very dense scintillation material, about 8.3 g/cm^3 , with a short radiation length 0.89 cm , making it an appropriate choice for a compact calorimeter. On the other hand, the light output is relatively low, about 4.5 photoelectrons per MeV, and thus requires the use of photo-multipliers to improve the signal collection. In the barrel, the calorimeter uses crystals with a size of $2.2 \times 2.2 \text{ cm}^2$ for the front face and 23 cm in length, as represented on [Figure 2.10](#). In terms of $\eta - \phi$, each crystal covers a region of approximately 0.0174×0.0174 .

In the endcaps, to help to discriminate between prompt photons and π^0 decaying to two directionally close photons, two preshower disks are placed in front of the ECAL. Their role are to initiate electromagnetic showers and provide a finer granularity with silicon strips 0.2 cm wide, to be compared to the $\sim 2 \times 2 \text{ cm}^2$ faces of the crystals.



Figure 2.10: PbWO_4 crystal used in the ECAL with the photo-diode glued to the back of the crystal.

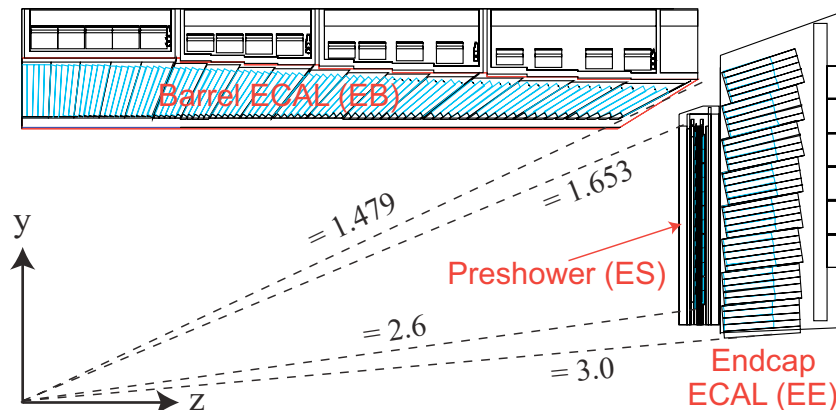


Figure 2.11: Layout of the electromagnetic calorimeter. Each of the blue segments represent a PbWO_4 crystal.

The general layout of the ECAL is presented on Figure 2.11. The ECAL barrel (EB) extends to $|\eta| = 1.479$, supplemented by the ECAL endcap (EC) up to $|\eta| = 3.0$. The preshower disks cover the region $|\eta| \in [1.653, 2.6]$. Overall, the system is 7.8 m long and lies within $1.2 < r < 1.8$ m in the barrel. The optical properties of the crystal are crucial parameters that depends on the temperature and radiations received. To obtain accurate measurements, a cooling system ensure that the crystal temperature is stable at $18 \pm 0.05^\circ\text{C}$ and the transparency is monitored in real time via a laser system.

The resolution measured during test beams using electrons is parametrized with the formula

$$\left(\frac{\sigma_E}{E}\right) = \left(\frac{S}{\sqrt{E}}\right) \oplus \left(\frac{N}{E}\right) \oplus C \quad (2.5)$$

with the different parameters

$$\begin{aligned}
 S &= 0.028 \text{ GeV}^{1/2}, \text{ the stochastic contribution,} \\
 N &= 0.12 \text{ GeV, the noise contribution,} \\
 C &= 0.003, \text{ the constant contribution.}
 \end{aligned}
 \tag{2.6}$$

This corresponds to a relative uncertainties of 12%, 1.5% and 0.4% for particles of 1, 10 and 100 GeV respectively.

Hadronic calorimeter

The hadronic calorimeter (HCAL) role is to complete the energy measurement of incoming charged and neutral hadronic particles, which will be in turn a crucial information to reconstruct jets and missing transverse energy.

The technology used for the HCAL consists of layers of dense absorbers and scintillation tiles. The absorbers are made of steel and brass, with which the incoming hadrons interact to develop a shower. As the particles of the shower travel through the calorimeter, they encounter scintillator layers in which they emit light. The light is gathered by fibers inside the tiles, which is then linked to readout electronics.

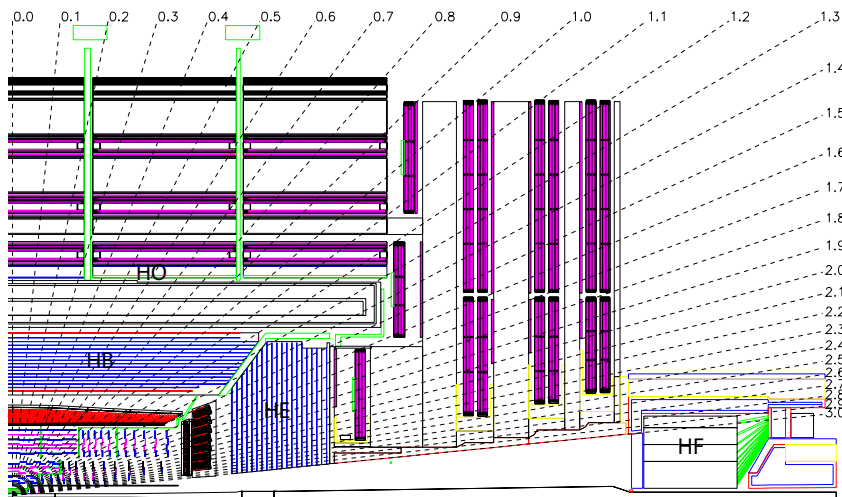


Figure 2.12: Layout of the hadronic calorimeter.

The layout of the HCAL is presented on [Figure 2.12](#). The HCAL barrel (HB) extends to $|\eta| \approx 1.4$ while the HCAL endcap (HE) extends up to $|\eta| \approx 3.0$. The segmentation term of η, ϕ is about 0.087×0.087 in the barrel which is 25 times coarser than ECAL. A last layer of the HCAL called the HCAL outer (HO) uses the magnet coil as an absorption layer. HO is exclusively made of scintillation tiles and complements the measurement of

the HB. Finally, to measure hadrons produced in the high-forward region, two calorimeters (HF) are located at $|z| \approx 11.2$ m to cover $|\eta|$ up to 5.2. As they receive a high flux of particles coming from underlying events, the material for these calorimeters must be able to endure the higher level of radiations and use hard quartz fibers instead of plastic ones.

The energy resolution measured during test beams for pions is

$$\left(\frac{\sigma_E}{E}\right) = \left(\frac{S}{\sqrt{E}}\right) \oplus C \quad (2.7)$$

with

$$\begin{aligned} S &= 0.084 \text{ GeV}^{1/2}, \text{ the stochastic contribution,} \\ C &= 0.074, \text{ the constant contribution.} \end{aligned} \quad (2.8)$$

This corresponds to a relative uncertainties of 11%, 7.9% and 7.4% for particles of 1, 10 and 100 GeV respectively.

Muon system

The muon system is composed of several subsystems placed in the return yoke of the superconducting magnet as represented in Figure 2.13. It aims to measure accurately the trajectory of muons.

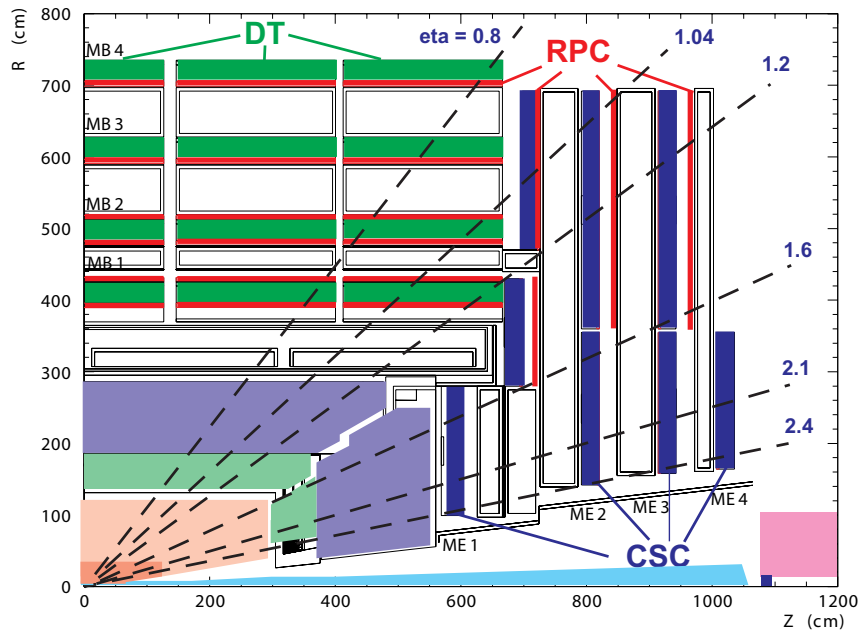


Figure 2.13: Layout of the muon system.

Three different gas-based technologies are used, whose choice was driven by the large

surface to be covered and the radiation environments:

- **Drift tubes (DT)** - This technology uses stretched wires within a gas volume. Charged particles travelling through the gas ionize atoms, leaving a cloud of electron along the track. These electrons then drift in the tube and are collected by the positively-charged wires. By measuring the difference of current collected at both extremity of the wire and knowing the drift time, it is possible to infer the position of the hit in the drift tube.
- **Cathode strip chambers (CSC)** - Cathode strip chambers are made of array of anode wires crossing cathode strips within a gas volume. A charged particle travelling through the gas ionizes atoms and provokes an avalanche of electrons. The electrons and ions move to the anode and cathode respectively, producing a signal in both of them which leads to a bidimensional information.
- **Resistive plate chambers (RPC)** - Resistive plate chambers are made of two plates of high-resistivity plastic acting as cathode and anode separated by a gas volume. After ionization of the gas causing an electron avalanche, the charges travel through the plastic plates to be collected by strips situated behind them.

The DT technology is used in the barrel, up to $|z| \approx 6.5$ m, covering pseudo-rapidities up to $|\eta| = 1.2$, while the CSC technology is used for the endcaps, where the background rate is large and the magnetic field is also large and non-uniform, between $|z| \approx 6$ m and $|z| \approx 10.5$ m covering up to $|\eta| = 2.4$. The RPC complements the previous technologies for $|\eta|$ up to 1.6, providing a coarser position resolution but a faster response and better time resolution.

When combining the information of the muon system with the tracker, one can obtain a relative resolution on the p_T typically of 1%, and a relative resolution on η and ϕ typically of the order of 10^{-4} [67].

2.2.2 Trigger system

The CMS detector must sustain a rhythm of one bunch crossing each 50 or 25 ns, depending on the condition of the LHC machine. The raw output of the detector is therefore about $\sim 20 - 40$ MHz. It is unrealistic to consider storing and reconstructing all these events considering the speed of the link to the network, the memory and the computing power it would require. Therefore, a selection must be applied online to reduce the rate to a more realistic one, set to about 400 Hz.

The system in charge of this task is called the trigger [68]. The reduction of the rate is done by performing a minimalist identification of the features in the event (such as significant calorimeter deposits, or hits in the muon system), followed by a more complete reconstruction of the objects, and applying thresholds at each steps to decide quickly whether the event might be or not relevant for physics analysis. The design of these thresholds must be done carefully to have an adequate balance between keeping the rate low, while maintaining a high efficiency for the relevant physics processes. In this sense, it is also important to optimize the execution time of the software as well as obtaining a good accuracy of the minimalist reconstruction to efficiently use the available resources.

The trigger system of CMS is composed of two levels. The level 1 (L1) trigger first reduces the rate from 40 MHz to 100 kHz, followed by the high-level trigger (HLT) which further reduces the rate to 400 Hz.

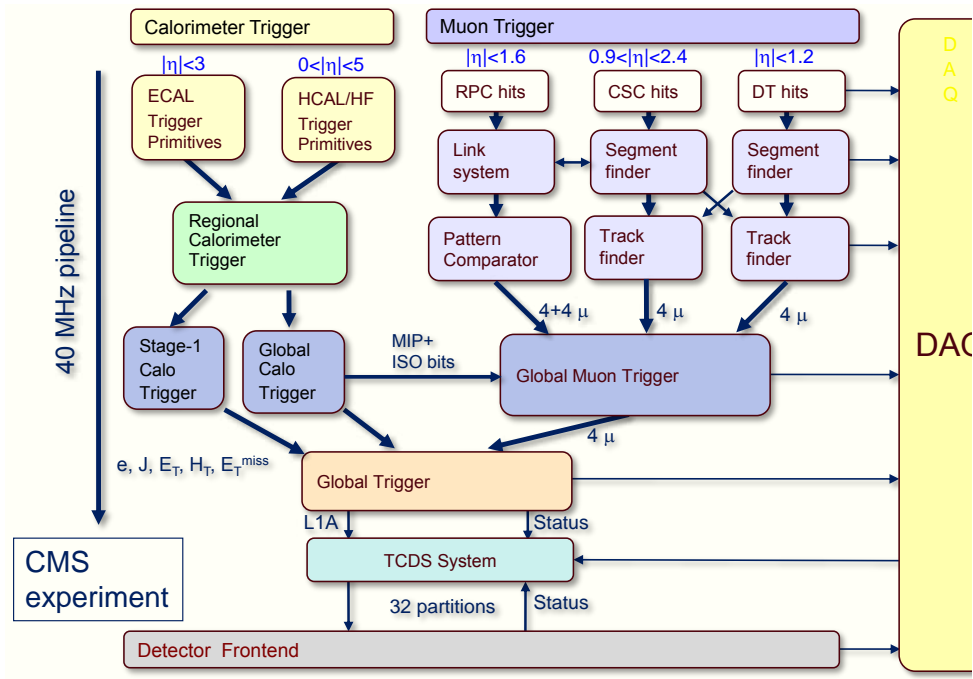


Figure 2.14: Architecture of the L1 trigger.

The L1 trigger takes information from the calorimeters and muon system as input and is itself composed of different stages as represented on Figure 2.14. The first stages, the trigger primitives, are from the front-end electronics, at the closest of the subsystems. These primitives are merged into the regional calorimeter and muon triggers, identifying significant energy deposits or muon hits in independent regions of the detector. These regional triggers produce a list of muons, e/γ candidates and local energy deposits. This information is fed to the global calorimeter and muon triggers which combine it and remove redundant information. The final global trigger applies the trigger menu, that is the set of requirements applied on the final list of objects. L1 triggers range from

simple single objects with a p_T threshold, for instance single electron triggers, to selection requiring the coincidence of several objects with topological conditions on them, such as a muon plus several jets. Generally speaking, the total rate of a given signature decreases as the variety and number of objects it contains increase. It is therefore possible to put lower threshold on complex selections compared to simpler ones: for instance, the p_T thresholds for an $e + \mu$ trigger can typically be set to lower values compared to a dimuon trigger for the same rate, itself having lower thresholds than a single muon trigger.

If the events pass any of the selection in the L1 menu, it is handled to the HLT. The HLT selection consists of a much larger list of paths compared to the L1. It is done on a computer farm able to perform a full reconstruction of the objects present in the event, including the information from the tracker. This reconstruction aims to be as close and accurate as possible as to the offline reconstruction described in the next sections. However, some particular techniques may not be used if they are too expensive in terms of CPU resources. Furthermore, the processing steps are carefully designed in order to optimize the processing time, especially by working with steps of increasing complexity and possibly filtering some of the events in the middle of the procedure. For instance, selection steps involving only calorimeters and muon detectors are performed before any tracking reconstruction is required, as this last step is CPU intensive. Once an event is selected, it is stored to be used in offline physics analysis.

2.2.3 Object and event reconstruction

After recording an event, the outputs of each subdetector are analyzed to identify the nature and properties of particles produced in the event. Ultimately, one wants to reduce step by step the complexity of an event down to a few objects that are meaningful for the particle physicist. Here, we briefly present some of the cornerstones of the CMS reconstruction. First, the tracking and vertexing steps correspond to the identification of tracks left by charged particles in the tracker and the collision vertices. This step is a crucial point for the second part, the particle flow algorithm, which combines measurements from the tracker, muon systems and calorimeters to produce a collection of reconstructed particles. In a third step, jets of particles can be constructed using clustering algorithms to reach the original parton momentum and direction, and a general momentum imbalance can be computed to sign the production of particles that escaped detection.

Tracking and vertexing

The challenge that the tracking step must address is to use the hits in the tracker layers to find and reconstruct the tracks of the $\mathcal{O}(10^3)$ charged particles produced in each bunch crossing. If badly designed, this step can lead to increased computing time because of the large possible combination of hits one has to try, or a high fake rate. The tracking algorithm must therefore be efficient in time, but also have a good reconstruction efficiency and a low fake rate.

The CMS tracking algorithm [67] starts by constructing seeds from pairs or triplets of hits in the pixel detector, compatible with coming from the beamspot. Then, assuming that these hits are coming from a charged particle, the trajectory is extrapolated to the next layers. If a hit is found compatible with the extrapolation, it is used to update the track parameters estimation. Finally, once no more hits are expected in the detector, the algorithm stops and a final fit is performed to determine the track parameters. Then, an iterative procedure removes the hits associated to reconstructed tracks, and repeats the track reconstruction from new seeds with looser criteria. The track reconstruction efficiency for muons is found to be very good as it is higher than 99% up to $|\eta| \sim 2.4$, whereas for pions the efficiency varies between 85 and 95% depending on p_T and η . Figure 2.15 shows on the left the relative resolution on the p_T of isolated muons, which is typically about 1-2% in the barrel and for $10 < p_T < 100$ GeV.

Reconstructed tracks are used to identify collision vertices, called primary vertices². Only good quality tracks are used in the process, based on their compatibility with the beam spot, the number of hits and their fit quality. A metric is defined from the closest approach of the track to the z -axis and the associated uncertainty coming from the track measurement. Then, a deterministic annealing algorithm [69] is used to cluster the tracks into vertices. Compared to the traditional jet algorithm that will be discussed later, this algorithm is a divisive clustering algorithm: at first, all tracks are put in a single group, which is then iteratively divided in smaller groups until a given condition is met. Once it is done, the tracks of each group are used to fit the position of the initial vertex. The resolution on the vertex position in (x, y, z) depends on the number of tracks associated to the vertex, being about 0.1 mm when the vertex has only 5 tracks, and down to 10-20 μm when it has more than 40 tracks as shown on Figure 2.15 for z . Figure 2.16 illustrates the vertexing capabilities in an event with 78 vertices reconstructed. Finally, the primary collision vertex is defined as the vertex with highest $\sum_{\text{tracks}}(p_T^2)$.

²As opposed to secondary vertices which occur for example in the hadronization of b quarks.

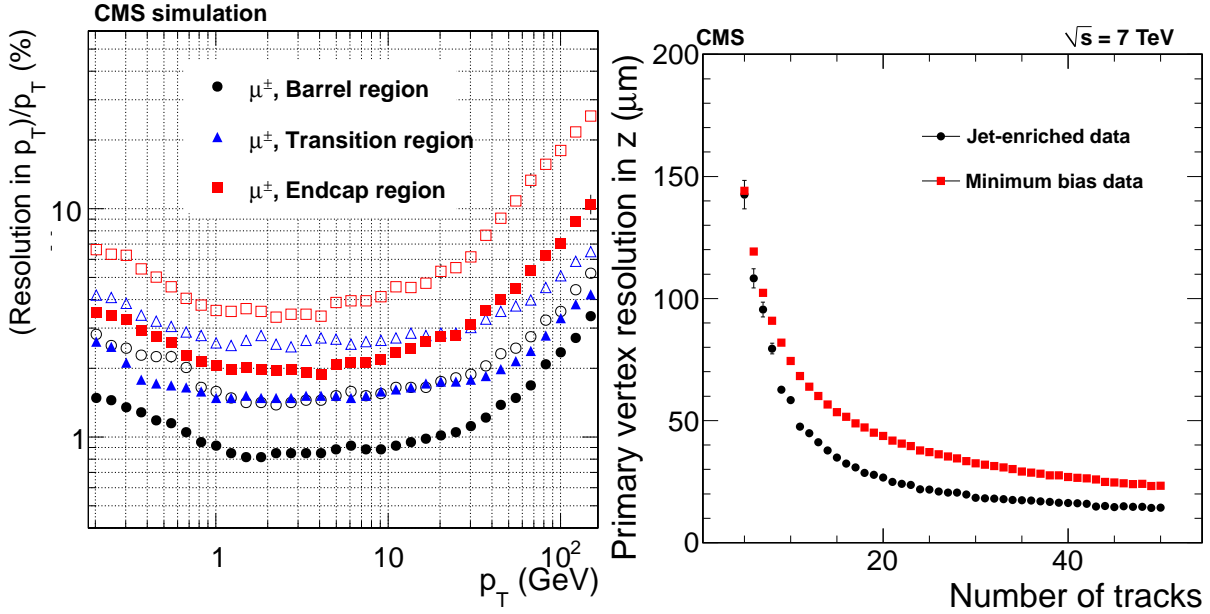


Figure 2.15: On the left: relative resolution in p_T , as function of the p_T , for the tracking of isolated muons in the different $|\eta|$ intervals corresponding to the barrel, the transition region and the endcap ; the solid and open dots correspond respectively to a half-width of 68% and 90%. On the right: absolute resolution on the primary position as function of the number of tracks of the vertex, for two kinds of events [67].

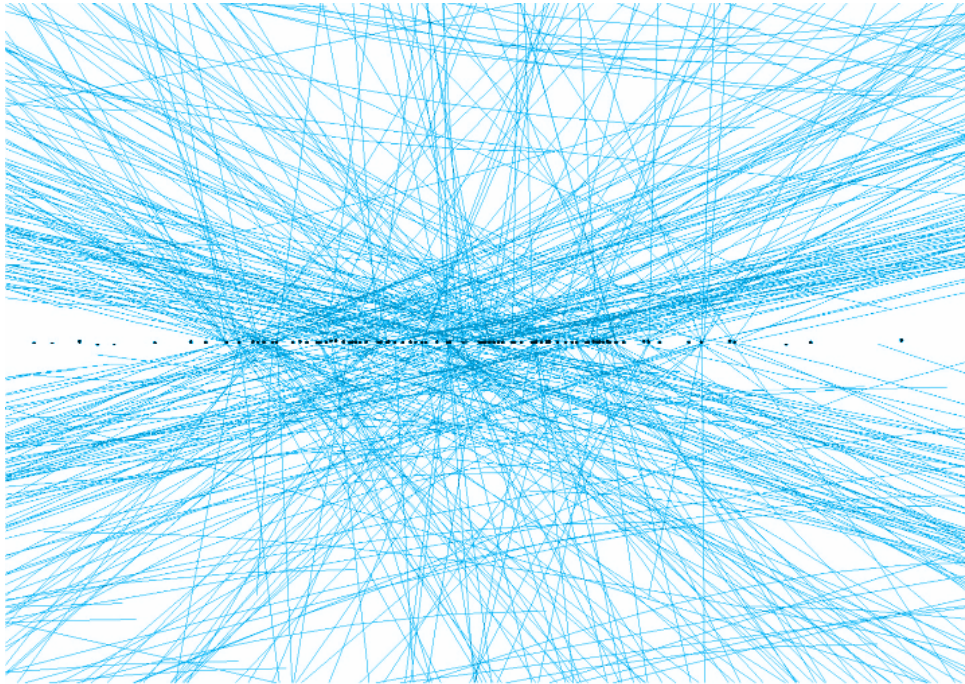


Figure 2.16: Zoom on the beamspot region of an impressive event containing 78 reconstructed vertices.

Particle flow algorithm

The role of the particle flow algorithm [70] is to efficiently combine the output of each subdetector to reconstruct each kind of particle according to its nature. Thanks to a

development before the data taking, it has quickly become the most common method of reconstruction used for physics analysis. Particle flow is especially relevant in the context of jet clustering that will be presented in the next section: the tracker provides key information such as the direction at the vertex for low p_T charged particles whereas the calorimeters are needed in the high p_T regime and for neutral particles.

To combine the outputs of the subdetectors, links are created between elements to create blocks. Given the granularity of the detector, blocks are typically made of one, two or three elements. For instance, reconstructed charged-particle tracks are used to extrapolate the trajectory of the particle to the ECAL and HCAL layers. If energy deposits are found nearby the predicted hit using the ΔR metric, the track is linked to the energy deposits. Similarly, tracks in the tracker can be linked to tracks in the muon system under the condition that the global fit of the two tracks is good enough, using a χ^2 as metric.

The reconstruction of electron is more challenging as they are significantly affected by Bremsstrahlung while traveling through the layers of the tracker and may radiate photons. In an attempt to collect and link those photons to the charged-particle track, tangents to a track at each layer are extrapolated to the ECAL and compatible energy deposits are linked to the track.

After this link step, the identification step is performed from the least ambiguous object to the most ambiguous object. Each time an object is identified, it is removed from the algorithm before starting the next identification step.

The least ambiguous objects, the muons, are identified from blocks made of compatible tracks in the tracker and the muon system. Then, electrons are considered from block made of tracks and energy deposits in the ECAL. The exact treatment for electrons is more careful than for other tracks, as the fit of the track must take into account the successive loss of energy due to Bremsstrahlung in the tracker layers. Therefore, the tracks are refitted using a Gaussian-Sum filter (GSF) [71] which takes this phenomena into account. The final identification involve criteria on the tracking, calorimetric and compatibility variables.

After the charged leptons identification, criteria are applied on the remaining tracks and those are considered to be charged hadron candidates. Their energy and momentum are computed either from the track alone assuming a charged pion hypothesis, or by combining the track and calorimeter information which is relevant in particular at high p_T or large η where the tracker resolution is degraded. Finally, after subtracting the energy deposits from charged particles in the ECAL and HCAL, the remaining significant energy deposits give rise to photon candidates and neutral hadron candidates.

Jet reconstruction

The concept of jets refers to collimated bunches of stable hadrons coming from partons (quarks or gluons) after they fragment and hadronize. Reconstructing jets can therefore yield information regarding quarks or gluons produced in the event. Jets are defined from the choice of algorithm to reconstruct them as well as the parameters used. It can not be stressed enough that there is no direct equivalence between a jet and a parton: the interpretation of a jet is fundamentally ambiguous as one parton shower can overlap with another. Moreover, a jet can be contaminated by other hadronic activity in the event, such as pile-up, which can degrade the energy and angular resolution. Jet physics is therefore a very rich topic and a field in itself, which goes from theoretical QCD to models of hadronization, jet reconstruction, calibration and study of the jet substructure.

Two main categories of algorithms exist to build jets: cone-based algorithm and incremental clustering algorithm. CMS mainly uses two incremental clustering algorithms. The starting point is the definition of the metric between objects in the event, which may be for instance the energy deposits in the calorimeters or the particle flow collection. The main algorithm is called anti- k_T [72] and uses a metric defined by

$$d_{ij} \equiv \min(p_{T,i}^{2p}, p_{T,j}^{2p}) \frac{\Delta R_{ij}^2}{r^2} \quad (2.9)$$

where $p = -1$ for anti- k_T , $p_{T,i}$ (resp. $p_{T,j}$) is the value of the transverse momentum of the i -ish (resp. j -ish) object, and r is a size parameter, analogous to the size of a cone and typically equal to 0.5 for CMS during Run I. Objects with the smallest d_{ij} are merged together into a protojet. The procedure is repeated until all the objects have d_{ij} larger than r . In the simple case with one high- p_T object surrounded by several softer objects, this leading object will aggregate all the softer ones and the result is a cone-like jet. When there are two or more high- p_T objects in the event, they either get merged into a single jet ($\Delta R < r$) with a cone-like shape around their barycenter, or lead to two separated jets ($\Delta R > r$) where the dominant object will first aggregate the softer objects. An example of jet reconstructed with this algorithm is shown in [Figure 2.17](#).

The second algorithm, called Cambridge/Aachen algorithm [73], uses the metric from [Equation \(2.9\)](#) but with $p = 0$, i.e. not relying on the p_T of the objects but only on their angular proximity. The shape of the jets obtained with this algorithm are less likely to be cone-like. Nevertheless, it has been found to yield better results for substructure-oriented studies of jets.

Experimentally, jets are typically made of 10-20 particles, and about 65% of the energy is carried by charged hadrons, 25% by photons and 10% by neutral hadrons at 100 GeV

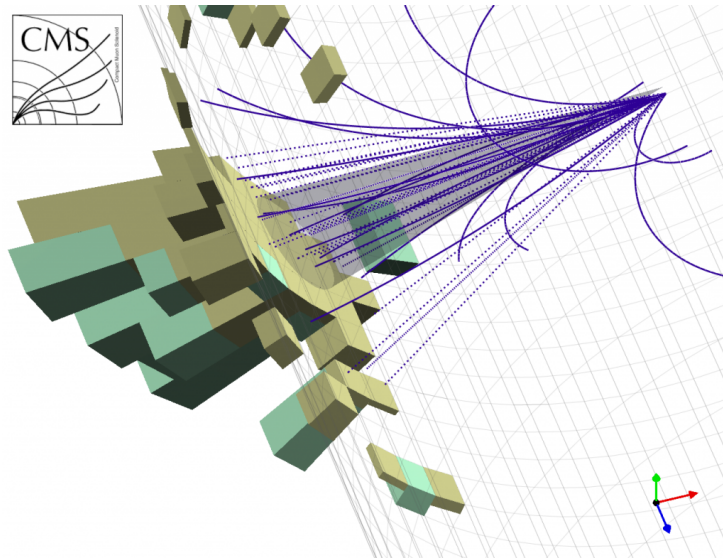


Figure 2.17: Representation of a 115 GeV jet reconstructed in CMS with the anti- k_t algorithm, showing the reconstructed tracks left by charged particles in plain blue lines, and the trajectory of neutral particles in dotted lines [75]. The electromagnetic and hadronic deposits in calorimeters are represented in lego plots in yellowish and teal respectively. One should note how the curved trajectory of some charged particles make it so that they actually leave the pseudo-cone when flying out of the vertex.

[74]. Figure 2.18 presents a comparison of the performances obtained for particle-flow jets and calorimeter-based jets. For a given initial parton, the probability to successfully reconstruct a jet in $\Delta R < 0.1$ reaches 90% for a parton of 30 GeV for particle-flow jets compared to 80 GeV for calorimeter-based jets. In terms of p_T resolution, the reconstructed p_T is roughly within $90\% \pm 15\%$ of the generated p_T for the particle-flow jets when $40 < p_T^{\text{gen.}} < 60$ GeV, whereas it is within $50\% \pm 15\%$ for calorimeter-based jets [70]. This bias in the reconstructed transverse momentum is typically due to thresholds and inefficiencies in the calorimeters and can be measured and corrected after the jet reconstruction. This correction is typically parametrized as function of p_T and η .

Missing transverse energy

So far it has been shown how to reconstruct charged leptons and photons and get information regarding quarks and gluons produced in the event. The remaining type of stable particles one expects from the Standard Model is neutrinos, which have very low rate of interaction with matter and therefore escape detection. Some theories beyond the Standard Model also include stable particles escaping detection such as neutralinos in R-parity conserving SUSY.

It is possible to infer information about the production of such particles via the energy-

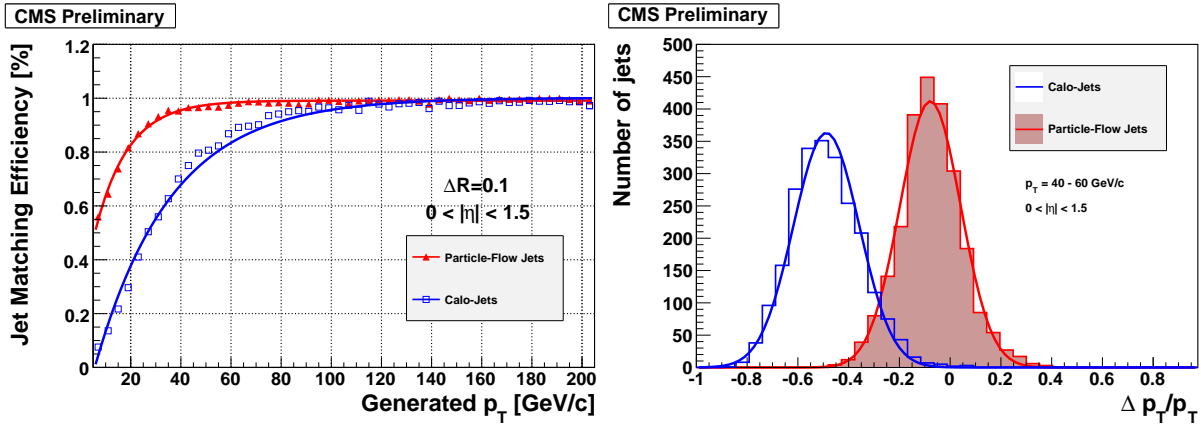


Figure 2.18: Comparison of some performances for the jet reconstruction using particle flow as input compared to a calorimeter-based approach [70]. On the left, jet matching efficiency as function of the generated p_T in the central region $|\eta| < 1.5$, effectively corresponding to the probability of successfully reconstructing a jet within $\Delta R < 0.1$ of the generated parton. On the right, relative difference between the reconstructed and generated p_T for initial partons with $40 < p_T^{\text{gen.}} < 60$ GeV.

momentum conservation in the transverse plane³. A significant imbalance may reveal the momentum carried by the sum of invisible particles. We define the missing transverse energy as the sum of transverse momenta:

$$E_T^{\text{miss}} \equiv - \sum_{\text{objects}} \vec{p}_T. \quad (2.10)$$

In this formula, one must define what are the objects to consider and this choice leads to several possible reconstructions, such as calorimeter-based, track-based or PF-based E_T^{miss} . Several effects may lead to artificial E_T^{miss} , in addition to the genuine E_T^{miss} from invisible particles, which can be classified in two categories: intrinsic condition and resolution of the detector, for instance the jet energy resolution ; and misreconstruction of the events or mismeasurement in the operation of the detector, for instance in the operating of the laser correction of the ECAL. One of the challenges of E_T^{miss} reconstruction is therefore to identify and understand the different sources of unphysical missing energy as well as biases and smearing, and either correct them to improve the resolution or veto the corresponding events. Figure 2.19, on the left, shows how sources of unphysical E_T^{miss} lead to an unexpected large tail in the reconstructed distribution for the data [76]. After identifying several causes and filtering out events likely to have unphysical E_T^{miss} , the agreement between data and simulation is restored.

Events with no genuine E_T^{miss} provide a mean to study the resolution. $Z \rightarrow \mu\mu$ events

³The longitudinal plane can however not be used, since the two incoming partons carry different, unknown momenta.

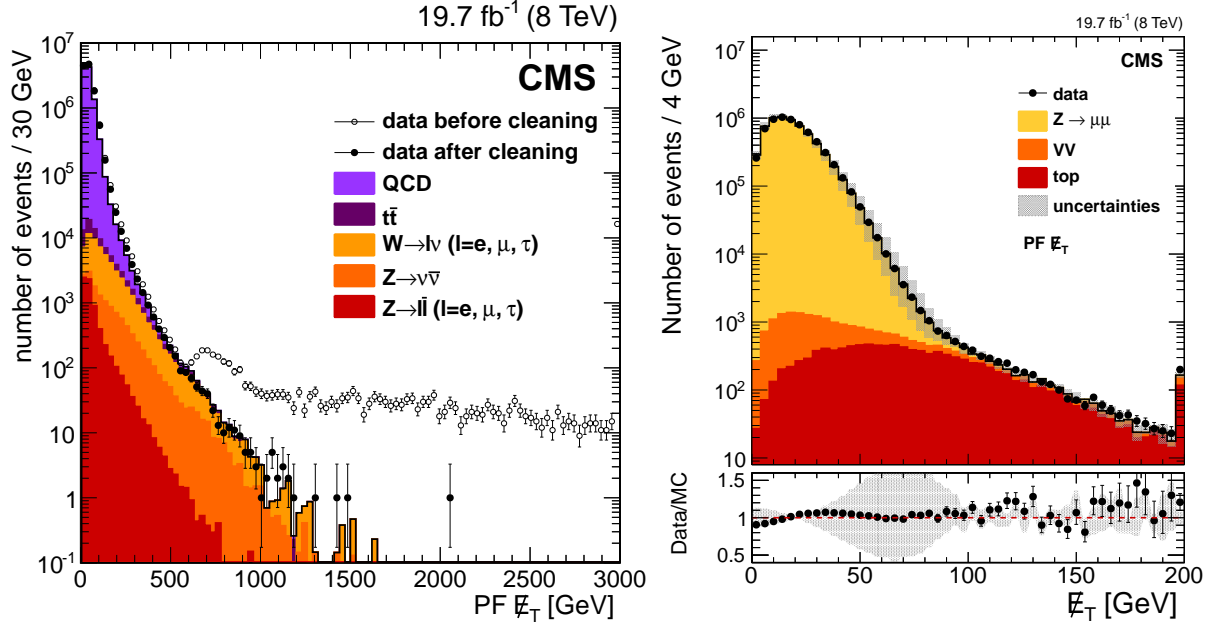


Figure 2.19: On the left, comparison of data with simulation of the particle-flow based E_T^{miss} distribution, before and after cleaning of the events likely to contain unphysical E_T^{miss} . On the right, distribution of E_T^{miss} in a $Z \rightarrow \mu\mu$ enriched sample [76].

fit well this purpose as muons are well-identified objects with a good resolution and a constraint can be put on the invariant mass of the dimuon system to obtain a sample with good purity. Figure 2.19, on the right, shows the distribution of the reconstructed particle-flow based E_T^{miss} in such events. The maximum of the distribution is around 10 – 20 GeV and drops by three orders of magnitude up to 70 – 80 GeV.

The resolution can be studied as function of the recoil of the $Z \rightarrow \mu\mu$ system due to initial state radiations, and also as function of the pile-up in the event, as presented on Figure 2.20. We introduce \vec{q}_T , the measurement of the energy-momentum of the Z from the dimuon system, i.e. $\vec{q}_T \equiv (\vec{p}_{T,\mu_1} + \vec{p}_{T,\mu_2})$. We use all the other reconstructed particles in the event to define $\vec{u}_T \equiv \sum_{\text{non-}\mu} \vec{p}_{T,i}$, which in the ideal case should correspond to the energy momentum of the sum of the ISR and perfectly balance with \vec{q}_T . Finally, we introduce u_{\parallel} as the projection of \vec{u}_T on the axis defined by $\hat{q}_T \equiv \vec{q}_T/q_T$, i.e. $u_{\parallel} \equiv \vec{u}_T \cdot \hat{q}_T$.

At low q_T , the ISR is essentially too soft to be measured accurately, and therefore $-u_{\parallel}$ is quite different from \vec{q}_T . At $q_T \sim 40$ GeV, however, the measurement of the ISR gets better and u_{\parallel} is within $\sim 3\%$ of q_T . In addition, the resolution of \vec{u}_{\parallel} strongly depends on the pile-up activity since more hadronic activity tends to increase jet energy mismeasurement.

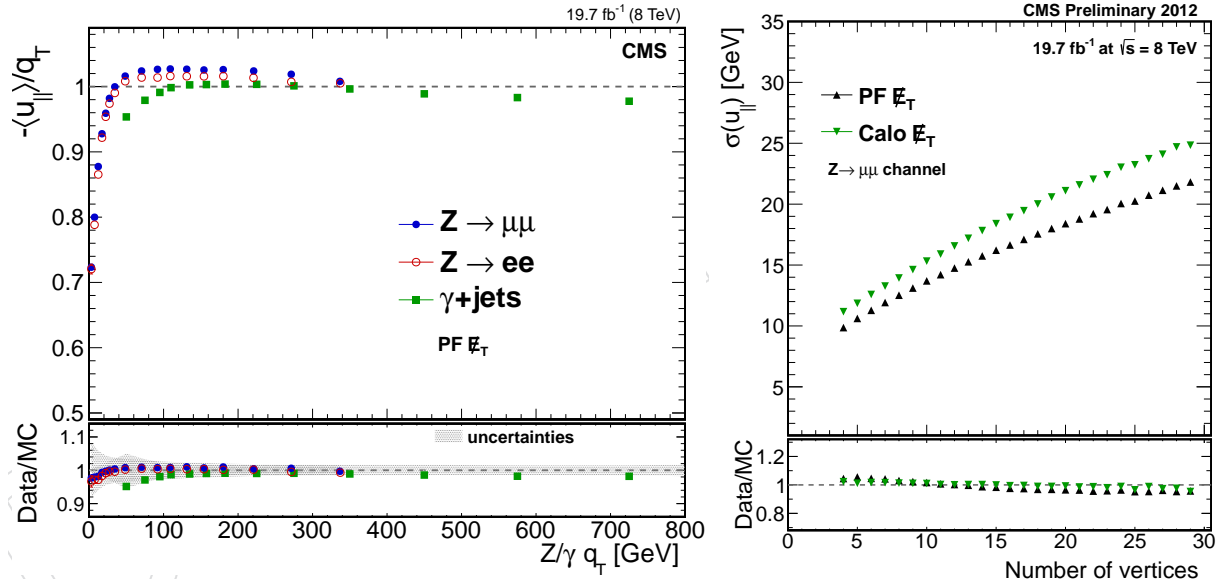


Figure 2.20: On the left, measurement of the ratio $-u_{||}/q_T$ as function of q_T in $Z \rightarrow \mu\mu$, $Z \rightarrow ee$ and γ +jets events using the particle-flow based E_T^{miss} . On the right, resolution of $u_{||}$ as function of the number of reconstructed primary vertices, for $Z \rightarrow \mu\mu$ events [76].

2.3 Collisions and detector simulations

After registering the events from the detector, and reconstructing the particles produced, one needs a mean to compare the experiment with theories. Given the complexity of a single bunch crossing, including the hard scattering, underlying events and pile-up, and the complexity of the detector, the distribution of observables can not in the general case be predicted analytically. One must instead rely on Monte-Carlo generators and an accurate detector simulation. Such a tool can also help in designing the detector in the first place, for instance by studying the performances on a given process, all the way from the hard scattering to the objects after reconstruction.

The full chain of simulation can be implemented as follow. First, the Lagrangian is implemented and the Feynman rules are computed. Then, for a given process, a Monte-Carlo generator computes all possible Feynman diagrams up to a given order, and randomly generates hard-scatterings. The underlying event as well as initial and final state radiations are then added, and the quarks are hadronized. Finally the particles are propagated to the detector and its response is simulated, after which the reconstruction process is essentially the same as for data.

2.3.1 Monte-Carlo generation of the hard scattering

To get a better idea on how Monte-Carlo event generation of the hard scattering is performed, it is useful to take a simple example such as the diagram $u\bar{u} \rightarrow Z \rightarrow d\bar{d}$ at tree level [77]. The corresponding infinitesimal cross section is

$$d\sigma(u\bar{u} \rightarrow Z \rightarrow d\bar{d}) = \frac{1}{2\hat{s}} \left| \mathcal{M}(u\bar{u} \rightarrow Z \rightarrow d\bar{d}) \right|^2 \frac{d\cos(\theta) d\phi}{32\pi^2} \quad (2.11)$$

where (θ, ϕ) are the angles of between the initial and final state particles, \mathcal{M} is the matrix element and \hat{s} is the center of mass energy. The matrix element is, for a given diagram, a number computable from the Feynman rules. To generate events according to this simple process, one may draw random values of $\cos(\theta)$ and ϕ , uniformly distributed in $[-1, 1]$ and $[0, 2\pi]$ respectively. From the masses constraints and the directions of the decay products, it is then possible to compute the quadri-momentum of the products.

The value of $d\sigma$ is directly related to the probability for this event to occur and is different for each value of $\cos(\theta)$ and ϕ . To obtain a set of events with distributions of $\cos(\theta)$ and ϕ corresponding to what is to be observed in Nature, it is possible to unweight these events using for instance a hit-and-miss technique.

With these simple steps, we presented the basic procedure to build a Monte-Carlo event generator. However in real life, and in particular in the case of the LHC, the initial state is made of protons. Therefore, in order to obtain a description of actual collisions, one must consider instead the process $pp \rightarrow Z \rightarrow d\bar{d}$ and integrate over the parton distribution function.

Furthermore, a complete description of such a process must also include diagrams with additional partons produced in the event, coming for instance from initial or final state radiation, e.g. $pp \rightarrow Z \rightarrow d\bar{d}, d \rightarrow dg$, or from other diagrams. This level can be called LO+jets. Generating diagrams with additional partons in the final state however induces an exponentially growing number of diagrams to consider, and one must find adequate ways to implement this from a purely software point of view.

Finally, this brief description focused on tree-level diagrams, but a more accurate description of the process can be obtained if one is able to take into account higher order diagrams (NLO, NNLO, ...). Generally speaking, NLO is more difficult to automatize and, even though softwares are now able to handle NLO generation, it is currently still an active field of development.

2.3.2 Hadronization

Partons are affected by the strong interaction and cannot exist in free state, as discussed in [Section 1.2.2](#). If partons move away from each other with a sufficient energy, this energy will be used to create new colored particles and bind into hadrons forming a jet of particles collimated in the direction of the initial partons. This process is referred to as hadronization, and is a crucial point of event generation as it determines the structure of generated jets.

The number of problematics related to hadronization makes it a quite rich and active topic. The interface between the generation of the hard scattering and the parton shower is not trivial as no technique rigorously factorizes these two problems. For instance, a gluon emission during the parton showering (so-called soft emission) may correspond to an additional parton during the generation of the hard process (so-called hard emission), ultimately causing double counting and biasing the event set. To solve this problem, a factorization prescription, called a matching scheme, must be defined to remove this double counting.

There are different techniques to simulate hadronization [\[78\]](#). In particular, the technique used in the software PYTHIA is based on the Lund string model. In this model, two partons moving away from each other are linked via a gluonic string being stretched, its potential energy growing at the expense of its kinetic energy. When its potential energy becomes of the order of the mass of two quarks, this string is likely to break and pull out a pair of quarks out of vacuum. This process goes on until hadrons are formed, which may in turn decay according to known branching fractions.

So far, however, hadronization models contain free parameters which are not known, essentially due to our lack of understanding at this point of non-perturbative QCD. Therefore, the free parameters in these models must be tuned according to experiments.

2.3.3 Detector simulation

Now knowing the final state after hadronization and decay of the hadrons, we want to put the events in the context of a bunch crossing at the LHC. In particular, we need to take into account the pile-up. To do so, a number of pile-up collisions is drawn according to a distribution similar to the one expected in the data. Pile-up collisions are added to the event from a set of pre-generated and hadronized events.

Then, we want to simulate the response of the entire CMS subdetectors. To do this, a detailed description of the detector is implemented in the software GEANT4 [\[79\]](#). Its

description can be tuned to study, for instance, misalignment condition. The interaction between particles emerging from the bunch crossing and the detector material is simulated using physical models of radiation-matter interaction, eventually generating a signal in the readout electronics. The trigger is simulated as well, though only to know which bits are fired rather than filtering out events at this stage. The simulation takes up to a few seconds per event.

Mainly for time constraints, it is in some cases good enough to perform a fast simulation of the detector [80]. In this simulation, the radiation-matter interaction is parametrized and leads directly to the hits in the tracker and muon systems, and to the showers in the calorimeter towers. Hence, the same low-level information as for the full simulation is obtained, i.e. hits and energy deposits as measured by the electronics, and the same reconstruction algorithms can be applied. Overall, avoiding the CPU-intensive simulation of the radiation-matter interaction in `GEANT4` allows to speed up the simulation by a factor 100-400 depending whether pile-up is included or not.

Chapter 3

b-tagging techniques and validation in CMS

« I'm going to need a SWAT team ready to mobilize, street level maps covering all Florida, a pot of coffee, twelve jammy dodgers and a fez..! »

The Eleventh Doctor

Contents

3.1	Topology of <i>b</i> jets and tagging algorithms	68
3.1.1	Properties of <i>B</i> hadrons and topology of <i>b</i> jets	68
3.1.2	<i>b</i> jets discriminating quantities and objects	70
3.1.3	<i>b</i> -tagging algorithms	74
3.2	<i>b</i>-tagging validation in the CMS collaboration	79
3.2.1	Context and validation method	80
3.2.2	Sample size and impact on performance estimation	80
3.2.3	Validation of the new jet size parameter for the Run II	82
3.2.4	Validation of new default pile-up rate for validation samples	83
3.2.5	Validation of the premixing technique for pile-up simulation	87
3.2.6	Studies of high pile-up scenario for Phase 2	89

b quarks are found in the final state of a large variety of Standard Model involving top quarks, Z or Higgs bosons, as well as in many BSM processes. The hadronization of b quarks produces B hadrons, i.e. hadrons with a structure involving a b quark. Thanks to the remarkable properties of B hadrons compared to other hadrons, it is possible to identify jets originating from the hadronization of b quarks. Such identification is done using b -tagging algorithms, and represents an important tool used by a large fraction of analyses in the CMS collaboration.

In [Section 3.1](#), we discuss the B hadrons and b jet properties, which are the starting point to construct discriminating observables between b jets and jets from other flavors. Then, we present how these variables are used to build the b -tagging algorithms. In [Section 3.2](#), we shall discuss the b -tagging validation activity within the CMS collaboration, in particular focusing on some major validations to prepare the Run II of the LHC.

3.1 Topology of b jets and tagging algorithms

3.1.1 Properties of B hadrons and topology of b jets

The B hadrons, produced by the hadronization of b quarks, are bound states composed of a b quark and one or two other quarks. The study of their decays is a field in its own, and of particular importance as such decays are related to the CKM matrix and CP violation. B hadrons have particular properties compared to other hadrons found in light jets, i.e. arising from the hadronization of u , d , s quarks or gluons, making it possible to identify b jets. It must be noted that C hadrons, which are bound states involving a c quark, also share to a lesser extent some of these properties, which in turn makes c jets naturally more difficult to distinguish from b jets. The properties can be listed as follow:

- **Large mass** - B hadrons have masses ranging from 5 to 10 GeV, as they contain at least a b quark which has a mass around 4.5 GeV. Such a mass is much larger than those of hadrons found in light jets, which have a mass typically less than 0.1 GeV.
- **Long life time and decay length** - B hadrons decay via the weak interaction, with a strength proportional to the CKM matrix elements V_{cb} and V_{ub} which are of the order of 10^{-2} and 10^{-3} respectively. Because of the smallness of these parameters, the life time of B hadrons is about 10^{-12} s, corresponding to a decay length of a few tenth of millimeters (10^{-4} m). In comparison, light hadrons have life time of the order of 10^{-16} s.
- **High charged multiplicity decays** - B hadron decays typically contain 5 charged

particles on average, whereas other light hadrons usually decay into 1 or 3 charged particles.

- **Leptonic decay** - As the decay of *B* hadrons involves a virtual *W* boson, they can directly decay leptonically, with a branching ratio of 11% per lepton family. This fraction goes up to about 20% if one considers the full decay cascade (which includes $B \rightarrow C + \text{hadrons} \rightarrow \ell\nu + \text{hadrons}$).

In the context of a *b* jet, several particles including a *B* hadron emerge from the primary vertex where the hard scattering and hadronization occurred. Due to its life time, the *B* hadron decays a few tenths of millimeters away from the primary vertex, producing a secondary vertex, as represented on Figure 3.1. In the cases where *B* hadrons decay into a *C* hadron, a tertiary vertex might be produced due to the life time of *C* hadrons.

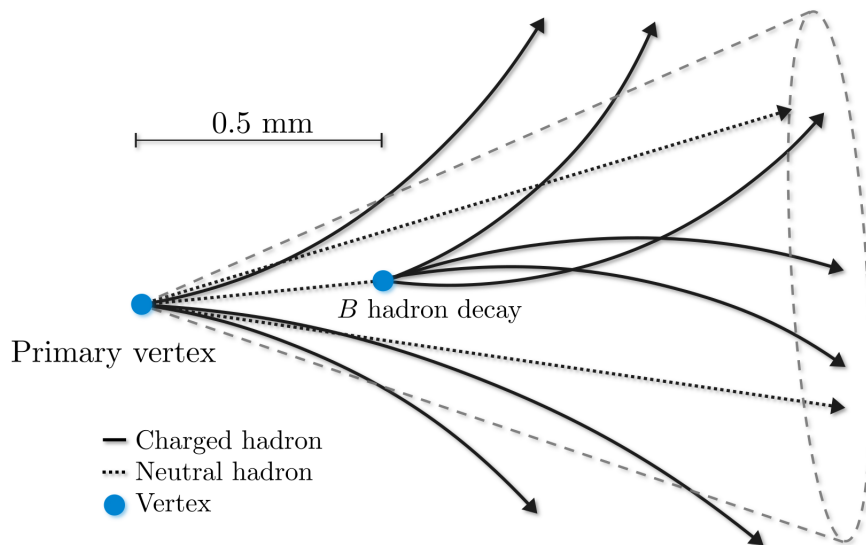


Figure 3.1: Topology of a jet originating from the hadronization of a *b* quark: the jet contains a neutral *B* hadron with a decay length around 0.5 mm, producing a secondary vertex with a high multiplicity of charged particles emerging from it.

Provided a good enough tracking resolution, such a topology can therefore be identified by looking for displaced tracks and the fact that several of them are compatible with originating from a common secondary vertex. Other properties may be used, such as the distribution of tracks inside the jet, or the presence of a charged lepton. A real life example of event containing *b*-tagged jets is shown on Figure 3.2, taken from a search for $H \rightarrow b\bar{b}$ in the CMS collaboration [81].

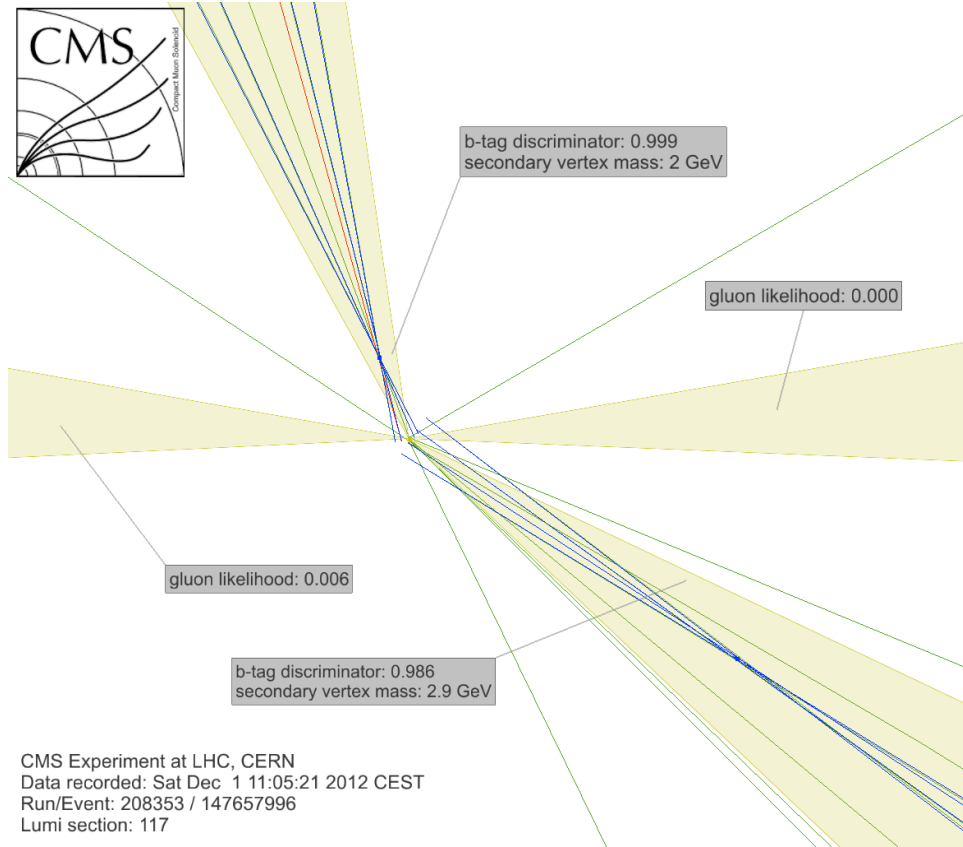


Figure 3.2: Illustration of b -tagging in an event at $\sqrt{s} = 8$ TeV. The display shows the longitudinal view of the surrounding region of the primary vertex and the tracks reconstructed, in a $H \rightarrow b\bar{b}$ candidate event produced through vector boson fusion (VBF) characterized by the two forward jets. The green tracks are prompt tracks while the blue tracks have a high impact parameter significance. On the jet at the top of the figure, the red line represents a reconstructed muon. One can clearly distinguish the secondary vertices in each of the central jets which have therefore a high b -tagging discriminant. The invariant mass of the two b candidates is found to be close to 125 GeV [81].

3.1.2 b jets discriminating quantities and objects

Track selection

For a given jet, the tracks considered for b -tagging studies must have a good quality (normalized $\chi_{\text{track fit}}^2 < 5$ as well as sufficient number of hits in the pixel and in the tracker as a whole) and $p_T > 1$ GeV. The tracks must also be within $\Delta R < 0.3$ of the jet axis (except for the track counting algorithm which uses $\Delta R < 0.5$). As illustrated on Figure 3.3, the points Q on the track and J on the jet axis are defined as the points of closest approach between the track and jet axis. In a similar way, the point P is defined as the point of closest approach on the track with respect to the primary vertex V . To reject contamination from pile-up and other jets that would be interpreted as displaced

tracks, several criteria are applied: the distance to jet axis, JQ , is required to be lower than $700 \mu\text{m}$; the so-called decay length of the track, VQ , is required to be lower than 5 cm ; and the track is required to be reasonably compatible in the transverse plane with the primary vertex by imposing a closest approach lower than 2 mm .

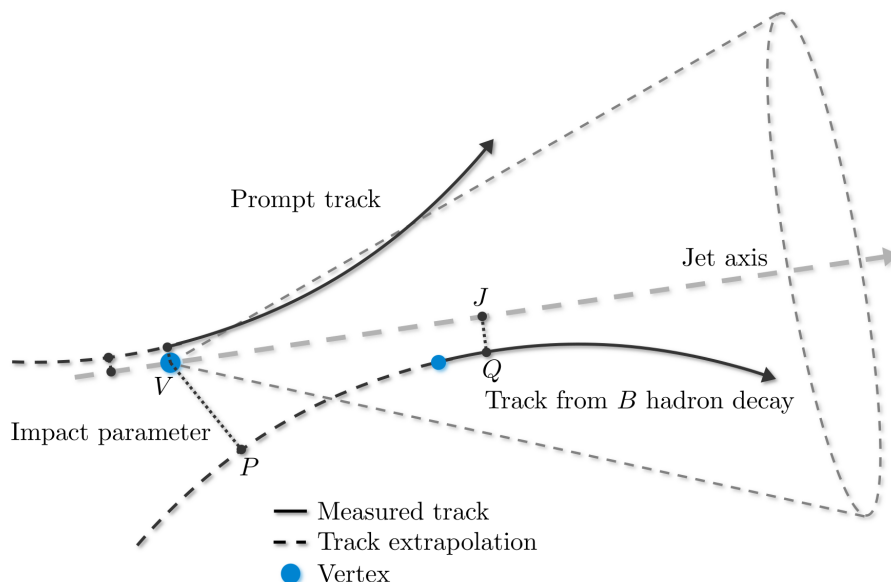


Figure 3.3: Representation of two tracks inside a b jet, one coming from a prompt charged hadron and the other from the decay of the B hadron. The prompt track has been slightly displaced from the primary vertex to illustrate resolution effects. One can define, along the track, the position of closest approach to the primary vertex, P , and the closest approach to the jet axis, Q . The impact parameter corresponds to the distance VP and it is given the sign of the scalar product $\vec{V}P \cdot \vec{j}$ (with \vec{j} being the jet direction).

Impact parameter

An important quantity to characterize the displacement of tracks is the impact parameter. As represented on Figure 3.3, the impact parameter is defined as the distance of closest approach, in the three dimensional space, between the track and the vertex, VP . Additionally, it is given the sign of the scalar product $\vec{V}P \cdot \vec{j}$ where \vec{j} is the jet direction.

Because of their displacement, tracks from the decay of B hadrons are expected to have a large, positive impact parameter. Tracks in light jets are instead expected to originate directly from the primary vertex and therefore to have non-zero value only due to resolution effects. To integrate the knowledge of the tracking resolution, the uncertainty on the impact parameter, σ_{IP} , can be computed for each track, and one can define the impact parameter significance, $S_{\text{IP}} \equiv \text{IP}/\sigma_{\text{IP}}$.

Figure 3.4 presents the distribution of the impact parameter (IP) and impact param-

eter significance for tracks in *b* jets, *c* jets and light jets. In particular, the distributions drop rapidly for tracks from light jets after $S_{IP} = 2$. The distributions for tracks from *b* jets shows a clear large tail in large positive values, but because *b* jets also contain some prompt tracks, a significant fraction ends up with low or negative S_{IP} values.

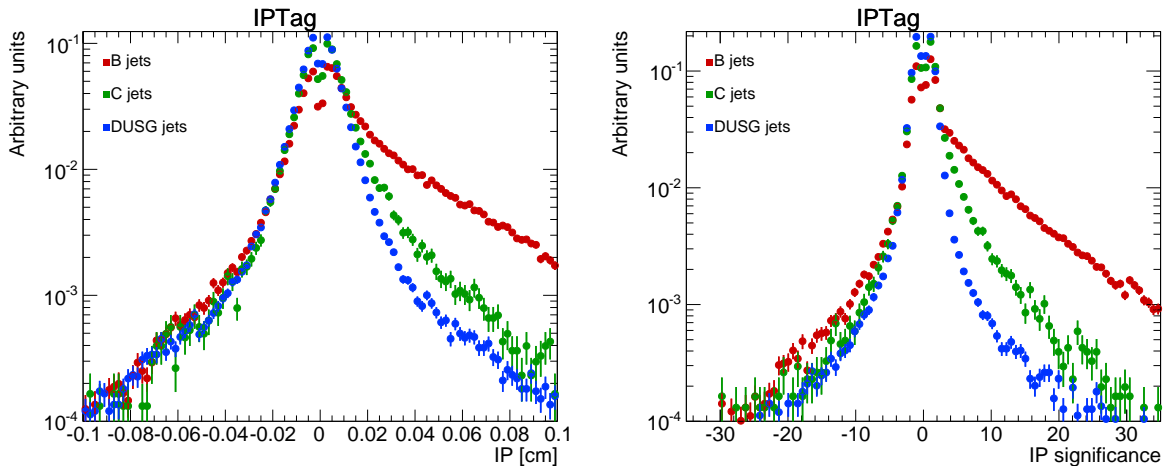


Figure 3.4: Distribution of the impact parameter (on the left) and impact parameter significance S_{IP} (on the right) for tracks inside the different jet categories, estimated using the validation framework from a $t\bar{t}$ Monte-Carlo sample with Run I conditions, including pile-up.

Secondary vertex

As discussed in Section 2.2.3, the resolution on the primary vertex position varies between 100 and 10 μm . This is less than the typical decay length of a *B* hadron, which makes it possible to attempt to reconstruct the corresponding secondary vertex. This can be done using adaptive vertex fitting techniques [82], similar to the technique used for primary vertices identification, but using parameters relevant to this context and in particular to be robust against outliers. Several quantities related to secondary vertex candidates can then be computed, such as the distance from the primary vertex (or flight distance), the flight direction and the vertex mass.

B hadrons are expected to have a flight distance of a few tenth of millimeters, a flight direction within $\Delta R < 0.5$ of the jet direction and a mass of a few GeV. To reduce contamination from vertices of long-lived mesons and particle interactions with the detector material, secondary vertices with a flight distance higher than 2.5 cm (i.e. much greater than what is expected for a *B* hadron) or a mass compatible with the mass of K_0 or larger than 6.5 GeV are rejected.

Figure 3.5 presents the distribution of the vertex mass and the flight distance signif-

inance for the different jet categories, showing a clear distinct shape for the distribution of b jets compared to light and c jets.

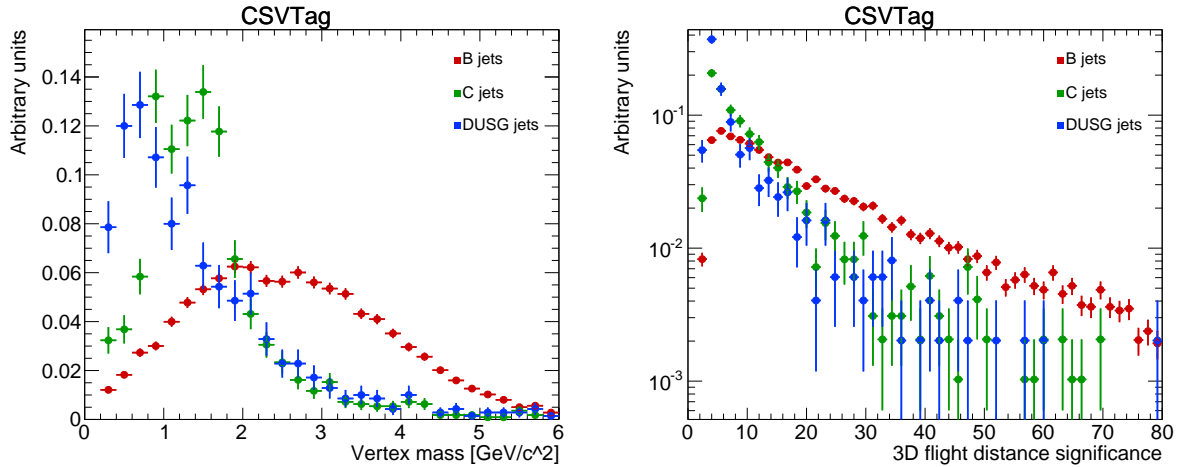


Figure 3.5: Distribution of the secondary vertex mass (on the left) and flight distance significance (on the right) for the different jet categories, estimated using the validation framework from a $t\bar{t}$ Monte-Carlo sample with Run I conditions, including pile-up.

Soft leptons

Due to the leptonic decay of B hadrons, a significant fraction of b jets are expected to contain a soft charged electron or muon. Despite the intrinsic limitation due to the low branching ratio, this specificity remains useful to complement other techniques and to enrich a sample of events in b jets as light jets have low probability to contain a lepton.

One useful variable, relating the soft lepton to the jet, is p_T^{rel} , defined as the projection of the lepton momentum to the plane perpendicular to the jet axis \vec{j} . In this definition, the jet direction is computed by also including the lepton. p_T^{rel} is expected to have larger values in b jets compared to light jets.

Additionally, the impact parameter significance of the lepton can be considered to characterize its displacement with respect to the primary vertex. In that particular case, the significance can benefit from the excellent resolution on muon tracking provided by the detector.

Figure 3.6 presents the distribution of the ΔR between the muon and the jet direction, as well as p_T^{rel} for muons inside the different categories of jets, showing the discriminating power that they provide.

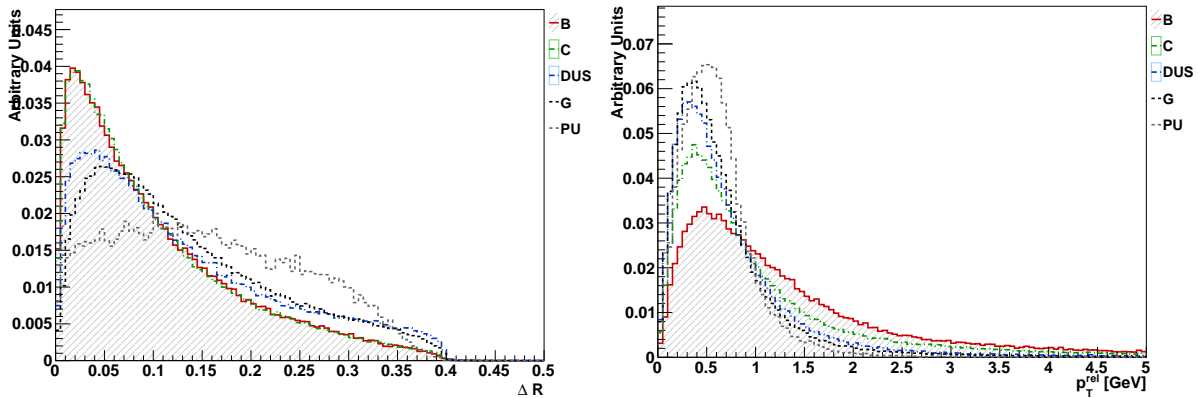


Figure 3.6: Distribution of $\Delta R(\mu, \text{jet})$ (on the left) and p_T^{rel} (on the right) for muons inside different jet categories [85].

3.1.3 *b*-tagging algorithms

Notion of performance

Before introducing the algorithms themselves, let's introduce the notion of performance of an algorithm. An algorithm associates to each jet a real value, the discriminant, whose distribution provides good discrimination between *b* jets and other jets flavors. One then defines an operating point, or threshold, such that jets with discriminant larger than the threshold are said *b*-tagged.

Typically, one wants to study the *b*-tagging efficiency as function of the threshold value, that is to say the probability for a given a *b* jet to be successfully *b*-tagged. Similarly, it is relevant to look at the fake rate, i.e. the probability that a non-*b* jet gets incorrectly *b*-tagged. Because the *c* jets are harder to differentiate from *b* jets, the fake rate of these jets is studied independently from light jets.

Performances are usually presented by showing the fake rate as function of the *b* jet efficiency, each point of the curve corresponding to a different threshold value. To benchmark the performances and allow easier comparisons between algorithms, three operating points, loose, medium and tight, are defined such that the fake rate for light jets is respectively 10, 1 and 0.1%.

Finally, the performances are likely to depend on the environment in which the jets are produced, in particular if there is other hadronic activity coming from the hard-scattering, or from pile-up contamination. In this section, the performances are obtained using the validation framework, and are computed from a $t\bar{t}$ Monte-Carlo sample at $\sqrt{s} = 8$ TeV with pile-up included. Performances at 7 TeV and 8 TeV are also discussed in [83], [84].

Track counting algorithm

The track counting algorithm is based on the impact parameter of tracks. Tracks are sorted according to the value of the impact parameter significance. Because of this ranking, the S_{IP} of the first track is biased and is likely to be high even for light jets. The second track offers a better compromise between background (light jets) rejection and signal (b jets) efficiency. A first version of the track counting algorithm is defined using the S_{IP} associated to this track and is called track counting high efficiency (TCHE). Using the third track S_{IP} as discriminant leads to a drop in the signal efficiency but on the other hand to a very low level of background. This alternative version of the algorithm is therefore called track counting high purity (TCHP).

Figure 3.7 presents the discriminant and performances for the different jet categories for the high efficiency version of this algorithm. The b jet efficiencies are around 77%, 60% and 18% for the loose, medium and tight working points respectively. The corresponding efficiencies for the high purity version are around 68%, 52% and 36% respectively, i.e significantly better performance for the tight working point.

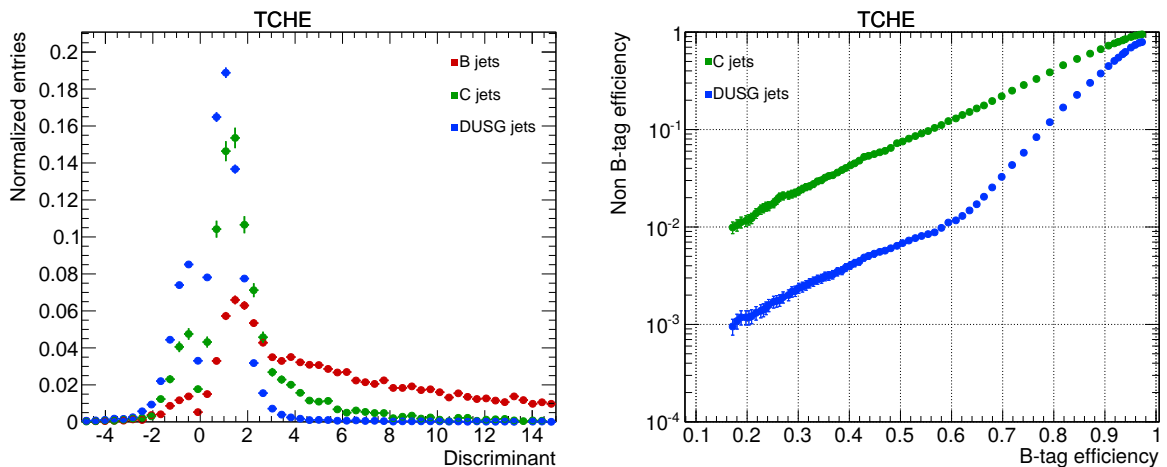


Figure 3.7: Superimposed discriminant distributions for light, c and b jets (on the left) and corresponding performances in term of misidentification rate versus b jet efficiency (on the right) for the track counting high efficiency algorithm. The distribution and performances are estimated using the validation framework and from a $t\bar{t}$ sample in 8 TeV conditions, including pile-up.

Jet probability

A more elaborate technique, but still based on track information alone, consists in using the impact parameter significance of several tracks in the jet. This can be done by computing a likelihood that all tracks associated to the jet originate from the primary

vertex. The starting point for this is to know the distribution of S_{IP} for prompt tracks and to compute, for each given track with impact parameter significance X , the probability $P_{\text{track}} = P(S_{\text{IP}} > X)$. To protect the algorithm from single, poorly reconstructed tracks, a lower bound is put on P_{track} at 0.005. The probability P_{jet} is then computed with the likelihood estimator, using the N tracks of the jet,

$$P_{\text{jet}} = \Pi \cdot \sum_{i=0}^{N-1} \frac{(-\ln \Pi)^i}{i!}, \quad \text{with} \quad \Pi = \prod_{i=1}^N \max(P_{\text{track } i}, 0.005) \quad (3.1)$$

The jet probability (JP) discriminant is finally defined as $-\ln P_{\text{jet}}$ to have a convenient range to work with. An alternative version of this algorithm is called jet B probability (JBP) and uses only the four tracks with highest S_{IP} .

Figure 3.8 presents the discriminant and performances for the different jet categories for the jet probability algorithm. The small spikes in the discriminant distribution, also visible in the performance curves, come from the lower bound on P_{track} . The b jet efficiencies are around 81%, 55% and 39% for the loose, medium and tight working points respectively.

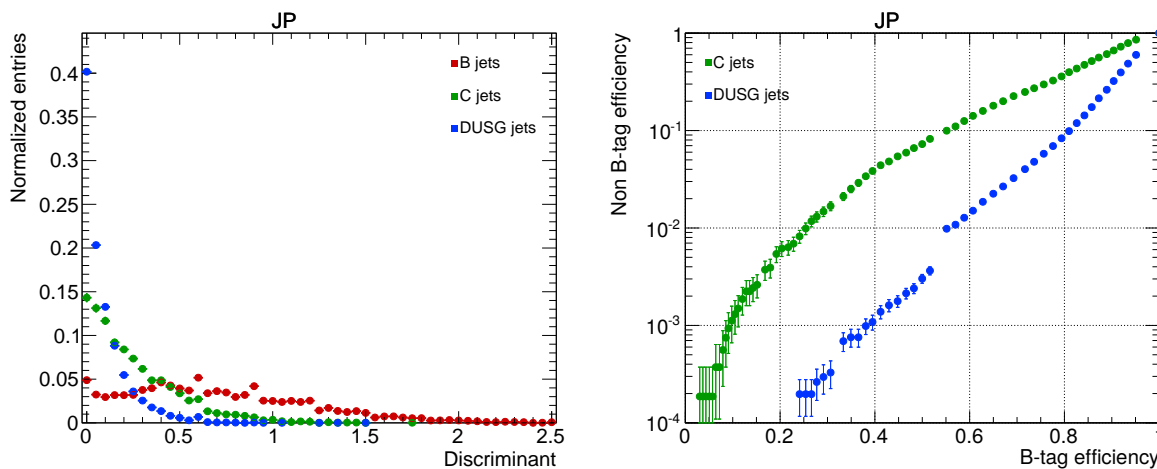


Figure 3.8: Superimposed discriminant distributions for light, c and b jets (on the left) and corresponding performances in term of misidentification rate versus b jet efficiency (on the right) for the jet probability algorithm. The distribution and performances are estimated using the validation framework and from a $t\bar{t}$ sample in 8 TeV conditions, including pile-up.

Simple secondary vertex

The simple secondary vertex (SSV) algorithm is based on secondary vertex reconstruction, and in particular uses the largest flight distance significance, among all secondary vertices

associated to the jet, as a discriminant. As for the track counting algorithm, two versions are defined to obtain either high efficiency (SSVHE) using secondary vertices with at least two tracks, either high purity (SSVHP) which requires at least three tracks.

Figure 3.9 presents the discriminant and performances for the different jet categories for the high efficiency of this algorithm. The maximum efficiency achievable is limited by the intrinsic efficiency of actually finding a secondary vertex which satisfies the constraints. For this version, it is around 62% for *b* jets and 20% for *c* jets, while the fake vertices rate (i.e. probability to find a vertex in light jets) is around 2%. The *b* jet efficiencies for the medium and tight working points are around 58% and 20% respectively. The high purity version has a tight working points with a *b* jet efficiency around 42%, significantly higher than the high efficiency version.

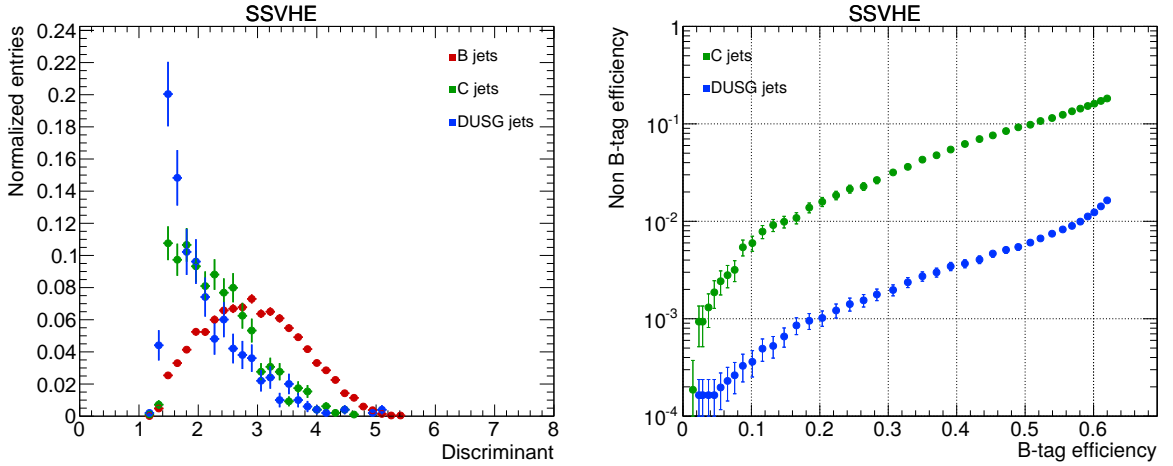


Figure 3.9: Superimposed discriminant distributions for light, *c* and *b* jets (on the left) and corresponding performances in term of misidentification rate versus *b* jet efficiency (on the right) for the simple secondary vertex high efficiency algorithm. The distribution and performances are estimated using the validation framework and from a $t\bar{t}$ sample in 8 TeV conditions, including pile-up.

Soft leptons algorithms

One can target the *b* jets containing soft leptons with dedicated algorithms. However, as no observable exhibits a strong discriminating power alone, a multivariate analysis has to be used. Several discriminating observables are fed into a neural network which is trained to differentiate signal jets (*b* jets) from background jets (light jets). These observables include p_T^{rel} , the ΔR between the lepton and jet axis, the relative lepton momentum, the impact parameter significance of the lepton and the lepton quality. Two algorithms are defined, targeting either jets with a muon (soft muon tagger, SMT) or an electron (soft electron tagger, SET). While muons are well-identified objects because they leave a

distinct signal in the muon system, electrons are more challenging due to the hadronic environment and dedicated in-jet electron identification must be defined. The maximum efficiency achievable for each lepton flavor tagger is intrinsically limited by the leptonic branching ratio of *B* hadrons, which is about 20% per flavor.

In practice, the maximum *b* jet efficiency for the soft electron tagger is around 14% compared to around 17% for the soft muon tagger. Figure 3.10 presents the discriminant and performances of the SMT algorithm. The *b* jet efficiencies at medium and tight working points are around 10% and 7% respectively.

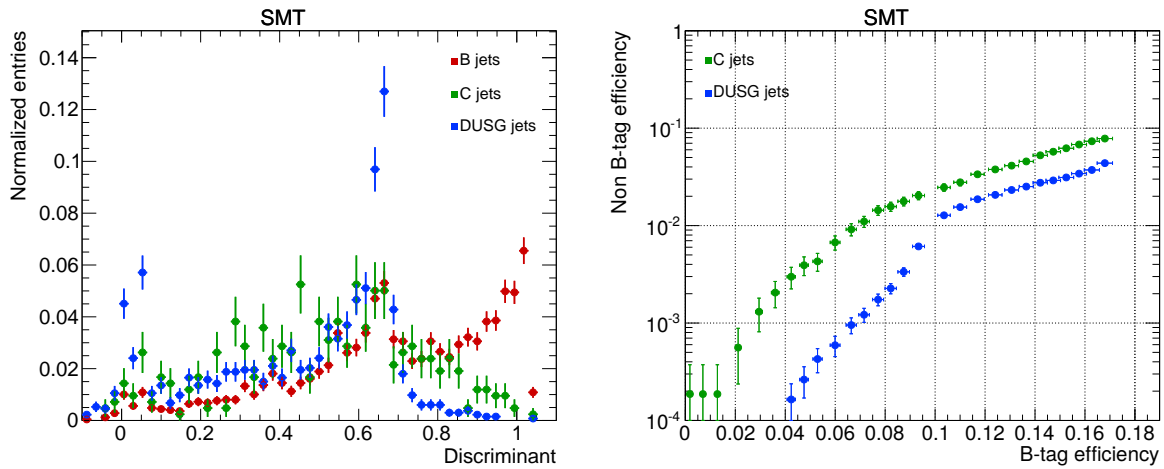


Figure 3.10: Superimposed discriminant distributions for light, *c* and *b* jets (on the left) and corresponding performances in term of misidentification rate versus *b* jet efficiency (on the right) for the soft muon algorithm. The distribution and performances are estimated using the validation framework and from a $t\bar{t}$ sample in 8 TeV conditions, including pile-up.

Combined secondary vertex

Finally, one may want to combine the techniques previously described as they complement each other. During the Run I, the track-based and secondary-based approach have been successfully combined into a combined secondary vertex algorithm (CSV). Developments are ongoing to include the soft lepton approaches in a new algorithm to be used during Run II. The CSV algorithm starts by dividing jets into categories according to whether or not a secondary vertex has been reconstructed. An intermediate category is designed for jets with no vertex fit but with still two tracks with $S_{\text{IP}} > 2$, which are used to define a pseudo-vertex in 15% of the cases where no vertex is found for *b* jets. With the goal of improving the rejection against *c* jets, for jets with a vertex or pseudo-vertex, the tracks are ordered according to their impact parameter significance, and the S_{IP} of the first track

to raise the invariant mass of the vertex above the charm threshold (1.5 GeV) acts as an additional good discriminating variable.

Likelihoods are trained as function of p_T and $|\eta|$, and based on the secondary vertex information, the energy and rapidity distribution of the tracks at the secondary vertex compared to the remaining tracks in the jet, as well as the S_{IP} of each track. Two likelihood ratios are defined, one to discriminate between light jets and b jets, and the other between c jets and b jets. These likelihoods are then combined by weighting them with a factor 0.75 and 0.25 respectively, accordingly to the typical needs of physics analyses.

Figure 3.11 presents the discriminant and performances of the CSV algorithm. At the loose working point, the b jet efficiency is around 78%, close to the track counting high efficiency algorithm. The b jet efficiency at the medium working point is around 65%, significantly better than track counting, simple secondary vertex and jet probability due to the completeness of the combined secondary vertex approach. The tight working point has a b jet efficiency of 40%, comparable to the jet probability algorithm.

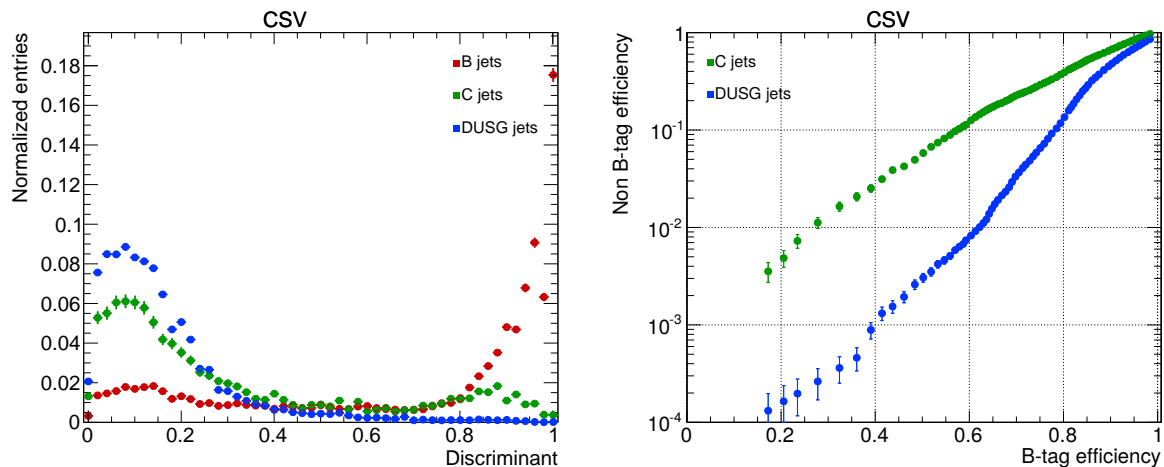


Figure 3.11: Superimposed discriminant distributions for light, c and b jets (on the left) and corresponding performances in term of misidentification rate versus b jet efficiency (on the right) for the combined secondary vertex algorithm. The distribution and performances are estimated using the validation framework and from a $t\bar{t}$ sample in 8 TeV conditions, including pile-up.

3.2 b -tagging validation in the CMS collaboration

In this section, we focus on my contributions on b -tagging during this thesis. After presenting the context of the work and discussing statistical aspects, some important validations are presented in particular related to the preparation of the Run II of the LHC, while the last subsection is dedicated to a preliminary study of the Phase 2 conditions.

3.2.1 Context and validation method

The software of the CMS collaboration is constantly evolving. The development cycle includes rigorous and recurring checks by all the detector groups, physics object groups and analysis groups. The frequency of such a validation procedure of the software ensures an early identification of bugs and to understand the evolution of distributions and performances. The types of changes in the CMS software include, but are not limited to:

- **Versions of dependencies** such as GEANT4 and ROOT which may in turn impact the description of particle-matter interaction or statistical aspects.
- **Generators and simulation workflow**, for instance related to the tuning of the parton shower software, or the simulation of pile-up.
- **Detector geometry and description**, which is likely to change during long shut-downs, as subdetectors have been and will be upgraded.
- **Alignment and calibration conditions** can be tuned for instance to simulate early data-taking with misaligned tracker layers.
- **Reconstruction techniques**, which are likely to evolve across time to include new methods, tune parameters or optimize performances.

In particular, *b*-tagging algorithms are highly dependent on *B* hadron modeling, tracking aspects, jet reconstruction and pile-up conditions.

The validation activity consists in comparing typical *b*-tagging variables and performances between a new version and an older one, the reference. The reference is usually taken to be the previous version to only consider the changes introduced in the new version. One can estimate the *b*-tagging performances for the two versions and check their compatibility.

3.2.2 Sample size and impact on performance estimation

The validation work is made on four different samples in order to cross-check results and factorize the impact of pile-up or simulation type:

- a $t\bar{t}$ sample with pile-up, and full simulation of the detector
- a $t\bar{t}$ sample without pile-up, and full simulation of the detector

Jet category	QCD sample		$t\bar{t}$ sample	
	Number	Critical efficiency	Number	Critical efficiency
u, d, s, g	17000	1.2%	19600	1.0%
c	1400	12%	4500	4%
b	700	22%	13000	1.5%

Table 3.1: Typical number of selected jets, per flavor category and for two sample types, and critical efficiency below which effects lower than 20% cannot be distinguished from statistical fluctuations at 2σ level.

- a $t\bar{t}$ sample without pile-up, and fast simulation of the detector
- a QCD sample with $50 < \hat{p}_T < 120$ GeV, with \hat{p}_T characterizing the energy of the process, and full simulation of the detector

As the validation is a recurrent process and the production of samples takes CPU resources and disk space, each sample contains only about 9000 events. This constraint impacts directly the magnitude of statistical fluctuations one will observe in variable distributions and in the performance estimation, in turn affecting the check of compatibility between the two versions.

The compatibility of the two versions, the release to be validated (val.) and the reference (ref.), can be quantified in the following way. The efficiency for a given cut on the discriminant is computed in both versions and yields the corresponding values $\epsilon_{\text{val.}}$ and $\epsilon_{\text{ref.}}$ with relative uncertainty $\sigma_\epsilon^{\text{rel.}}$. The ratio $r \equiv \epsilon_{\text{val.}}/\epsilon_{\text{ref.}}$ is computed, and one wants to check if the ratio is significantly different from 1. The relative uncertainty on this ratio is $\sigma_r^{\text{rel.}} = \sqrt{2} \cdot \sigma_\epsilon^{\text{rel.}}$, assuming that $\epsilon_{\text{val.}}$ and $\epsilon_{\text{ref.}}$ are uncorrelated.

To get an idea of the sensitivity of the validation, let's investigate what are the conditions to be able to see effects of magnitude lower than 20% on ϵ at 2 sigma level. We want $2 \cdot \sigma_r^{\text{rel.}} < 0.2$, and therefore approximately $\sigma_\epsilon^{\text{rel.}} < 7\%$. Considering the efficiency estimate $\epsilon = k/n$ from observing k objects passing a selection among n , one can define a critical efficiency such that the relative uncertainty on the efficiency estimation will be higher than 7%:

$$\sigma_\epsilon^{\text{rel.}} = \frac{\sigma_\epsilon}{\epsilon} = \sqrt{\frac{1}{n} \frac{1-\epsilon}{\epsilon}} > 0.07 \quad \Rightarrow \quad \epsilon < \frac{1}{\frac{n}{200} + 1} \quad (3.2)$$

Table 3.1 presents the number of jets according to their flavor, for the QCD and $t\bar{t}$ samples, as well as the critical efficiency associated to these numbers. This efficiency is about 1% for light jets, meaning that effects lower than 20% won't be distinguishable (at 2σ level) from statistical fluctuations below the medium working point.

To avoid this problem, some validations, only intended to study the impact of new reconstruction techniques and algorithms, recycle the Monte-Carlo generation and detector simulation steps of previous validation samples, in order to remove the statistical fluctuations coming from these steps.

3.2.3 Validation of the new jet size parameter for the Run II

The preparation of the Run II of the LHC involves a change in the jet size parameter. Because the jets are expected to be narrower on average due to the energy increase, and the pile-up contamination higher, this parameter is moved from $R = 0.5$ to 0.4 .

The validation of this change is made using two sets of samples using the same generated events and the same simulation to limit the effect of statistical fluctuations, but different jet size parameters for reconstruction. The sample used to produce the following figures is a $t\bar{t}$ sample at $\sqrt{s} = 13$ TeV with a pile-up of 10.

A comparison of the jets p_T and η spectra between the two reconstructions is presented on Figure 3.12. The η response is quite identical. However, small differences are seen in the p_T spectrum which are interpreted as coming from the jet energy corrections in the $R = 0.4$ reconstruction being still preliminary.

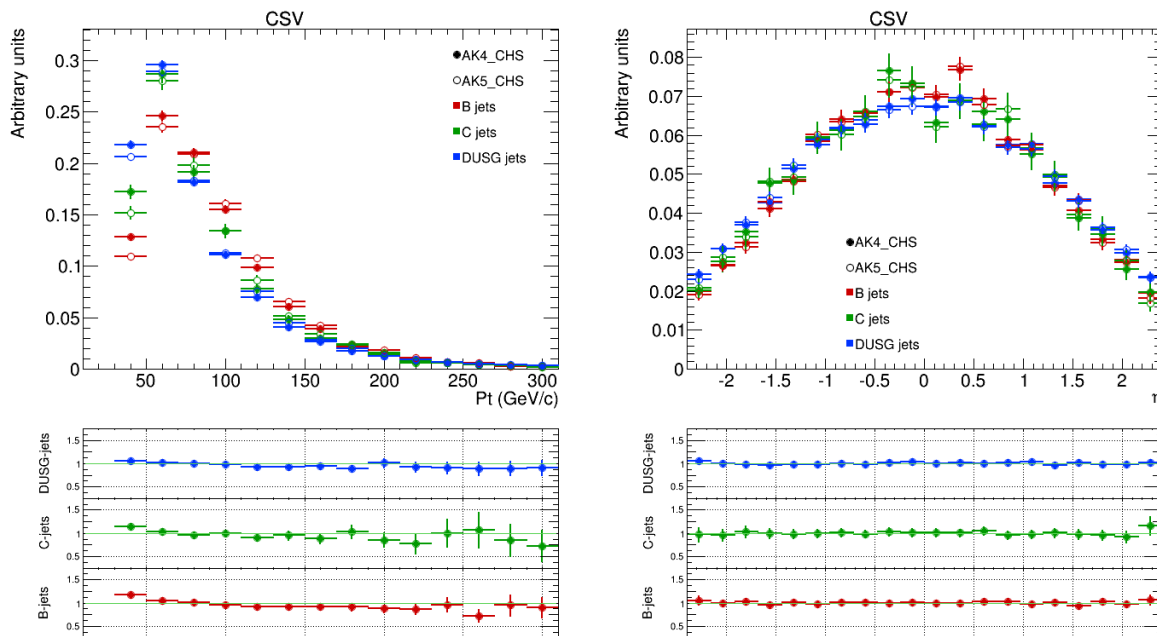


Figure 3.12: Comparison of the p_T (left) and η (right) spectrum of the selected jets in the context of the validation of the new jet size parameter for the Run II.

Figure 3.13 on the top left presents the distribution of the ΔR between the tracks in the jet and the jet axis. Small differences are observed at low $\Delta R(\text{track, jet axis})$, pointing

towards tracks being slightly closer to jet axis in $R = 0.4$ compared to $R = 0.5$. This is interpreted as coming from the fact that the jet axis is more likely to be disrupted by particles near the edge of the cone with $R = 0.5$ compared to 0.4. On the top right, the comparison is done for the ratio of the energy of the track sum and the jet energy. This distribution exhibits a clear shift towards 1 for $R = 0.4$ compared to 0.5. This is because the selected tracks (i.e. in $R < 0.3$) represents a more significant fraction of the total jet energy in $R = 0.4$ compared to 0.5.

Two other *b*-tagging variables are presented on the bottom of [Figure 3.13](#), namely the impact parameter significance and the flight distance significance of secondary vertices. Overall, a little improvement is observed for $R = 0.4$ in the distribution of the impact parameter significance for *b* jets as a lower fraction of the tracks ends up with negative values. The flight distance significance of secondary vertices is stable.

The impact on the performances is presented in [Figure 3.14](#) for four algorithms, TCHE, JP, SSVHE and CSV. The performances for TCHE and SSVHE are relatively stable while JP, dependent on the exact shape of the impact parameter significance for all tracks, has a *b* jet efficiency improved by a few percents attributed to the observed small change in the impact parameter significance distribution. This also propagates to the performance of CSV where, at constant *b* jet efficiency, the fake rate is lowered by about 20%.

To conclude, as the observations in this validation are well understood from a physics point of view, the change of jet size parameter has been validated for the *b*-tagging aspects.

3.2.4 Validation of new default pile-up rate for validation samples

In this validation of the CMS software, the default pile-up rate for the validation samples was changed from 10 to 35. This should be differentiated from the pile-up rate used for analysis samples which follows a particular pile-up distribution. As tracking and *b*-tagging variables strongly depend on pile-up effects, this new condition is expected to impact significantly the performances.

In this document, we investigate this change using a $t\bar{t}$ sample at $\sqrt{s} = 13$ TeV with pile-up. Because of the change in pile-up, the simulation step had to be performed separately for the two samples to be compared.

[Figure 3.15](#) compares the efficiency and fake rate of track reconstruction, as function of η , for a pile-up rate of 10 (*old*) and 35 (*new*) [86]. The new pile-up condition decreases the track reconstruction efficiency by about 2% in the central region, and increases the

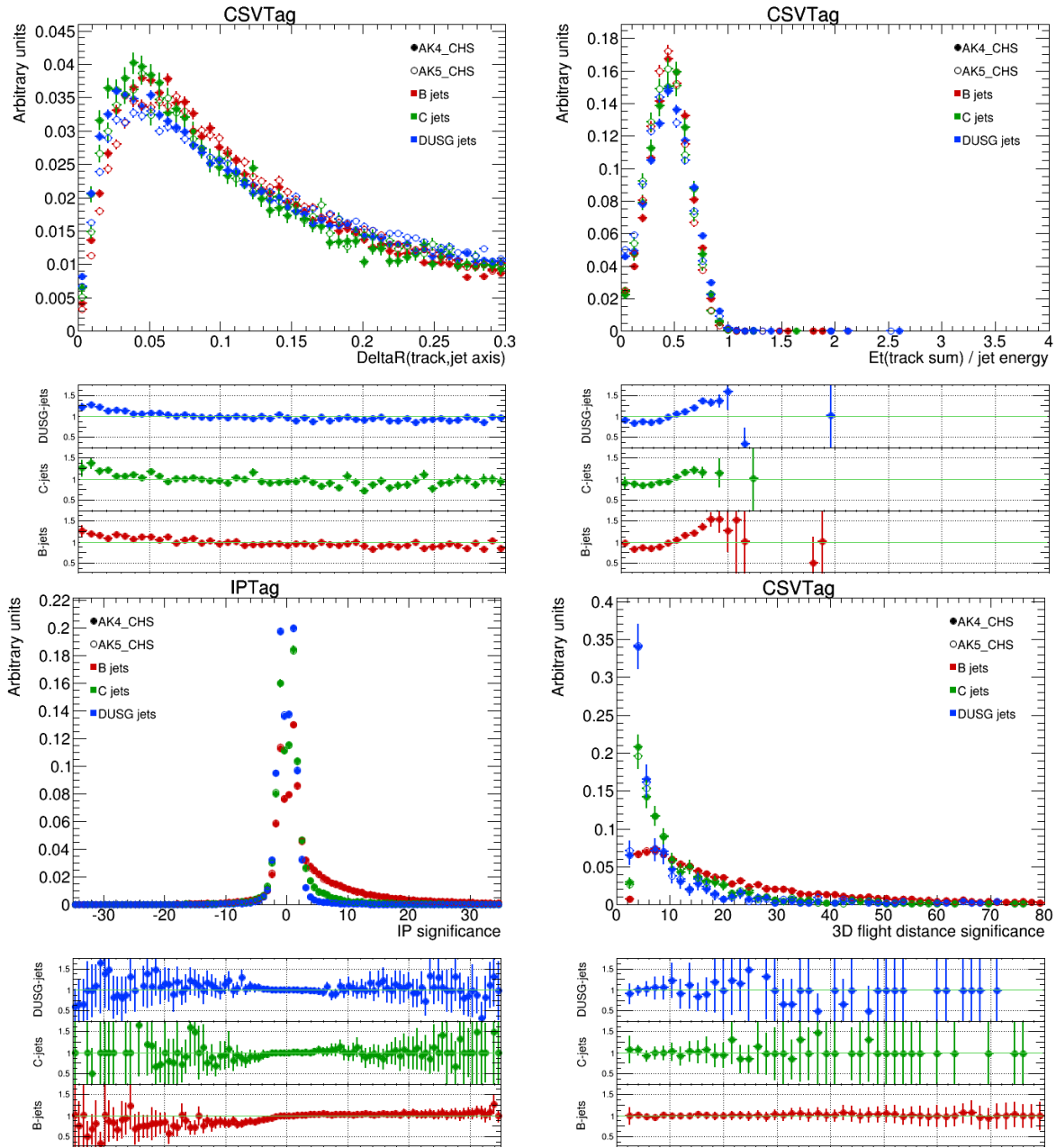


Figure 3.13: Comparison of the $\Delta R(\text{track, jet axis})$ (top left), the ratio of track sum energy to jet energy (top right), the impact parameter significance (bottom left) and the flight distance significance of the secondary vertex (bottom right) in the context of the validation of the new jet size parameter for the Run II. On the bottom of the plots, the histogram corresponds to the ratio of the distribution between $R = 0.4$ and $R = 0.5$.

fake rate from 3% to 8%.

On the *b*-tagging side, this translates to more contamination from pile-up and fakes, likely to have large impact parameters or to create fake secondary vertices. Figure 3.16 shows the comparison of the impact parameter significance and secondary vertex category between the two pile-up conditions. The impact parameter distribution for tracks in light

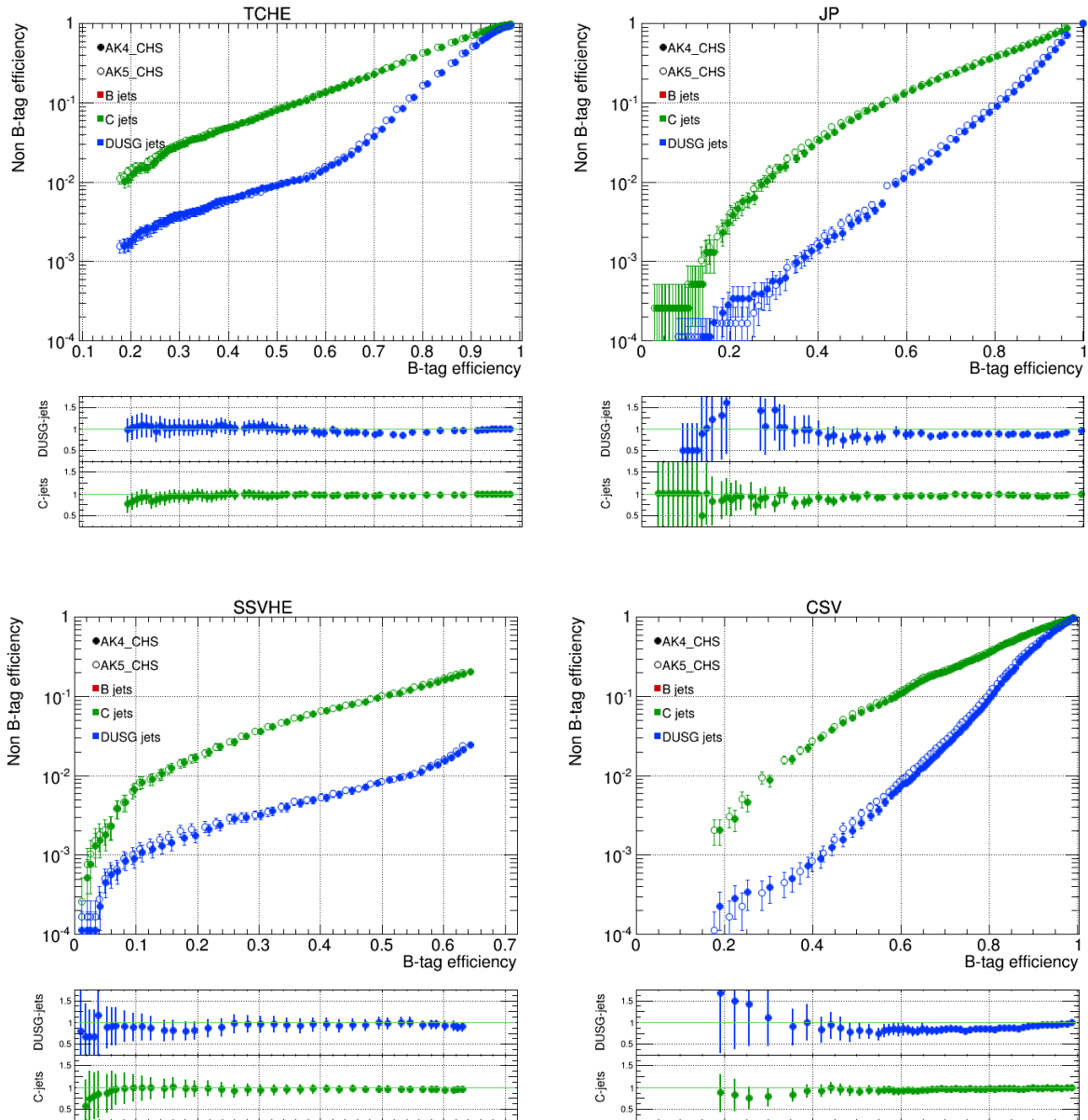


Figure 3.14: Comparison of the algorithm performances for the track counting high efficiency (top left), jet probability (top right), simple secondary vertex (bottom left) and combined secondary vertex (bottom right) in the context of the validation of the new jet size parameter for the Run II. On the bottom of the plots, the histogram corresponds to the ratio of the distribution between $R = 0.4$ and $R = 0.5$.

jets gets a wider peak around 0, from which we can expect an increase in fake rate for all algorithm based on this variable. The secondary vertex categorization shows also a 5% absolute loss in vertexing efficiency for b jets, and a relative increase of around 35% for light jets containing a secondary vertex. From this, we can expect that algorithms based on secondary vertex reconstruction will not only suffer from a higher fake rate from light jets, but also a lower maximum efficiency for b jets.

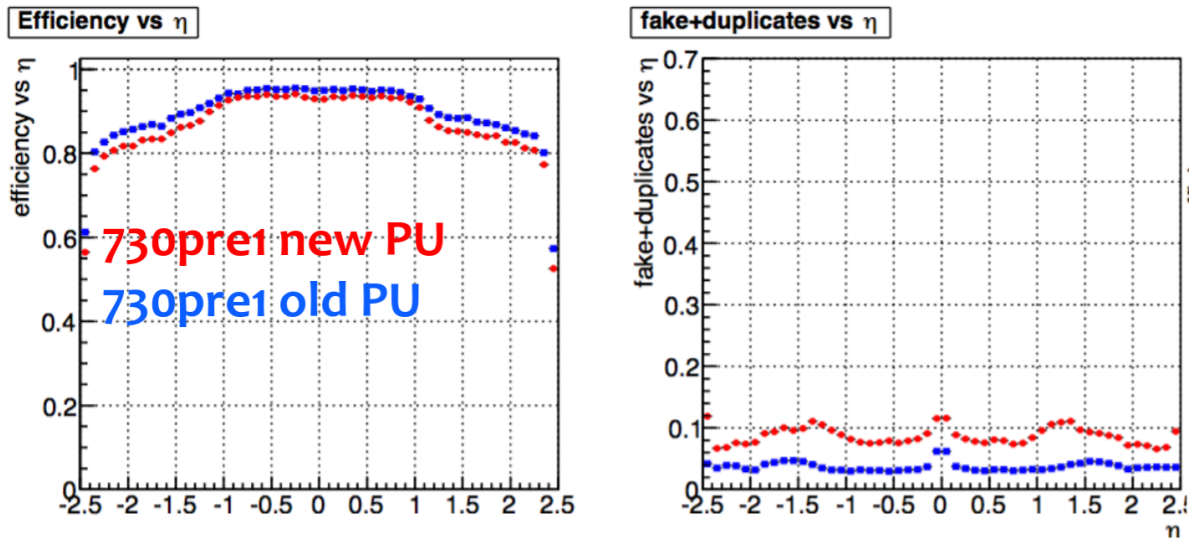


Figure 3.15: Comparison of the tracking performances as function of η between the pile-up level of 10 (old) and 35 (new). The left plot shows the efficiency for real tracks while the right plot shows the fake and duplicate rate [86].

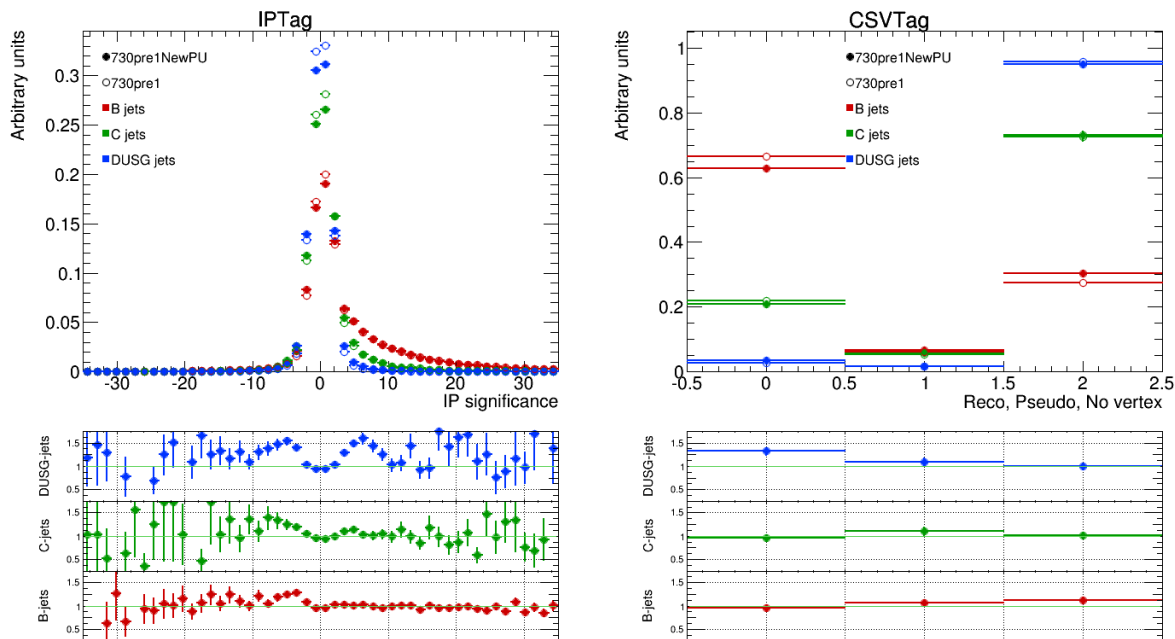


Figure 3.16: Comparison of the impact parameter significance (on the left) and vertex category for the CSV algorithm (on the right) in the context of the validation of the new default pile-up rate.

Figure 3.17 presents the impact on the performances for the four main algorithms TCHE, JP, SSVHE and CSV. The overall impact is a higher fake rate from light jets by about 50% and from *c* jets by about 5-10%. The maximum efficiency for *b* jets for SSVHE is decreased by about 5%, directly related to what is observed on the vertex category in Figure 3.16.

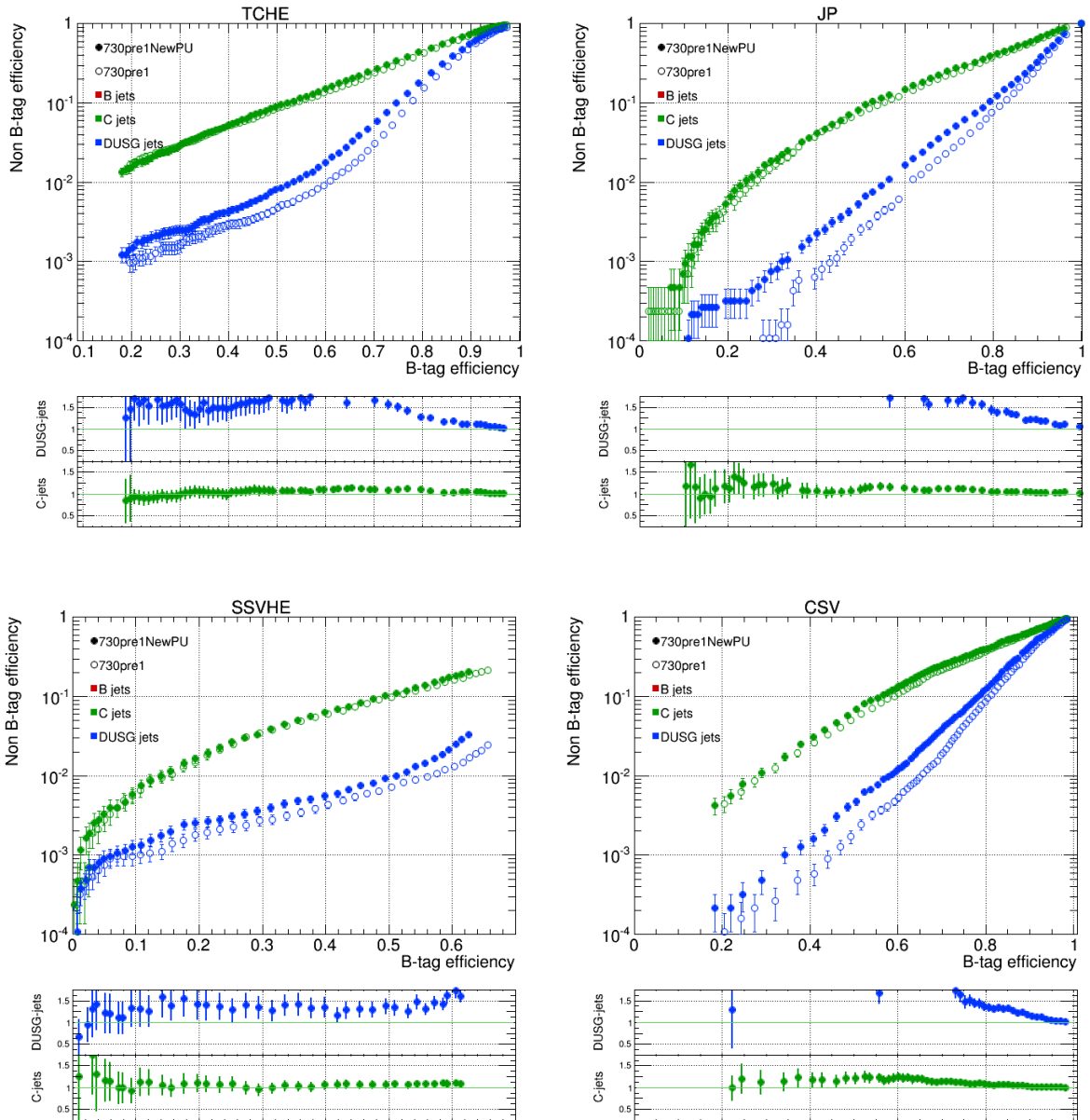


Figure 3.17: Comparison of the algorithm performances for the track counting high efficiency (top left), jet probability (top right), simple secondary vertex (bottom left) and combined secondary vertex (bottom right) in the context of the validation of the new pile-up rate. On the bottom of the plots, the histogram corresponds to the ratio of the distribution between $PU = 10$ and $PU = 35$.

3.2.5 Validation of the premixing technique for pile-up simulation

In this validation, a new technique, called premixing, started being developed. The motivation for this technique starts from the observation that, when generating and simulating events, the simulation of the detector response to the pile-up represents a large fraction

of the CPU time, compared to one single hard-scattering.

In order to reduce the CPU cost of simulation, strategies can be developed. In the case of premixing, the idea is to factorize the simulation of the interaction of the particles with the detector, coming from on one hand, the pile-up, and on the other hand, the hard-scattering of interest. By doing so, the interaction of the pile-up particles can be computed once for all, and their contribution to the signal in the sensors can be overlaid to any hard-scattering event, drastically reducing the simulation time per event [87].

In order for this to work, one must however be careful regarding the way that the pile-up and hard-scattering are digitized and combined together. For instance, thresholds in the subdetectors (e.g. a given calorimetric tower), may impact the digitization such that the hard-scattering alone, or the pile-up alone, may not produce a significant signal, but the combination of the two may. To work around this problem, thresholds are initially set to zero when the digitization is done, and applied only after mixing of the pile-up with the hard-scattering.

Overall, one wants the premixing technique to not impact the physics at the reconstruction level. *b*-tagging, as a high-level technique, is highly sensitive to the description of tracks, pile-up, and to a lesser extent calorimeter deposits and therefore allows an overall check that premixing does not introduce any unphysical behavior. While there were several validations related to this work, this document focuses on a pathological validation done in version 7.4.0 of the CMS software.

Validation results are shown on [Figure 3.18](#) from a $t\bar{t}$ sample with pile-up included and full simulation. The version of the premixing used led to tracks having an artificially higher number of hits in the pixels on average, and therefore a better track quality, which manifests as a lower tail for the normalized χ^2 distribution, and overall a better resolution. This in turn impacts the number of tracks at the secondary vertex for light jets, and the impact parameter significance.

For this validation, the use of premixing therefore impacts the performances of both impact parameter-based algorithms and secondary vertex-based algorithms significantly, as shown on [Figure 3.19](#): for TCHE, the fake rate from light jets decreases by about 35% for a constant *b* jet efficiency of 65%, while SSVHE gets about 20% lower fake rate from *c* jets.

This validation has therefore contributed to the identification of the problems with this version of the premixing. Since then, premixing has been developed further and proved to be in agreement with the regular mixing. It has been estimated to speed up the simulation by a factor 3 [87] and became part of the CMS workflow.

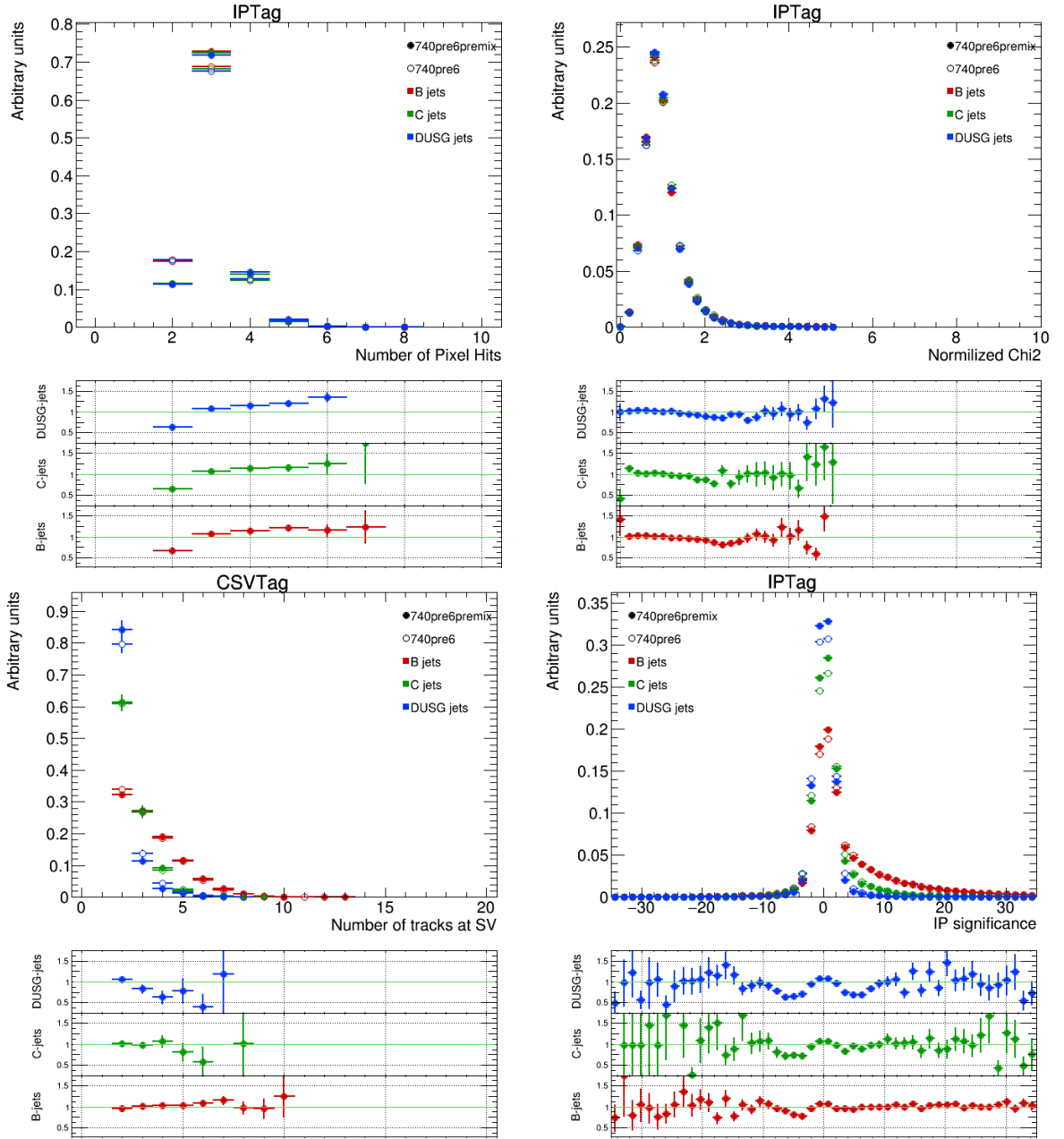


Figure 3.18: Comparison of the number of pixel hits (top left), track χ^2 (top right), number of tracks at the secondary vertex (bottom left) and impact parameter significance (bottom right) in the context of the premixing validation. On the bottom of the plots, the histogram corresponds to the ratio of the distribution between premixing and standard mixing.

3.2.6 Studies of high pile-up scenario for Phase 2

This validation study relates to one of the early investigations of *b*-tagging at high pile-up rate ($\mathcal{O}(150)$). Such conditions are foreseen for the high-luminosity LHC (HL-LHC) program, also called Phase 2, which should start around 2027. Such prospective work is therefore crucial to obtain a first idea of the performances of the detector in these

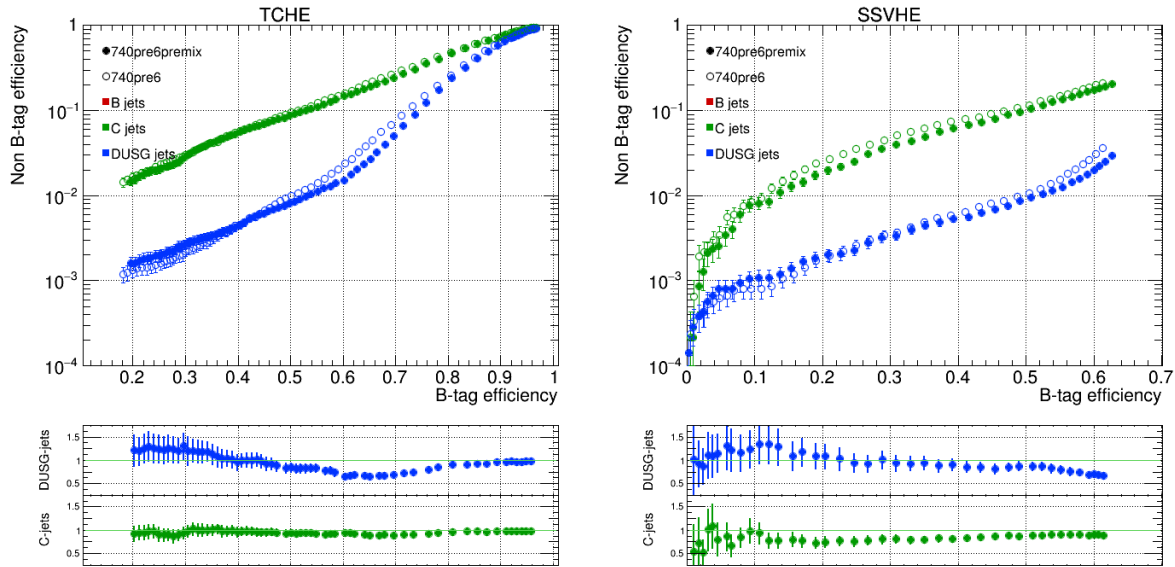


Figure 3.19: Comparison of the algorithm performances of track counting high efficiency (left) and simple secondary vertex high efficiency (right). On the bottom of the plots, the histogram corresponds to the ratio of the distribution between pre-mixing and standard mixing.

conditions, anticipate possible problems and guide the orientation of the development for object reconstruction.

The reference used for this validation is a $t\bar{t}$ sample generated with $\sqrt{s} = 14$ TeV. The detector is simulated with the Phase 1 geometry with a pile-up of 50, in the conditions of the technical design report (TDR) [88]. The comparison is made with a $t\bar{t}$ sample with a Phase 1 aged geometry and a pile-up of 140.

Figure 3.20 presents the comparison of the kinematic distributions of the jets between the two samples. The first observation is that the increase of pile-up significantly bias the p_T spectrum of the jets towards higher values, while the generated energy of the underlying partons are expected to have the same spectrum between the two releases. This is interpreted as coming from the jet energy corrections which are not yet adapted for the pile-up conditions of Phase 2, and points to a necessity of improving the mitigation of pile-up in jet reconstruction in general. The higher pile-up rate also creates a significantly higher number of jets in the central region ($|\eta| < 0.7$), contributing to the gluon jet category.

Figure 3.21 shows track level information, namely the distribution of the number of selected tracks per jet, and the distribution of the impact parameter significance for these tracks. In the high pile-up scenario, the number of selected tracks is significantly lower

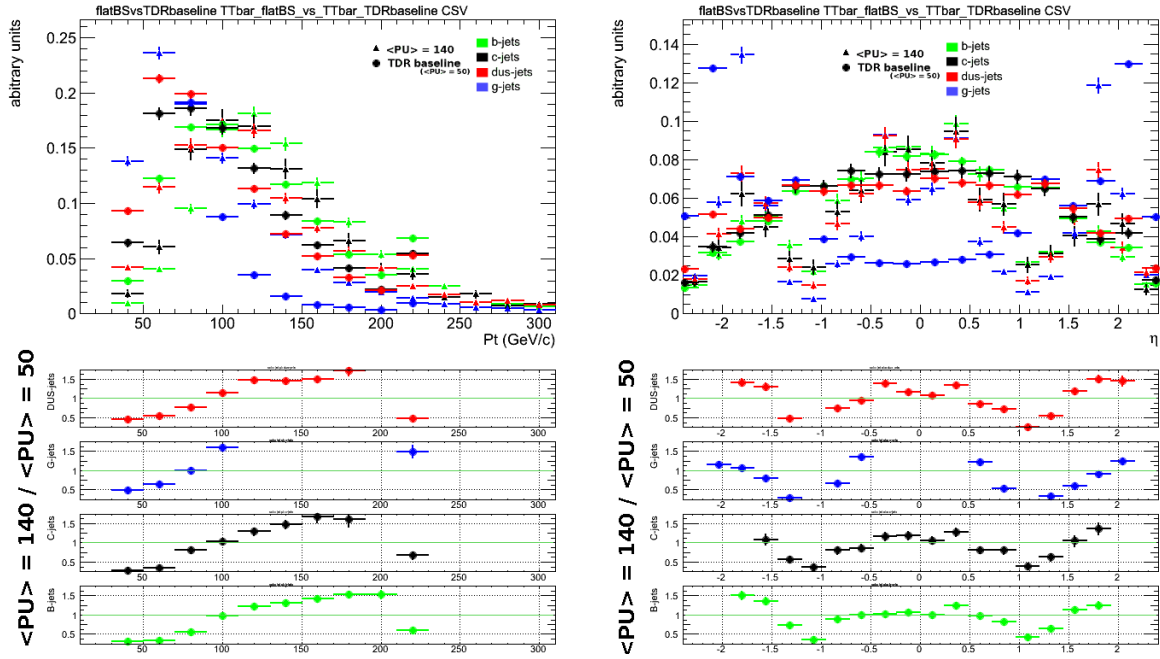


Figure 3.20: Comparison of the p_T and η spectra of the selected jets in the context of the studies of a high pile-up scenario for Phase 2. On the bottom of the plots, the histogram corresponds to the ratio of the distribution between the PU = 140 and PU = 50 scenario. (Note that the color code is different from the previous plots.)

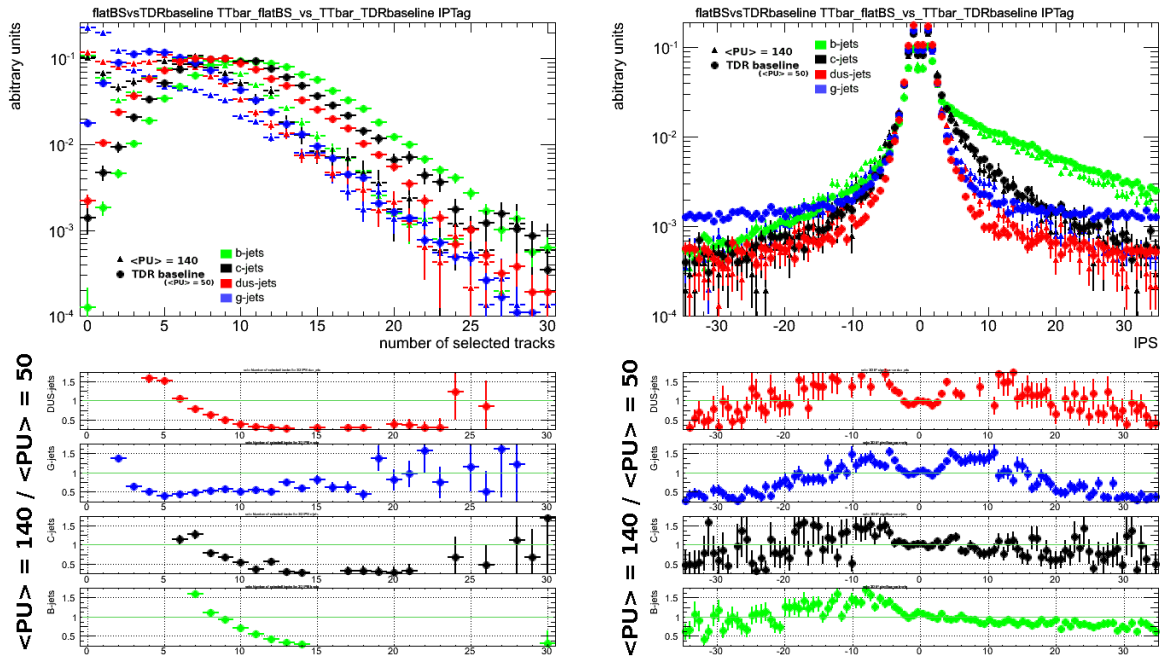


Figure 3.21: Comparison of the number of selected tracks per jet (left) and impact parameter significance (right) in the context of the studies of a high pile-up scenario for Phase 2. On the bottom of the plots, the histogram corresponds to the ratio of the distribution between the PU = 140 and PU = 50 scenario. (Note that the color code is different from the previous plots.)

for all jets categories, interpreted as coming from the aging of the pixel detector. In particular for the b jet category, the distribution peaks around 7 or 8 selected tracks per jet in the Phase 2 scenario, compared to around 10 in the Phase 1. From this observation, one can expect a significant decrease in the b jet efficiency. The distribution of the impact parameter significance also exhibits a worsening of the discriminating power. First, the distribution for light jets exhibits a much wider peak and increase of the fraction with large positive values. Secondly, the ratio of the distribution for the b jets shows a trend in the positive-tail such that the distribution in high pile-up conditions is less in favor of b jets discrimination.

Figure 3.22 shows the comparison of the performance curves obtained for the two scenarios for the four main algorithms: track counting high efficiency, simple secondary vertex high efficiency, jet probability and combined secondary vertex. Track counting and jet probability, both relying essentially on the impact parameter significance distribution, show a dramatic increase of the fake rate by a factor 5 to 10 in the high PU scenario. The maximum b jet efficiency for simple secondary vertex is also significantly affected and gets down to about 55%, while the fake rate for is only increased by a factor between 2 and 5. The combined secondary vertex performances finally give information to what can be expected from combining the techniques together. The fake rate for light jets is overall increased by a factor 5 to 10 while it is increased by a factor 1.5-2 for c jets. The b jets efficiency in the high pile-up scenario becomes 65%, 42% and about 20% for the loose, medium and tight working points respectively.

Moreover, all these algorithms (with a particular case for simple secondary vertex) shows a maximum b -tagging efficiency around 80-85% which is much unexpected. This was later [89] tracked down as coming from the misidentification of the right primary vertex in the event due to the high level of pile-up. We recall that the primary vertex is typically chosen as the vertex with higher $\sum_{\text{tracks}} p_T^2$. However, as shown on Figure 3.23 on the left in open green triangles, this technique becomes quite less efficient at high pile-up, with an efficiency between 80 and 90% for events with a leading jet with $100 < p_T < 200$ GeV. To solve this issue, a new technique has been developed. This technique starts by clustering tracks to create jets, and the choice of the primary vertex is based on $\sum_{\text{jets}} p_T^2$ (though also including unclustered tracks to the sum). This new technique allows to significantly recover the vertex choice efficiency as shown with filled green triangles.

Furthermore, an investigation of the performances using this time the foreseen Phase 2 geometry has been pursued. On Figure 3.23 on the right, the performances are compared for three scenarios, namely Phase 1 geometry with a pile-up rate of 50, aged Phase 1 geometry with a pile-up of 140, and Phase 2 geometry with a pile-up of 140. The Phase 2 geometry has been demonstrated to significantly reduce the fake rate from light jets to

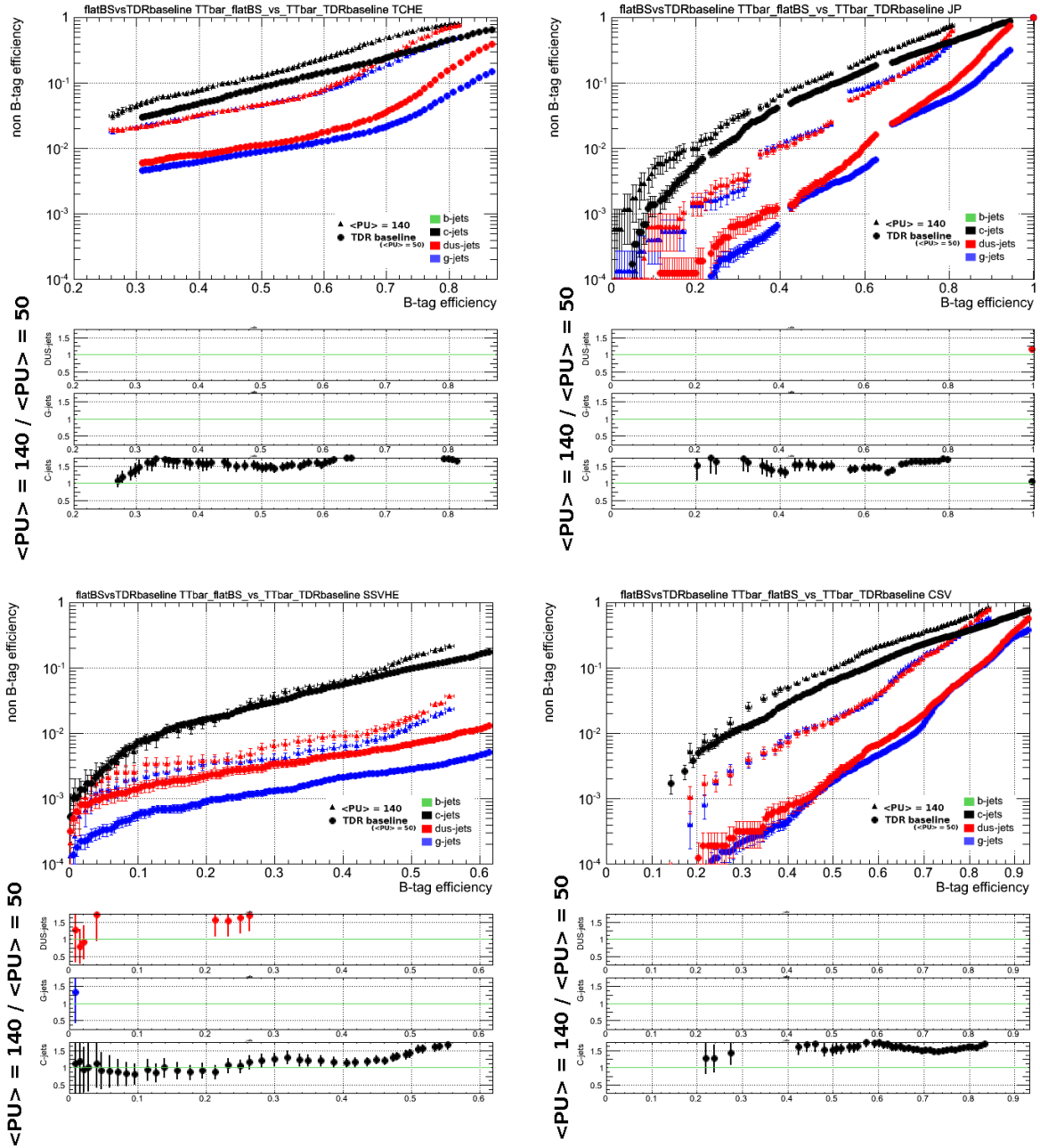


Figure 3.22: Comparison of the performances for track counting high efficiency (top left), jet probability (top right), simple secondary vertex (bottom left) and combined secondary vertex (bottom right) in the context of the studies of a high-pile-up scenario for Phase 2. On the bottom of the plots, the histogram corresponds to the ratio of the distribution between the $\text{PU} = 140$ and $\text{PU} = 50$ scenario. (Note that the color code is different from the previous plots.)

obtain performances comparable to Phase 1 with a pile-up rate of 50.

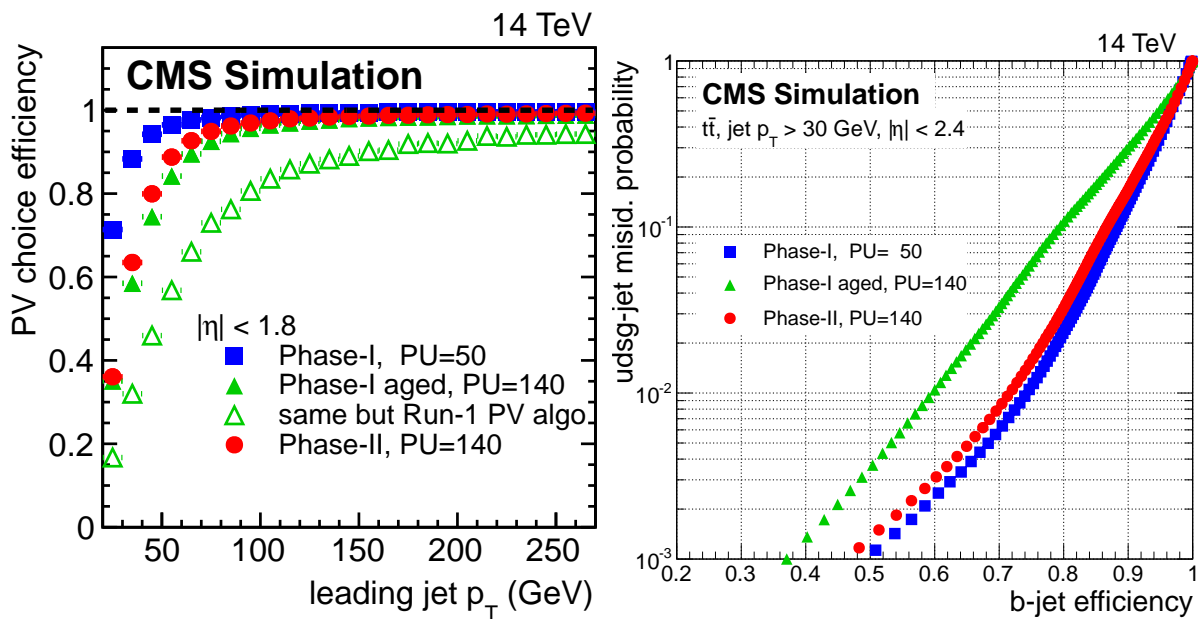


Figure 3.23: On the left: comparison of the primary vertex choice efficiency as function of the leading jet p_T , for different scenario corresponding to Phase 1 with a pile-up rate of 50 (blue squares), Phase 1 aged detector with pile-up rate of 140 using the old (open green triangles) or new (filled green triangles) vertex choice technique, and Phase 2 detector with a pile-up rate of 140 (red dots). On the right: comparison of the b -tagging performances for the same scenarios, showing how the Phase 2 detector is able to recover performances comparable to Phase 1 [89].

Chapter 4

Search for stop pair production at $\sqrt{s} = 8 \text{ TeV}$

« There are worlds out there where the sky is burning, and the sea's asleep, and the rivers dream; people made of smoke and cities made of song. Somewhere there's danger, somewhere there's injustice, and somewhere else the tea's getting cold. Come on, Ace. We've got work to do. »

The Seventh Doctor

Contents

4.1	Context and phenomenology	97
4.1.1	Theoretical context and constraints	97
4.1.2	Phenomenology and signature	100
4.2	Analysis strategy and overview	106
4.3	Monte-Carlo generation and datasets	107
4.4	Objects and events selection	108
4.4.1	Trigger	108
4.4.2	Leptons	108
4.4.3	Jets and missing transverse energy	112
4.4.4	Events preselection	113
4.5	Signal region design and optimisation	114
4.5.1	Discriminating variables	117
4.5.2	Figure of merit and sensitivity estimation	125
4.5.3	Cut-based signal regions	128
4.5.4	BDT-based signal regions	130
4.6	Background estimation	132

4.6.1	Overview	132
4.6.2	Background normalization in the M_T -peak region	134
4.6.3	M_T -tail correction in the 0 b -tag region	135
4.6.4	Control of the $t\bar{t} \rightarrow \ell\ell$ component and second lepton veto	139
4.6.5	Control of variables at preselection level	141
4.6.6	Background prediction in the signal regions	143
4.7	Systematic uncertainties	144
4.7.1	Systematic uncertainties on the background	144
4.7.2	Systematic uncertainties on the signal	146
4.8	Signal contamination handling	147
4.9	Results and interpretation	149
4.9.1	Results and limits for the cut-based and BDT approaches	149
4.9.2	Combination with the search in two lepton channel	153
4.9.3	Comparison of polarization scenarios	153
4.9.4	Examination of an individual event and discussion	154
4.9.5	Comparison with other direct stop pair production searches	156
4.10	Perspectives	159
4.10.1	W -tagging in the high Δm regime	159
4.10.2	Sensitivity estimation for the Run II	166

This chapter focuses on an analysis performed within the CMS collaboration and searching for the production of stop pair using the data recorded during the Run I of the LHC at $\sqrt{s} = 8$ TeV. In [Section 4.1](#), we concentrate on the context and phenomenology of the signature while [Section 4.2](#) to [Section 4.9](#) discuss the different aspects of the analysis itself, namely the object and event selection, the signal region design, the background estimation, the systematics uncertainties, and finally the results and their interpretation. In the last [Section 4.10](#), some of the perspectives for this analysis are investigated, in particular regarding the use of W -tagging, followed by a sensitivity estimation for the Run II.

4.1 Context and phenomenology

4.1.1 Theoretical context and constraints

Motivation and constraints on the stop sector from the Higgs sector

As introduced in [Section 1.4.2](#), one of the best assets of supersymmetry is its ability to explain why the Higgs boson can be light, via the boson-fermion symmetry which protects the mass of the Higgs from diverging because of quantum corrections. This is illustrated in [Figure 4.1](#), showing the one-loop corrections to m_h^2 from a fermionic field f and a bosonic field b coupled to the Higgs via the Lagrangian terms $-\lambda_f h \bar{f} f$ and $\lambda_b |h|^2 |b|^2$.

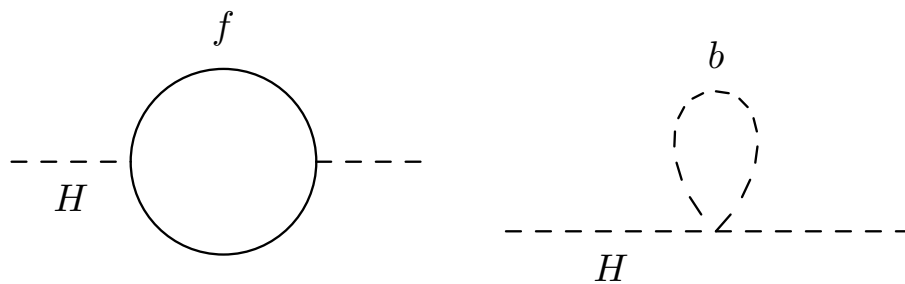


Figure 4.1: One-loop correction to the Higgs for a fermionic field f (left) and a bosonic field b (right).

The leading order corrections associated to these diagrams are:

$$\Delta m_h^2 = -\frac{|\lambda_f|^2}{8\pi^2} \Lambda_{\text{UV}}^2 \quad \text{and} \quad \Delta m_h^2 = \frac{\lambda_b}{16\pi^2} \Lambda_{\text{UV}}^2 \quad (4.1)$$

where Λ_{UV}^2 is the ultraviolet momentum cutoff which regulates the loop integral. In the

most ideal case, one can have $|\lambda_f|^2 = \lambda_b$, which corresponds to $m_f = m_b$, and associate two scalars to each fermion (one for each chirality) so that the corrections cancel each others. If the masses of f and b are not the same, however, the corrections do not perfectly cancel each other and tuning has to be reintroduced to keep the corrections to the Higgs mass low. Since the top quark has the biggest Yukawa coupling λ , a particular attention in supersymmetry goes into the study of its superpartner which is expected to play an important role in stabilizing the mass of the Higgs.

One can study the level of tuning needed as a function of the mass of the superpartner of the top, called the stop, for the theory to keep providing a natural explanation to the hierarchy problem, and use it as a guidance for experimental searches. It is possible to quantify fine-tuning by studying how the quantity of interest, in our case m_h , the Higgs mass, varies as function of p_i , the parameters of the theory:

$$\Delta m_h \equiv \max_i \left| \frac{\partial \ln m_h^2}{\partial \ln p_i} \right| \quad (4.2)$$

Despite the fact that such a study is highly dependent on hypotheses made on the SUSY parameters, it is commonly admitted that stop quarks should have a mass below or around 1 TeV for SUSY to remain natural [90, 91, 92, 50]. This makes the search for stops an important channel to constrain naturalness or possibly discover SUSY at the LHC.

In addition to the argument of naturalness, one may derive constraints on the stop sector directly from the knowledge of the Higgs mass [93]. In the context of supersymmetry, the Higgs mass may indeed be expressed as function of the other parameters of the theory. Assuming that $m_A \gg m_Z$:

$$m_h^2 = m_Z^2 \cos^2 2\beta + \frac{3\lambda_t^2 m_t^2}{4\pi^2} \left[\log \left(\frac{m_S^2}{m_t^2} \right) + X_t^2 \left(1 - \frac{X_t^2}{12} \right) \right] + \dots \quad (4.3)$$

where here, X_t , the stop mixing parameter, is defined as $(A_t + \mu \cot \beta)/m_S$ and $m_S \equiv \sqrt{m_{\tilde{t}_1} m_{\tilde{t}_2}}$ is the average stop mass. From this computation, constraints can be put on the value of m_S as function of X_t , as shown on the left of Figure 4.2 when assuming $\tan \beta = 20$. For $m_h = 125$ GeV, one finds that the minimum value of m_S is around 600 GeV, obtained for the so-called maximal mixing value $X_t = \sqrt{6}$. Interestingly, the observed Higgs mass therefore points to relatively “heavy” stops compared to the naturalness argument favoring light stops.

Moreover, it is remarkable that constraints on the stop sector can also be derived from the loop to the decay $h \rightarrow gg$ and $h \rightarrow \gamma\gamma$ as described in [93]. As the photon is not massive, the decay $h \rightarrow \gamma\gamma$ must involve virtual loops of massive particles, such as the top, but also possibly its superpartner the stop which would then affect the branching

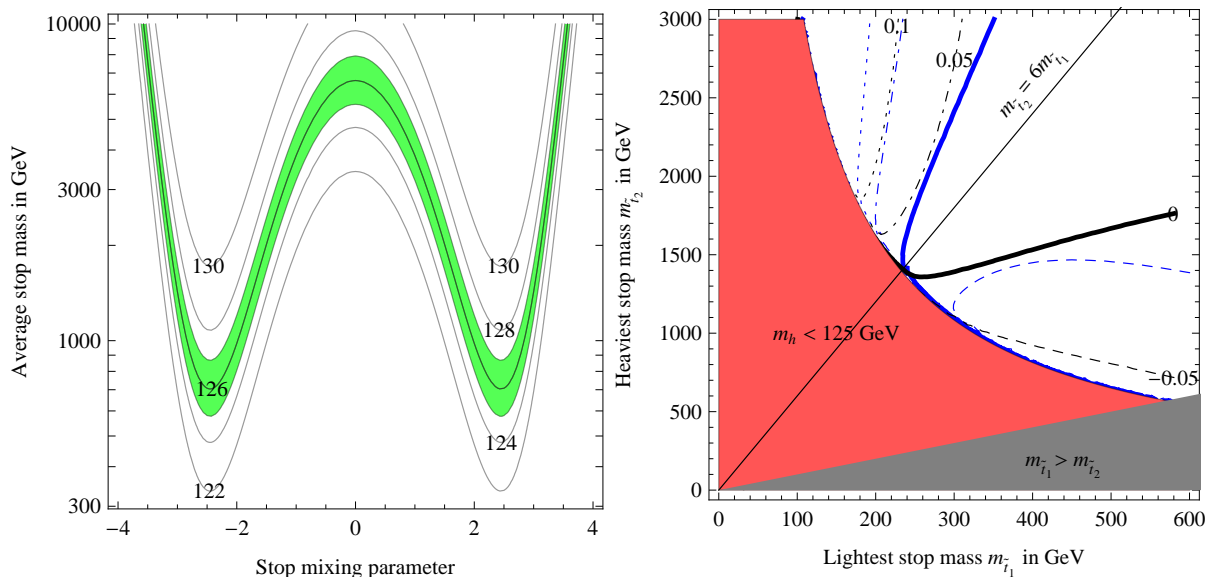


Figure 4.2: Constraints on the stop sector from the Higgs measurement [93]. On the left, constraints on m_S as function of X_t from for different values of the Higgs mass. On the right, constraints in the $(m_{\tilde{t}_1}, m_{\tilde{t}_2})$ space: the red area is forbidden because, as seen on the left plot, m_S should be higher than about 600 GeV for $m_h = 125$ GeV ; the lines corresponds to a few different values of Δ_t , namely -0.05 , 0 , 0.05 and 0.1 , with $X_t^2 > 6$ (in blue) or $X_t^2 < 6$ (in black).

ratio $\text{BR}(h \rightarrow \gamma\gamma)$. The impact can be expressed as function of the stop sector parameters m_S , X_t , $m_{\tilde{t}_1}$ and $m_{\tilde{t}_2}$:

$$\frac{\text{BR}(h \rightarrow \gamma\gamma)}{\text{BR}(h \rightarrow \gamma\gamma)_{\text{SM}}} = (1 - 0.28\Delta_t)^2 \quad \text{with} \quad \Delta_t \approx \frac{m_t^2}{4} \left(\frac{1}{m_{\tilde{t}_1}^2} + \frac{1}{m_{\tilde{t}_2}^2} - \frac{X_t^2}{m_S^2} \right). \quad (4.4)$$

At this point, the experimental measurement of $\text{BR}(h \rightarrow \gamma\gamma)$ does not allow to significantly constrain the value of Δ_t . Nevertheless, the lines in the right plot of Figure 4.2 plot illustrate how given values of Δ_t would in turn constrain the $(m_{\tilde{t}_1}, m_{\tilde{t}_2})$ space.

Motivation from the dark matter evidence

A second appealing feature of supersymmetry is that it provides dark matter candidates. This happens in particular in R-parity conserving models, where the lightest supersymmetric particle (LSP) is a good dark matter candidate if it is not a charged particle. In the context of the MSSM, the lightest neutralino $\tilde{\chi}_1^0$, the gravitino \tilde{G} and the lightest sneutrino $\tilde{\nu}$ can be the LSP. The lightest neutralino is the one that is most often studied as its relation to the electroweak sector makes it a perfect WIMP candidate. An advantage of the WIMP phenomenology is that their relic density can be calculated precisely in the framework of standard cosmology, assuming that they are thermally produced [94].

Moreover, the naturalness argument also motivates the Higgsino mass μ to be around 150 – 200 GeV [50]. Following this, it means that the first neutralinos should be relatively light, and though the exact constraint depend on assumptions on $\tan \beta$, M_1 and M_2 , it is reasonable to consider that the lightest neutralino should be lighter than around 500 GeV. Scenarios with a sneutrino as LSP might be studied as well, in particular in models attempting to explain the mass of the neutrinos, while the gravitino as LSP appears in gauge mediated SUSY breaking models.

Experimental constrains on the stop and neutralino LSP masses prior to the LHC

Before the LHC, searches for supersymmetry have been conducted at the LEP and the Tevatron and were used to put constrains on the masses of supersymmetric particles and in particular the stop and the LSP. First, the LEP experiments were able to derive an absolute lower limit of 43 GeV on the mass of the lightest neutralino if it is the LSP [95]. Additionally, an absolute lower limit of about 100 GeV was derived on the lightest stop [96]. These results were completed by searches at the Tevatron for direct stop pair production, $p\bar{p} \rightarrow \tilde{t}_1\tilde{t}_1^*$. The decay mode considered are similar to those that will be introduced in the next section. In particular, D0 considered the decay mode $\tilde{t}_1 \rightarrow b\tilde{\nu}$ where the sneutrino $\tilde{\nu}$ is assumed to be the LSP. As presented in Figure 4.3 on the left, the corresponding search allowed to exclude stop masses up to 240 GeV and sneutrino masses up to 120 GeV assuming a branching ratio of 100% [97]. Another decay mode, $\tilde{t}_1 \rightarrow b\tilde{\chi}_1^\pm$ with $\tilde{\chi}_1^\pm \rightarrow \ell\nu\tilde{\chi}_1^0$, was investigated by the CDF collaboration. As presented in Figure 4.3 on the right, limits were put on the stop mass up to 195 GeV and neutralino mass up to 90 GeV with the exact values varying as function of the chargino mass and branching ratios considered [98].

4.1.2 Phenomenology and signature

In the context of this document, we focus on a SUSY spectra built from the previous arguments, which motivates a stop \tilde{t}_1 with a mass lower than around 1 TeV and a dark matter candidate, which we take to be the lightest neutralino $\tilde{\chi}_1^0$ assumed to be the LSP. While we could simply concentrate on these two particles, we will also consider cases where the lightest chargino $\tilde{\chi}_1^\pm$ is the NLSP, i.e. has a mass higher than the neutralino $\tilde{\chi}_1^0$ but lower than the stop \tilde{t}_1 . The $\tilde{\chi}_1^\pm$ is indeed expected to have a mass close to the $\tilde{\chi}_1^0$ when the SUSY parameters M_1 and M_2 are large compared to μ . Experimentally, we now want to look for this particle spectrum via a search for a direct pair production of \tilde{t}_1

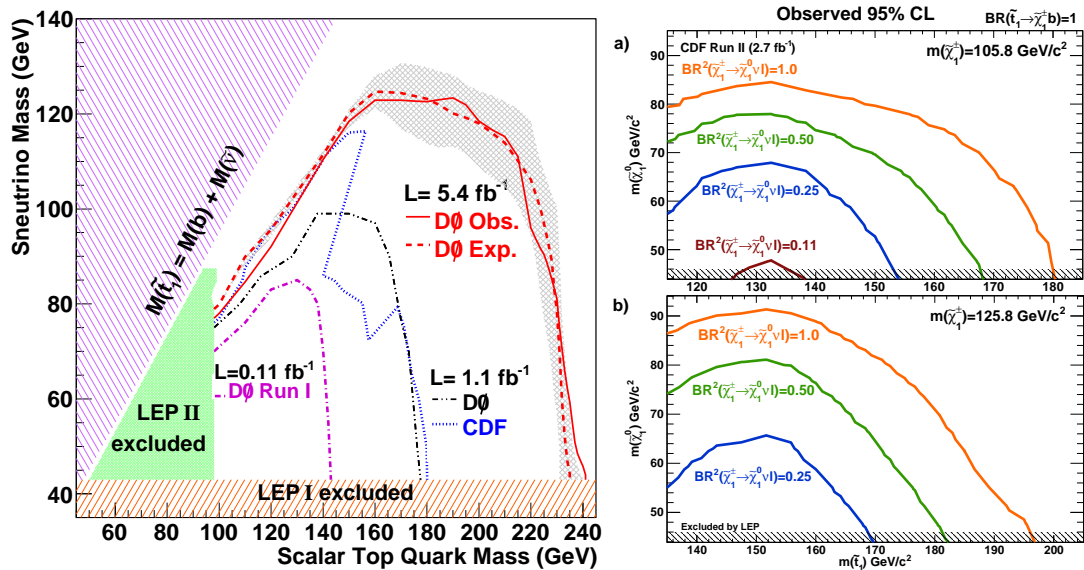


Figure 4.3: On the left, exclusion at 95% confidence level in terms of $(m_{\tilde{t}_1}, m_{\tilde{\nu}})$ obtained from a search [97] for $p\bar{p} \rightarrow \tilde{t}_1\tilde{t}_1^* \rightarrow b\bar{b}\tilde{\nu}\tilde{u}^*$ using 5.4 fb^{-1} recorded by D0 at the Tevatron. On the right, exclusion at 95% confidence level in terms of $(m_{\tilde{t}_1}, m_{\tilde{\chi}_1^0})$ obtained from a search [98] for $p\bar{p} \rightarrow \tilde{t}_1\tilde{t}_1^* \rightarrow b\bar{b}\tilde{\chi}_1^\pm\tilde{\chi}_1^\pm$ with $\tilde{\chi}_1^\pm \rightarrow \tilde{\chi}_1^0\nu\ell$.

in the pp collisions of the LHC.

As it is in practice impossible to perform such a search across the whole phase space of SUSY models, a pragmatic approach often consists in using simplified SUSY models where an effective Lagrangian introduces a limited set of new physics features. In such simplified models, the free parameters are usually taken to be experimentally meaningful quantities, such as the masses of the SUSY particles. This makes it possible for experimental searches to produce generic results that can later be reinterpreted in specific realizations of SUSY [99, 100] or other BSM theories. In our case, let's consider the existence of only three new particles¹: the lightest stop quark \tilde{t}_1 , the lightest neutralino $\tilde{\chi}_1^0$ and the lightest chargino $\tilde{\chi}_1^\pm$.

First, let's assume that $m_{\tilde{\chi}_1^\pm} \gg m_{\tilde{t}_1}$ and therefore the stop decays through $\tilde{t}_1 \rightarrow t\tilde{\chi}_1^0$, as represented on Figure 4.4 on the left. This signal is referred to as T2TT in the simplified model nomenclature and depends on two free parameters $m_{\tilde{t}_1}$ and $m_{\tilde{\chi}_1^0}$.

A second case is considered with $m_{\tilde{\chi}_1^\pm} \in [m_{\tilde{\chi}_1^0}, m_{\tilde{t}_1}]$ and the stop decays through $\tilde{t}_1 \rightarrow b\tilde{\chi}_1^\pm \rightarrow bW^\pm\tilde{\chi}_1^0$. This signal is referred to as T2BW in the simplified model nomenclature. In addition to the free parameters $m_{\tilde{t}_1}$ and $m_{\tilde{\chi}_1^0}$, $m_{\tilde{\chi}_1^\pm}$ is set through a third parameter x defined such that $m_{\tilde{\chi}_1^\pm} = x \cdot m_{\tilde{t}_1} + (1-x) \cdot m_{\tilde{\chi}_1^0}$. We study three cases $x = 0.75, 0.50$ and 0.25 , as represented on Figure 4.4 on the right.

¹The remaining SUSY particles can be assumed to be too heavy to have any significant impact on what is discussed here.

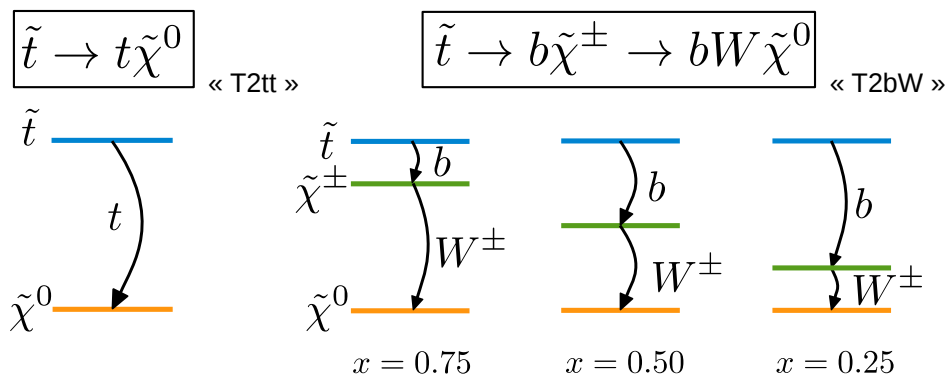


Figure 4.4: Representation of the mass hierarchy in the $\tilde{t}_1 \rightarrow t \tilde{\chi}_1^0$ decay mode (left) and $\tilde{t}_1 \rightarrow b \tilde{\chi}_1^\pm \rightarrow b W^\pm \tilde{\chi}_1^0$ decay mode (right). For the later, the chargino mass $m_{\tilde{\chi}_1^\pm}$ is parametrized using $m_{\tilde{\chi}_1^\pm} = x \cdot m_{\tilde{t}_1} + (1-x) \cdot m_{\tilde{\chi}_1^0}$ and three different values of x are studied, $x = 0.75$, 0.50 and 0.25 .

All of these four decay hypotheses are studied independently of each other² and with a branching ratio equal to 1. It should also be noted that the polarization of the top quarks in the $\tilde{t}_1 \rightarrow t \tilde{\chi}_1^0$ mode, and $\tilde{\chi}_1^\pm$ and W bosons in the $\tilde{t}_1 \rightarrow b \tilde{\chi}_1^\pm \rightarrow b W^\pm \tilde{\chi}_1^0$ mode, are dependent on the mixing matrices of the \tilde{t}_1 , $\tilde{\chi}_1^\pm$ and $\tilde{\chi}_1^0$. This can later significantly affect the distributions of variables and the acceptance of the signal. We first assume that the top is unpolarized and will discuss alternative hypothesis during the interpretation of the results in Section 4.9.

Figure 4.5 shows the two Feynman diagrams that are considered. It is relevant to target both those signals with the same analysis considering that, in T2TT, the top quark almost exclusively decays through $t \rightarrow b W^+$ and therefore lead to the same intermediate state $b\bar{b}W^+W^- + \tilde{\chi}_1^0 \tilde{\chi}_1^0$ as in T2BW. Because the $\tilde{\chi}_1^0$ are assumed to be dark matter candidates and do not interact with the detector, the signature left by this new physics process is a final state much like Standard Model $t\bar{t}$ production but with extra missing transverse energy (E_T^{miss}) coming from the two $\tilde{\chi}_1^0$.

The cross-section of direct \tilde{t}_1 pair production, which depends only on $m_{\tilde{t}_1}$, is presented on Figure 4.6 for 8 TeV and 13 TeV pp collisions as computed at next-to-leading-order by the software PROSPINO [51, 52]. At 8 TeV, the cross-section ranges from $\mathcal{O}(100 \text{ pb})$ at $m_{\tilde{t}_1} = 150 \text{ GeV}$ to $\mathcal{O}(1 \text{ fb})$ at $m_{\tilde{t}_1} = 900 \text{ GeV}$.

The search is performed across the $(m_{\tilde{t}_1}, m_{\tilde{\chi}_1^0})$ plane represented on Figure 4.7. Depending on the value of $\Delta m \equiv m_{\tilde{t}_1} - m_{\tilde{\chi}_1^0}$, different phenomenologies appear as discussed hereafter.

²We do not consider mixed decays where one stop of the pair decays through $\tilde{t}_1 \rightarrow t \tilde{\chi}_1^0$ and the other decays through $\tilde{t}_1 \rightarrow b \tilde{\chi}_1^\pm \rightarrow b W^\pm \tilde{\chi}_1^0$.

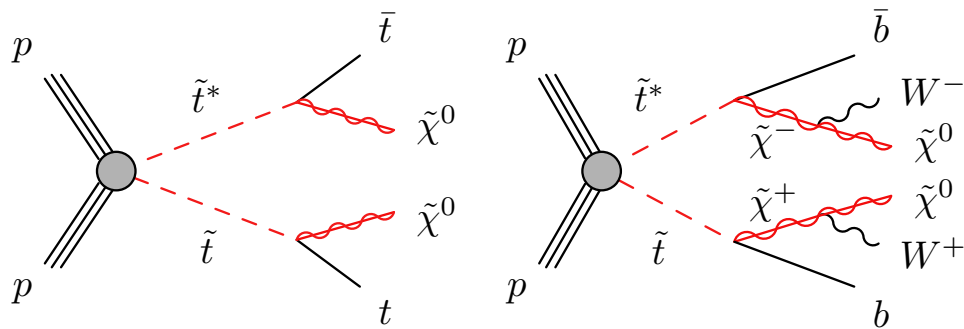


Figure 4.5: Feynman diagrams of stop pair production in pp collisions for the $\tilde{t}_1 \rightarrow t\tilde{\chi}_1^0$ decay mode (on the left) and $\tilde{t}_1 \rightarrow b\tilde{\chi}_1^\pm \rightarrow bW^\pm\tilde{\chi}_1^0$ decay mode (on the right). The lines of the supersymmetric particles are drawn in red.

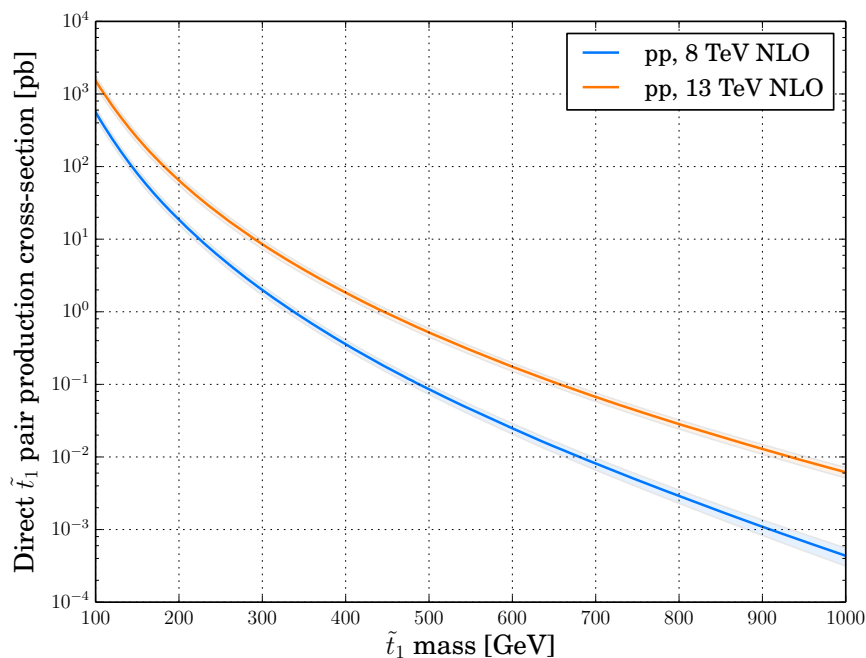


Figure 4.6: Direct \tilde{t}_1 pair production cross-section as function of $m_{\tilde{t}_1}$, computed at next-to-leading-order for 8 TeV (in blue) and 13 TeV (in orange) proton-proton collisions. The bands represent uncertainty from PDF.

The $\tilde{t}_1 \rightarrow t\tilde{\chi}_1^0$ decay mode is allowed starting from $\Delta m > m_W + m_b$. In the region where $m_W + m_b < \Delta m < m_t$, the available energy in the center of mass is however not sufficient to have an on-shell top, and the top is therefore off-shell. This type of kinematic is also called a three-body decay of the stop. Around the $\Delta m \sim m_t$ limit, the kinematic is quite challenging as the signal looks almost identical to the Standard Model $t\bar{t}$ production. Because of this, this region is called stealthy as such a signal is difficult to bring out. In the part of the phase space corresponding to $\Delta m > m_t$, the top is on-shell. The E_T^{miss} from $\tilde{\chi}_1^0$, as well as the p_T of the visible decay products, are expected to grow as function

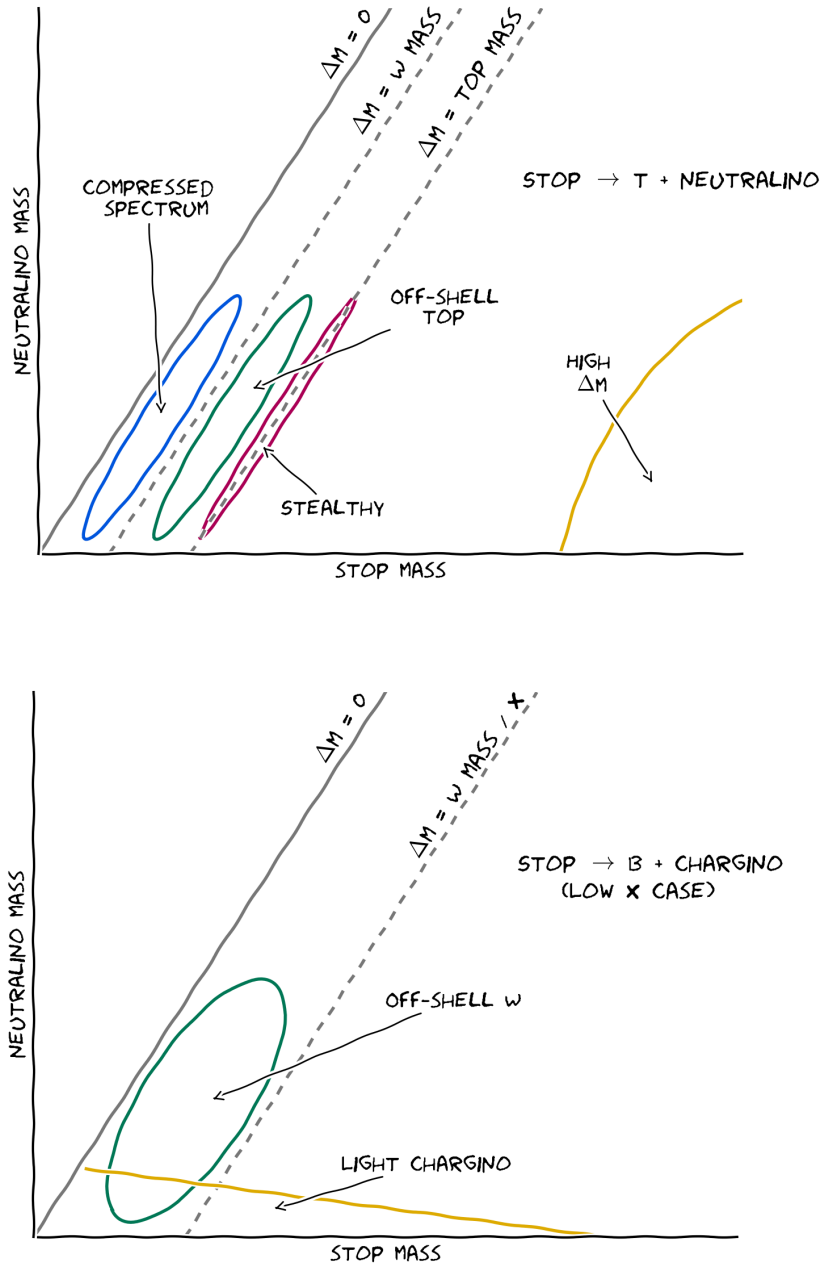


Figure 4.7: Mass space of the stop pair production search for the $\tilde{t}_1 \rightarrow t\tilde{\chi}_1^0$ decay mode (top) and $\tilde{t}_1 \rightarrow b\tilde{\chi}_1^\pm \rightarrow bW^\pm\tilde{\chi}_1^0$ decay mode when x is close to 0 (bottom).

of Δm as illustrated in Figure 4.8 on top left. The remaining part of the phase space, with $0 < \Delta m < m_W + m_b$, does not allow the decay through a top but instead is expected to decay through $c + \tilde{\chi}_1^0$ (flavor-violating two-body decay) or $b\nu_\ell + \tilde{\chi}_1^0$ (four-body decay). This topology, called compressed spectra, will not be considered here as it requires a dedicated analysis.

The $\tilde{t}_1 \rightarrow b\tilde{\chi}_1^\pm \rightarrow bW\tilde{\chi}_1^0$ decay mode also has a kinematic transition around $\Delta m \sim$

m_W/x , corresponding to the limit above which the W in the decay of the chargino is on-shell. Overall, in the case where x is close to 1, the evolution of the kinematic across the plane is quite similar to $\tilde{t}_1 \rightarrow t\tilde{\chi}_1^0$ in the on-shell top case, i.e. depends essentially of Δm . However, as x gets close to 0, the mass of the intermediate $\tilde{\chi}_1^\pm$ plays a much important role in the understanding of the kinematic. For instance, at a constant $m_{\tilde{t}_1} = 400$ GeV, $m_{\tilde{\chi}_1^\pm}$ varies between 100 and 325 GeV for $x = 0.25$, compared to a variation between 300 and 375 GeV for the same situation at $x = 0.75$. The fact that $m_{\tilde{\chi}_1^\pm}$ gets to lower values directly impacts the energy of the decay products, an in particular the resulting E_T^{miss} from $\tilde{\chi}_1^0$. The effect is visible in the bottom right plot of Figure 4.8 where the mean E_T^{miss} is for example lower at $(m_{\tilde{t}_1}, m_{\tilde{\chi}_1^0}) = (400, 0)$ GeV compared to $(m_{\tilde{t}_1}, m_{\tilde{\chi}_1^0}) = (400, 100)$ GeV.

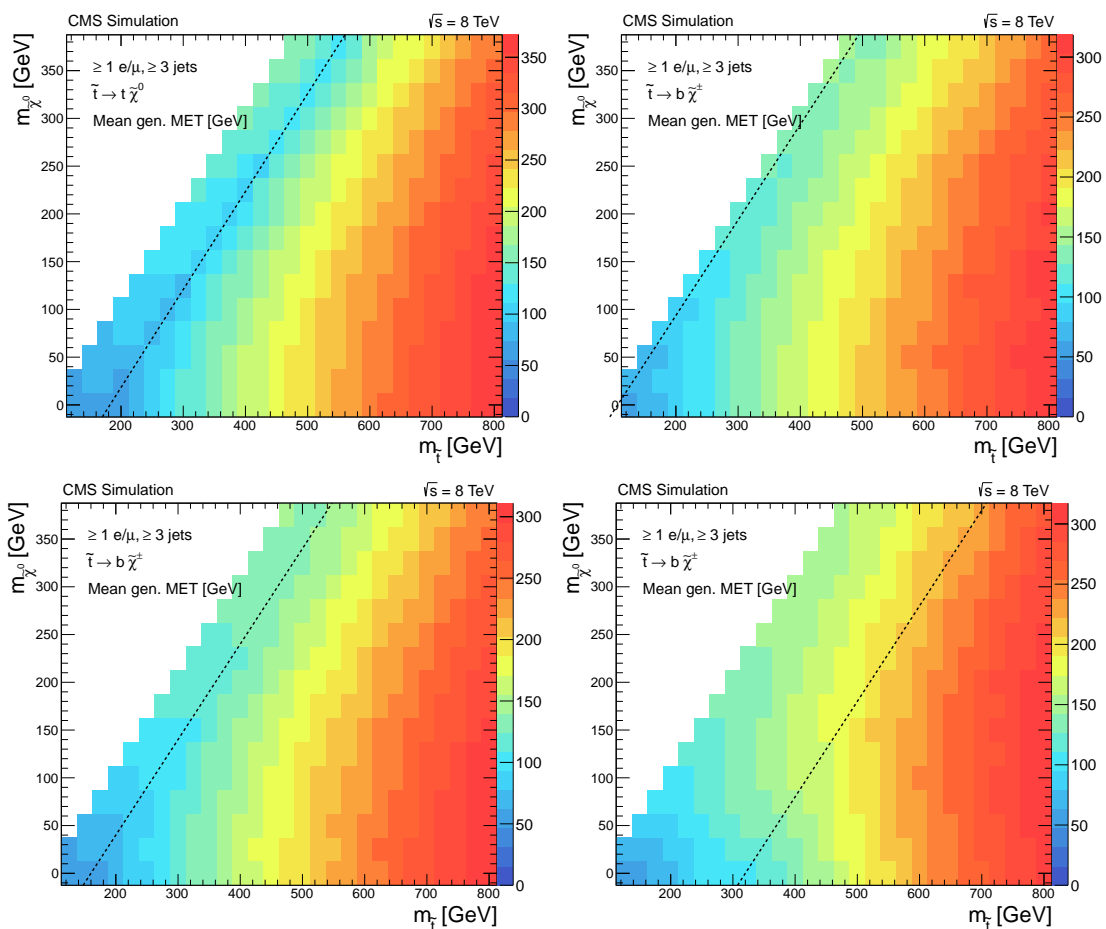


Figure 4.8: Evolution of the mean generated missing transverse energy from neutrinos and neutralinos for the $\tilde{t}_1 \rightarrow t\tilde{\chi}_1^0$ decay mode (top left) and $\tilde{t}_1 \rightarrow b\tilde{\chi}_1^\pm$ with $x = 0.75$ (top right), 0.50 (bottom left) and 0.25 (bottom right). A selection requiring at least one high- p_T central electron or muon and at least three high- p_T central jets is applied.

After the decay of the tops or charginos, each W can decay hadronically (i.e. into a pair of quarks, $W \rightarrow q\bar{q}$) or leptonically (i.e. into a charged lepton and a neutrino, $W \rightarrow \ell\nu_\ell$). It is common to refer to the channel of interest via the number of charged leptons in the final state: 0-lepton (or fully hadronic) channel, 1-lepton (semi-leptonic)

channel or 2-lepton (di-leptonic) channel. In Section 4.2 to Section 4.9, we focus on a search in the 1-lepton channel. This channel has the advantage to be less sensitive to multijet background while still having a relatively large branching ratio. In the 0-lepton, one can however profit from the fact that the main backgrounds are expected to contain no genuine E_T^{miss} , and benefit from the ability to fully reconstruct the decay of the tops in the $\tilde{t}_1 \rightarrow t\tilde{\chi}_1^0$ decay mode. Finally, the 2-lepton channel, despite its relatively low branching ratio, tends to be competitive for the low Δm region because of the p_T threshold of the dilepton triggers are generally lower than the hadronic or single lepton triggers.

4.2 Analysis strategy and overview

While there has been several version of this analysis in the context of the CMS collaboration [101, 102, 103], this document focuses on the 8 TeV legacy version of it [103]. Furthermore, it emphasizes on some aspects which have been studied during the thesis. This short section aims to give to the reader a general overview of the analysis strategy and its key parts, which will then help to understand how each piece fits into the bigger picture while they will be further described in the next sections.

First, we select events with one high- p_T and isolated electron or muon, four jets among which at least one is b -tagged, at least 80 GeV of missing transverse energy, and veto events with a second lepton.

Then, the key variable M_T is introduced as the first main discriminant between signal and background. It is defined as the transverse mass of the lepton+ E_T^{miss} system. This variable is useful to suppress backgrounds for which the only source of genuine E_T^{miss} is one neutrino ν coming from a leptonically-decaying W . It is however less relevant to reduce processes with several sources of E_T^{miss} , in particular the dileptonic $t\bar{t}$ background with one lepton escaping selection, which then becomes a main background. This motivates the need for an efficient second lepton veto to reject this kind of events in the first place, which is discussed in detail as it represents a part of this thesis's work.

To further increase the sensitivity, two parallel approaches are followed to define signal regions that target different parts of the $(m_{\tilde{t}_1}, m_{\tilde{\chi}_1^0})$ space. The first one is a cut-and-count approach, in which a counting experiment is performed after a minimal set of cuts. The second one is a multivariate approach, in which boosted decision trees (BDT) are trained on a set of variables and a counting experiment is performed after cutting on the BDT discriminant. This document focuses in particular on the design of the cut-and-count approach, and its optimization using a figure of merit, which also represents a personal contribution.

A background prediction is computed for each signal region using data-driven methods in control regions, i.e. enriched in a specific type of background. In particular, we show how the Monte-Carlo description of the tail of the M_T variable needs to be corrected, and which method is put in place to obtain a reliable prediction. It has also recently been noticed that signal contamination in the control regions of this analysis can significantly bias the data-driven aspects of the analysis. It is explained how one can correct the background prediction to produce a rigorous interpretation of the counting experiments. Both these aspects, the data-driven background estimation and the signal contamination correction, have been taken care of in the context of this thesis.

Finally, the results and interpretations of the analysis are discussed. At the end of this chapter, some further studies for the future of the analysis are presented, namely the use of W -tagging techniques and the sensitivity estimation for the Run II at $\sqrt{s} = 13$ TeV.

4.3 Monte-Carlo generation and datasets

The analysis is performed on the dataset of pp collisions recorded by the CMS detector during the Run I of the LHC at $\sqrt{s} = 8$ TeV, with a total integrated luminosity $\mathcal{L} = 19.5 \text{ fb}^{-1}$.

Background samples are generated from Monte-Carlo simulations: the $t\bar{t}$ and single top processes are simulated using POWHEG [104] while W +jets, Drell-Yan, diboson, triboson, $t\bar{t}W$ and $t\bar{t}Z$ simulations are performed using MADGRAPH [105]. For all the background samples, the parton shower step is performed with PYTHIA6 [106] and the response of the detector is simulated through a GEANT4-based model of the detector.

Signal benchmark samples are generated according to a grid in term of $m_{\tilde{t}_1}$ and $m_{\tilde{\chi}_1^0}$ with 25 GeV steps. The stop pair production is simulated using MADGRAPH with up to two additional partons generated in the hard scattering, and the decay of the stops and parton shower are performed with PYTHIA6. Because of the number of benchmarks considered and resource constraints, the detector response is simulated using the CMS fast simulation package [80].

Simulated events are weighted to match the integrated luminosity and pile-up distribution of the recorded collisions. For each trigger category used, as described later, the efficiencies are derived from data as function of the p_T and η of the objects and are used to weight the Monte-Carlo to simulate the effect of trigger. Additionally, $t\bar{t}$ events are reweighted as function of the p_T of the generated top quark to correct for a known disagreement [107]. Finally, we also reweight signal events to correct for a mismodeling

of initial-state radiations observed in the recoil of Z +jets and $t\bar{t}$ events [108].

4.4 Objects and events selection

This section focuses on the first aspect of the experimental search, namely the objects and events selection. The goal here is to, first, present the criteria used to define the objects in the context of this analysis, and secondly, the baseline event selection.

4.4.1 Trigger

The data used in this analysis are recorded from three triggers, that require the presence of a muon or an electron in the event.

The single muon trigger requires an isolated muon candidate with $p_T > 24$ GeV and a relative isolation lower than 0.15 in a cone of $\Delta R = 0.3$. Under the present analysis selection, the efficiency of this trigger ranges from 78% to 95% depending on the p_T and $|\eta|$ of the muon. In addition to this single muon trigger, a muon+jets trigger is used, allowing a lower p_T threshold for the muon. This trigger requires a muon candidate with $p_T > 17$ GeV and $|\eta| < 2.1$ and at least three jets with $p_T > 30$ GeV and $|\eta| < 3.0$. In the context of this analysis, the trigger efficiency depends essentially on the muon p_T and η and varies from 76% to 97% for a $p_T > 20$ GeV.

The single electron trigger requires an electron candidate with $p_T > 27$ GeV. Because the reconstruction of electron is more challenging and subject to fakes than muons, extra criteria are applied on the shower shape, the matching between track and supercluster, and the ratio between of hadronic versus electromagnetic energy. In the context of this analysis, the trigger efficiency ranges from 86% to 97% depending on the p_T of the electron.

The analysis makes also use of dilepton triggers to control the dileptonic $t\bar{t}$ component. For these, electrons candidates are identified using loose requirements on the isolation and information from tracker and calorimeters. The leading lepton must have $p_T > 17$ GeV while the second lepton must have $p_T > 8$ GeV.

4.4.2 Leptons

After full reconstruction of the events, further criteria are applied on the lepton candidates. In the context of this analysis, we define two categories of leptons: *selected* leptons, i.e. well-identified high- p_T isolated leptons, and a second category used to veto events with

a lost second lepton, constructed from the particle-flow candidates directly, with loose requirements.

Selected leptons

To enter the selected lepton category, muon candidates are requested to have $p_T > 20$ GeV and $|\eta| < 2.1$ as well as a good vertex compatibility, good fit quality for the track and a minimum number of hits in both the tracker and the muon subdetectors using the tight identification working point [109].

Electron candidates are requested to have $p_T > 30$ GeV, to be in the barrel ($|\eta| < 1.4442$) and have good vertex compatibility, low number of missing hits and low amount of radiation in the tracker using the medium identification working point [110].

For both muons and electrons, we quantify their isolation by considering the particles inside a cone of $\Delta R = 0.3$ around the lepton. The absolute isolation, i_{abs} , is computed using the particle-flow information by summing the p_T of charged particles inside the cone, as well as neutral particles. An estimation of the neutral pile-up contribution is subtracted from the neutral component, using an effective-area scheme for electrons and $\Delta\beta$ scheme for muons. The relative isolation, $i_{rel} \equiv i_{abs}/p_T(\ell)$ is required to be lower than 0.15 while the absolute isolation is required to be lower than 5 GeV.

Leptons for second lepton veto

As announced in Section 4.2, the dileptonic $t\bar{t}$ process is the main background of this analysis after cutting on the variable M_T , representing about 60% of the total background. This motivates the development of efficient ways to reject this specific background, in particular via a veto targeting events with a 'lost' lepton.

To characterize the problem, the dileptonic $t\bar{t}$ events passing a selection requiring exactly one selected lepton and at least three jets are classified according to the nature and kinematics of the lost lepton taken from the Monte-Carlo truth. Five categories are considered:

- (e/μ) Electrons or muons with $p_T > 5$ GeV, $|\eta| < 2.5$;
- ($\tau \rightarrow e/\mu$) Taus decaying to an electron or muon with $p_T > 5$ GeV, $|\eta| < 2.5$;
- (1-prong τ) Taus decaying to one charged hadron with $p_T > 10$ GeV, $|\eta| < 2.5$;

- (≥ 3 -prong τ) Taus decaying to three or more charged hadrons with total visible energy > 20 GeV, $|\eta| < 2.5$;
- (Not in acceptance) Other cases fall in this category as their reconstruction is considered too challenging.

Figure 4.9 shows a diagram representing the contribution of each category to the dileptonic $t\bar{t}$ events. To address all the categories (apart from the lepton not in acceptance), two vetoes are designed.

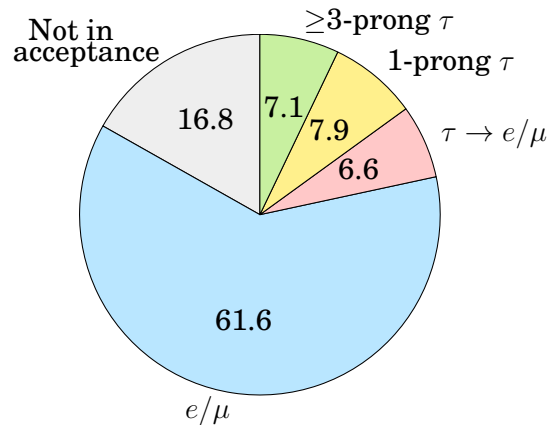


Figure 4.9: Nature of the lost lepton in dileptonic $t\bar{t}$ events after a selection requiring exactly one high- p_T selected lepton and at least three high- p_T jets

The first veto category targets the (e/μ), ($\tau \rightarrow e/\mu$) and (1-prong τ) categories. We look for a reconstructed isolated particle in the event, discarding those that are within $\Delta R < 0.1$ of an already selected lepton. To remove fakes from pile-up activity, we require the track of the particle to be compatible with the primary vertex with $d_z < 0.05$ cm. If the particle is flagged as an electron or muon candidate by the particle flow algorithm, it is required to have $p_T > 5$ GeV and a relative isolation lower than 0.2. If the particle is not flagged as an electron or muon candidate, the p_T requirement is tightened to 10 GeV, the relative isolation must be lower than 0.1, and its charge must be opposite to the one of an already selected lepton. Figure 4.10 shows the distribution of d_z and the relative isolation before cutting on these variables. Particle-flow candidates are categorized depending if they are flagged as e/μ candidate by the particle flow, and if they are matched to a generated lepton or not.

The second veto category targets a τ lepton that decayed hadronically into one or more charged hadron. τ candidates are reconstructed using the hadron-plus-strips (HPS) algorithm [111]. The reconstruction is based on the excellent performances of the particle-flow, and the topology of the τ lepton decay containing a low average number of hadrons

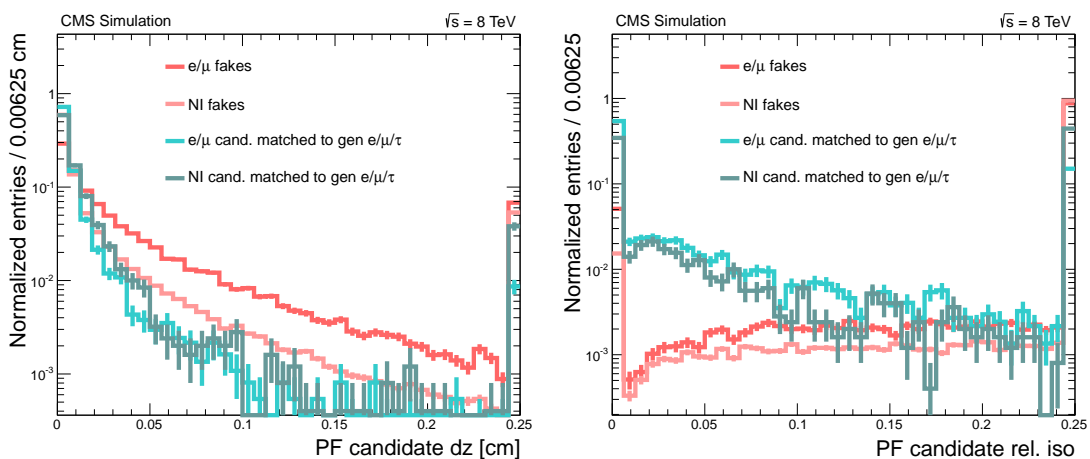


Figure 4.10: Distribution of d_z (on the left) and relative isolation (on the right) for the particle-flow candidates. On both plots, a cut on $p_T > 5$ GeV for candidates flagged as e/μ is applied while $p_T > 10$ GeV is required for the other candidates (non-identified, NI).

(h^\pm) and π^0 with a high probability of decay through $\pi^0 \rightarrow \gamma\gamma$. The algorithm therefore reconstruct candidates from jets with low charged multiplicity, and strips of electromagnetic energy deposits along ϕ . The motivation behind the strips idea is that photons from π^0 are likely to convert to e^+e^- pairs in the tracker material, spreading the energy along ϕ as e^+e^- are affected by the magnetic field. Depending on the exact topology, several constrains are applied by the algorithm based on the mass of the π^0 and τ . After the reconstruction step, to reject fake τ 's, we use a discriminant based on a multivariate analysis of the parameter and topology of the jet. The medium working point is used, leading to a tagging efficiency around 70 – 80% for a fake rate of about 1% as shown on Figure 4.11 on the left. The τ candidates must be separated from an already selected lepton by $\Delta R > 0.4$ and to be oppositely charged. In addition, to reject fakes at low p_T as shown on Figure 4.11 on the right, we require the τ candidate to have $p_T > 20$ GeV.

Table 4.1 summarizes the performances of the second lepton vetoes by showing the efficiency on the different categories estimated on $t\bar{t}$ events. It is important to keep an eye also to the category of events with no generated second lepton (i.e. semileptonic $t\bar{t}$), especially because we don't want to loose too much efficiency for signal events. This is what is shown in the first column 'no 2nd ℓ ', while the last column shows the global impact on all dileptonic $t\bar{t}$ event. The isolated track veto is particularly useful for rejecting prompt e/μ , leptonically-decaying τ 's and 1 prong τ 's. This is complemented by the τ veto which covers the ≥ 3 prong τ case, as well as additional coverage of the prompt e/μ and 1 prong τ .

Overall, more than 60% of the dilepton background is rejected when applying both vetoes, while only 11% of events with no second lepton are lost. An estimation of the

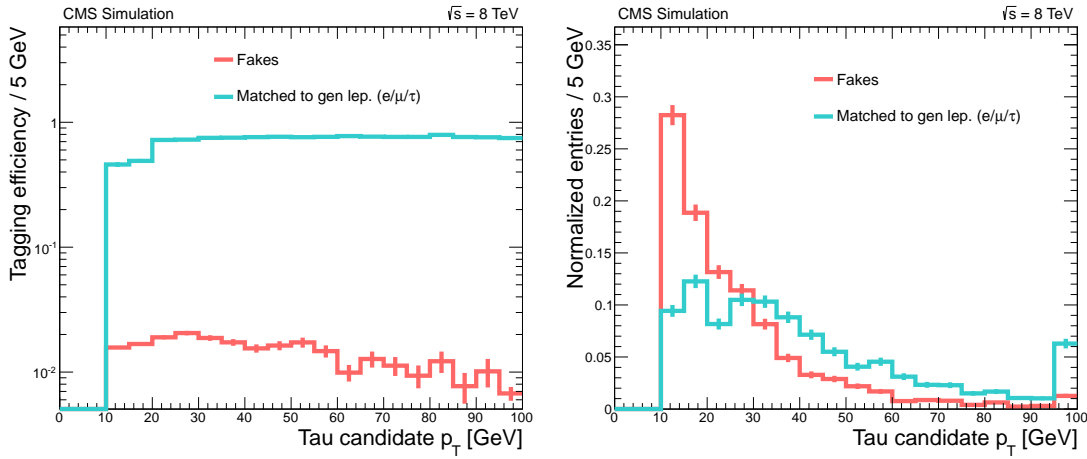


Figure 4.11: Tagging efficiency of the τ MVA discriminant as function of the p_T of the τ candidate (on the left) and p_T spectrum (on the right) of the fakes and candidates matched to generated leptons.

selection	no 2 nd ℓ	not in accept.	e/μ	$\tau \rightarrow e/\mu$	1 prong τ	≥ 3 prong τ	all 2ℓ
iso. track veto	0.91	0.91	0.31	0.24	0.24	0.91	0.44
τ veto	0.97	0.98	0.65	0.80	0.57	0.68	0.71
iso. track + τ veto	0.89	0.90	0.26	0.22	0.21	0.62	0.38

Table 4.1: Selection efficiencies when applying the two vetoes, estimated on the different categories of second leptons of a $t\bar{t}$ sample. The first column shows the case with no generated second lepton (i.e. semileptonic $t\bar{t}$) and is related to fake second leptons. The next columns detail the efficiency on each category of second lepton. The last column corresponds to the global efficiency for events with two generated leptons (i.e. dileptonic $t\bar{t}$).

impact of this veto on the final analysis sensitivity can be computed considering the significance S/\sqrt{B} . Assuming that the dilepton $t\bar{t}$ represents a fraction $f = 75\%$ of the background before applying the veto, the gain on the significance is about 25%.

4.4.3 Jets and missing transverse energy

Jets are reconstructed using the anti- k_t clustering algorithm with a size parameter $R = 0.5$ on the particle-flow candidates. Three types of corrections are applied sequentially: an energy offset, a η and p_T dependent correction, and a residual correction accounting for remaining discrepancies between data and simulation.

Selected jets are required to have $p_T > 30$ GeV and $|\eta| < 2.4$. They also have to be separated from lepton candidates in $\Delta R > 0.4$ and to pass a jet identification criterion with loose requirements on the neutral and charged fractions, charged multiplicity and number of constituents [112]. Furthermore, a pile-up identification algorithm is used

which combines the primary vertex compatibility, the topology of the jet shape and the jet object multiplicity into a discriminant that helps to better reject jets from pile-up [113].

b -tagged jets are defined by, on top of the previous requirements, using the medium working point of the Combined Secondary Vertex (CSV) tagging algorithm [84]. The efficiency of this tagger is typically around 60% for b jets while the fake rate of light jets is around 1%. To account for known data/MC discrepancies, the value of the CSV discriminant is corrected in the simulation via a reshaping technique, function of the p_T , η and flavor of the jet.

The missing transverse energy, $E_T^{\vec{\text{miss}}}$, is computed by considering the negative vector sum of all particle-flow candidates in the event and corrected by propagating the previous corrections applied on the jets. Because this quantity is crucial in this analysis, a particular attention is given to it. Especially, not only the energy resolution is important, but also the ϕ resolution. This is why a correction is applied on the $E_T^{\vec{\text{miss}}}$ direction to remove a modulation seen in both data and simulations, function of the pile-up level. The direction of this particle-flow-based E_T^{miss} is also checked to be consistent with a calorimeter-based approach and we veto events where the difference is higher than 1.5 rad. Finally, we filter events that suffer from high noise, anomalous subdetector operation or known misreconstruction issues that lead to unphysical E_T^{miss} [76].

4.4.4 Events preselection

The baseline selection, or preselection, is defined by asking exactly one electron or muon, at least four jets among which at least one is b -tagged, and a missing transverse energy higher than 80 GeV. A veto is applied on events containing a second lepton as defined in Section 4.4.2. For data, we require that events with an electron fired the single electron trigger, while for events with a muon, the cross-trigger has to be fired if the muon p_T is between 20 and 26 GeV otherwise the single muon trigger is used.

We group the backgrounds in four categories: 1ℓ top, W +jets, $t\bar{t} \rightarrow \ell\ell$ and rare. The 1ℓ top category consists of semi-leptonic $t\bar{t}$ production and single top production (s and t modes). The W +jets category is the production of a W decaying leptonically, associated with the production of several jets from initial or final state radiation. The $t\bar{t} \rightarrow \ell\ell$ category corresponds to dileptonic $t\bar{t}$ production. Finally, the rare category regroups several different processes from Drell-Yan, diboson, triboson and $t\bar{t}$ +boson. The QCD background is not considered in this analysis as its contribution has been found to be negligible, following the isolated lepton requirement and the E_T^{miss} cut.

Table 4.2 presents a breakdown of the yields of the backgrounds at different steps of the preselection. Figure 4.12 shows the selection efficiency of the signal across the $(m_{\tilde{t}_1}, m_{\tilde{\chi}_1^0})$ plane for the four signal scenarios which are studied.

	$=1\ell, \geq 4$ jets	$+\geq 1b$ -tag	$+E_T^{\text{miss}} > 80$ GeV	$+2^{\text{nd}} \ell$ veto (preselection)
1ℓ top	253909 ± 211	212568 ± 193	61066 ± 100	54036 ± 94
$t\bar{t} \rightarrow \ell\ell$	26240 ± 67	22193 ± 61	11235 ± 43	4169 ± 26
W +jets	128327 ± 239	18224 ± 94	4791 ± 44	4460 ± 43
rare	41243 ± 102	16630 ± 79	4925 ± 45	3835 ± 40
total SM	449720 ± 342	269616 ± 237	82019 ± 127	66502 ± 115
$\tilde{t}_1 \rightarrow t\tilde{\chi}_1^0$ (450/50)	341 ± 7	289 ± 7	263 ± 6	224 ± 6
$\tilde{t}_1 \rightarrow b\tilde{\chi}_1^\pm$ (0.5/450/50)	398 ± 21	356 ± 20	306 ± 19	248 ± 16

Table 4.2: Event yields for each background categories at different stages of the selection, estimated from Monte-Carlo at $\sqrt{s} = 8$ TeV and for $\mathcal{L} = 19.5 \text{ fb}^{-1}$. Two signal benchmark examples are also considered, for the $\tilde{t}_1 \rightarrow t\tilde{\chi}_1^0$ decay mode and $\tilde{t}_1 \rightarrow b\tilde{\chi}_1^\pm$ with $x = 0.5$ decay mode, both with $(m_{\tilde{t}_1}, m_{\tilde{\chi}_1^0}) = (450, 50)$ GeV. Uncertainties reflects the statistics from the Monte-Carlo samples.

4.5 Signal region design and optimisation

At the preselection level, the dominant background category is the 1ℓ top, as can be seen from Table 4.2. For the 1ℓ top and W +jets backgrounds, the only source of genuine missing energy is a neutrino ν_ℓ coming from the leptonic decay of a W boson ($W \rightarrow \ell\nu_\ell$). In comparison, the signal has three main sources of genuine missing energy which are a neutrino and the two neutralinos. One can exploit this difference by introducing the transverse mass of the $(\ell, E_T^{\vec{\text{miss}}})$ system, called M_T and defined as

$$M_T \equiv m_T(\vec{p}(\ell), E_T^{\vec{\text{miss}}}) = \sqrt{2E_T^{\vec{\text{miss}}} \cdot p_T(\ell) \cdot (1 - \cos(\Delta\phi))} \quad (4.5)$$

where $\Delta\phi$ is the azimuthal angle between the lepton and the $E_T^{\vec{\text{miss}}}$ directions. This variable has a kinematic end point at $m_W \sim 80$ GeV for the 1ℓ top and W +jets background, while the same variable can get to higher values for the signal because of the additional missing energy coming from the two neutralinos.

Figure 4.13 shows the M_T distribution for the different backgrounds and two signal benchmarks at preselection level. Despite the sharp drop after $M_T \sim 80$ GeV, the 1ℓ top, W +jets and rare $\ell\ell$ components still contribute in the tail because of $E_T^{\vec{\text{miss}}}$ resolution effects and off-shell W contributions. The $t\bar{t} \rightarrow \ell\ell$ background however has no kinematic end point because of its second neutrino contributing to $E_T^{\vec{\text{miss}}}$.

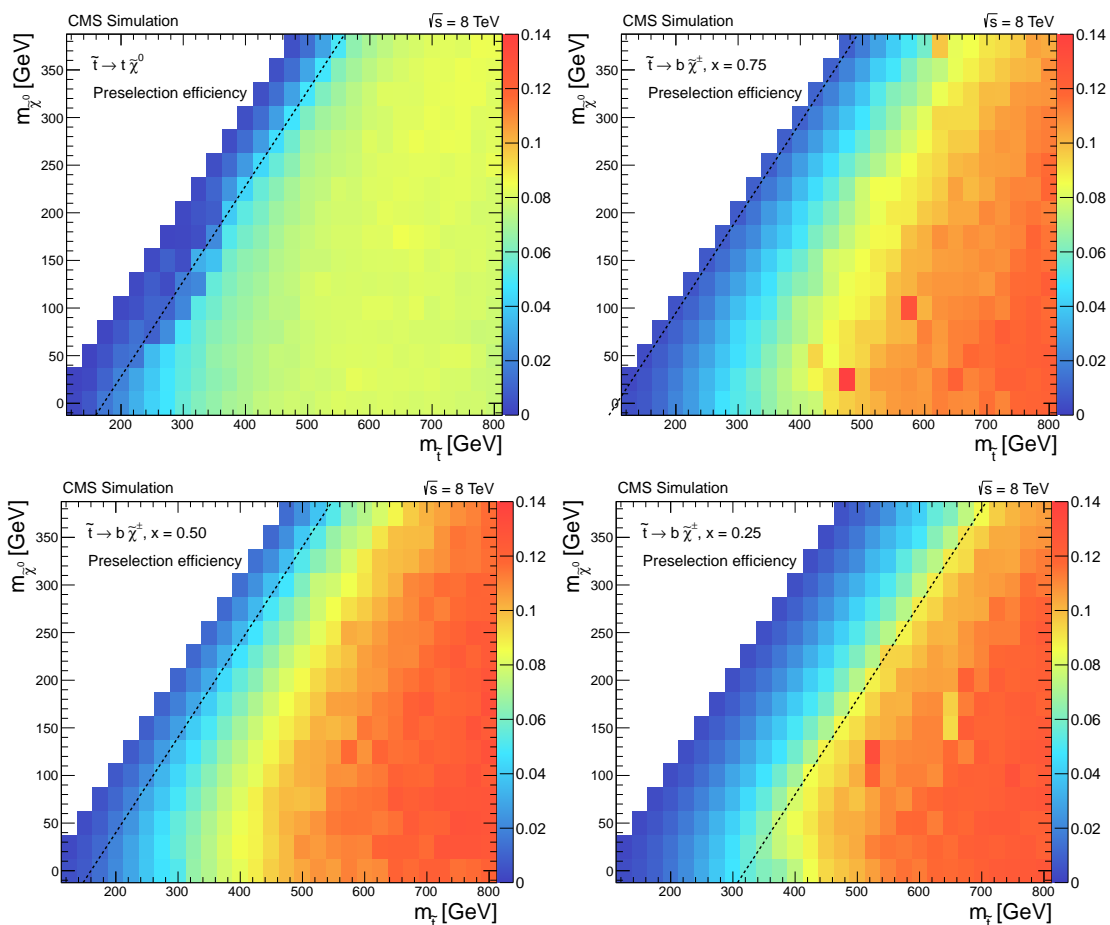


Figure 4.12: Preselection efficiency for the signal across the $(m_{\tilde{t}_1}, m_{\tilde{\chi}_1^0})$ space for the $\tilde{t}_1 \rightarrow t\tilde{\chi}_1^0$ decay mode (top left) and the $\tilde{t}_1 \rightarrow b\tilde{\chi}_1^\pm$ decay mode for $x = 0.75$ (top right), 0.50 (bottom left) and 0.25 (bottom right). The efficiency is computed with respect to the inclusive process (i.e. not only to the 1-lepton channel which corresponds to a branching ratio of about 44%).

Given the discriminating power of this variable, cutting on it is the starting point of all the signal region definitions of the analysis. Two approaches are used to define the signal regions. The first one, called cut-based approach or cut-and-count, consists in applying a sequential list of cuts on variables, followed by a counting experiment using the expected yields of background and signal. The second one uses a boosted decision tree (BDT) that combines multiple inputs into a single discriminating variable, the BDT output, on which a cut is applied to also perform a counting experiment. While the BDT approach exploits the information more efficiently than the cut-based, and therefore is expected to have better performances, the cut-based approach is often seen as a more transparent tool as it offers the possibility to control one by one the effect of each cut.

For the cut-based approach, we use $M_T > 120$ GeV as a starting point whereas for the BDT approach we use $M_T > 100$ GeV to allow more phase space for the training

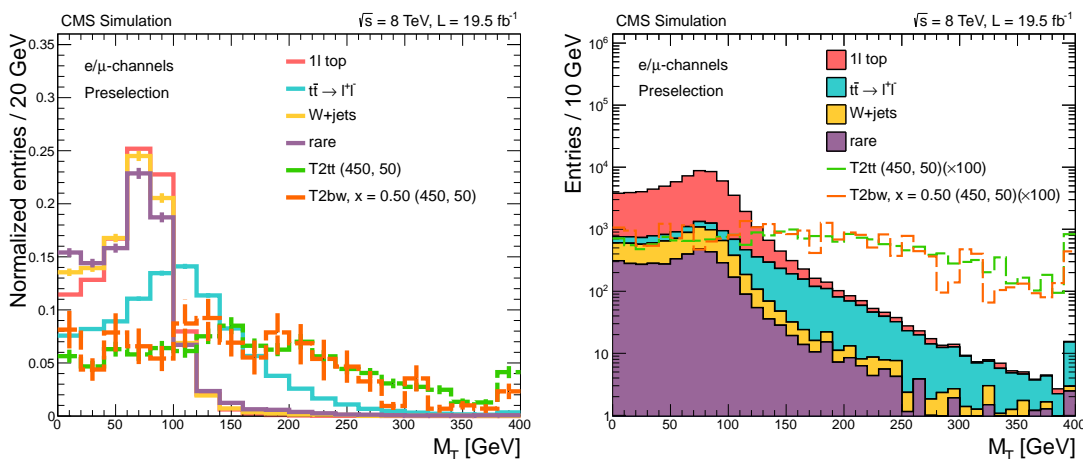


Figure 4.13: Distribution of M_T for the different backgrounds, superimposed after normalization to one (on the left) or stacked after normalization to the luminosity (on the right). Two signal examples are shown, with their cross-sections multiplied by 100 on the right.

and higher initial selection efficiency for the signal. Table 4.3 shows the breakdown of the yields after the M_T cut for the different backgrounds and two signal benchmarks. For $M_T > 120$ GeV, 96% of the 1ℓ top and W +jets contributions is rejected while about 65% of the signal is conserved. The $t\bar{t} \rightarrow \ell\ell$ category is less impacted and represents about 42% of the total background after the cut.

	Preselection	$+M_T > 100$ GeV	$+M_T > 120$ GeV
1ℓ top	54036 ± 94	5970 ± 31	1663 ± 16
$t\bar{t} \rightarrow \ell\ell$	4169 ± 26	2117 ± 18	1529 ± 16
W +jets	4460 ± 43	477 ± 13	170 ± 8
rare	3835 ± 40	490 ± 13	233 ± 9
total SM	66502 ± 115	9055 ± 41	3596 ± 26
$\tilde{t}_1 \rightarrow t\tilde{\chi}_1^0$ (450/50)	224 ± 6	160 ± 5	146 ± 5
$\tilde{t}_1 \rightarrow b\tilde{\chi}_1^\pm$ (0.5/450/50)	248 ± 16	167 ± 14	146 ± 13

Table 4.3: Event yields for each background categories, after $M_T > 100$ GeV and $M_T > 120$ GeV, estimated from Monte-Carlo at $\sqrt{s} = 8$ TeV and for $\mathcal{L} = 19.5$ fb $^{-1}$. Two signal benchmark examples are also considered, for the $\tilde{t}_1 \rightarrow t\tilde{\chi}_1^0$ decay mode and $\tilde{t}_1 \rightarrow b\tilde{\chi}_1^\pm$ with $x = 0.5$ decay mode, both with $(m_{\tilde{t}_1}, m_{\tilde{\chi}_1^0}) = (450, 50)$ GeV. Uncertainties reflects the statistics from the Monte-Carlo samples.

In the following, we first present the discriminating variables that are used to design the signal regions, and then detail the sensitivity estimation and optimization procedure.

4.5.1 Discriminating variables

This section describes the variables which are later used to define the signal regions. For each of them, we discuss the motivation behind the construction and usage of this variable, and compare the distribution for the background and two signal benchmarks. This comparison is shown at preselection level with an additional cut on $M_T > 100$ GeV. However, it should be kept in mind that the usefulness of some variables only shows up after cutting on other variables or in specific regions of the $(m_{\tilde{t}_1}, m_{\tilde{\chi}_1^0})$ space.

E_T^{miss} and E_T^{miss} significance

While the preselection already includes a cut on the missing transverse energy, cutting further on it can significantly increase the signal-to-noise ratio especially since the mean E_T^{miss} is expected to grow as a function of Δm as shown in Figure 4.8. However, signal at low Δm is more challenging because of the lower E_T^{miss} . To address this particular region of the $(m_{\tilde{t}_1}, m_{\tilde{\chi}_1^0})$ space, one can turn to the significance of E_T^{miss} [76, 114]. The uncertainty on E_T^{miss} is, in the gaussian approximation, $\sqrt{\sum_{\text{particles}} E_T}$, which can be approximated by $\sqrt{H_T}$ with $H_T \equiv \sum_{\text{jets}} p_T$. The variable $E_T^{\text{miss}}/\sqrt{H_T}$ can therefore be used as an approximation of the real E_T^{miss} significance. Overall, it effectively provides a better discriminating power compared to the regular E_T^{miss} at low Δm . This can be qualitatively understood by considering that some background events may have large E_T^{miss} coming from mismeasurement due to high hadronic activity, and will therefore have a low $E_T^{\text{miss}}/\sqrt{H_T}$ value. On the contrary, signal with relatively low E_T^{miss} can be recovered provided that the event contains a comparably low level of hadronic activity, making it more likely that the E_T^{miss} is essentially real.

Figure 4.14 illustrates this fact by showing the distribution of $\sqrt{H_T}$ versus E_T^{miss} for the 1ℓ top background and a signal benchmark, and as an example the line corresponding to a cut at $E_T^{\text{miss}}/\sqrt{H_T} < 10$. The distributions for E_T^{miss} and $E_T^{\text{miss}}/\sqrt{H_T}$ are compared for backgrounds and signal on Figure 4.15 and shows how the signal populates the tail of both distributions.

M_{T2}^W

As the sharp decrease of M_T is a quite appealing feature, developments have been carried [115] to construct similar variables, adapted to other kind of topologies than a unique source of genuine E_T^{miss} from a $W \rightarrow \ell\nu_\ell$. These extensions are often called M_{T2} . Here, we make use of M_{T2}^W which is specifically designed for the topology of the $t\bar{t} \rightarrow \ell\ell$ background,

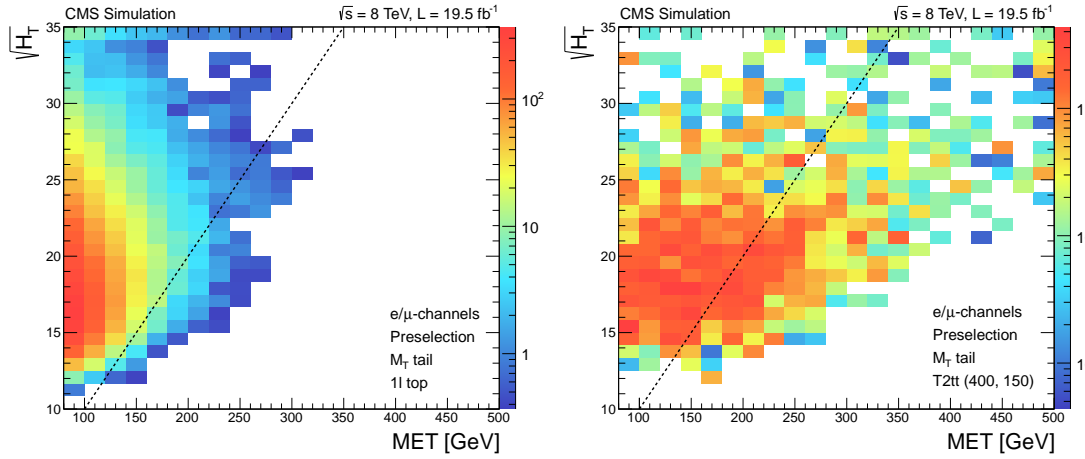


Figure 4.14: Distribution of $\sqrt{H_T}$ versus E_T^{miss} for the 1ℓ top background (on the left) and a benchmark for $\tilde{t}_1 \rightarrow t\tilde{\chi}_1^0$ (on the right). The line illustrates a cut on $E_T^{\text{miss}}/\sqrt{H_T} < 10$.

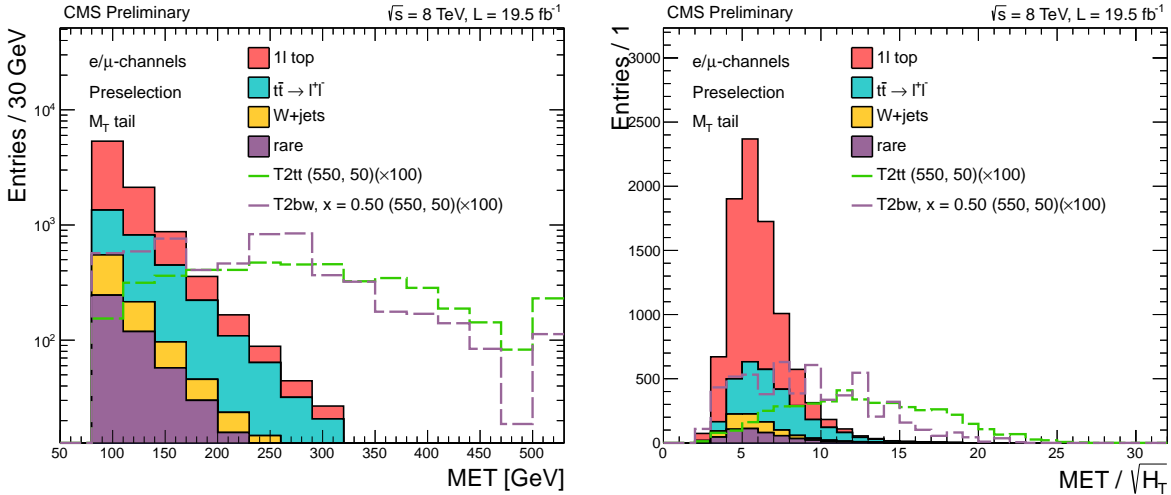


Figure 4.15: Stacked plots presenting the distribution of E_T^{miss} and $E_T^{\text{miss}}/\sqrt{H_T}$ for the different background categories. Two signal benchmarks are superimposed, with cross section multiplied by 100, to show the discriminating power: $\tilde{t}_1 \rightarrow t\tilde{\chi}_1^0$ with $(m_{\tilde{t}_1}, m_{\tilde{\chi}_1^0}) = (550, 50)$ GeV (in dashed green), and $\tilde{t}_1 \rightarrow b\tilde{\chi}_1^\pm$ with $x = 0.5$ and $(m_{\tilde{t}_1}, m_{\tilde{\chi}_1^0}) = (550, 50)$ GeV (in dashed purple). The preselection is applied as well as a cut on $M_T > 100$ GeV.

with one missing lepton. M_{T2}^W is designed by decomposing $E_T^{\vec{\text{miss}}}$ into two components: one corresponding to the neutrino ν_1 , and the other one to the lost leptonic W_2 , such that $\vec{p}_{W_2} + \vec{p}_{\nu_1} = E_T^{\vec{\text{miss}}}$, as sketched on Figure 4.16. The momenta must fit into the constraints that each W -like systems, $(\ell + \nu_1)$ and W_2 , should have a mass $m_W \sim 80$ GeV. Finally, it is imposed that $m(b_2 + W_2) = m(b_1 + \ell + \nu_1) \equiv m_Y$. The computation is summarized in Equation (4.6). The resulting value for M_{T2}^W is the minimum value of m_Y found across all possible decomposition of $E_T^{\vec{\text{miss}}}$. For the $t\bar{t} \rightarrow \ell\bar{\ell}$ background, this variable has an end point at $m_t \sim 172$ GeV while the signal can get to larger values because it contains three

sources of E_T^{miss} .

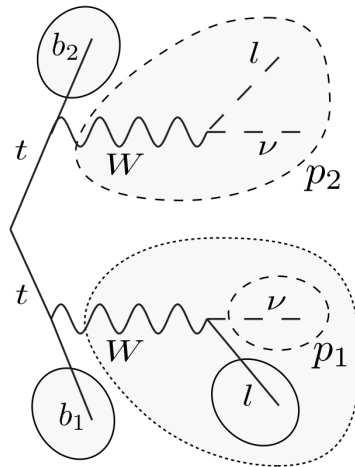


Figure 4.16: Sketch of the object naming in the context of M_{T2}^W and assuming that the event follows the topology of a dileptonic $t\bar{t}$ event with one lepton not reconstructed.

$$M_{T2}^W = \min \left\{ m_y \text{ consistent with: } \left[\begin{array}{l} \vec{p}_{T,1} + \vec{p}_{T,2} = E_T^{\vec{\text{miss}}}, p_1^2 = 0, (p_1 + p_l)^2 = p_2^2 = m_W^2, \\ (p_1 + p_l + p_{b_1})^2 = (p_2 + p_{b_2})^2 = m_Y^2 \end{array} \right] \right\} \quad (4.6)$$

The resulting distribution of M_{T2}^W is shown on Figure 4.17 for backgrounds and signal. The distribution exhibits a particularly good discriminating power with the majority of the background, including the $t\bar{t} \rightarrow \ell\ell$ component, is found to have $M_{T2}^W < 175$ GeV while the signal has a much broader distribution from about 125 to 350 GeV.

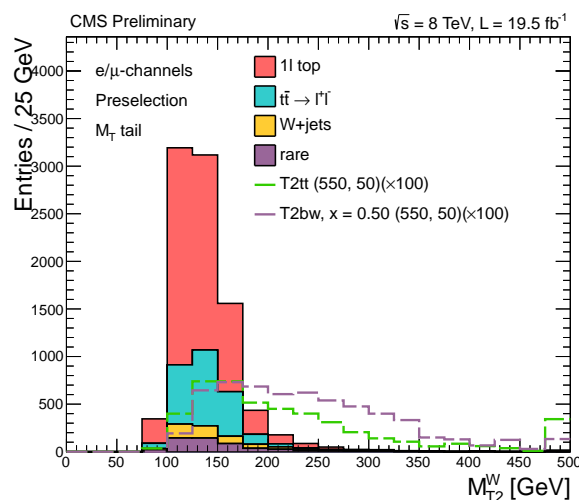


Figure 4.17: Stacked plots presenting the distribution of M_{T2}^W with the same conditions of Figure 4.15.

Hadronic top χ^2

An other way to reject the $t\bar{t} \rightarrow \ell\ell$ background, complementary to the approach offered by M_{T2}^W , is to try to reconstruct an hadronic top from the jets in the event. It can be done by finding the best couple of jets, among selected jets, that fits into the constraint of the W mass of the and then to the top mass by adding a third jet. The value of the hadronic top χ^2 is defined as

$$\chi_{\text{hadronic top}}^2 = \frac{(m_{j_1 j_2 j_3} - m_t)^2}{\sigma_{j_1 j_2 j_3}^2} + \frac{(m_{j_1 j_2} - m_W)^2}{\sigma_{j_1 j_2}^2} \quad (4.7)$$

where the σ are the uncertainties on the mass of the jet systems obtained by propagating the jet energy resolution. This observable is particularly relevant to discriminate signal events, expected to contain an hadronic top, from $t\bar{t} \rightarrow \ell\ell$ and some of the processes of the rare category, that have no hadronic top. The distribution of this variable is shown on Figure 4.18.

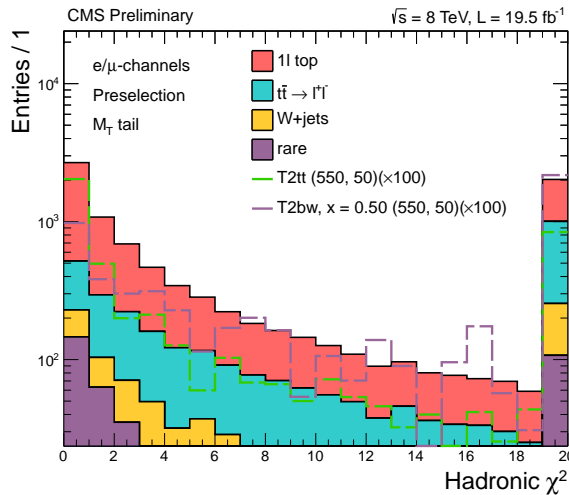


Figure 4.18: Stacked plots presenting the distribution of $\chi_{\text{hadronic top}}^2$ with the same conditions of Figure 4.15.

$p_T(\text{leading } b)$

The p_T of the selected objects are a natural source of discriminating power as the signal is expected to have a larger momentum than the background on average. However for the $\tilde{t}_1 \rightarrow b\tilde{\chi}_1^\pm$ decay mode, the p_T of the b jets is expected to be particularly high (compared to the typical p_T of b jets in the background) as it originates directly from the decay of the stop. It is therefore interesting for the low x cases, i.e. where the gap between \tilde{t}_1 and $\tilde{\chi}_1^\pm$ is large. The distribution of the p_T of the leading b -tagged jet is compared for the

background and signal in Figure 4.19 and illustrates the good discriminating power for the $\tilde{t}_1 \rightarrow b\tilde{\chi}_1^\pm$ decay mode.

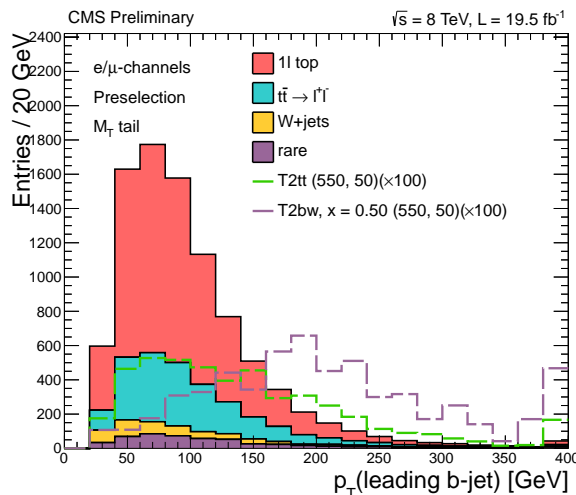


Figure 4.19: Stacked plots presenting the distribution of $p_T(\text{leading } b)$ with the same conditions of Figure 4.15.

ISR-tagged jets

As described in Section 4.1, the low Δm , off-shell and stealthy regions are challenging because looking quite like the SM $t\bar{t}$ production, of have lower p_T decay products. One approach to work around this issue is inspired by direct dark matter production searches [116] and other searches for new physics involving soft objects [117]. The production of heavy particles, in our case stops, requires more energetic partons compared to the production of lighter objects, such as tops. As the rate and energy of initial-state radiation (ISR) grows according to the energy of the incoming partons, the presence of an ISR and its energy in the event allow to discriminate between the $t\bar{t}$ background and a low Δm signal. Moreover, the production of an ISR can enhance the E_T^{miss} magnitude in the event, as the system is recoiling in the opposite direction of the ISR as sketched on Figure 4.20 for a SUSY signal. This is further illustrated in Figure 4.21 showing, at $\Delta m = 125$ GeV, the evolution of the mean stop pair recoil as function of $m_{\tilde{t}_1}$, as well as the evolution of the mean generated E_T^{miss} as function of the stop pair recoil.

To take advantage of this phenomenological aspect, one can design criteria to select jets that are likely to originate from ISR [118, 119]. In the present analysis, we define the ISR-tagging criterion by asking that the event contains at least five jets, among which one of them with $p_T > 200$ GeV and not b -tagged. To illustrate this, Figure 4.22 shows the distribution of the p_T of the leading non b -tagged jet for events with at least five jets. The signal benchmark used on this plot is taken with $(m_{\tilde{t}_1}, m_{\tilde{\chi}_1^0}) = (300, 200)$ GeV.

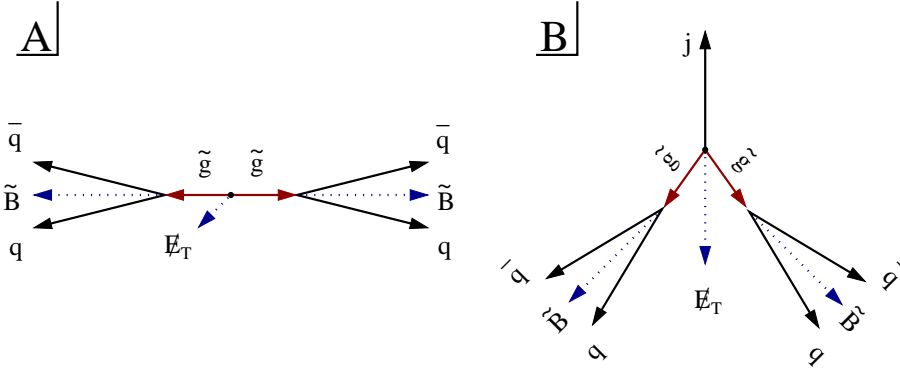


Figure 4.20: Topology of a SUSY signal without (A, on the left) and with (B, on the right) an ISR jet labeled as j , boosting in that case the initial pair of SUSY particles in the opposite direction. The scenario with the ISR jet therefore leads to an increase of E_T^{miss} in the overall event, coming from the \tilde{B} in the decay of the initial pair of gluino \tilde{g} (illustration from [118]).

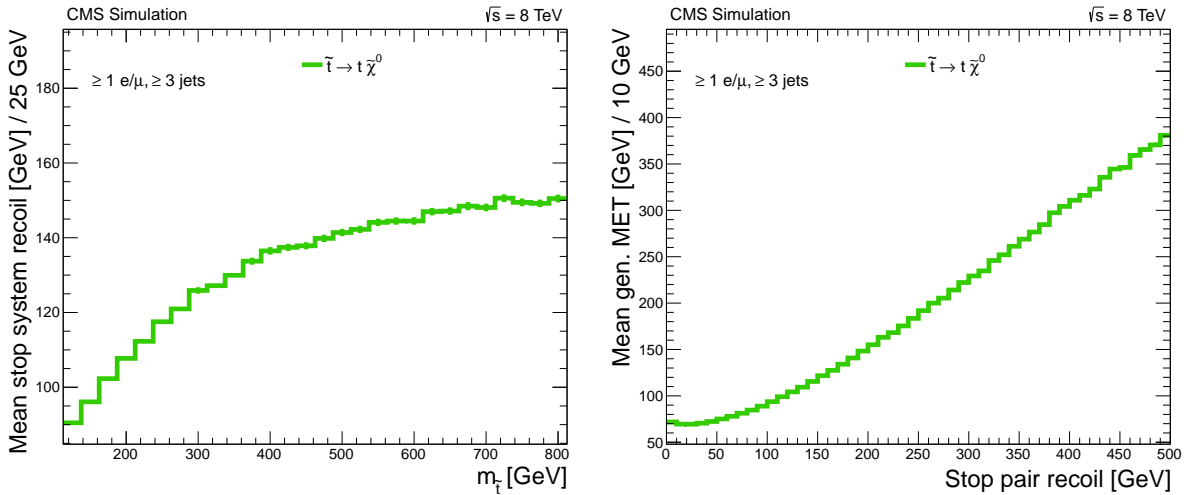


Figure 4.21: On the left, mean recoil of the stop pair system as function of the stop mass. On the right, mean E_T^{miss} as function of the stop pair system recoil. The signal benchmarks used here have $\Delta m = 125$ GeV and a preselection requiring at least 1 high- p_T electron or muon, and at least three jets has been applied.

$$\Delta\phi(\mathbf{j}_{1,2}, E_T^{\vec{\text{miss}}})$$

A topological difference between the signal and the background is the correlation between the direction of $E_T^{\vec{\text{miss}}}$ and the two leading jets, j_1 and j_2 . $\Delta\phi(j_{1,2}, E_T^{\vec{\text{miss}}})$ is defined as the minimum of $\Delta\phi$ between the $E_T^{\vec{\text{miss}}}$ direction and the leading jet, and $\Delta\phi$ between the $E_T^{\vec{\text{miss}}}$ direction and the next-to-leading jets:

$$\Delta\phi(j_{1,2}, E_T^{\vec{\text{miss}}}) \equiv \min(\Delta\phi(j_1, E_T^{\vec{\text{miss}}}), \Delta\phi(j_2, E_T^{\vec{\text{miss}}})) \quad (4.8)$$

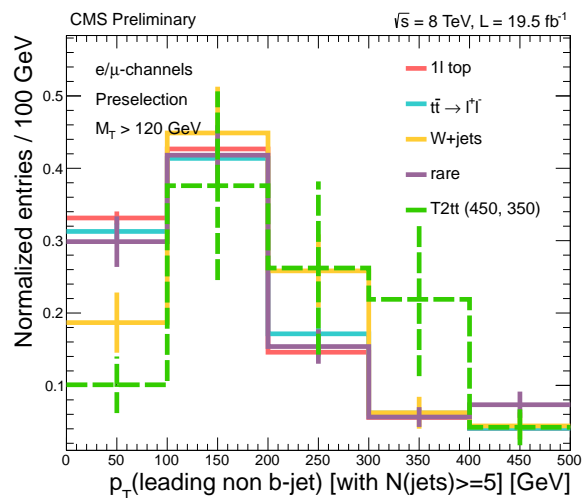


Figure 4.22: Stacked plots presenting the distribution of the p_T of the leading non b -tagged jet with the same conditions of Figure 4.15, except that the signal benchmarks used is with $(m_{\tilde{t}_1}, m_{\tilde{\chi}_1^0}) = (450, 350)$ GeV, i.e. in the Δm region where this variable is expected to be discriminant due to the presence of an ISR.

As illustrated in Figure 4.23, $t\bar{t}$ background tends to get lower values for this variable because the ν_ℓ direction is linked to the b quark from the top parent. In signal events, E_T^{miss} is less correlated to the b jet and $\Delta\phi(j_{1,2}, E_T^{\text{miss}})$ can easily take higher values.

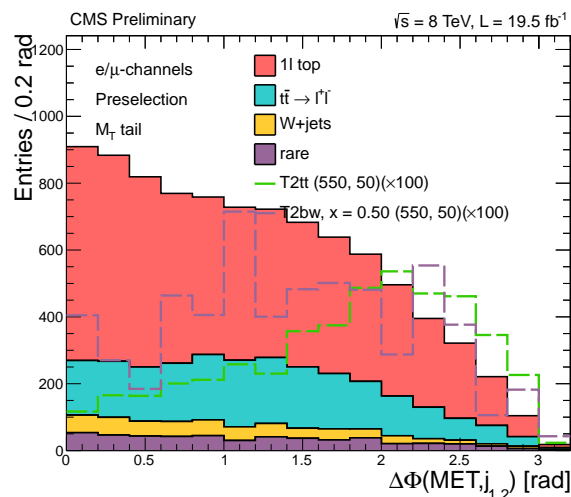


Figure 4.23: Stacked plots presenting the distribution of $\Delta\phi(j_{1,2}, E_T^{\text{miss}})$ with the same conditions of Figure 4.15.

Other variables used in the BDT approach

Other variables are used for the BDT approach and are more briefly described in this section. Four of them are illustrated on Figure 4.24.

- $p_T(\ell)$, $p_T(\text{leading jet})$; As already mentioned, the p_T of the selected objects are a natural source of discriminating power. In addition to $p_T(\text{leading } b)$, the p_T of the lepton and of the leading jet are expected to grow as function of Δm and can help the BDT to identify difference of correlations between this variable and others, between the signal and background.
- H_T ; In a similar fashion, one can look at $H_T \equiv \sum_{\text{jets}} p_T$. This variable is expected to get a larger average value for the signal compared to standard $t\bar{t}$ production because of the contribution of the stop rest mass to the momentum of the decay products.
- $\Delta R(\ell, \text{leading } b\text{-tagged jet})$; In the $\tilde{t}_1 \rightarrow t\tilde{\chi}_1^0$ decay mode, as Δm grows, the top quarks become more and more boosted and their decay products are more collimated in one single direction. This variable aims to exploit this fact, expecting more signal events at lower ΔR . It however offers less discriminating power for the $\tilde{t}_1 \rightarrow b\tilde{\chi}_1^\pm$ as the b is less closely related to the lepton due to the intermediate $\tilde{\chi}_1^\pm$ in the decay chain.
- H_T^{ratio} ; Another way of using the $E_T^{\vec{\text{miss}}}$ direction is to compute the ratio of the hadronic activity in the same hemisphere as $E_T^{\vec{\text{miss}}}$ compared to the total hadronic activity of the event, H_T . Because the visible energy recoils on the LSP in signal events, this variable tends to have low values for signal while being around 0.5 for background.
- $M_{\ell b}$ and $M'_{\ell b}$; We consider also the invariant mass of the ℓ +leading b -tagged jet system. This variable is a simple attempt to reconstruct the mass of the leptonic top system despite missing the information on the neutrino. It appears to be useful in the search for $\tilde{t}_1 \rightarrow b\tilde{\chi}_1^\pm$ where no end point at m_t is expected for this variable as there is no top in the decay chain, and larger values can thus be obtained for signal events. $M'_{\ell b}$ is an extension of this variable to the case where no b -tagged jet is found in the event, where in this case the jet with the highest b -tagging discriminant value is used.
- M_{3b} ; In a similar way, one can attempt to reconstruct the mass of the hadronic top system by considering the three jets most back-to-back to the selected lepton. Here again, values larger than m_t can be expected for the $\tilde{t}_1 \rightarrow b\tilde{\chi}_1^\pm$ signal compared to the background, as the decay chain does not involve any top quark.
- Jet multiplicity ; The jet multiplicity also tends to provide discriminating power. This is related to the previous ISR discussion: in a more general case, signal at higher Δm will contain more jets because of ISR. The BDT is likely to be able to exploit

the correlation between this variable and the others to increase its discriminating power.

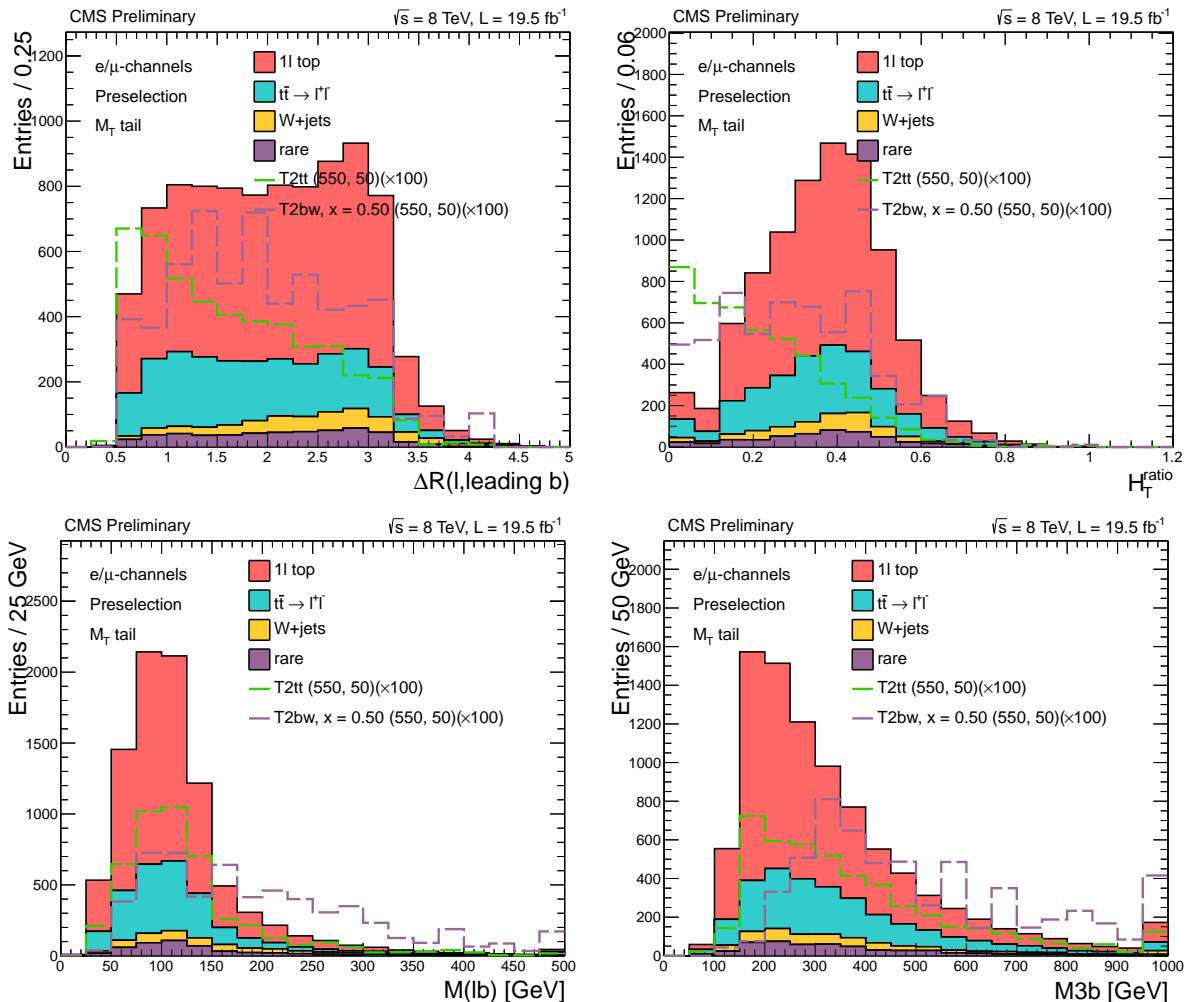


Figure 4.24: Stacked plots presenting the distribution of a subset of the other variables used in BDT, namely $\Delta R(\ell, \text{lead. } b)$ (top left), H_T^{ratio} (top right), M_{lb} (bottom left) and M_{3b} (bottom right), with the same conditions of Figure 4.15

4.5.2 Figure of merit and sensitivity estimation

Before going into the details of the signal region optimization, we first need to introduce the metric used to do so. The problem of defining cuts to be applied on a variable can be summarized as knowing how to compromise between the quantity of selected signal, $S(\text{cut})$, versus selected background, $B(\text{cut})$, such that the sensitivity of the analysis is maximized. Ideally, one would run the full statistical interpretation which, in the context of the LHC experiments, is based on the CL_S approach [120]. However, such a procedure is CPU intensive as it requires toy-data generation, and not suitable for a highly iterative

process such as scanning all possible cuts. In the case of a single-bin counting experiment, a more flexible way is to use analytical formula, called figure of merit (FoM) that gives an immediate estimation of the sensitivity of the counting experiment.

Let's consider the background-only hypothesis H_0 , also called null hypothesis, and the signal hypothesis H_1 . These hypotheses are modeled by a probability density function (pdf), describing the probability to observe N events in the data, as sketched on Figure 4.25.

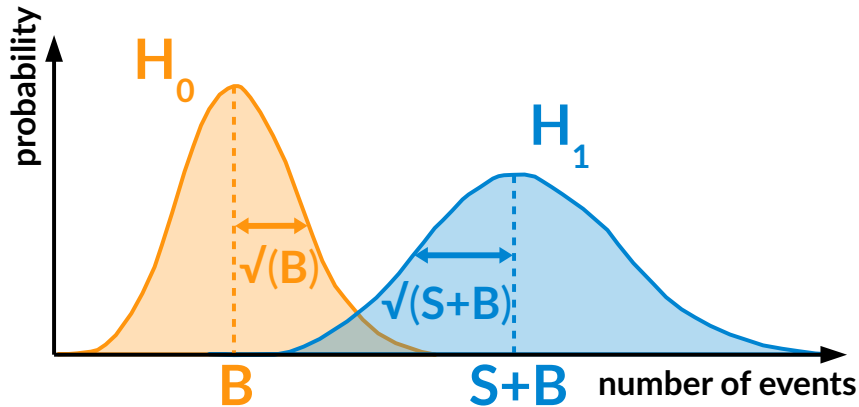


Figure 4.25: Illustration of the modeling of the hypotheses H_0 and H_1 by Poisson distributions with (μ, σ) being respectively (B, \sqrt{B}) and $(S + B, \sqrt{S + B})$.

From the point of view of excluding the signal hypothesis, a statistical hypothesis test consists in computing the probability p to observe less than D events in the data under H_1 , $P(N < D|H_1)$. If this probability is lower than a threshold β , one may exclude the signal hypothesis with a confidence level $1 - \beta$. A common practice is to use a confidence level of 95%, or $\beta = 5\%$. For each hypothesis H , let's define $\mu[H]$ and $\sigma[H]$, respectively the mean and standard deviation of the number of events under this hypothesis. The exclusion potential of a counting experiment can be defined via the probability $P(N < \mu[H_0]|H_1)$, i.e. the probability to observe a background-like realization in the data, if the signal exists. It is generally more practical to express this potential in term of a significance \mathcal{S} , that is to say by expressing the distance $\mu[H_0] - \mu[H_1]$ in terms of standard deviations $\sigma[H_1]$:

$$\mathcal{S}_{\text{exclu.}} = \frac{\mu[H_0] - \mu[H_1]}{\sigma[H_1]}. \quad (4.9)$$

If H_1 follows a gaussian distribution, then there is a direct correspondence between the value of \mathcal{S} and the probability $P(x \notin [-\mathcal{S}, +\mathcal{S}])$ for the normal distribution $\mathcal{N}(0, 1)$. This probability is around 32%, 5% and 0.3% for $\mathcal{S} = 1, 2$ and 3 respectively. Considering that H_0 and H_1 have (μ, σ) being respectively (B, \sqrt{B}) and $(S + B, \sqrt{S + B})$ as in Figure 4.25, one ends up with:

$$\mathcal{S}_{\text{exclu.}} = \frac{S}{\sqrt{S + B}}. \quad (4.10)$$

The same reasoning can be applied to the point of view of a discovery claim, where one is interested in $P(N > \mu[H_1]|H_0)$, i.e. the probability to observe a signal-like realization in the data, if the signal doesn't exist. Assuming the situation sketched in [Figure 4.25](#), one obtains a significance:

$$\mathcal{S}_{\text{disc.}} = \frac{S}{\sqrt{B}}. \quad (4.11)$$

This significance definition can be easily used as a figure of merit when optimizing cuts. The picture may be completed by incorporating systematic uncertainties on the background to $\sigma[H_0]$ and $\sigma[H_1]$, leading to:

$$\mathcal{S}_{\text{disc.}} = \frac{S}{\sqrt{B + f^2 \cdot B^2}} \quad \text{and} \quad \mathcal{S}_{\text{exclu.}} = \frac{S}{\sqrt{S + B + f^2 \cdot B^2}} \quad (4.12)$$

where f represents an estimate of the relative systematic uncertainty on the background.

While both $\mathcal{S}_{\text{disc.}}$ and $\mathcal{S}_{\text{exclu.}}$ sometimes give a reasonable estimate of the true sensitivity of a counting experiment, one should remain conscious of their caveats [\[121\]](#):

1. Their interpretation is not straightforward as it does not tell the physicist what can be expected to be excluded or discovered for a given counting experiment. It remains a 'number of sigmas' and not a physical quantity like an expected excluded cross-section.
2. [Equation \(4.12\)](#) does not take into account that the observed number of events is an integer. By design, it will favor a situation with 0.1 signal events and expected background of 10^{-5} over a situation with 10 signal events and 1 background event, despite the fact that the later will definitely bring more information.
3. It ultimately relies on a Gaussian approximation which can cause significant discrepancies with respect to an accurate computation of $P(N|H)$. For instance, the Poisson and Gaussian tail integrals are significantly different at low means. More specifically, $\mathcal{S}_{\text{disc.}}$ is known to overestimate the true significance while $\mathcal{S}_{\text{exclu.}}$ underestimates it. This is illustrated on [Figure 4.26](#), which compares S/\sqrt{B} to an exact computation.

Caveat 1 can be addressed by reinterpreting \mathcal{S} in terms of excludable (or discoverable) signal strength μ or cross-section σ . Replacing S with $\epsilon \times \sigma \times \mathcal{L}$, and introducing the discovery and exclusion threshold a and b (typically set to 5 and 2 respectively) yields:

$$\sigma_{\text{disc.}} = a \cdot \frac{\sqrt{B + f^2 B^2}}{\epsilon \cdot \mathcal{L}} \quad \sigma_{\text{exclu.}} = \frac{b}{2} \times \frac{b + \sqrt{b^2 + 4(B + f^2 B^2)}}{\epsilon \cdot \mathcal{L}} \quad (4.13)$$

where ϵ and \mathcal{L} are the signal selection efficiency and luminosity respectively.

Caveat 2 can be worked around by imposing a minimum number of background and signal events when computing the figure of merit, by replacing B with $\max(B, 1)$ and ignoring cases with a too low expected signal yields (for instance, the FoM is manually set to 0 when the expected number of signal events is lower than 3).

Finally, to address caveat 3, an empirical fit is proposed in [121] to adjust the shape of the FoM with the accurate computation, as a function of the parameters of the FoM. Alternative significances based on other approaches of the problem also exist and are discussed and compared in [122, 123, 124]. Figure 4.26 shows one of them, sometimes referred to as Asimov Z and based on a likelihood approach, compared to the exact computation.

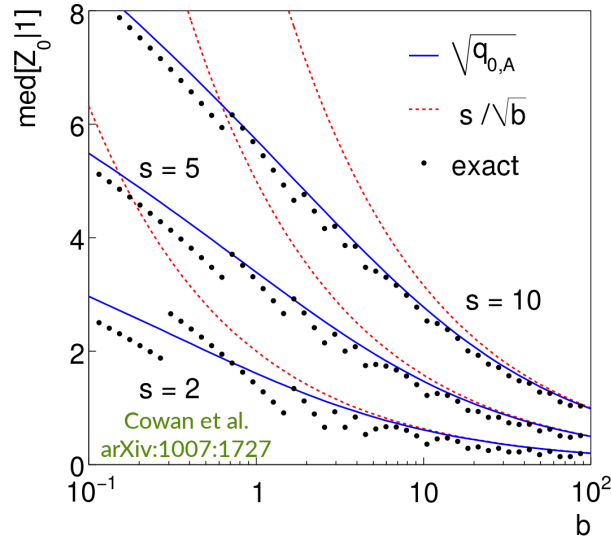


Figure 4.26: Comparison from [124] of the significance (denoted by $\text{med}[Z_0|1]$) when considering S/\sqrt{B} , the Asimov Z significance (denoted by $\sqrt{q_{0,A}}$) and the exact significance computation as a function of B and for $S = 2, 5$ and 10 .

4.5.3 Cut-based signal regions

Optimization procedure

To design the cut-based signal regions of the analysis, the variables are first classified by their individual discriminating power, estimated by taking the maximum FoM ($\mathcal{S}_{\text{exclu.}}$ from Equation (4.12) here) achievable on a few signal benchmarks when scanning the possible cuts. The most discriminating variables are found to be M_T , E_T^{miss} , $E_T^{\text{miss}}/\sqrt{H_T}$ and M_{T2}^W . The variables $\Delta\phi(j_{1,2}, \vec{E}_T^{\text{miss}})$, hadronic top χ^2 , $p_T(\text{lead. } b)$ and the 5th jet (ISR) requirement are also found to be helpful in particular cases or after cutting on the most

discriminant variables. However we found that variables such as H_T^{ratio} , M_{3b} and $M_{\ell b}$ offer lower potential.

On a few signal benchmarks, we then proceed to a n -dimensional optimization of the cuts on these variables. During this procedure, we impose some constraints in the use of the variables. First, either E_T^{miss} or $E_T^{\text{miss}}/\sqrt{H_T}$ should be used, but not both at the same time. We allow tighter cuts on M_T compared to the starting point > 120 GeV, but not tighter than 140 GeV especially to keep enough statistics for the background estimation related aspects.

The optimization of the cuts is done with respect to the exclusion-oriented figure of merit defined in Equation (4.12). To work around cases with very low background or signal yields, i.e. caveat 2, we use $\tilde{B} \equiv \max(B, 1)$ and set the FoM to 0 if $S < 3$. The relative systematic uncertainty on the background is set to vary between 15 and 30% depending on the tightness of the cuts. We also incorporate some feedback of the background estimation that will be described later, by rescaling the 1ℓ top and W +jets contributions with a factor 1.3. This favors the rejection of these backgrounds over the $t\bar{t} \rightarrow \ell\ell$ and rare components.

After optimizing a limited bunch of benchmarks, we test all the sets of cuts on each benchmark of the $(m_{\tilde{t}_1}, m_{\tilde{\chi}_1^0})$ plane and map the most performing set for each benchmark. At this stage the number of set of cuts is large. For the sake of keeping things manageable, we aim to reduce this number by manually clustering similar sets while making sure to not significantly loose in terms of performance.

Results and performances

The resulting signal region definitions are presented on Table 4.4. As announced in Section 4.5.1, $E_T^{\text{miss}}/\sqrt{H_T}$ tends to be preferred at low Δm compared to E_T^{miss} . In the off-shell and stealthy regimes, the ISR jet requirement plays an important role to gain sensitivity, despite the fact that this leaves little room for other cuts given the already low preselection efficiency and the tightness of requiring a 5th jet with high p_T . In the medium and high Δm regimes, cutting on M_{T2}^W provides a good gain in sensitivity because the large E_T^{miss} of the signal is less likely to be decomposable in such a way that it fits the constraints while still yielding a light m_Y mass. At low and medium Δm regimes for the $\tilde{t}_1 \rightarrow t\tilde{\chi}_1^0$ decay channel, the hadronic top χ^2 provides a good alternative or complementary approach to M_{T2}^W for rejecting the $t\bar{t} \rightarrow \ell\ell$ background. For the $\tilde{t}_1 \rightarrow b\tilde{\chi}_1^\pm$ scenario, at low and medium x values, the p_T of the leading b -tagged jet is an important feature, related to the high $\tilde{t}_1 - \tilde{\chi}_1^\pm$ mass gap. Finally, in almost all signal regions, $\Delta\phi(j_{1,2}, \vec{E}_T^{\text{miss}})$ proves to be useful by providing a way to reject the 1ℓ top component where E_T^{miss} is expected

to be close to a b jet.

$\tilde{t}_1 \rightarrow t\tilde{\chi}_1^0$	M_T	E_T^{miss}	$E_T^{\text{miss}}/\sqrt{H_T}$	M_{T2}^W	Hadronic top χ^2	$\Delta\phi(j_{1,2}, E_T^{\text{miss}})$	5th, ISR jet
1) off-shell (loose)	> 125	-	> 8	-	-	-	yes
2) off-shell (tight)	> 130	> 300	-	-	-	-	yes
3) low $m_{\tilde{t}_1}$	> 140	-	> 8	-	< 5	> 0.8	-
4) medium Δm	> 140	> 200	-	> 180	< 3	> 0.8	-
5) high Δm	> 130	> 350	-	> 190	-	-	-

$\tilde{t}_1 \rightarrow b\tilde{\chi}_1^\pm, x = 0.25$	M_T	E_T^{miss}	$E_T^{\text{miss}}/\sqrt{H_T}$	M_{T2}^W	$p_T(\text{lead. } b)$	$\Delta\phi(j_{1,2}, E_T^{\text{miss}})$	5th, ISR jet
1) off-shell	> 120	-	> 9	-	-	> 0.2	yes
2) low Δm	> 120	-	> 6	> 200	> 180	> 0.8	-
3) high Δm	> 120	> 300	-	> 200	> 180	> 0.8	-

$\tilde{t}_1 \rightarrow b\tilde{\chi}_1^\pm, x = 0.50$	M_T	E_T^{miss}	$E_T^{\text{miss}}/\sqrt{H_T}$	M_{T2}^W	$p_T(\text{lead. } b)$	$\Delta\phi(j_{1,2}, E_T^{\text{miss}})$	5th, ISR jet
1) off-shell	> 120	-	> 9	-	-	> 0.2	yes
2) low masses	> 135	-	> 6	> 180	-	> 0.8	-
3) medium Δm	> 140	-	> 7	> 190	> 100	> 0.8	-
4) high Δm	> 120	> 300	-	> 200	> 100	> 0.8	-

$\tilde{t}_1 \rightarrow b\tilde{\chi}_1^\pm, x = 0.75$	M_T	E_T^{miss}	$E_T^{\text{miss}}/\sqrt{H_T}$	M_{T2}^W	$p_T(\text{lead. } b)$	$\Delta\phi(j_{1,2}, E_T^{\text{miss}})$	5th, ISR jet
1) low Δm	> 120	-	> 12	-	-	> 0.8	yes
2) medium Δm	> 130	-	> 10	> 180	-	> 0.8	-
3) high Δm	> 140	> 300	-	> 200	-	> 0.8	-

Table 4.4: Description of the signal regions defined and optimized for the cut-based approach.

Figure 4.27 shows the best performing set across the $(m_{\tilde{t}_1}, m_{\tilde{\chi}_1^0})$ plane as well as the corresponding FoM. While these results are purely based on the FoM, the final choice of the signal region to be used for each benchmark is later done by choosing the minimum expected cross-section upper limit from the CL_s computation.

4.5.4 BDT-based signal regions

For the multivariate approach, several BDT are trained on slices of Δm in the $(m_{\tilde{t}_1}, m_{\tilde{\chi}_1^0})$ space against the $t\bar{t}$ background only. The choice of the variables is driven by an iterative method where variables are added to BDT and kept if the performances are overall significantly improved across different slices of Δm . The performances of the BDTs are quantified by optimizing the cut on the BDT output with respect to a discovery-oriented FoM, considering all the backgrounds and assuming a relative systematic uncertainty of 15%.

The set of variables used are presented on Table 4.5 as function of the decay mode. The definition of the training regions in the $(m_{\tilde{t}_1}, m_{\tilde{\chi}_1^0})$ is then being looked at, noticing that some of the Δm slices can be merged together as the performances of the trainings are similar, essentially because the kinematic is not strongly different when moving from one

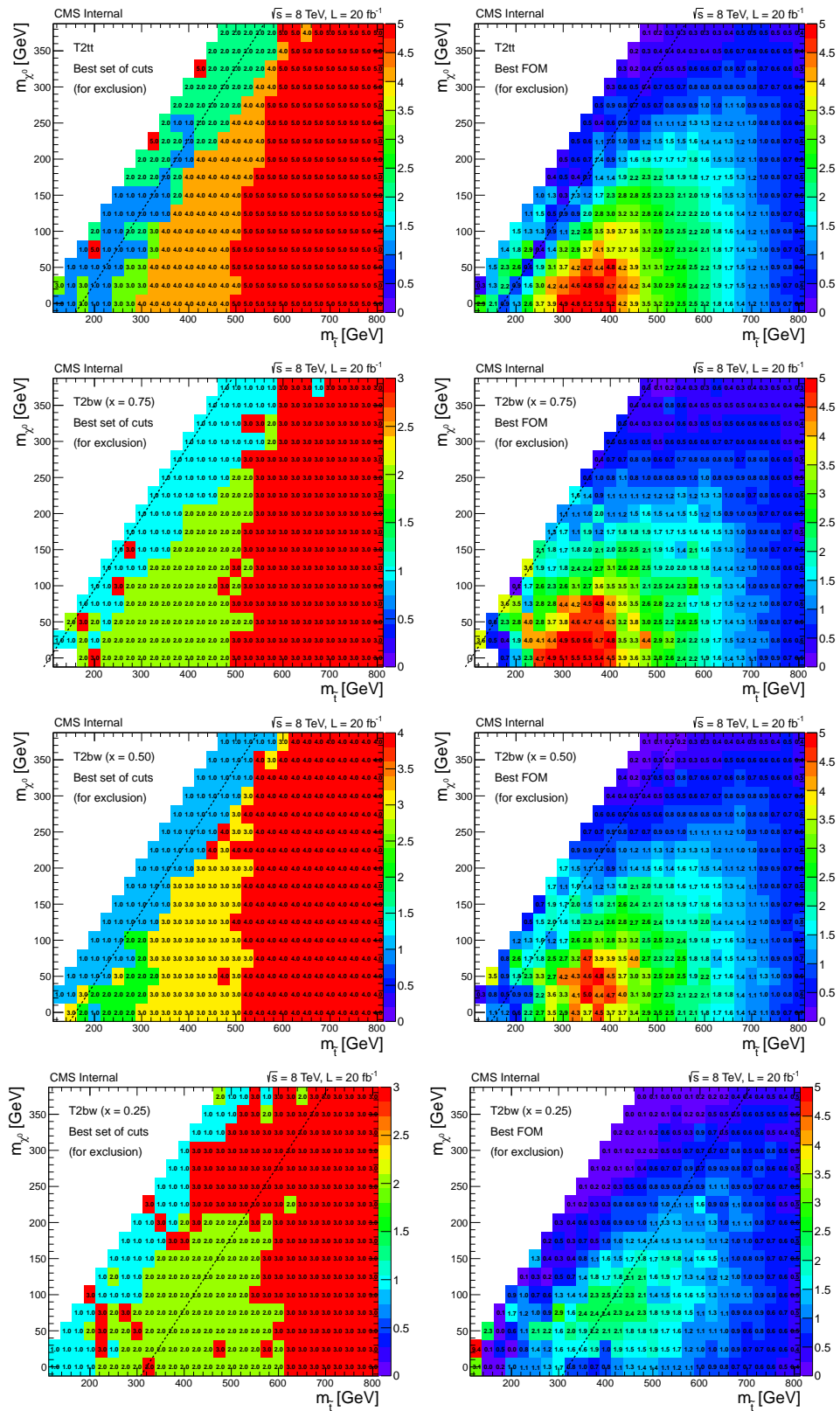


Figure 4.27: Best set of cuts (on the left) and performances in term of FoM_{exclusion} (on the right) for the $\tilde{t}_1 \rightarrow t\tilde{\chi}_1^0$ decay mode (first row) and $\tilde{t}_1 \rightarrow b\tilde{\chi}_1^{\pm}$ decay mode with $x = 0.75$ (second row), 0.50 (third row) and 0.25 (last row).

slice to the other. The optimization of the cut on the BDT output is then performed by iteratively looking at the excluded cross-section after the full procedure explained in the following sections. The cuts are tuned manually to optimize the sensitivity accordingly. Here, because the cross-section regimes lead to different amount of signal statistics, there is sometimes a significant gain in loosening or tightening the cut inside a same training region.

The final definition of the training regions is presented on [Figure 4.28](#). Each number represents a different BDT training. The dashed lines represent the cases when one training region leads to several cuts applied to define signal regions.

Variable	T2TT off-shell	T2TT on-shell	Variable	T2BW $x = 0.25$	T2BW $x = 0.50$	T2BW $x = 0.75$
E_T^{miss}	×	×	E_T^{miss}	×	×	×
H_T^{ratio}	×	×	M_{T2}^W	×	×	×
$p_T(\text{lead. } \ell)$	×	×	$M_{\ell b}$	×	×	×
$\Delta\phi(j_{1,2}, \vec{E}_T^{\text{miss}})$	×	×	M_{3b}	×	×	×
N_{jets}	×	×	$p_T(\text{lead. } \ell)$	×	×	×
$p_T(\text{lead. jet})$		×	$\Delta\phi(j_{1,2}, \vec{E}_T^{\text{miss}})$	×	×	×
$\Delta R(\ell, \text{lead. } b)$		×	N_{jets}	×	×	×
hadronic top χ^2		×	$p_T(\text{lead. } b)$	×	×	
M_{T2}^W		×	$\Delta R(\ell, \text{lead. } b)$		×	
$M_{\ell b}$	×		H_T			×
$p_T(\text{lead. } b)$	×		$p_T(\text{lead. jet})$			×

Table 4.5: List of variables considered for the training of the BDT as function of the decay mode. A \times mark indicates that the variable is used in the final trainings.

4.6 Background estimation

4.6.1 Overview

In this section, we focus on the estimation of the different background contributions. Four kinds of control regions are defined by inverting some of the requirements of the preselection and signal regions, as illustrated on [Figure 4.29](#). Each of these aims to provide a map of signal-free sectors in which to check how good is the modeling of the backgrounds by the Monte-Carlo and perform data-driven estimations.

The M_T -peak control region is defined by looking at events satisfying $50 < M_T < 80$ GeV instead of the signal region M_T requirement. This control region is enriched in

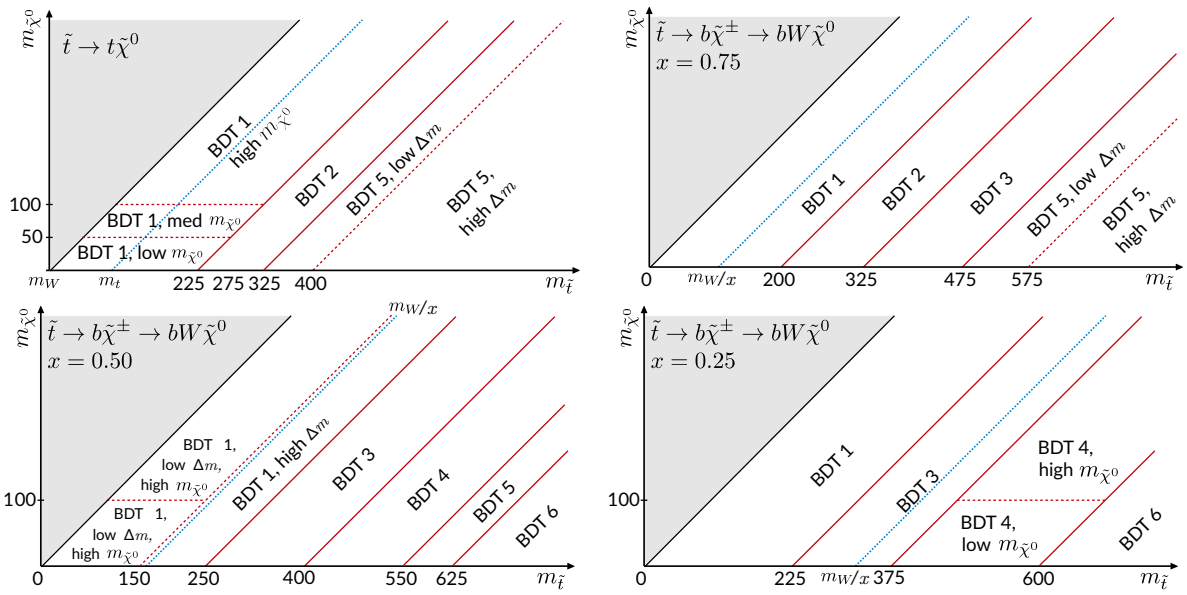


Figure 4.28: Slicing of the $(m_{\tilde{t}_1}, m_{\tilde{\chi}_1^0})$ space to define the training regions of the BDTs. Some training regions are subdivided into subregions where different cuts are applied on the BDT output in order to adapt the sensitivity to the local signal yields.

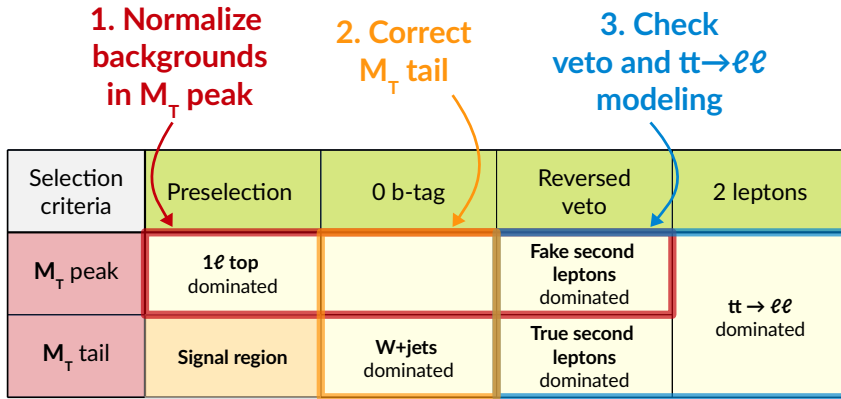


Figure 4.29: Overview of the control regions used in the background estimation method.

1 ℓ top and is used as a well-controlled region in which to normalize the 1 ℓ top, W +jets and $t\bar{t} \rightarrow \ell\ell$ as documented in Section 4.6.2. Without applying any signal region cuts, the proportion of 1 ℓ top in this region is about 85%.

The 0 b -tag control region is defined by requiring no b -tagged jet in the event. This region is enriched in W +jets and 1 ℓ top and is used to control and correct the tail of M_T for these two components as described in Section 4.6.3. While it might seem counterintuitive that 1 ℓ top represents a significant contribution in this region, it can easily be explained by noticing that with a rough 60% b jet efficiency of the b -tagging working point, there is a rough 15% probability that both b jets won't be tagged. Overall, without applying any signal region cuts, the proportion of W +jets and 1 ℓ top in this region is around 60% and 27% respectively.

The 2ℓ control region is designed to control the modeling of the $t\bar{t} \rightarrow \ell\ell$ background category, and is defined by requiring exactly two selected leptons instead of one, at least one jet, and lowering the E_T^{miss} cut to 50 GeV. Additionally, to limit the contribution from Drell-Yan, we veto events where the invariant mass of the dilepton system, $m_{\ell\ell}$, is such that $|m_{\ell\ell} - m_Z| < 15$ GeV. As the notion of M_T peak does not really exist for the $t\bar{t} \rightarrow \ell\ell$ process, the full M_T range is considered. Without applying any signal region cuts, the fraction of $t\bar{t} \rightarrow \ell\ell$ in this region is about 93%.

Finally, the reversed veto control region is defined by requiring exactly one selected lepton and reversing the second lepton veto, effectively asking for an isolated track or τ candidate as defined in Section 4.4.2. This region is intended to control the modeling of the second lepton veto. It is being looked at in both the M_T peak, dominated by fake second leptons in 1ℓ top, and in the M_T tail dominated by true second leptons in $t\bar{t} \rightarrow \ell\ell$. Without applying any signal region cuts, the proportion of 1ℓ top and $t\bar{t} \rightarrow \ell\ell$ is about 45% for each category.

No correction is extrapolated from the 2ℓ and reversed veto control regions to the signal region as the agreement is found to be good. However, systematic uncertainties are derived to assess the level of confidence in the modeling of the $t\bar{t} \rightarrow \ell\ell$ as detailed in Section 4.7.1.

Table 4.6 shows a breakdown of the background contributions in the different control regions at the preselection level.

	M_T -peak	0 b -tag (M_T tail)	reversed veto	2 leptons
1ℓ top	18523 ± 55	1213 ± 14	7030 ± 34	41 ± 2.7
$t\bar{t} \rightarrow \ell\ell$	656 ± 10	382 ± 8	7066 ± 34	9211 ± 39
W +jets	1470 ± 24	2669 ± 33	331 ± 11	2.1 ± 0.9
rare	1209 ± 23	198 ± 7	1093 ± 20	626 ± 15
total SM	21859 ± 66	4462 ± 38	15521 ± 53	9882 ± 42

Table 4.6: Breakdown of the yield of the different background categories in the four control regions without applying any signal region cuts. Uncertainties are statistical only.

4.6.2 Background normalization in the M_T -peak region

The M_T -peak control region, defined as $50 < M_T < 80$ GeV, is the first step of the background estimation method. It is used to normalize the 1ℓ top, W +jets and $t\bar{t} \rightarrow \ell\ell$ components while the rare component is taken directly from Monte-Carlo. It is important to note that this normalization is done for each signal region individually, effectively allowing to absorb disagreements caused by cuts on variables that may not be perfectly

modeled, as well as uncertainties on the jet energy scale, the trigger efficiency, the lepton identification efficiency and the luminosity.

To separate the effect of the second lepton veto, the normalization is done in two steps: first, a scale factor $SF_{\text{pre-veto}}^{\text{peak}}$ is computed before the application of the second lepton veto, subtracting the rare component:

$$SF_{\text{pre-veto}}^{\text{peak}} \equiv \left(\frac{N(\text{data}) - N(\text{rare})}{N(1\ell \text{ top}) + N(W+\text{jets}) + N(t\bar{t} \rightarrow \ell\ell)} \right). \quad (4.14)$$

$SF_{\text{pre-veto}}^{\text{peak}}$ is used to normalize only the $t\bar{t} \rightarrow \ell\ell$ component. Another scale factor, $SF_{\text{post-veto}}^{\text{peak}}$ is used after application of the second lepton veto, subtracting the rare and the corrected $t\bar{t} \rightarrow \ell\ell$ component:

$$SF_{\text{post-veto}}^{\text{peak}} \equiv \left(\frac{N(\text{data}) - N(\text{rare}) - SF_{\text{pre-veto}}^{\text{peak}} \times N(t\bar{t} \rightarrow \ell\ell)}{N(1\ell \text{ top}) + N(W+\text{jets})} \right). \quad (4.15)$$

When applying no signal region cuts, $SF_{\text{pre-veto}}^{\text{peak}}$ and $SF_{\text{post-veto}}^{\text{peak}}$ are equal to (1.06 ± 0.01) and (1.05 ± 0.01) respectively. These values, while not being compatible with 1, can be interpreted as a relatively small disagreement which is attributed to the misknowledge of the previously listed effects. Across the different cut-based signal regions, these scale factors range from 0.8 to 1.4, sometimes only compatible with unity at 3 standard deviations. The magnitude of this effect is attributed to bad modeling of the far tail of some variables in the Monte-Carlo.

4.6.3 M_T -tail correction in the 0**b**-tag region

The 0**b**-tag control region allows to control the tail of M_T for the $W+\text{jets}$ and 1ℓ top components. Before looking at the tail, however, we start by normalizing the background in the M_T peak of this control region, in a similar fashion to what is done in [Section 4.6.2](#). This is done by introducing $SF_{0b\text{-tag}}^{\text{peak}}$, used to normalize the $W+\text{jets}$ and 1ℓ top contributions:

$$SF_{0b\text{-tag}}^{\text{peak}} \equiv \left(\frac{N(\text{data}) - N(\text{rare}) - N(t\bar{t} \rightarrow \ell\ell)}{N(1\ell \text{ top}) + N(W+\text{jets})} \right) \quad (4.16)$$

Without applying any signal cuts, $SF_{0b\text{-tag}}^{\text{peak}}$ is found to be (0.99 ± 0.01) . After normalization to the peak, a clear disagreement in the tail of M_T is observed for $M_T > 100$ GeV between the data and Monte-Carlo, as shown on [Figure 4.30](#). This disagreement is a

known feature also observed by several other analyses [125, 126, 127]. This is an important point of the analysis as it means that the Monte-Carlo needs to be corrected to have a reliable prediction of the 1ℓ top and W +jets in the M_T tail.

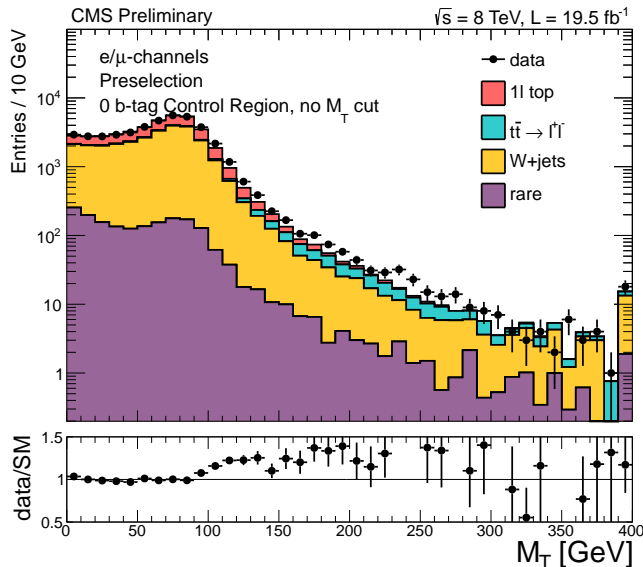


Figure 4.30: Data/MC comparison on the full M_T distribution in the 0 b -tag control region at preselection level, after propagation of $SF_{0b\text{-tag}}^{\text{peak}}$. A clear discrepancy is visible for $M_T > 100$ GeV.

One can investigate the origin of the disagreement by first getting a better idea from the Monte-Carlo simulation of what is causing 1ℓ top and W +jets events to reach the tail of M_T . The resolution of M_T is strongly related to both the resolution in energy of $E_T^{\vec{miss}}$, and its $\Delta\phi$ with the lepton. The relative resolutions of $E_T^{\vec{miss}}$ and $\Delta\phi$ are investigated in the Monte-Carlo, defined as the ratio of the reconstructed quantity versus the generated quantity, constructed from the generated prompt neutrinos in the event. Figure 4.31 shows the distributions of the relative resolutions of $E_T^{\vec{miss}}$ and $\Delta\phi$ as function of M_T for the 1ℓ top background and their mean values for each background.

The results of this quick investigation tends to point out that the M_T tail for the 1ℓ top, W +jets and rare backgrounds originates more from the misreconstruction of the magnitude of the $E_T^{\vec{miss}}$ rather than its direction. Small features are however observed in the $\Delta\phi$ spectra which can originate from other sources of genuine $E_T^{\vec{miss}}$ in the event such as neutrinos inside b jets.

So far, the method used to correct the discrepancy is to compute ad-hoc scale factors using a template fit that estimate separately the contribution of 1ℓ top and W +jets backgrounds from the data. To do this, we use M'_{bb} which was found to have a good discriminating power between the two process categories and being well described in the peak of M_T , as shown on Figure 4.32.

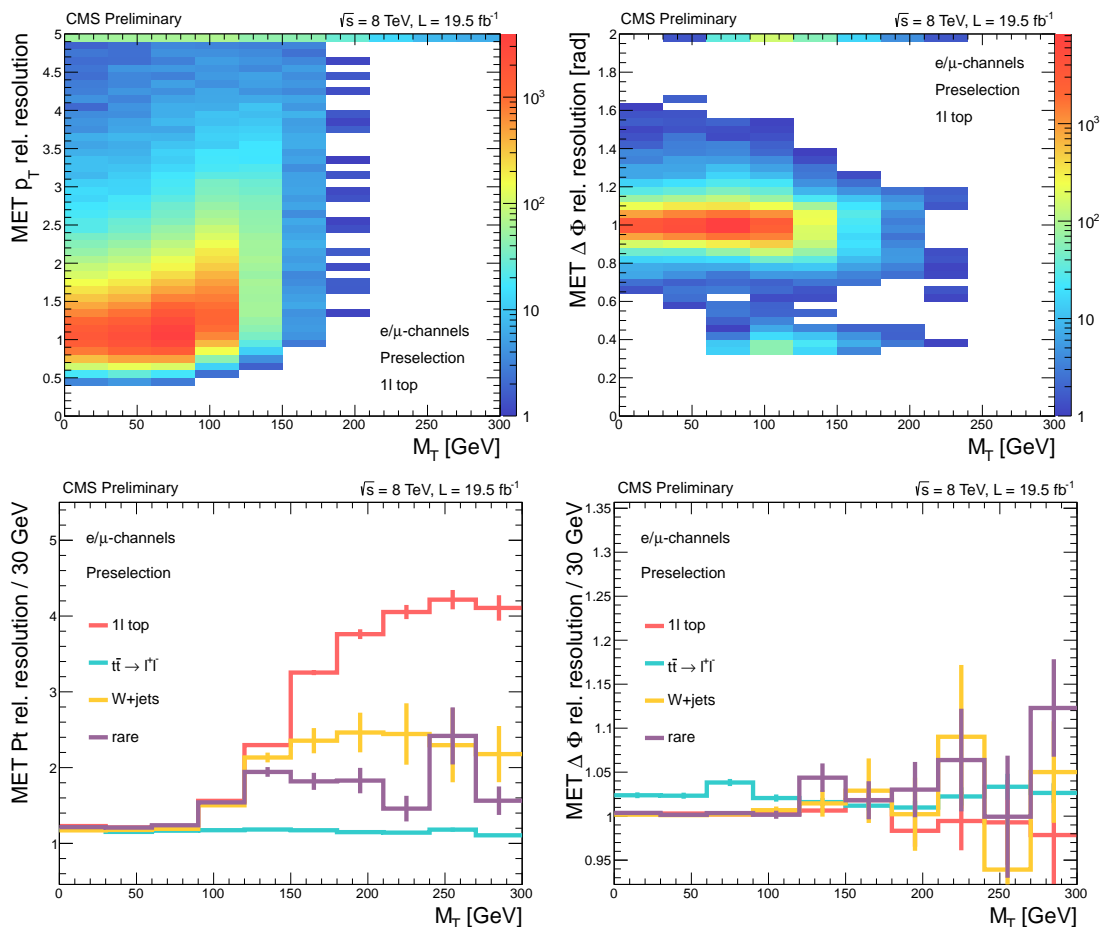


Figure 4.31: E_T^{miss} and $\Delta\phi$ relative resolutions as function of M_T , using the generated E_T^{miss} from neutrinos coming from a W boson, on top showing the full 2 dimensional distribution and on bottom showing the evolution of the mean resolution for each background. Error bars correspond to the uncertainties on the mean estimation.

The method is implemented using the ROOFIT toolbox [128] with the Minuit2 implementation of the MIGRAD minimizer algorithm. The normalization of the 1ℓ top and W +jets components are free parameters translated in term of scale factors, $SF_{1\ell \text{ top}}$ and $SF_{W+\text{jets}}$, while the normalization of the $t\bar{t} \rightarrow \ell\bar{\ell}$ and rare components are taken from the Monte-Carlo and constrained with a 20% uncertainty during the fit process. To validate the method, a closure test is performed by generating toy data from the Monte-Carlo where arbitrary scale factors were injected. The estimated scale factors are then compared to the input scale factors. A very good linearity is found for scale factors varying from 0.10 to 3.

The fit is performed both in the M_T peak and tail regions and we extract $SFR = SF^{\text{tail}}/SF^{\text{peak}}$ for both processes, representing the discrepancy in the tail independently from the peak normalization. Different sources of systematic uncertainty are considered: the jet energy scale, the normalization of the rare and $t\bar{t} \rightarrow \ell\bar{\ell}$ background, the

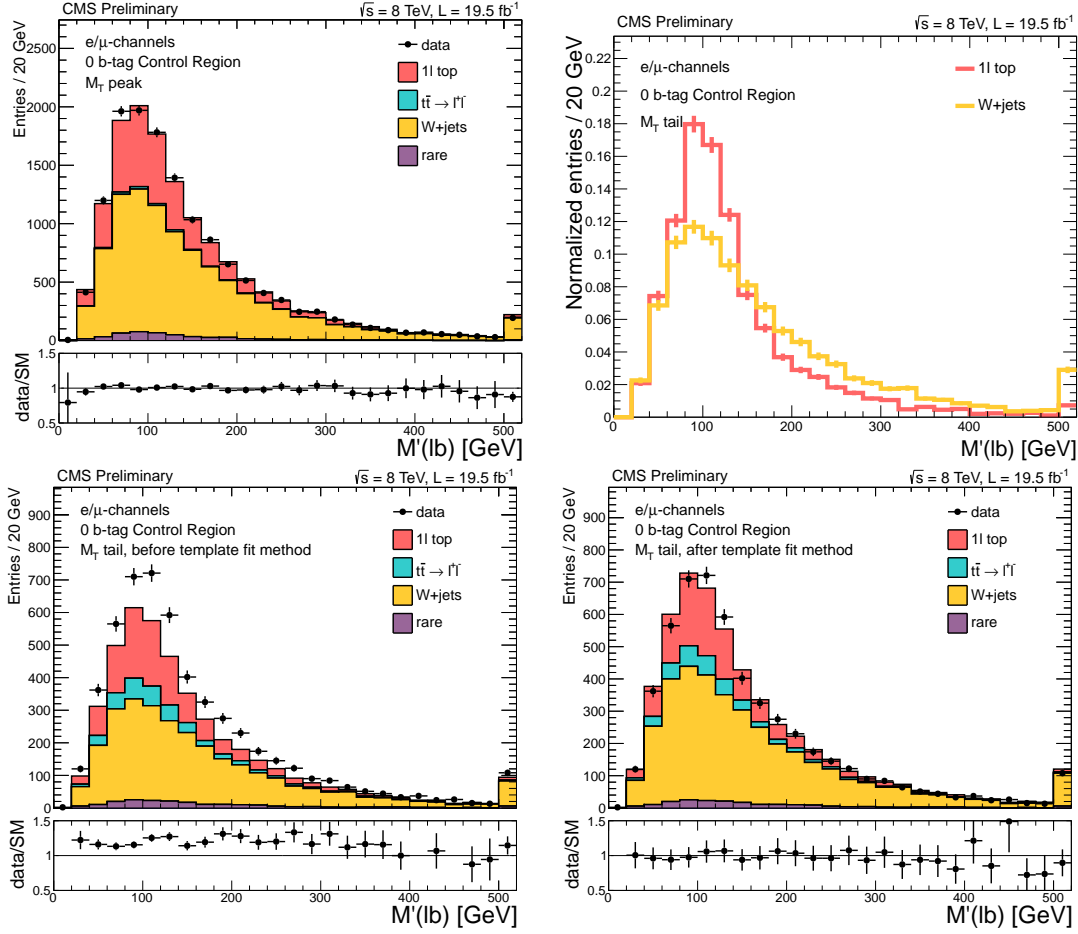


Figure 4.32: Distribution of M'_b in the 0 b -tag control region, data/MC comparison in the M_T peak (top left), superimposed and normalized 1 l top and W +jets components in the M_T tail (top right), data/MC comparison in the M_T tail before correction of the Monte-Carlo (bottom left) and after correction (bottom right). On the bottom right, the uncertainties on the scale factors are propagated in the ratio.

Monte-Carlo statistics, the choice of the minimizer algorithm, the choice of the initial fit conditions, the generator setup for $t\bar{t}$ (using POWHEG or MADGRAPH, varying the matching parameters, RGE scale, top mass, applying or not the top p_T reweighting). The most important sources are the Monte-Carlo statistics (leading to 11% of relative uncertainty on SFR), the generator scale (9%) and the jet energy scale. A conservative 20% is used as relative systematic uncertainty.

Without applying any signal region cuts, $SFR_{1l \text{ top}}$ and SFR_{W+jets} are found to be $(1.04 \pm 0.16(\text{stat.}) \pm 0.21(\text{syst.}))$ and $(1.33 \pm 0.10(\text{stat.}) \pm 0.27(\text{syst.}))$ respectively. The plot on bottom right of Figure 4.32 illustrates the impact on the M'_b data/MC comparison after propagating the scale factors.

For the cut-based signal regions, we use the scale factors derived from a single M_T cut associated to the signal region as shown on Figure 4.33. It is found that the $SFR_{1l \text{ top}}$

increases as function of the M_T cut applied while $SFR_{W+\text{jets}}$ is relatively constant around 1.33. This is a clear indication that a separate treatment is necessary between these two background categories. To cover possible correlation between the SFR and E_T^{miss} or $E_T^{\text{miss}}/\sqrt{H_T}$, the computation of the scale factors is also studied for single E_T^{miss} or $E_T^{\text{miss}}/\sqrt{H_T}$ cuts, as shown on Figure 4.34. The final scale factors applied for a given signal region are the SFR derived for the single M_T cut associated to that signal region, to which we quadratically add the uncertainty extracted from the SFR computed with the single E_T^{miss} or $E_T^{\text{miss}}/\sqrt{H_T}$ cut associated to that signal region.

For the BDT signal regions, to be as close as possible to the kinematic of the BDT tails, we choose cuts on each BDT outputs such as at least 25% of the background is still selected and apply the template fit method in that region. Two common scale factors to be applied to each BDT are then computed by averaging across all the trainings. The values found are $SFR_{1\ell \text{ top}} = (1.38 \pm 0.61)$ and $SFR_{W+\text{jets}} = (1.21 \pm 0.36)$.

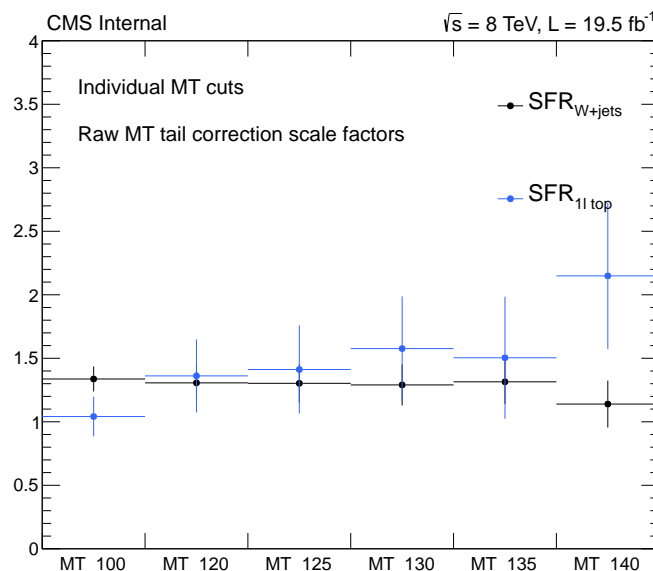


Figure 4.33: Template fit results for individual cuts on M_T after preselection. The uncertainties shown are statistical only.

4.6.4 Control of the $t\bar{t} \rightarrow \ell\bar{\ell}$ component and second lepton veto

The 2-lepton and reversed veto control regions allow to check for the good modeling of the $t\bar{t} \rightarrow \ell\bar{\ell}$ background and the second lepton veto definition. In the 2 lepton control region, M_T is defined using the leading lepton and ignoring the second one. The M_T -peak of the reversed veto control region is dominated by $1\ell \text{ top}$ where a fake second lepton is reconstructed while the M_T -tail is dominated by $t\bar{t} \rightarrow \ell\bar{\ell}$ with a true second lepton. As

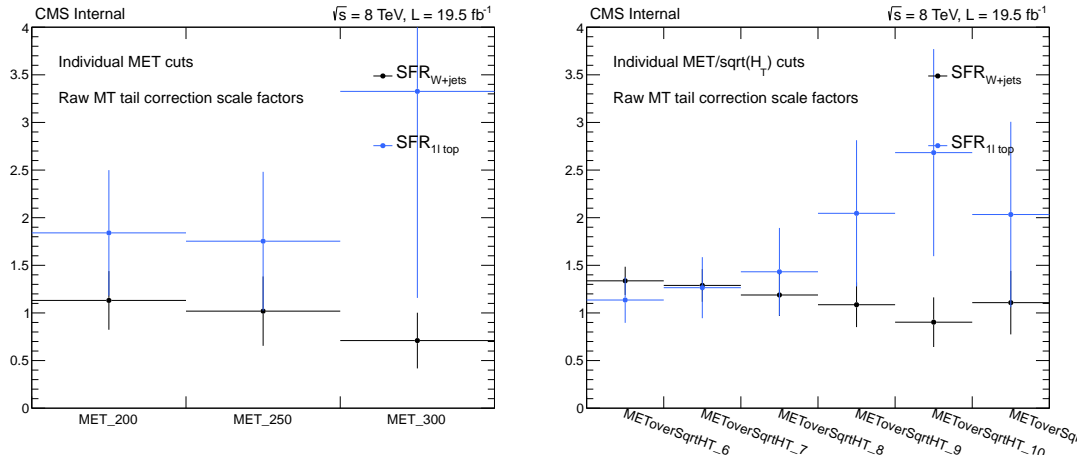


Figure 4.34: Template fit results for individual cuts on E_T^{miss} (left) and $E_T^{\text{miss}}/\sqrt{H_T}$ (right) after preselection + $M_T > 100$ GeV. The uncertainties shown are statistical only.

for the M_T -peak normalization, we introduce scale factors to normalize the backgrounds in the peak of M_T and then quantify the agreement in the tail.

In the reversed veto region, we define $SF_{\text{rev-veto}}^{\text{peak}}$ in a similar fashion as $SF_{\text{post-veto}}^{\text{peak}}$, to control the fake-dominated region, and $SF_{\text{rev-veto}}^{\text{tail}}$ to control region dominated by true second lepton, after propagation of all the relevant scale factors including $SFR_{1\ell \text{ top}}$ and $SFR_{W+\text{jets}}$. Without applying any signal region cuts, we find $SF_{\text{rev-veto}}^{\text{peak}} = (1.18 \pm 0.03)$ and $SF_{\text{rev-veto}}^{\text{tail}} = (1.07 \pm 0.02)$. The relatively large value of $SF_{\text{rev-veto}}^{\text{peak}}$ is interpreted as a mismodeling of the fake rate of the lepton veto by the Monte-Carlo. Despite being not compatible with unity, this SF is not used to compute the prediction in the signal region because its effect is already included in $SF_{\text{post-veto}}^{\text{peak}}$. The value of $SF_{\text{rev-veto}}^{\text{tail}}$ also manifests a discrepancy in the lepton veto selection efficiency. Despite the fact that this scale factor is not propagated to the signal region, a systematic is later introduced to cover this effect.

In the 2 leptons control region, we define $SF_{2\ell}$ and $SF_{2\ell}^{\text{tail}}$ to control respectively the whole M_T distribution and the tail of it. Without applying any signal region cuts, we find $SF_{2\ell} = (0.96 \pm 0.01)$ and $SF_{2\ell}^{\text{tail}} = (1.01 \pm 0.02)$ showing therefore a good modeling of M_T for this background.

Figure 4.35 presents the full M_T distributions for the reversed veto and two leptons control regions where a good agreement is found after propagating the scale factors $SF_{\text{pre-veto}}^{\text{peak}}$, $SF_{\text{rev-veto}}^{\text{peak}}$, $SFR_{1\ell \text{ top}}$ and $SFR_{W+\text{jets}}$ where it is relevant. Another important check in the 2 leptons control region is the jet multiplicity modeling of $t\bar{t} \rightarrow \ell\ell$ as the four jets requirement corresponds to two additional jets coming from radiations or pile-up for this background. Figure 4.36 presents the distribution of the number of selected jets after application of $M_T > 100$ GeV, which is found in good agreement.

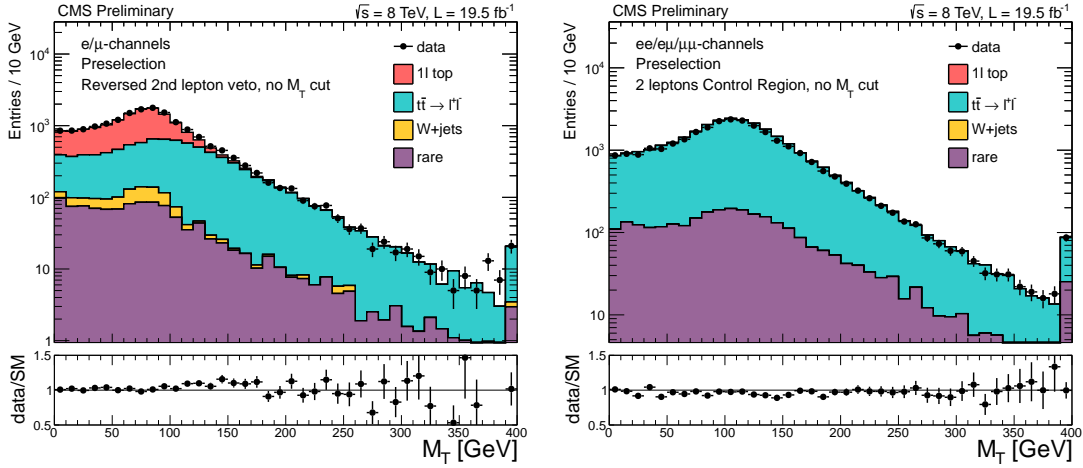


Figure 4.35: Full M_T distributions for the reversed veto control region (on the left) and two leptons control region (on the right). On the left, $SF_{\text{pre-veto}}^{\text{peak}}$, $SF_{\text{rev-veto}}^{\text{peak}}$, $SFR_{1l \text{ top}}$ and $SFR_{W+\text{jets}}$ are propagated. On the right, no scale factors are applied.

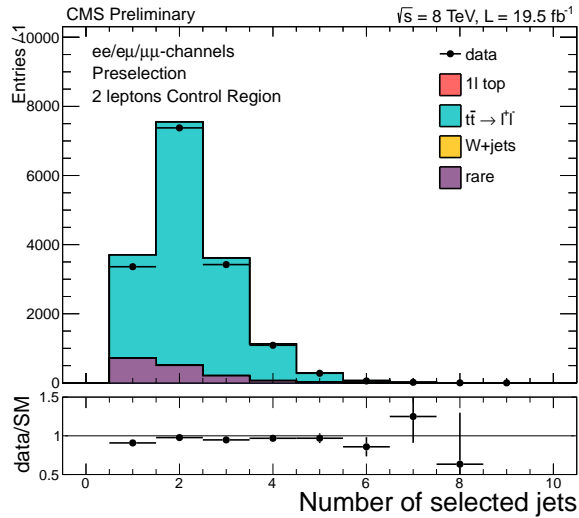


Figure 4.36: Distribution of the number of selected jets in the two leptons control region after applying $M_T > 100$. No scale factor is applied on the distribution.

4.6.5 Control of variables at preselection level

The modeling of each variable is validated in each control region without applying any signal region cut yet, and by propagating the relevant scale factors discussed before. Figure 4.37 shows a subset of the control plots in particular for the variables M_T , E_T^{miss} and M_{T2}^W . Overall, a good agreement is observed. Nevertheless, it can be criticized that some trends seem to be present in the data/MC for instance in the tail of E_T^{miss} and M_{T2}^W in the M_T peak region, indicating a small mismodeling of these variables by the simulation. However, as the final background estimation is performed for each signal region independently and after application of the cuts, these disagreements are expected

to be absorbed during the computation of $SF_{\text{pre-veto}}^{\text{peak}}$ and $SF_{\text{post-veto}}^{\text{peak}}$.

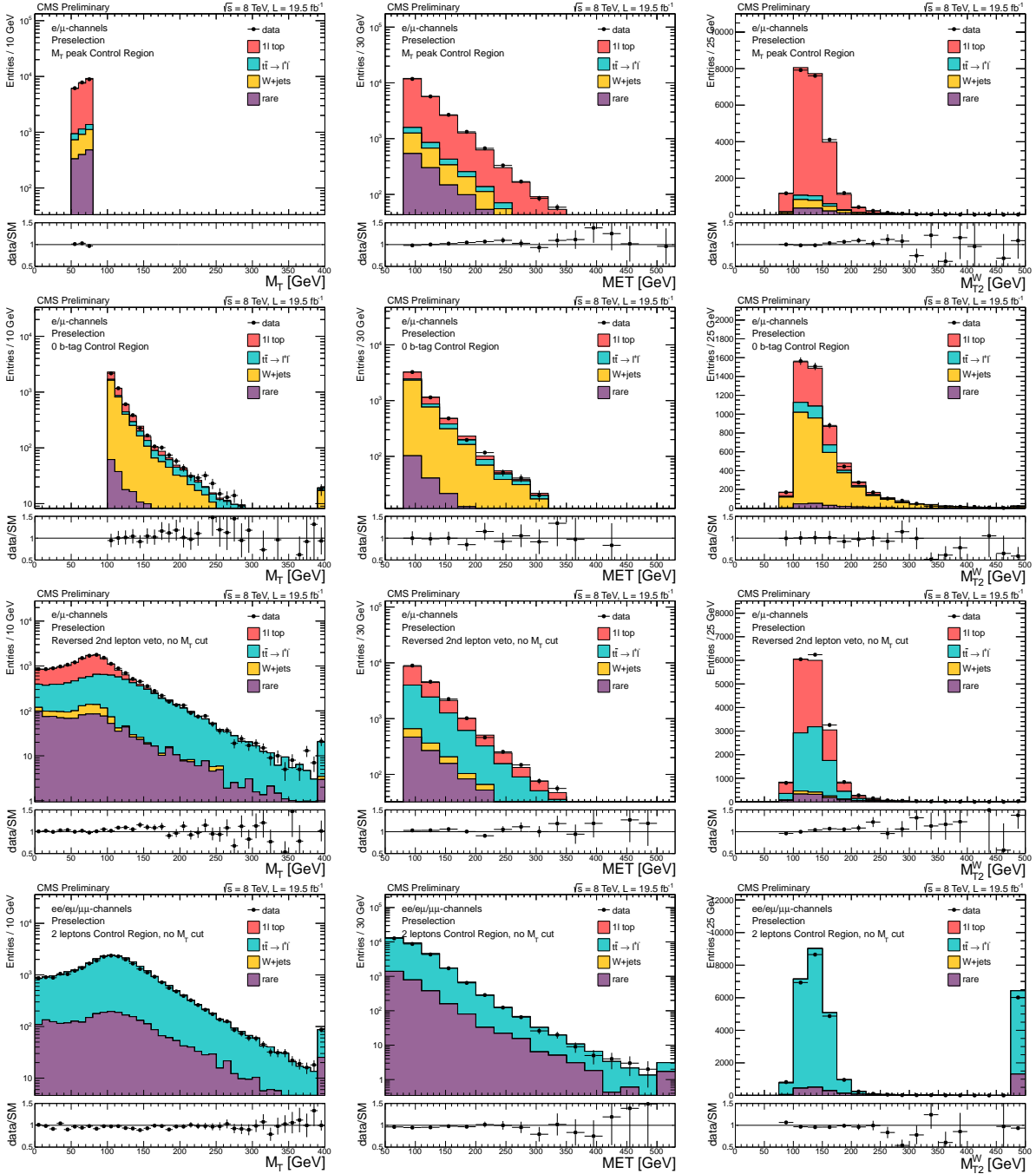


Figure 4.37: A few control plots, showing the data/MC comparison for M_T (left column), E_T^{miss} (middle column) and M_{T2}^W (right column) in the different control regions: M_T -peak (first row), $0b$ -tag (second row), reversed veto (third row) and 2 leptons (fourth row). The M_T -peak normalization and M_T -tail correction scale factors are propagated where relevant.

4.6.6 Background prediction in the signal regions

The background prediction in a given signal region is obtained by taking the Monte-Carlo yield in the M_T -tail and propagating $SF_{\text{pre-veto}}^{\text{peak}}$ to the $t\bar{t} \rightarrow \ell\ell$ component and $SF_{\text{post-veto}}^{\text{peak}}$ to the 1ℓ top and W +jets component. The 1ℓ top and W +jets are also corrected with $SFR_{1\ell \text{ top}}$ and $SFR_{W+\text{jets}}$ respectively. The prediction for the rare component is directly the Monte-Carlo yield in M_T -tail. Equation (4.17) to Equation (4.20) summarize the computation of the prediction. The procedure is repeated for each signal region as all the scale factors involved are signal-region dependent. As an illustration, Table 4.7 shows the comparison between the raw Monte-Carlo and the prediction obtained at preselection level, while Table 4.8 presents in particular the predictions for the cut & count approach for the $\tilde{t}_1 \rightarrow t\tilde{\chi}_1^0$ mode.

$$N_{\text{tail}}^{\text{pred}}(1\ell \text{ top}) = N_{\text{tail}}^{\text{MC}}(1\ell \text{ top}) \times SF_{\text{post-veto}}^{\text{peak}} \times SFR_{1\ell \text{ top}} \quad (4.17)$$

$$N_{\text{tail}}^{\text{pred}}(W+\text{jets}) = N_{\text{tail}}^{\text{MC}}(W+\text{jets}) \times SF_{\text{post-veto}}^{\text{peak}} \times SFR_{W+\text{jets}} \quad (4.18)$$

$$N_{\text{tail}}^{\text{pred}}(t\bar{t} \rightarrow \ell\ell) = N_{\text{tail}}^{\text{MC}}(t\bar{t} \rightarrow \ell\ell) \times SF_{\text{pre-veto}}^{\text{peak}} \quad (4.19)$$

$$N_{\text{tail}}^{\text{pred}}(\text{rare}) = N_{\text{tail}}^{\text{MC}}(\text{rare}) \quad (4.20)$$

	Raw MC	Prediction
1ℓ top	5970 ± 31	6526 ± 1632
$t\bar{t} \rightarrow \ell\ell$	2117 ± 18	2253 ± 229
W+jets	477 ± 13	669 ± 364
rare	490 ± 13	490 ± 245
Total SM	9055 ± 41	9940 ± 1666

Table 4.7: Background prediction at the preselection + $M_T > 100$ GeV level. The raw MC uncertainties are only coming from the Monte-Carlo sample statistics while the uncertainties on the prediction include all the effects discussed in Section 4.7.1.

	Off-shell loose	Off-shell tight	Low Δm	Medium Δm	High Δm
1ℓ top	4.32 ± 1.69	0.15 ± 0.20	28.18 ± 13.71	2.26 ± 1.28	0.00 ± 0.00
$t\bar{t} \rightarrow \ell\ell$	29.07 ± 7.58	8.65 ± 4.16	130.01 ± 11.29	4.86 ± 1.86	2.20 ± 1.16
W+jets	0.87 ± 0.82	0.75 ± 0.79	6.73 ± 4.19	0.85 ± 0.83	0.00 ± 0.00
rare	4.26 ± 2.35	1.86 ± 1.15	13.97 ± 7.21	2.69 ± 1.43	1.22 ± 0.78
total SM	38.53 ± 8.38	11.40 ± 4.40	178.90 ± 21.82	10.66 ± 2.60	3.42 ± 1.40

Table 4.8: Background predictions for the signal regions of the cut & count approach targeting the $\tilde{t}_1 \rightarrow t\tilde{\chi}_1^0$ decay mode. Uncertainties correspond to all systematics described in Section 4.7.1

4.7 Systematic uncertainties

This section describes the sources of systematic uncertainties that are considered for the background and the signal.

4.7.1 Systematic uncertainties on the background

Several sources of systematic uncertainties are considered for the background, the most important ones being from the M_T -peak normalization, the M_T -tail correction and the $t\bar{t} \rightarrow \ell\ell$ modeling of the M_T tail.

Modeling of $t\bar{t} \rightarrow \ell\ell$ in M_T tail

As discussed in Section 4.6.4, the modeling by the Monte-Carlo of the M_T tail of the $t\bar{t} \rightarrow \ell\ell$ background is found to be good in the 2 leptons and reversed veto control regions. As it is a major background of the analysis, a systematic uncertainty is nevertheless asserted to quantify the trust in the Monte-Carlo on a per-signal-region basis.

To do this, one wants to probe the 2 leptons and reversed veto control regions as close as possible of the signal region. However, as the signal region cuts are sometimes quite tight, the remaining statistics in these control regions is too low and doesn't allow a reasonable check of the distributions. To work around this problem while still probing the tail of M_T near the signal region, we define loosened cuts to check these scale factors with more statistics. These cuts are designed by requiring to have at least 30 events remaining in the tail of M_T for the 2 lepton control region.

For each of the relaxed control regions, we compute the value of $SF_{2\ell}^{\text{tail}}$ and $SF_{\text{rev-veto}}^{\text{tail}}$ to quantify the agreement between data and simulations in the tail of M_T . An envelope is then computed for each signal region to account for the spread of the scale factors for each of the associated control regions. For the cut-based signal regions, this leads to a relative uncertainty on the total background yield varying from 1.5 to 35%. For the BDT signal regions, this relative uncertainty is between 7 and 40%.

Second lepton veto efficiency

The uncertainty on the efficiency of the second lepton veto is propagated to the fraction of $t\bar{t} \rightarrow \ell\ell$ events that have a second lepton in the acceptance. For the isolated track veto, this is defined as having a second generated e/μ or a one prong $\tau \rightarrow h$ with $p_T >$

5 or 10 GeV, respectively, with $|\eta| < 2.4$. This fraction is between 50-70% for all signal regions. The uncertainty for these events is 6% and is obtained from tag-and-probe studies [129]. Regarding the τ candidates, the events considered are those with a hadronic τ in the acceptance, with true visible transverse energy > 20 GeV in $|\eta| < 2.4$. This fraction is about 10 \sim 20% of the total. The uncertainty on the efficiency of the τ -ID algorithm is 7%, taken from τ group studies [111].

Uncertainty on $SFR_{1\ell \text{ top}}$ and $SFR_{W+\text{jets}}$

As described in Section 4.6.3, the M_T -tail correction scale factors for 1ℓ top and W +jets are computed with an uncertainty coming from statistics in the $0b$ -tag control region and systematic effects from the template fit method itself. This uncertainty is propagated to the total background yield uncertainty and is one of the major contribution for the signal regions with a large remaining fraction of 1ℓ top. For the cut-based signal regions, this corresponds to a relative uncertainty on the total background ranging from 0 to 15%, and up to 17% for the BDT signal regions.

Statistic uncertainty in M_T peak

The M_T -peak normalization scale factors are an important part of the background estimation procedure, but are nevertheless limited by the statistics available in the peak region. Therefore, the $SF_{\text{pre-veto}}^{\text{peak}}$ and $SF_{\text{post-veto}}^{\text{peak}}$ scale factors come associated with an uncertainty, dominated by the event count of data. This uncertainty is propagated to the prediction in the tail. This leads to a relative uncertainty on the total background ranging from 2 to 15% for the cut-based signal regions and between 3 and 40% for the BDT signal regions.

Other sources of systematic uncertainties

Other sources of uncertainties are taken into account though being small compared to the ones described in the previous subsections:

- To cover the modeling of ISR and FSR jets, the N_{jets} distribution is studied in the 2 leptons control region. An uncertainty of 2% is asserted on the $t\bar{t} \rightarrow \ell\ell$ background from this check.
- To account for possible mismodeling of the relative proportions of the backgrounds, the 1ℓ top component cross-section is varied by 10% while the W +jets cross-section is varied by 50% during the background estimation procedure.

- As it is difficult to design a control region for the rare category, in part due to the variety of processes it contains, its contribution is taken directly from MC. We however put a conservative 50% uncertainty in the rate of this category.
- The Monte-Carlo statistics available in the M_T tail being limited, it also contributes to the systematic uncertainty on the final prediction.

Summary of background uncertainties

Table 4.9 shows a breakdown of the different systematic uncertainties that are considered, at preselection level and the range of them for the two kinds of signal regions. The relative importance of the individual systematics varies depending on the signal regions as the composition of the backgrounds itself varies: at preselection level, the importance of the $SFR_{1\ell \text{ top}}$ uncertainty is high as the 1ℓ top component is still large. However for some signal regions, the $t\bar{t} \rightarrow \ell\ell$ is the dominant contribution and the uncertainty from the M_T -tail modeling becomes the leading systematic source.

	Preselection + $M_T > 100$ GeV	Cut-based signal regions	BDT signal regions
$t\bar{t} \rightarrow \ell\ell$ (M_T -tail modeling)	1.6	2-35	7-40
$t\bar{t} \rightarrow \ell\ell$ (jets modeling)	1.1	1-4	0.5-4
$t\bar{t} \rightarrow \ell\ell$ (2nd lepton veto)	1.2	0-4	1-4
$SFR_{W+\text{jets}}$ uncertainty	1.4	0-6	0-5
$SFR_{1\ell \text{ top}}$ uncertainty	16.4	0-15	0-17
M_T -peak SF uncertainties	0.7	2-15	3-40
Cross-sections and MC stat	1.9	7-48	7-47
total	16.8	12-50	25-60

Table 4.9: Summary of the relative uncertainties (in %) at preselection+ $M_T > 100$ GeV and range of relative uncertainties with respect to the total predicted background yield for cut-based signal regions and BDT signal regions.

4.7.2 Systematic uncertainties on the signal

While the background prediction is dominated by data-driven systematic uncertainties, the signal uncertainty sources are more related to the confidence in the different elements of the construction of the Monte-Carlo samples and algorithms used.

The limited available statistics of the signal sample leads to a maximal 2% uncertainty. The integrated luminosity is known with a precision of 2.2% and is propagated to the uncertainty of the yield. The trigger efficiency used in the very first steps of the selection

is known with a precision of 3%. The lepton identification and isolation efficiency are observed to be consistent between data and Monte-Carlo within an envelope of 5%.

The jet energy scale uncertainty is studied by varying the jet energy corrections within their $\pm 1\sigma$ uncertainty before the jet selection. The variation is properly propagated into the E_T^{miss} value. During the process, we also assume a 10% uncertainty on the unclustered energy defined as $(E_T^{\text{miss}} + \sum_{\text{jets}} \vec{p} + \sum_{\text{leptons}} \vec{p})$ where jets and leptons are selected with looser p_T and $|\eta|$ requirements. This effect leads to a maximum 10% uncertainty on the signal yields.

The uncertainty on the reshaping of the b -tagging discriminant is also considered by varying the technique within the $\pm 1\sigma$ uncertainty before the application of b -tagging requirements. This leads to a 3% uncertainty on the signal yields.

The uncertainty on the ISR jets reweighting applied on signal is taken from data/MC scale factors derived from the analysis of events with high $t\bar{t} \rightarrow \ell\ell$ purity. The scale factors depends on the p_T recoil of the system. They are varied within their uncertainties and lead to a maximum variation of 8 and 10% on the signal yield, depending on the decay mode.

Finally, the uncertainty on PDF are calculated, following the PDF4LHC prescription, using the CT10, NNPDF 2.1, and MSTW2009 PDF sets [130]. The impact on the signal efficiency is about 5%.

4.8 Signal contamination handling

Signal contamination occurs when a significant fraction of signal events is present in the control regions. While it doesn't affect the predicted yield for the background-only hypothesis (H_0), a significant contamination can bias the data-driven aspects of the background estimation when predicting the expected yield under the signal hypothesis (H_1). As a consequence, it leads to an overestimation of the expected background under the signal hypothesis, therefore increasing the probability to incorrectly reject the signal hypothesis (type II error).

The signal contamination level is studied across the $(m_{\tilde{t}_1}, m_{\tilde{\chi}_1^0})$ plane by computing the $C \equiv S/B$ in the M_T -peak control region and 0 b -tag control region and comparing it to the signal purity, $P \equiv S/B$, in the signal region:

$$R \equiv \frac{C}{P} = \frac{(S/B)_{\text{control region}}}{(S/B)_{\text{signal region}}} \quad (4.21)$$

This ratio R is found to be sometimes higher than an arbitrary threshold value of $\sim 15\text{-}20\%$. This is especially true when considering the low Δm region of the $(m_{\tilde{t}_1}, m_{\tilde{\chi}_1^0})$ plane, as the signal is likely to get smaller values of M_T and the b jets are less likely to be selected or correctly b -tagged as their momenta decrease. This is illustrated on [Figure 4.38](#) which shows the differences in shape of M_T and b -tagged jet multiplicity for two benchmarks of the $\tilde{t}_1 \rightarrow t\tilde{\chi}_1^0$ decay mode.

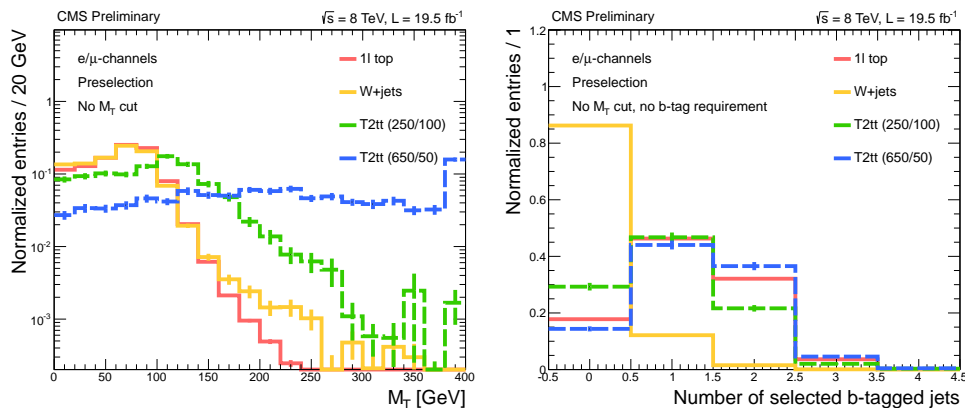


Figure 4.38: Illustration of the signal contamination evolution using two signal examples T2TT (250/100) and T2TT(650/50). The low Δm benchmark, T2TT (250/100), has 30% of events with 0 b -tagged jets and a large fraction of events at low M_T .

We conclude that the signal contamination can not be neglected. One needs therefore to correct the modeling of the H_1 hypothesis by performing a different background estimation \tilde{B} compared to the H_0 hypothesis.

To do this, the data-driven aspects are corrected by including the signal when computing the scale factors for the M_T -peak normalization and M_T -tail correction. In the case of $SF_{\text{pre-veto}}^{\text{peak}}$ and $SF_{\text{post-veto}}^{\text{peak}}$, the scale factors are corrected by subtracting also the signal component to the data when normalizing the 1ℓ top, W +jets and $t\bar{t} \rightarrow \ell\ell$ components:

$$\tilde{S}F_{\text{pre}}^{\text{peak}} \equiv \left(\frac{N(\text{data}) - N(\text{rare}) - N(\text{signal})}{N(1\ell \text{ top}) + N(W+\text{jets}) + N(t\bar{t} \rightarrow \ell\ell)} \right), \quad (4.22)$$

$$\tilde{S}F_{\text{post}}^{\text{peak}} \equiv \left(\frac{N(\text{data}) - N(\text{rare}) - N(\text{signal}) - \tilde{S}F_{\text{pre}}^{\text{peak}} \times N(t\bar{t} \rightarrow \ell\ell)}{N(1\ell \text{ top}) + N(W+\text{jets})} \right). \quad (4.23)$$

In the case of the M_T -tail correction scale factors, they are corrected by including the signal contribution to the rare category before fitting the 1ℓ top and W +jets components to the data using the template fit method. We however constrain, a posteriori to the fit, $\tilde{S}FR_{1\ell \text{ top}}$ to be ≥ 1 .

The corrected background \tilde{B} is computed as described in [Equation \(4.17\)](#) to [Equa-](#)

tion (4.20) using the corrected scale factors. As the correction depends on the signal, it has to be performed on a per-benchmark basis. However, as it is a CPU intensive task, it is done only with a step of 50 GeV instead of the 25 GeV of the signal samples. The background prediction for other benchmarks is corrected using an interpolation of the ratio \tilde{B}/B across the $(m_{\tilde{t}_1}, m_{\tilde{\chi}_1^0})$ plane. Figure 4.39 shows the obtained ratio \tilde{B}/B for each signal type, showing an effect up to 25% at low masses.

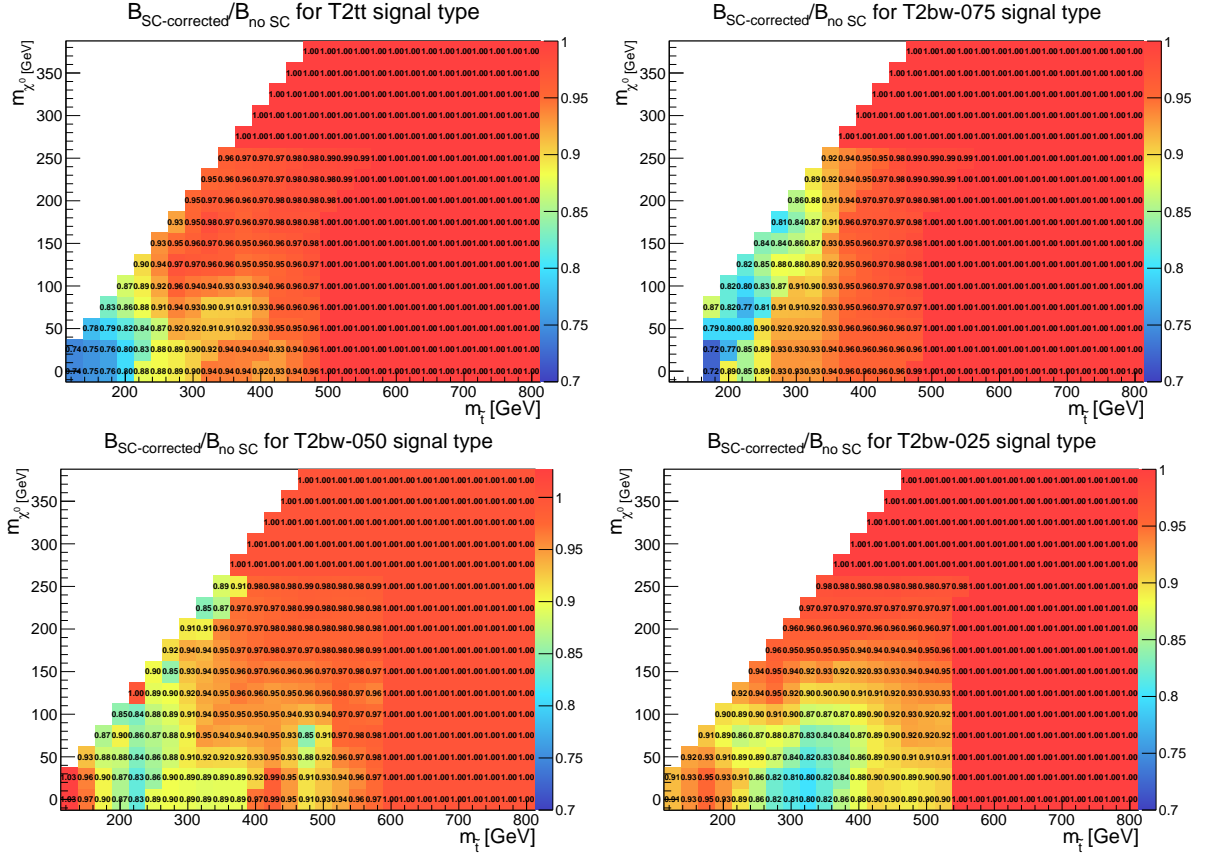


Figure 4.39: Map of the ratio \tilde{B}/B , i.e. signal-contamination corrected background prediction versus uncorrected prediction, using the BDT signal regions and for the $\tilde{t}_1 \rightarrow t\tilde{\chi}_1^0$ decay mode (top left) and $\tilde{t}_1 \rightarrow b\tilde{\chi}_1^\pm$ decay mode with $x = 0.75$ (top right), $x = 0.50$ (bottom left) and $x = 0.25$ (bottom right).

4.9 Results and interpretation

4.9.1 Results and limits for the cut-based and BDT approaches

On the top of Figure 4.40 and Figure 4.41, comparisons of the yields between data and background prediction under the null hypothesis H_0 are presented for each signal regions of the cut-based approach and BDT approach respectively. A good compatibility is observed

with the background-only expectation. The results are therefore interpreted in terms of upper limit on $\sigma(\tilde{t}_1\tilde{t}_1) \times \text{BR}$ with a 95% confidence level (CL) and where BR refers to the branching ratio of the considered decay mode (i.e. $\tilde{t}_1 \rightarrow t\tilde{\chi}_1^0$ or $\tilde{t}_1 \rightarrow b\tilde{\chi}_1^\pm$ with a given x). The computation of the upper limit is based on the CLs technique [120]. Comparing the upper limit with the theoretical expectation for a branching ratio of 1, one can derive limits in terms of excluded region of the $(m_{\tilde{t}_1}, m_{\tilde{\chi}_1^0})$ space, as reported on the bottom of Figure 4.40 and Figure 4.41. During the interpretation, the background estimation is corrected to account for the signal contamination effects as discussed in Section 4.8.

The comparison of the observed limits with the expected one is directly related to the difference of the yields between the observed data and the background prediction: for instance, in the cut-based signal regions of the $\tilde{t}_1 \rightarrow t\tilde{\chi}_1^0$, on top of Figure 4.40, the Off-shell loose region has a 1.5σ excess, translating to a less restrictive observed limit. On the other hand, the Medium Δm signal region has a deficit of around 0.5σ , translating to a higher observed limit in this region, compared to the expectation.

Overall, the BDT approach leads to limits which are typically about 50 GeV higher compared to the cut-based approach, in terms of $m_{\tilde{t}_1}$. For the $\tilde{t}_1 \rightarrow t\tilde{\chi}_1^0$ decay mode, the observed exclusion using the BDT approach goes up to $m_{\tilde{t}_1} \sim 700$ GeV and $m_{\tilde{\chi}_1^0} \sim 250$ GeV in the on-shell region and up to $m_{\tilde{\chi}_1^0} \sim 150$ GeV in the off-shell region. As discussed in Section 4.1.2, the case with $\Delta m \sim m_t$ is challenging as the kinematic here is very close to Standard Model $t\bar{t}$ production and cannot be efficiently probed directly. The decay mode $\tilde{t}_1 \rightarrow b\tilde{\chi}_1^\pm$ is also challenging in the low x case as the decays of the two W 's are typically softer compared to higher x cases. In particular, at low $m_{\tilde{\chi}_1^0}$, the mass of the $\tilde{\chi}_1^\pm$ is also low and on average, leads to less E_T^{miss} in the event and therefore lower selection efficiency. The final shape of the limit for $x = 0.25$ is due to concurrence between having a high-enough signal cross-section, having an off-shell W to have high- p_T objects to pass the selection, and sufficient E_T^{miss} from the decay of the $\tilde{\chi}_1^\pm$.

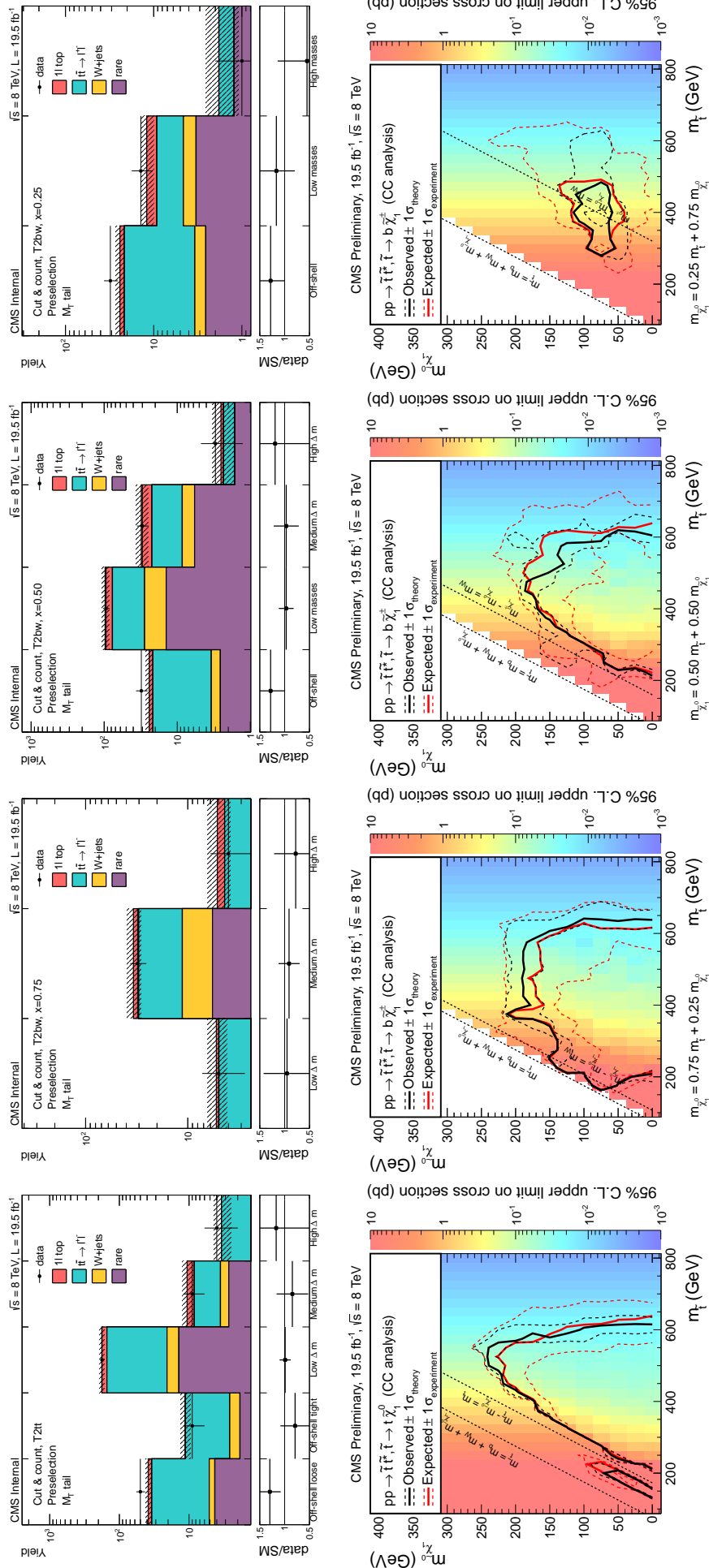


Figure 4.40: On the top: comparison of the yields in the different cut-based signal regions between data and the background prediction under the null hypothesis. The grey hatching represents the systematic uncertainty, propagated on the ratio plot. On the bottom: upper limit on $\sigma(\tilde{t}_1\tilde{t}_1) \times \text{BR}$ at 95% confidence level and exclusion in terms of $(m_{\tilde{t}_1}, m_{\tilde{\chi}_1^0})$, assuming $\text{BR} = 1$. On the first column, for $\tilde{t}_1 \rightarrow t\tilde{\chi}_1^0$ decay mode and on the second, third and last columns for $\tilde{t}_1 \rightarrow b\tilde{\chi}_1^\pm$ decay mode with $x = 0.75, 0.50$ and 0.25 respectively.

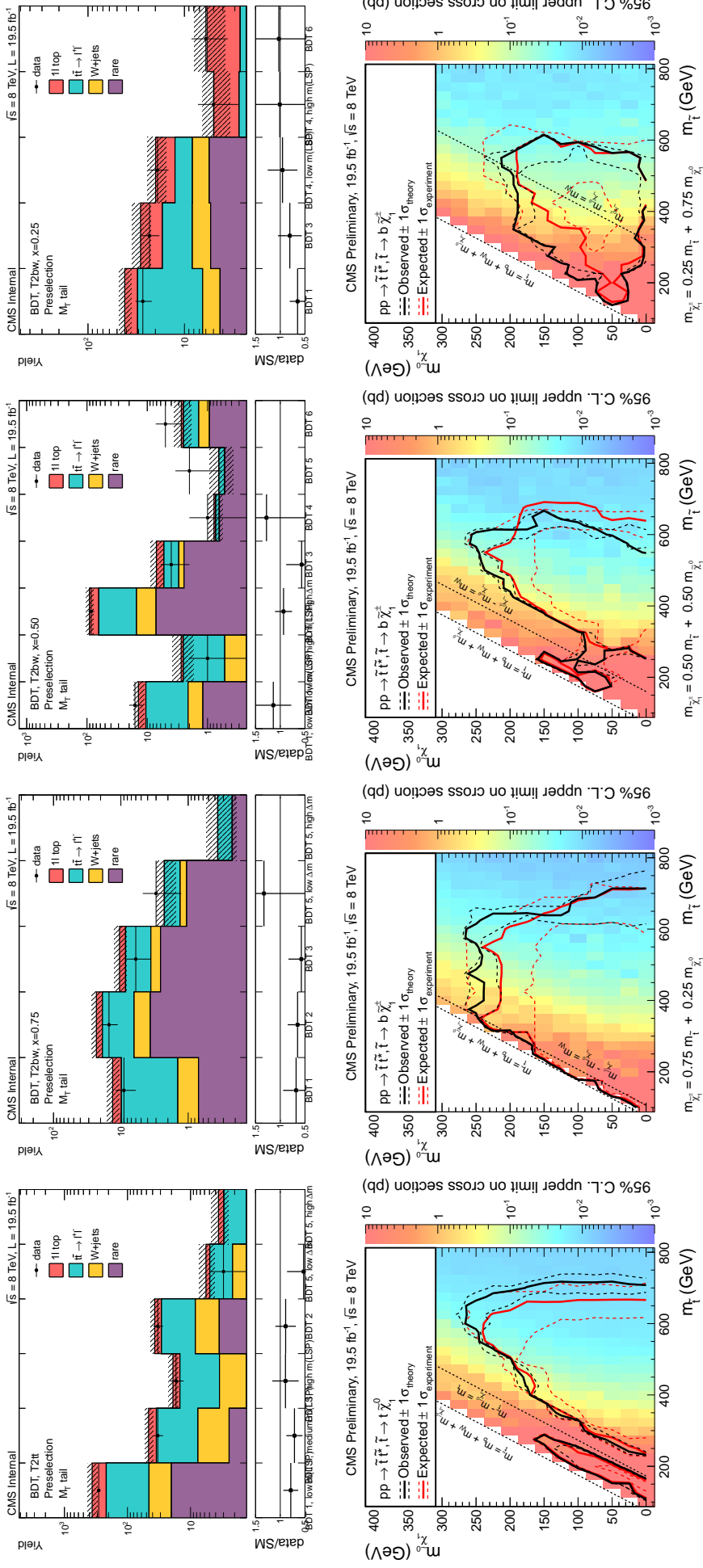


Figure 4.41: On the top: comparison of the yields in the different BDT-based signal regions between data and the background prediction under the null hypothesis. The grey hatching represents the systematic uncertainty, propagated on the ratio plot. On the bottom: upper limit on $\sigma(\tilde{t}_1 \tilde{t}_1^*) \times \text{BR}$ at 95% confidence level and exclusion in terms of $(m_{\tilde{t}_1}, m_{\tilde{\chi}_1^0})$, assuming $BR = 1$. On the first column, for $\tilde{t}_1 \rightarrow \tilde{t}_1^0$ decay mode and on the second, third and last columns for $\tilde{t}_1 \rightarrow b\tilde{\chi}_1^0$ decay mode with $x = 0.75, 0.50$ and 0.25 respectively.

4.9.2 Combination with the search in two lepton channel

The results of this analysis have been combined with an analysis targeting the same signals, this time in the dilepton channel [131]. While this channel does not reach comparable performances at high Δm , it is competitive in the low Δm cases as it benefits from typically lower thresholds in p_T at trigger level compared to the semileptonic and all hadronic channels. The strategy of the dilepton channel search is based on the variable $M_{T2}(\ell\ell)$ constructed with ideas similar to the M_{T2}^W observable discussed before. The signal regions are designed with increasing cuts on this variable. In both the semileptonic and dileptonic analyses, the background estimation is mainly data-driven and, provided that the overlap between the analyses is close to zero, no correlation between the background systematics are taken into account. However, the signal systematic uncertainties such as the uncertainties on jet energy corrections, the luminosity and the ISR reweighting, are taken to be correlated at 100%. The results of the analyses are combined and interpreted in terms of limits, shown on Figure 4.42. The combination allowed small but significant improvements, in particular around the $\Delta m \sim m_t$ region in the $\tilde{t}_1 \rightarrow t\tilde{\chi}_1^0$ case, and at low Δm in the $\tilde{t}_1 \rightarrow b\tilde{\chi}_1^\pm$ case with $x = 0.25$ and 0.50 .

4.9.3 Comparison of polarization scenarios

Different alternative polarization scenarios can be investigated [132, 133], directly related to the mixing of the stops and the mixing matrices of the neutralinos and charginos introduced in Section 1.4.2. In the $\tilde{t}_1 \rightarrow t\tilde{\chi}_1^0$ decay mode, we investigate two alternative scenarios in the on-shell case depending on the handedness of the top from the decay of the stop, either purely left-handed or purely right-handed. As presented on Figure 4.43, these alternative polarization scenarios impact the limits by ± 50 GeV. In the $\tilde{t}_1 \rightarrow b\tilde{\chi}_1^\pm$, both the polarization of the chargino and the handedness of the $W\tilde{\chi}_1^0\tilde{\chi}_1^\pm$ coupling can be taken as either symmetric, left or right. In particular, four cases have been investigated and compared to the nominal case (i.e. unpolarized) as shown on Figure 4.43. In each polarization scenario, the signal contamination is correctly recomputed and taken into account, such that the corrected background estimation is consistent. Overall, the maximum increase in the limits reach is found for the scenario with a right-handed $\tilde{\chi}_1^\pm$ with right-handed $W\tilde{\chi}_1^0\tilde{\chi}_1^\pm$ coupling, and the maximum decrease is for a right-handed $\tilde{\chi}_1^\pm$ with left-handed $W\tilde{\chi}_1^0\tilde{\chi}_1^\pm$ coupling.

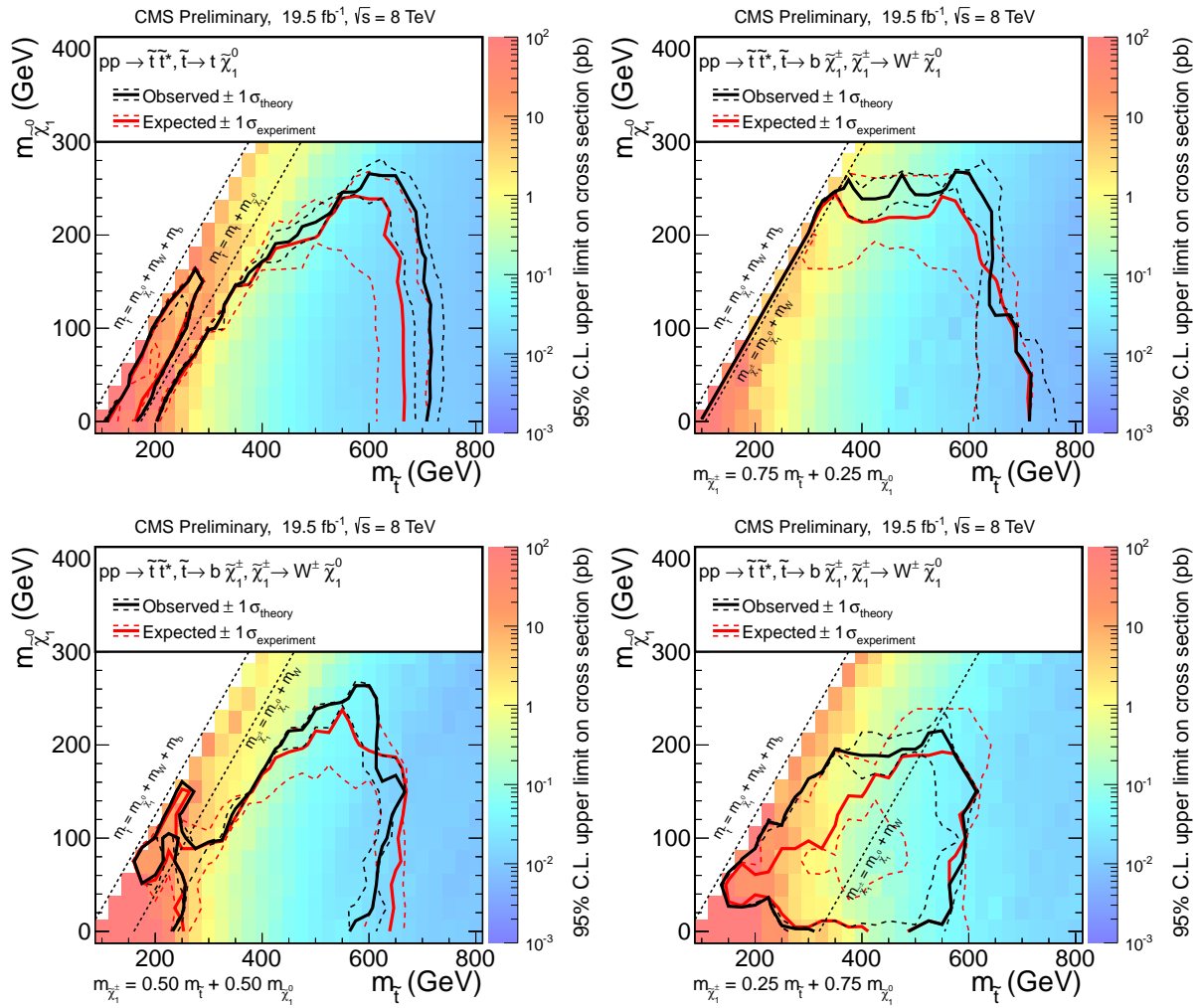


Figure 4.42: Upper limit at 95% confidence level after combining the semileptonic and dileptonic searches, and corresponding exclusion in terms of $(m_{\tilde{t}_1}, m_{\tilde{\chi}_1^0})$ after comparison to the theory, assuming $BR = 1$. On the top left, for $\tilde{t}_1 \rightarrow t \tilde{\chi}_1^0$ decay mode and on the top right, bottom left and bottom right for $\tilde{t}_1 \rightarrow b \tilde{\chi}_1^\pm$ decay mode with $x = 0.75, 0.50$ and 0.25 respectively.

4.9.4 Examination of an individual event and discussion

Finally, one may be tempted to directly inspect the events in the recorded data, that are the most signal-like, to look for any pathological reconstruction or simply obtain a better feeling of what are the remaining events after the full selection. Figure 4.44 shows one of these events in the high- Δm signal region of the cut-based approach for $\tilde{t}_1 \rightarrow t \tilde{\chi}_1^0$. This event contains four jets among which two are b -tagged, a muon with $p_T = 114$ GeV, $E_T^{\text{miss}} = 392$ GeV and a value of $M_T = 300$ GeV. For this particular event, one may find suspicious that the E_T^{miss} direction is collinear with the highest p_T jet in the event and may indicate a large mismeasurement of the energy of these jets. This hypothesis is also supported by the fact that these jets have pseudo-rapidities corresponding to the transition

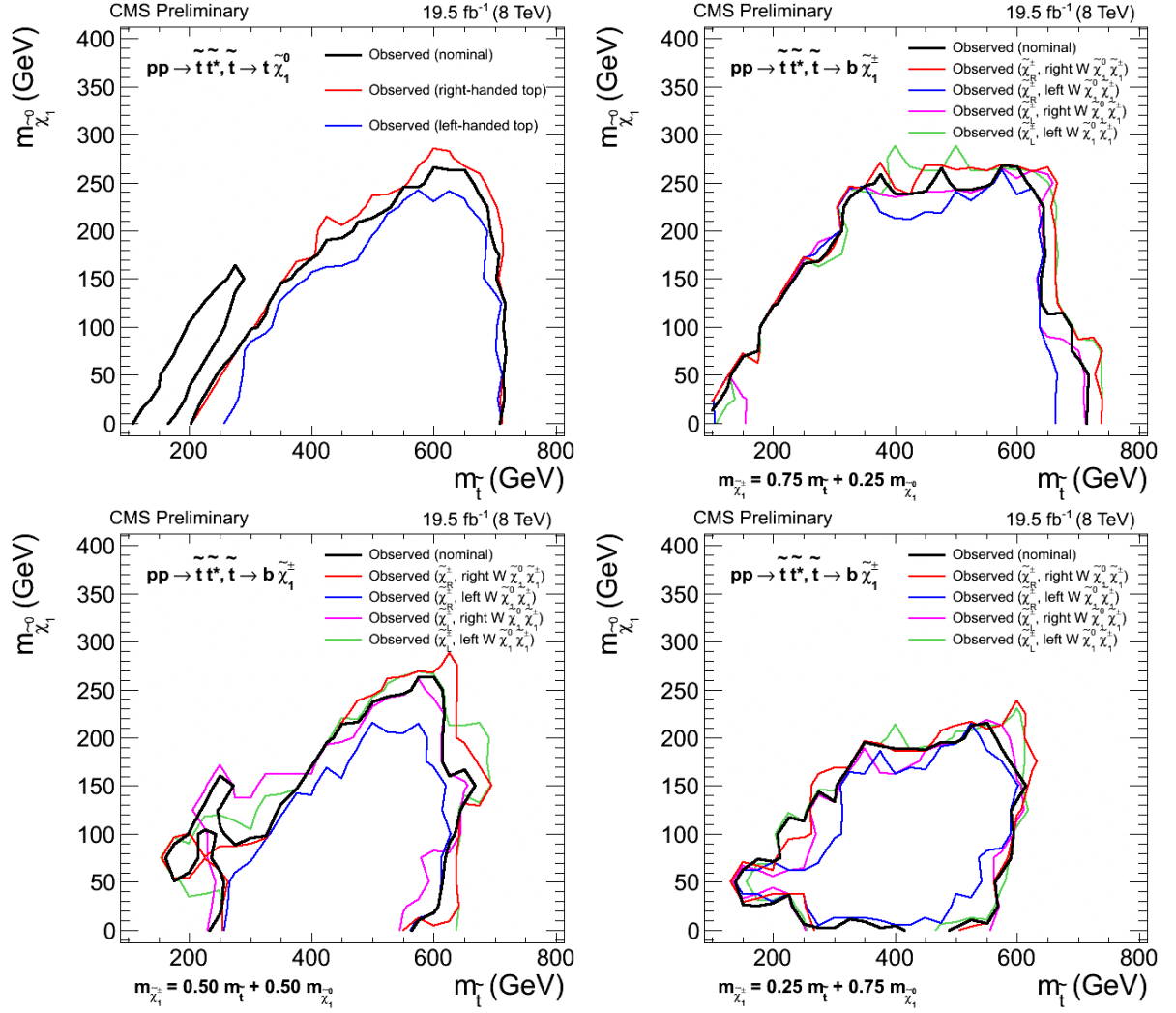


Figure 4.43: Exclusion limits for the combined semileptonic and dileptonic searches when considering alternative polarization scenarios: on the top left, for $\tilde{t}_1 \rightarrow t\tilde{\chi}_1^0$ decay mode with pure left-handed or right-handed top compared to the unpolarized scenario ; on the top right, bottom left and bottom right for $\tilde{t}_1 \rightarrow b\tilde{\chi}_1^\pm$ decay mode with $x = 0.75, 0.50$ and 0.25 respectively with four polarization scenarios.

region between the barrel and the endcap, in which mismeasurements are likely to occur in the tracker and hadronic calorimeter. This kind of topology could be investigated further and kept in mind when developing the analysis of the Run II.

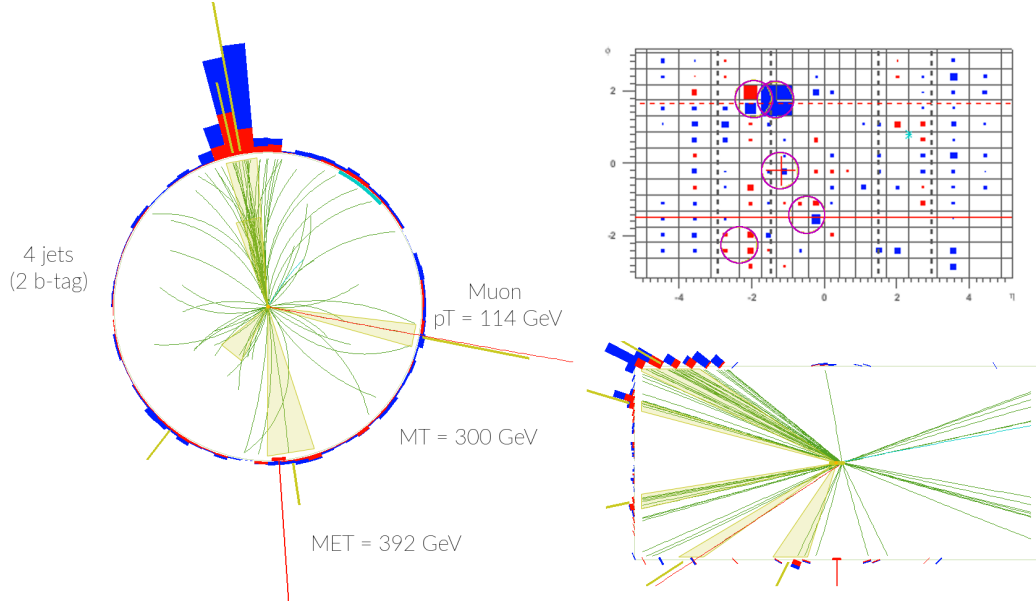


Figure 4.44: One of the most signal-like event for the $\tilde{t}_1\tilde{t}_1^* \rightarrow tt\tilde{\chi}_1^0\tilde{\chi}_1^0$ decay-mode in the high- Δm cut-based approach. The event has one muon with $p_T = 114$ GeV, four jets among which two are b -tagged, $E_T^{\text{miss}} = 392$ GeV and $M_T = 300$ GeV. Only tracks coming from the primary vertex are shown.

4.9.5 Comparison with other direct stop pair production searches

In this section, we finally present the place of this analysis with respect to other direct stop pair production searches using data from the Run I. We briefly discuss the key aspects of a few of these analyses, namely the search in the fully hadronic channel for the $\tilde{t}_1 \rightarrow t\tilde{\chi}_1^0$ decay mode, searches targeting compressed-spectra scenarios ($\Delta m < 80$ GeV), and strategies to attempt to cover the stealthy regime ($\Delta m \sim 172$ GeV).

Figure 4.45 presents a summary of the limits obtained in CMS and ATLAS with the Run I of the LHC on direct stop searches for the $\tilde{t}_1 \rightarrow t\tilde{\chi}_1^0/c\tilde{\chi}_1^0/bf'f'\tilde{\chi}_1^0$ decay modes. The top polarization in the $\tilde{t}_1 \rightarrow t\tilde{\chi}_1^0$ decay mode is assumed right-handed in the ATLAS analyses instead of unpolarized for CMS. Overall, both experiments obtain comparable sensitivity, reaching stop masses up to 750–780 GeV and neutralino masses up to 275 GeV.

Search in fully hadronic channel

The searches in the fully hadronic channel (i.e. both W decaying hadronically) [134, 135] benefit at high Δm from the higher branching ratio. In the low Δm regime however, these analyses are impacted by the tighter trigger requirement to limit the large multijet backgrounds: in CMS, a trigger with $E_T^{\text{miss}} > 80$ GeV and two central jets with $p_T > 50$ GeV is used, to be compared to the 24 and 27 GeV trigger thresholds of the 1-lepton

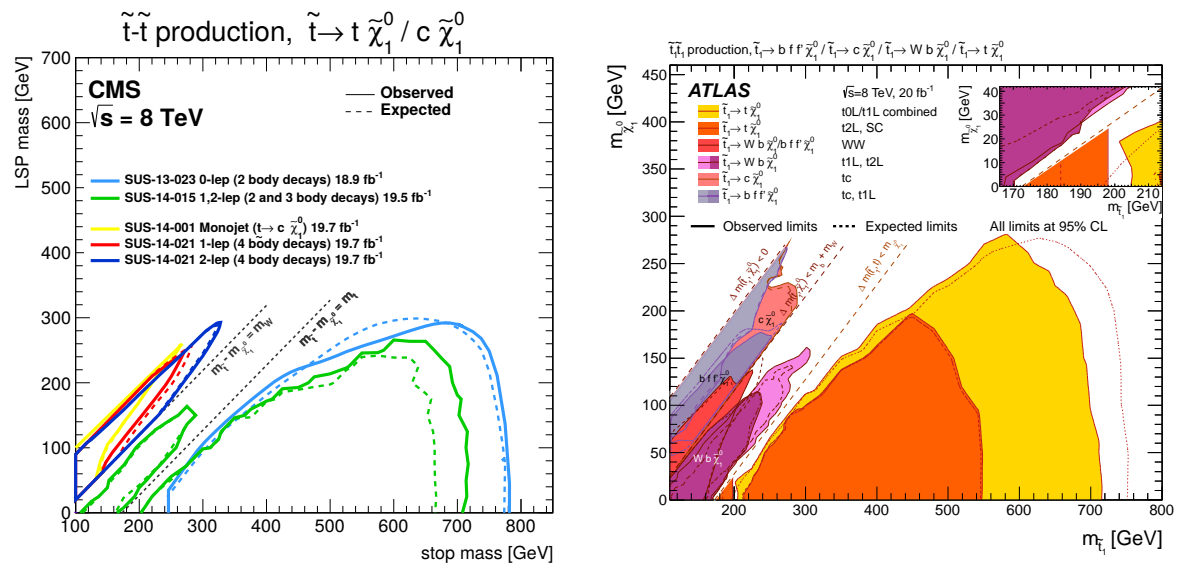


Figure 4.45: Summary of expected (dashed lines) and observed (solid lines) limits for direct stop production searches decaying through $\tilde{t}_1 \rightarrow t\tilde{\chi}_1^0/c\tilde{\chi}_1^0/bff'\tilde{\chi}_1^0$, with Run I data in CMS (left) and ATLAS (right).

analysis.

Interestingly, this analysis also requires a dedicated strategy to find and veto event with lost lepton as the semi-leptonic $t\bar{t}$ becomes a major background after requiring large E_T^{miss} in the event.

The fully-hadronic channel also offers the possibility to reconstruct both tops. A variable jet-size clustering algorithm have been developed to efficiently reconstruct tops over the wide range of momenta of the analysis, from soft ($p_T(\text{jets}) \sim \mathcal{O}(20 \text{ GeV})$) to boosted tops. In the $\tilde{t}_1 \rightarrow t\tilde{\chi}_1^0$ channel, the analysis is able to exclude up to $m_{\tilde{t}_1} = 780 \text{ GeV}$ when $m_{\tilde{\chi}_1^0} < 200 \text{ GeV}$.

Searches in compressed spectra regions

The compressed spectra region, i.e. with $0 < \Delta m < m_W$, is cosmologically motivated as a mass splitting of 15 – 30 GeV is preferred to obtain the right density of dark matter due to $\tilde{t}_1 - \tilde{\chi}_1^0$ annihilation [93, 136]

In this region, the stop is expected to decay through flavor changing neutral current $\tilde{t}_1 \rightarrow c\tilde{\chi}_1^0$ (2-body decay), or $\tilde{t}_1 \rightarrow bff'\tilde{\chi}_1^0$ (4-body decay) depending of the exact parameters of the theory.

In the first decay type ($\tilde{t}_1 \rightarrow c\tilde{\chi}_1^0$) [137, 135], the jets from c are expected to be low p_T . The CMS analysis strategy is therefore centered instead around ISR jet identification,

following the same arguments described in Section 4.5.1. The analysis is most sensitive in the region with very low Δm , and decreases as Δm increases because the c jets start to carry a significant momentum. The ATLAS analysis follows a similar strategy but also uses c -tagging techniques to reject some of the background of the analysis.

In the second decay type ($\tilde{t}_1 \rightarrow b f f' \tilde{\chi}_1^0$) [138, 135], the signal is expected to contain 1 or 2 soft leptons in the semi- and fully-leptonic channel. The CMS event preselection requires a high- p_T jet coming from ISR, one muon with $p_T > 5$ GeV, possibly another lepton (electron or muon), and $E_T^{\text{miss}} > 200$ GeV. The two lepton channels ends up having the best overall sensitivity and excluded stop masses up to about 300 GeV.

Searches in stealthy region

As discussed in Section 4.1.2 and Section 4.9, when $\Delta m \sim m_t \approx 172$ GeV in the $\tilde{t}_1 \rightarrow t \tilde{\chi}_1^0$ decay mode, the kinematic of the signal is very close to Standard Model $t\bar{t}$ production and is quite difficult to bring out. It should be noted that at 8 TeV, the cross-section for stop pair production with $m_{\tilde{t}_1}$ around 172 GeV is about ten times lower than the $t\bar{t}$ cross-section, to be compared to the $\mathcal{O}(5\%)$ theoretical and $\mathcal{O}(3\%)$ experimental uncertainty on the $t\bar{t}$ cross-section. A first strategy to target the stop stealthy regime consists in reinterpreting $t\bar{t}$ cross-section measurements. In CMS, this has been used to exclude stop masses between 150 and 190 GeV for $m_{\tilde{\chi}_1^0} = 1$ GeV, as presented in Figure 4.46 [139]. This strategy can be refined using the lack of spin correlation for tops produced via stops compared to Standard Model $t\bar{t}$ production [140]. In ATLAS, this technique has been used to exclude stops up to 200 GeV for $m_{\tilde{\chi}_1^0} = 1$ GeV [141].

An alternative approach consists in looking for the second stop production, \tilde{t}_2 , decaying to the first stop \tilde{t}_1 via a Higgs (h) or a Z boson, and \tilde{t}_1 still decaying to $t + \tilde{\chi}_1^0$ with $\Delta m \sim m_t$. The full decay chain is therefore, assuming $\text{BR}(\tilde{t}_2 \rightarrow \tilde{t}_1 h) = 1$, $\tilde{t}_2 \tilde{t}_2^* \rightarrow \tilde{t}_1 \tilde{t}_1^* + hh \rightarrow t\bar{t} \tilde{\chi}_1^0 \tilde{\chi}_1^0 + hh$. The analyses [142, 135] targeting this process is able to constrain the $(m_{\tilde{t}_2}, m_{\tilde{t}_1})$ space, as shown on Figure 4.46 for CMS, which can be put in parallel to theoretical constrains such as discussed in Section 4.1.1.

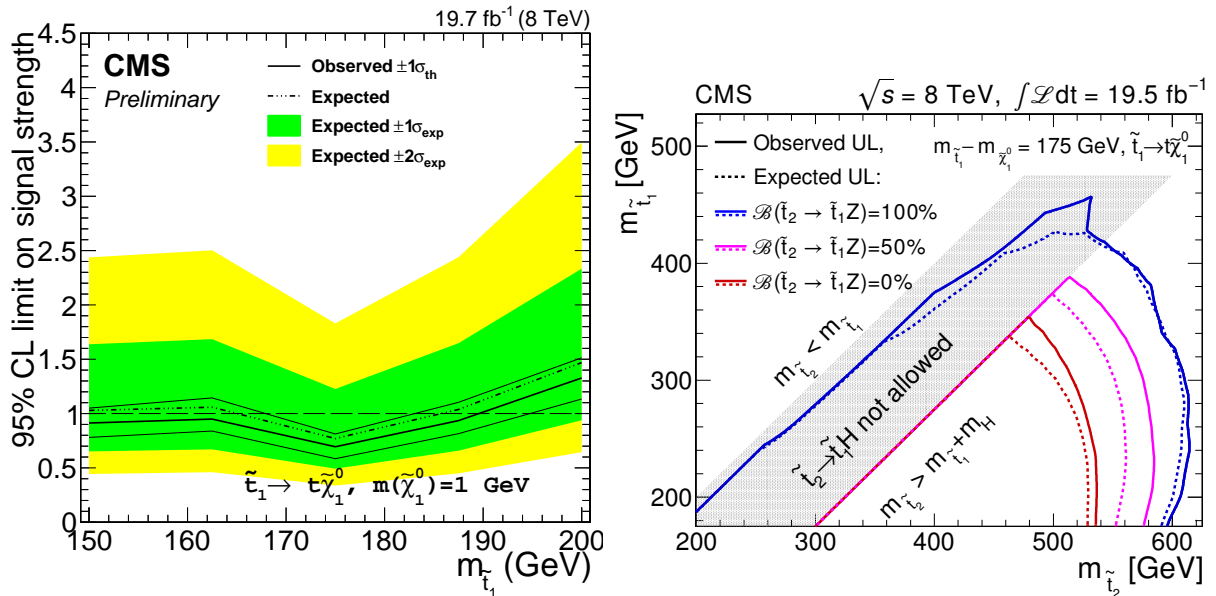


Figure 4.46: On the left, upper limit on $\sigma_{\tilde{t}_1\tilde{t}_1}/\sigma_{\tilde{t}_1\tilde{t}_1}^{\text{theo}}$ as function of $m_{\tilde{t}_1}$ and for $m_{\tilde{\chi}_1^0} = 1$ GeV [139]. On the right, exclusion limit in the $(m_{\tilde{t}_2}, m_{\tilde{t}_1})$ space from a search for $pp \rightarrow \tilde{t}_2\tilde{t}_2$, $\tilde{t}_2 \rightarrow \tilde{t}_1 h/Z$ with variable branching ratio, and $\tilde{t}_1 \rightarrow t\tilde{\chi}_1^0$ with $\Delta m = 175$ GeV [142].

4.10 Perspectives

4.10.1 W -tagging in the high Δm regime

Motivation

As one considers higher Δm values for the signal, the mean momentum of the decay products increases. In particular, if we consider the hadronically decaying W boson, an increase of the p_T translates into more collimated objects, in that case the pair of quarks that will hadronize. This is illustrated on the Figure 4.47 showing the distribution of the ΔR between the quarks coming from the decay of a W boson as a function of the p_T of the generated W . In the situation where the ΔR between the quarks approaches the size parameter used by the standard clustering algorithm (i.e. $\Delta R \sim 0.5$), only one big jet gets reconstructed instead of two smaller ones. This topology is referred to as boosted hadronic W .

Driven by the fact that some new physics signatures are expected to contain such boosted hadronic W (e.g. [143]), techniques have been developed to address this topology by providing variables to tag jets originating from boosted W decays. The strategy consists in using a wider radius parameter when clustering the jets, clean and correct the jets from pile-up contamination, and analyze the substructure of the jets to derive

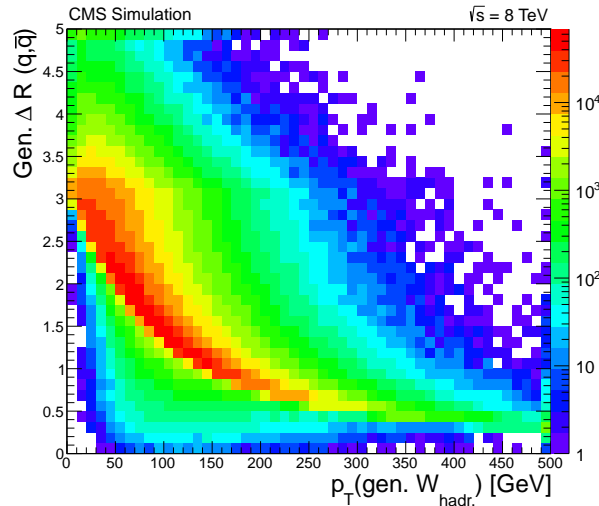


Figure 4.47: Distribution, estimated on a semileptonic $t\bar{t}$ sample, of the ΔR between the quarks coming from the decay of the hadronic W boson, as function of the generated p_T of the W . The mean ΔR approaches 0.5, the standard size parameter used at 8 TeV, at $p_T \sim 200$ GeV, meaning that jets coming from the two quarks will be merged by the clustering algorithm.

variables that discriminate between boosted W decays and fakes.

Figure 4.48 illustrates the interest that these techniques might have to select the signal: on the left plot, the mean p_T of the generated W bosons for the signal across the $(m_{\tilde{t}_1}, m_{\tilde{\chi}_1^0})$ space grows as function of Δm . For $\Delta m > 650$ GeV, the mean p_T is about 200 GeV and we can expect a large fraction of boosted W . Figure 4.48, on the right, compares the distribution of the p_T of the hadronic W for one particular signal benchmark at high- Δm against the different backgrounds and shows that the presence a boosted W tends to be discriminating.

Selection and performances

As discussed in Section 2.2.3, alternatives to the standard anti- k_T clustering algorithm with a size parameter $R = 0.5$ (AK5) can be considered. In the following, we consider in addition the jet collection built from the Cambridge-Aachen clustering algorithm with a size parameter $R = 0.8$ (CA8). This algorithm is known to yield better performances in the context of resolving jet substructures, as discussed in [144, 145].

To clean the jet from pile-up contributions and improve rejection of quark/gluon jets, different grooming techniques can be applied on the jet as illustrated on Figure 4.49 and discussed in [145, 146]. While the filtering and trimming techniques aim to clusterize subjets inside the initial fat jet, the pruning technique consists in reclustering the whole

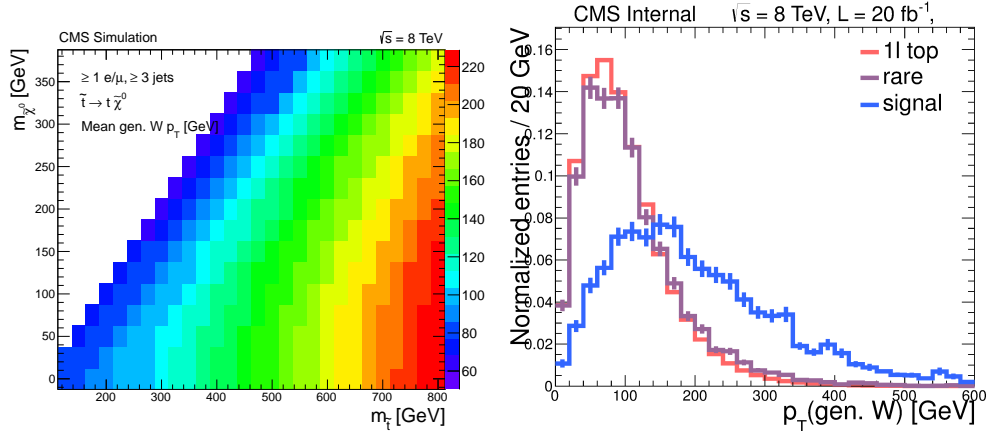


Figure 4.48: On the left: mean p_T of the generated W for the signal across the $(m_{\tilde{t}_1}, m_{\tilde{\chi}_1^0})$ space. On the right: comparison of the p_T spectra of the generated hadronic W for the 1ℓ top and rare backgrounds, and the signal benchmark $(m_{\tilde{t}_1}, m_{\tilde{\chi}_1^0}) = (700, 25)$ GeV. The $t\bar{t} \rightarrow \ell\ell$ and W +jets backgrounds are not represented as they do not contain a generated hadronic W by definition.

Jet grooming methods are used to clean the jet of soft QCD and PU contributions

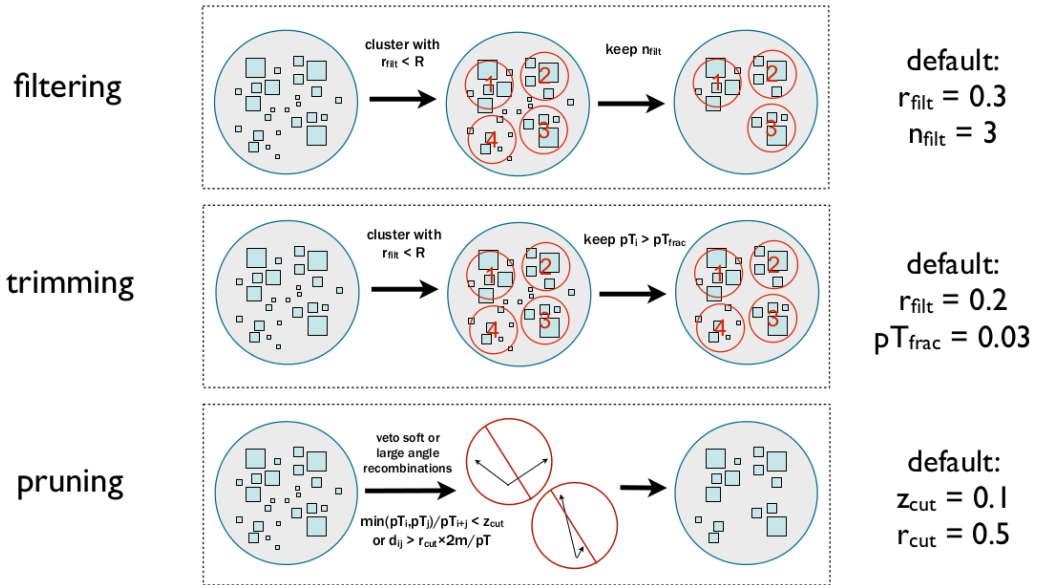


Figure 4.49: Illustration (from [147]) of the three available jet grooming techniques. The filtering technique consists in reclustering components of the jets with a smaller jet size parameter (e.g. 0.3) and keeping only a given number (e.g. three) of the subjets. The trimming techniques also reclusters the components with a smaller jet size parameter, but keeps all subjets with a significant p_T fraction of the fat jet p_T . Finally, the pruning techniques veto soft or large angle recombinations between the jet components, likely to come from pile-up.

jet, but with conditions applied during the process to forbid the combinations of softer components (e.g. with energy smaller than 10% of the protojet) or large angular combi-

nations.

The substructure of the jet is analyzed via the N -subjettiness variables, which are designed to quantify how likely a jet is to be composed of N sub-jets [148]. These variables are denoted $\tau_1, \tau_2, \dots, \tau_N$. A value close to 0 for τ_N tends to indicate a good compatibility with the N -subjettiness hypothesis. In the context of W -tagging, it is common to focus on the use of the ratio τ_2/τ_1 which provides good discriminability between real W and quark/gluons jets.

To define selection criteria, we study the distribution of a few variables on a $t\bar{t}$ Monte-Carlo sample after applying the preselection defined in Section 4.4. We however allow events with at least three regular (i.e. based on the anti- k_T algorithm with a size parameter 0.5) jets instead of four. W candidates are matched to generated hadronically-decaying W : if the candidate is within $\Delta R < 0.4$, it is considered as matched, whereas candidates which are in $\Delta R > 2$ are considered to be fakes originating from quark or gluons. The quantities investigated are the pruned mass of the jet, the N -subjettiness ratio τ_2/τ_1 and the distance to the selected lepton $\Delta R(\ell, \text{jet})$. The latter variable is relevant in this context of $t\bar{t}$ -like event as the lepton is expected to be in the hemisphere opposite to the hadronic W .

Figure 4.50 shows the distribution of the pruned mass of the jet and the N -subjettiness ratio τ_2/τ_1 for candidates with $p_T > 150$ GeV and with $\Delta R(\ell, \text{jet}) > 1.5$. A good working point is found by requiring $\text{mass}(\text{jet}) > 70$ GeV and $\tau_2/\tau_1 < 0.5$. The resulting tagging efficiency is estimated as function of the p_T of the candidate as presented on Figure 4.51. The efficiency for candidates matched to true W is about 30% at 200 GeV and reaches a plateau to 70% at 270 GeV. It however starts decreasing around 350 GeV as it gets more difficult to resolve the two subjets. The fake rate is about 5% for candidates of 200 GeV and grows linearly with the p_T as momentum tends to create unphysical large mass for the jets.

Impact on the analysis sensitivity

In this section, we investigate the potential benefit of the use of W -tagging in the context of the analysis and in term of sensitivity. Figure 4.52 shows the fraction of background and signals containing or not a W -tagged jet with $p_T > 250$ GeV at preselection level with $M_T > 100$ GeV. The rare category has around 5% of events containing such a W -tagged jet compared to less than 3% for the other categories. The fact that rare have a higher fraction of event with a W -tagged jet can be explained by noticing that diboson, triboson and $t\bar{t}$ +boson events are likely to contain not only true boosted hadronic W , but also boosted hadronic Z which may be selected. The fraction of signal with a W -tagged jet

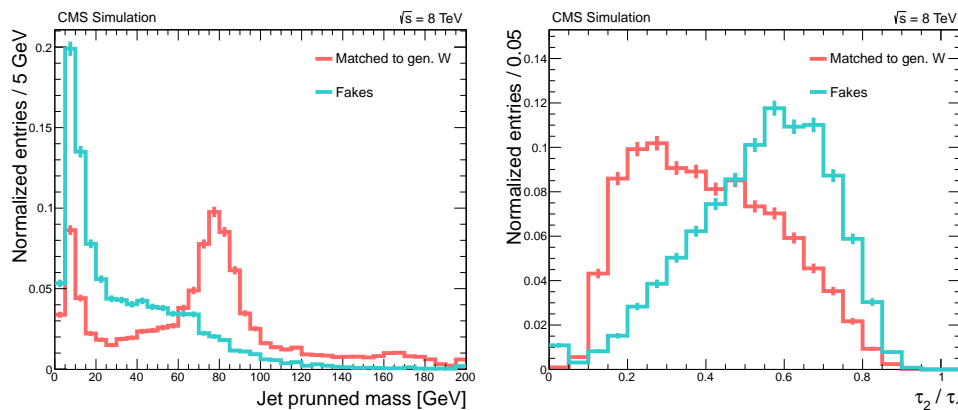


Figure 4.50: Distribution of the pruned mass (on the left) and τ_2/τ_1 (on the right) for CA8 jets with $p_T > 150$ GeV and $\Delta R(\ell, \text{jet}) > 1.5$ in $t\bar{t}$ events with preselection applied. The red curve represents the jets matched to a generated hadronic W while the teal curve represents fakes, i.e. not matched to a generated W .

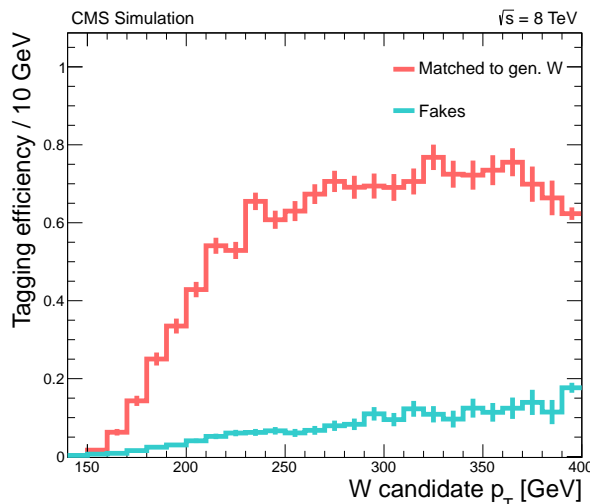


Figure 4.51: Tagging efficiency for the true W jets (in red) and fakes from quark/gluon jets (in blue), as function of the p_T of the reconstructed jet.

increases from 20 to 30% between the two benchmarks $(m_{\tilde{t}_1}, m_{\tilde{\chi}_1^0}) = (600, 0)$ GeV and $(800, 0)$ GeV for the $\tilde{t}_1 \rightarrow t\tilde{\chi}_1^0$ decay mode.

At this stage, one can already estimate that the significance gain, $\epsilon_S/\sqrt{\epsilon_B}$, of requiring at least one W -tag in the event, is around 1.34 for the signal benchmark $(800, 0)$. However, while this alone shows that W -tagging is an interesting technique, the question we actually want to address is whether or not it is possible to increase the performances of the analysis compared to a set of optimized cuts on M_T , E_T^{miss} and M_{T2}^W as in Section 4.5.3 for the high Δm region.

To answer this question, we consider the analysis (noted ‘ref.’) that makes no use of W -tagging and relies only on optimized cuts on M_T , E_T^{miss} and M_{T2}^W . In parallel, we

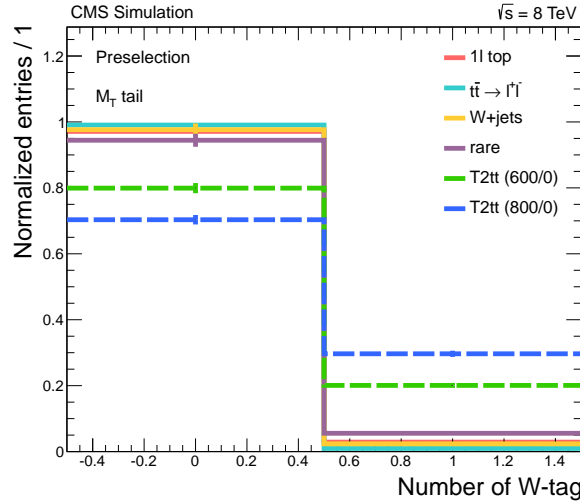


Figure 4.52: Fraction of background and signal events without and with a W -tagged jet with $p_T > 250$ GeV, at preselection level with $M_T > 100$ GeV. The two signal benchmarks considered are the $\tilde{t}_1 \rightarrow t\tilde{\chi}_1^0$ decay mode with $(m_{\tilde{t}_1}, m_{\tilde{\chi}_1^0}) = (600, 0)$ GeV and $(800, 0)$ GeV.

consider two populations of events: the first one, (1W), passing the preselection, but also allowing events with three regular jets to pass, and requiring at least one CA8 W -tagged jet with $p_T > 250$ GeV ; the second one (0W) passing the preselection (with at least four jets) and requiring that no CA8 jet is W -tagged.

After each of these selections, we train cuts on M_T , E_T^{miss} and M_{T2}^W to maximize an exclusion-oriented figure of merit, i.e. of the form $S/\sqrt{S+B+f^2B^2}$, as described in Section 4.5.2. The optimization is done using five signal benchmarks with increasing Δm from 600 to 800 GeV, and a rough averaging is done to obtain a single set of cut. The relative systematic uncertainty on the background is set to 30% and to avoid extreme cut values, the figure of merit is set to 0 if the signal yield is lower than 0.5^3 , and the background yield B is replaced by $\max(B, 1)$. Furthermore, no constraint is put on the maximum value of the M_T cut as it was done in the analysis.

The resulting cuts are presented on Table 4.10, as well as a breakdown of the yield of the background and several signal benchmarks with increasing Δm . The optimal cuts for the (ref) and (0W) selections are found to be roughly the same. In comparison, the optimal cuts for the (1W) selection are found to be looser, which is expected due to the already tight requirement of having at least one W -tagged jet in the event.

We are now interested in combining the information in (1W) and (0W), and compare it to the case with no W -tagging usage (ref). A straightforward approach consists in

³This constraint is different from what was done for the analysis, where the minimum signal yield was set to 3. However as it is a quite harsh constraint in the high Δm region, because of the low cross-section, this constraint is loosened to a minimum of 0.5.

	(ref) Preselection No W -tagging usage	(1W) Preselection with ≥ 3 AK5 jets + ≥ 1 W -tagged CA8 jet	(0W) Preselection (≥ 4 AK5 jets) + 0 W -tagged CA8 jet
E_T^{miss}	>350	>325	>350
M_T	>150	>130	>150
M_{T2}^W	>220	>190	>220
Total SM	1.91 ± 0.57	0.97 ± 0.26	1.66 ± 0.56
T2tt (600/0)	6.61 ± 0.28	3.02 ± 0.18	5.02 ± 0.25
T2tt (650/0)	4.50 ± 0.17	2.30 ± 0.12	3.30 ± 0.15
T2tt (700/0)	2.87 ± 0.10	1.49 ± 0.07	2.08 ± 0.08
T2tt (750/0)	2.01 ± 0.07	0.99 ± 0.05	1.43 ± 0.06
T2tt (800/0)	1.33 ± 0.04	0.73 ± 0.03	0.89 ± 0.04

Table 4.10: Optimized cuts on E_T^{miss} , M_T and M_{T2}^W in the high Δm (> 600 GeV) region, and corresponding yields for the background and five signal benchmarks with increasing Δm .

	(ref)	(1W)	(0W)	(1W+0W)	Gain (ref) \rightarrow (1W+0W)
T2tt (600/0)	2.22	1.50	1.90	2.39	1.08
T2tt (650/0)	1.73	1.26	1.44	1.88	1.09
T2tt (700/0)	1.27	0.93	1.04	1.37	1.08
T2tt (750/0)	0.97	0.69	0.79	1.02	1.05
T2tt (800/0)	0.70	0.55	0.53	0.73	1.05

Table 4.11: Exclusion-oriented significance for signal benchmarks with increasing Δm in the different scenarios (ref), (1W), (0W) and (1W+0W), as well as the gain of significance between (ref) and (1W+0W).

summing the yields of the two categories (1W) and (0W) together, compute the global exclusion-oriented significance of this sum (1W+0W), and compare it to the case with no W -tagging usage. The resulting (1W+0W) selection we have built here can be seen as a decision tree (though not boosted) with a different treatment depending if the event contains or not a W -tagged jet. The result of the comparison is presented on [Table 4.11](#).

From this comparison, one observes that the use of W -tagging may provide a mild gain of ~ 5 -10% on the total significance of the analysis in the high- Δm region. While it is counterintuitive that the gain at $\Delta m = 600$ GeV is around 8% compared to 5% at $\Delta m = 800$ GeV, this is understood to be an artefact coming from the rough averaging of the optimal cuts across the five benchmarks. The average chosen is actually biasing the performances in the $\Delta m \sim 650$ GeV region towards significantly suboptimal ones in (ref) and (0W). The gain provided by the (1W) category then appears bigger for these benchmarks compared to higher Δm . This was confirmed by redoing the comparison using the optimal cuts for each benchmarks, which then yields a consistent 5-6% gain for all benchmark.

While this gain can be thought to be small, other investigations have been performed to try to improve it. For example, one may look for quantities related to the W -tagged jet that may help to further increase the performances. For example, it can be expected to find a b -tagged jet (or a jet with high b -tagging discriminant) in the proximity of the W -tagged jet to reconstruct the hadronic top. Nevertheless, this attempt did not yield any discriminating variable likely to improve the performance. Finally, it must be kept in mind that the statistical usage of the W -tagging category can be done in different ways. The presence of a W -tagged jet or related kinematic or angular quantity may be used as input to a boosted decision tree able to exploit the correlation between these variables and the others. One may also statistically combine the two categories (1W) and (0W) with multi-bins techniques, instead of merging them together into a single bin.

4.10.2 Sensitivity estimation for the Run II

Let us now estimate the sensitivity of the analysis at the beginning of Run II. One can get a basic estimation of the integrated luminosity \mathcal{L} required at 13 TeV to obtain equivalent sensitivity compared to 8 TeV, starting from the following equation:

$$\left(\frac{S}{\sqrt{B}}\right)_{8 \text{ TeV}} = \left(\frac{S}{\sqrt{B}}\right)_{13 \text{ TeV}}. \quad (4.24)$$

Using $N = \mathcal{L} \times \sigma \times \epsilon$ and assuming that the selection efficiencies ϵ remain the same between 8 and 13 TeV, one finds that

$$\mathcal{L}_{13 \text{ TeV}}^{\text{equiv.}} = \mathcal{L}_{8 \text{ TeV}} \times \frac{\kappa_B}{\kappa_S^2}, \quad (4.25)$$

where $\kappa \equiv \sigma_{13 \text{ TeV}}/\sigma_{8 \text{ TeV}}$. For $m_{\tilde{t}_1} \sim 800$ GeV, $\kappa_S \sim 10$. From the experience at 8 TeV using the high- Δm selection, the dominant backgrounds are $t\bar{t}$ and $t\bar{t} + Z$. For these processes, one gets $\kappa_B \sim 3.3$. One ends up with

$$\mathcal{L}_{13 \text{ TeV}}^{\text{equiv.}} \sim 0.7 \text{ fb}^{-1}. \quad (4.26)$$

The sensitivity is further studied on two Monte-Carlo benchmarks for the $\tilde{t}_1 \rightarrow t\tilde{\chi}_1^0$ signal type with $(m_{\tilde{t}_1}, m_{\tilde{\chi}_1^0}) = (650, 325)$ and $(850, 100)$ GeV. An object selection strongly inspired from [Section 4.4](#), though simplified for this study, was used. A similar preselection is applied, requiring one electron or muon with $p_T > 30$ GeV, at least four jets among which one b -tagged, at least 50 GeV for E_T^{miss} and vetoing on a second lepton with $p_T > 5$ GeV. However at this point, no sophisticated tool is used to, for instance, reject jets

from pile-up as it was the case in Section 4.4.3, nor the full second lepton veto based on isolated track and hadronic τ 's. This directly impacts the selection efficiency of the $t\bar{t} \rightarrow \ell\ell$ process which may therefore be overestimated compared to when these tools will be available. Table 4.12 shows the Monte-Carlo yields for $\mathcal{L} = 1 \text{ fb}^{-1}$ obtained at preselection and after cutting on $M_T > 120 \text{ GeV}$.

	preselection	+ $M_T > 120 \text{ GeV}$
1ℓ top	9868 ± 18	614 ± 4
$t\bar{t} \rightarrow \ell\ell$	2073 ± 8	1039 ± 5
W+jets	908 ± 74	55 ± 18
rare	148 ± 10	36 ± 3
total SM	12998 ± 77	1745 ± 20
T2tt (850/100)	2.57 ± 0.02	2.18 ± 0.02
T2tt (650/325)	12.11 ± 0.11	8.89 ± 0.09

Table 4.12: Yields for the background and two signal benchmarks at preselection level and with an additional cut on $M_T > 120 \text{ GeV}$, using the Monte-Carlo samples for the preparation of the Run II, considering $\mathcal{L} = 1 \text{ fb}^{-1}$.

We define three signal regions SR1, SR2 and SR3 inspired from the high- Δm selection at 8 TeV using a constant cut at $M_T > 160 \text{ GeV}$ and increasing cuts on E_T^{miss} and M_{T2}^W as defined on Table 4.13. Table 4.14 shows the yield obtained from Monte-Carlo considering $\mathcal{L} = 1 \text{ fb}^{-1}$. Because of the limited Monte-Carlo statistics available in the W+jets sample, and due to the tight requirement on the jet and b -tag multiplicity, no event is found for this background category.

Signal Region	M_T	E_T^{miss}	M_{T2}^W
SR1	>160	>250	>180
SR2	>160	>300	>190
SR3	>160	>350	>200

Table 4.13: List of cuts used to define the signal regions for the estimation of sensitivity for the Run II.

	SR1	SR2	SR3
1ℓ top	2.10 ± 0.26	0.98 ± 0.18	0.59 ± 0.14
$t\bar{t} \rightarrow \ell\ell$	8.47 ± 0.53	3.17 ± 0.32	1.57 ± 0.23
W+jets	0.00 ± 0.00	0.00 ± 0.00	0.00 ± 0.00
rare	2.56 ± 0.46	1.38 ± 0.29	0.81 ± 0.21
total SM	13.12 ± 0.75	5.54 ± 0.47	2.97 ± 0.34
T2tt (850/100)	1.34 ± 0.02	1.19 ± 0.01	1.03 ± 0.01
T2tt (650/325)	2.61 ± 0.05	1.82 ± 0.04	1.15 ± 0.03

Table 4.14: Yields obtained for the backgrounds and two signal benchmarks in the regions SR1, SR2 and SR3 when considering $\mathcal{L} = 1 \text{ fb}^{-1}$.

The sensitivity is estimated from the yields in the SR3 region, as function of the integrated luminosity. We express the sensitivity in terms of excluded or discoverable signal strength $\mu \equiv \sigma/\sigma_{\text{theo.}}$, as discussed in Section 4.5.2. The background systematic uncertainty is set to 15%. Because the $t\bar{t} \rightarrow \ell\ell$ fraction is likely to be overestimated due to the absence of the full second lepton veto and pile-up jet rejection in this implementation, three scenarios are studied when lowering this fraction by 0, 25 and 50%.

The results are presented on Figure 4.53. One wants to look in particular for the luminosity required to have an excluded or discoverable signal strength lower than 1, meaning that the analysis is effectively sensitive to what the theory predicts. In the case of the two benchmarks considered, no possibility of discovery at 3σ level is found to be possible with a luminosity lower than 30 fb^{-1} . However, a 2σ exclusion can happen for the (650/325) benchmark between 15 and 30 fb^{-1} depending on the optimism of the scenario. For the (850/100) benchmark, it can also be excluded at the 2σ level with 20 fb^{-1} provided that 50% of the $t\bar{t} \rightarrow \ell\ell$ is successfully rejected.

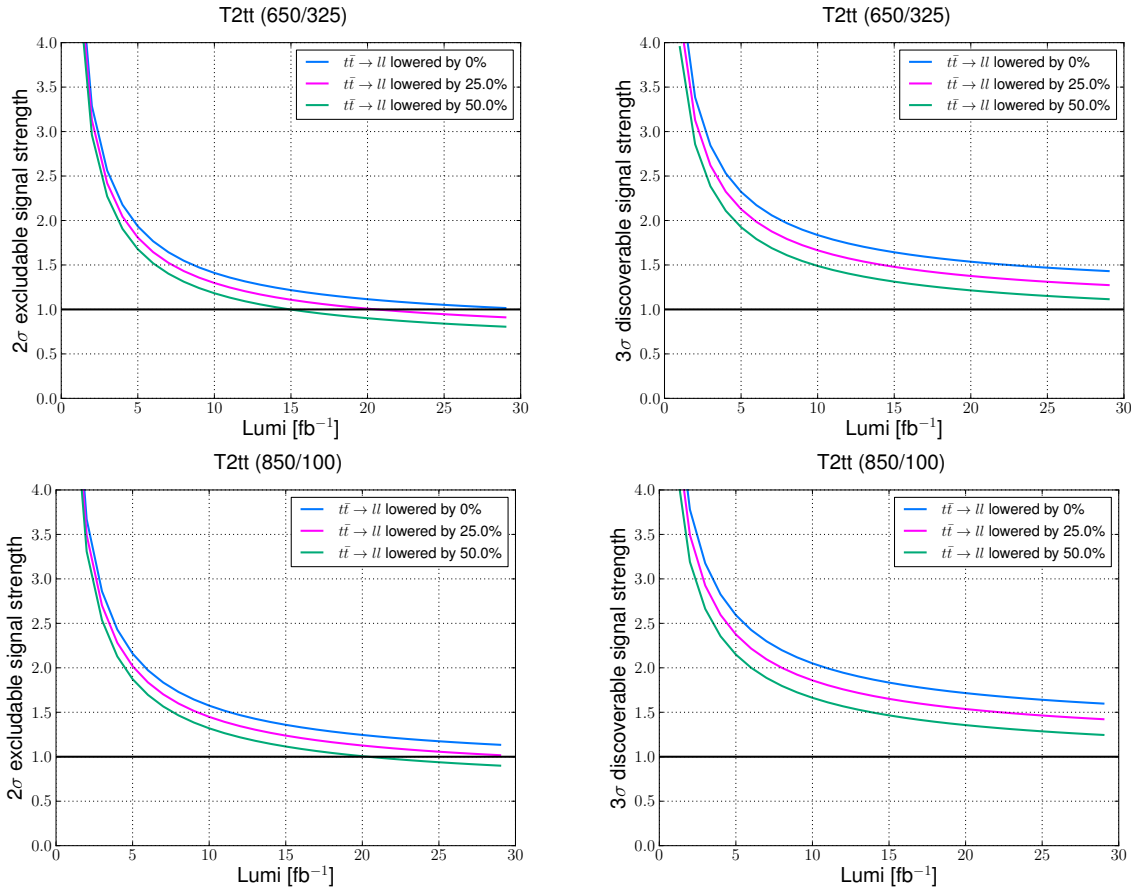


Figure 4.53: Evolution of the sensitivity in terms of excludable signal strength at 2σ level (on the left), and discoverable signal strength at 3σ level (on the right) for the T2tt (650/325) (on the top) and T2tt (850/100) (on the bottom) benchmarks. Three scenarios are considered when lowering the $t\bar{t} \rightarrow \ell\ell$ background by 0, 25 and 50%.

Conclusion

« Follow your most intense obsessions mercilessly. »

Frank Kafka

During the Run I of the LHC, collisions of proton-proton were produced at the energy of $\sqrt{s} = 7$ and 8 TeV. The analysis of the $5 + 20 \text{ fb}^{-1}$ of integrated luminosity recorded by the CMS detector allowed the discovery of a Standard Model-like Higgs boson with a mass around 125 GeV. This discovery reinforces the need to address the hierarchy problem. Supersymmetry, in addition to proposing dark matter candidates, can provide a natural solution to the hierarchy problem. Natural supersymmetry favors the lightest stop \tilde{t}_1 and neutralino $\tilde{\chi}_1^0$ to have masses below about 1 TeV and 500 GeV respectively.

This thesis is centered precisely on the search for such particles using the CMS detector, and in particular for direct stop pair production. Two possible decay chains are considered for the stop: $\tilde{t}_1 \rightarrow t\tilde{\chi}_1^0$, and $\tilde{t}_1 \rightarrow b\tilde{\chi}_1^\pm$ with $\tilde{\chi}_1^\pm \rightarrow W^\pm\tilde{\chi}_1^0$. The search is performed in the semileptonic channel, corresponding to a final state containing one lepton, four jets, and a large amount of missing transverse energy (E_T^{miss}). The analysis is built around the M_T variable, defined as the transverse mass of the lepton + E_T^{miss} system, which provides great discriminating power between signal and backgrounds.

An initial contribution to the analysis is dedicated to the improvement of the second lepton veto based on isolated track identification, and the development of an hadronic τ veto using τ -tagging algorithms. This second lepton veto effectively rejects one of the main backgrounds of the analysis, the dileptonic $t\bar{t}$ process, where one of the leptons is lost. It is estimated that the current veto rejects about 60% of this background, corresponding to a gain in sensitivity about 25% in $t\bar{t} \rightarrow \ell\bar{\ell}$ dominated signal regions.

This contribution is followed by the design and optimization of a cut-based oriented analysis, motivated by the better control and transparency offered by this approach, compared to more sophisticated techniques such as boosted decision trees. This work required to develop a good understanding of the relevance of the different variables depending on the region of phase space considered for the signal, as well as methods to estimate the sensitivity of a counting experiment. Based on these elements, the cuts were chosen to maximize the sensitivity of the analysis. The results obtained allows to cross-check the

boosted decision tree approach, and are sometimes found to provide comparable performances.

Then, I took the responsibility of the background estimation, and particularly the integration of a new method, based on a template fit, to correct for a mismodeling of the tail of M_T caused by the semileptonic $t\bar{t}$ and W +jets backgrounds. This method allows a reliable prediction of the contribution of these backgrounds in the control region. In addition, signal contamination was noticed to be non-negligible in the control regions of the analysis. This is true in particular at low stop mass, $m_{\tilde{t}_1}$, and low $\Delta m \equiv m_{\tilde{t}_1} - m_{\tilde{\chi}_1^0}$ where the signal cross-section is high and the kinematics remains close to the semileptonic $t\bar{t}$ background. To take this into account, the background estimation is modified to obtain a more rigorous prediction of the background, depending on the signal hypothesis made.

After the Run I of the LHC, no significant excess is observed, and the results are interpreted in terms of upper limit on the signal cross-section, as function of the masses $m_{\tilde{t}_1}$ and $m_{\tilde{\chi}_1^0}$. By comparing this upper limit to the theoretical prediction, one can directly constrain the $(m_{\tilde{t}_1}, m_{\tilde{\chi}_1^0})$ space. In the $\tilde{t}_1 \rightarrow t\tilde{\chi}_1^0$ decay mode, this constraint goes up to around 700 GeV for the mass of the stop, and around 250 GeV in term of neutralino mass, assuming $\text{BR}(\tilde{t}_1 \rightarrow t\tilde{\chi}_1^0) = 100\%$. While these results disfavor the idea of a natural supersymmetry, there are still a large portion of phase space where this signal might hide, not only at higher masses but also in the stealthy region and compressed spectra region.

The quest for natural supersymmetry will therefore continue during the Run II of the LHC, which is just starting as this thesis ends. To pave the way for the future of the analysis, the use of W -tagging is investigated as a potential source of improvement in the high Δm region. This technique, based on the analysis of the jet substructure, is relevant for boosted and hadronically decaying W bosons. We demonstrate that this technique indeed holds potential that could be exploited during the Run II. In parallel, we estimate the sensitivity of the analysis at the beginning of the Run II. Using a simplified version of the Run I analysis, one can expect for instance to probe the region around $(m_{\tilde{t}_1}, m_{\tilde{\chi}_1^0}) = (650, 325)$ GeV with the first $15 - 20 \text{ fb}^{-1}$ of data taking.

Overall, the conclusions that will come out of the Run II will definitely shape the future of particle physics. If the promised land of New Physics is discovered, be it supersymmetry or another phenomena beyond the Standard Model, it will set a strong and clear direction for the next decades and the future of theory and experiments. On the other hand, it might as well be that Nature has other surprises in store and that we are missing a theoretical key to really understand and address the shortcomings of the Standard Model. In both cases, we will only progress by searching for the answer.

Bibliography

- [1] J. Polonyi, *Elements of Quantum Field Theory*. [Lectures at the University of Strasbourg]
- [2] L. H. Ryder, *Quantum field theory*. [ISBN 978-0521749091]
- [3] E. Noether, *Invariant Variation Problems (translation by M. A. Tavel)*. [Gott.Nachr (1918), doi:10.1080/00411457108231446, arXiv:physics/0503066]
- [4] C. N. Yang, R. Mills, *Conservation of Isotopic Spin and Isotopic Gauge Invariance*. [Phys.Rev. 96 (1954), doi:10.1103/PhysRev.96.191]
- [5] M. E. Peskin, D. V. Schroeder, *An Introduction To Quantum Field Theory*. [ISBN 978-0201503975]
- [6] S. L. Glashow, *Partial-symmetries of weak interactions*. [Nucl.Phys. 22 (1961), doi:10.1016/0029-5582(61)90469-2]
- [7] S. Weinberg, *A Model of Leptons*. [Phys.Rev.Lett. 19 (1967), doi:10.1103/PhysRevLett.19.1264]
- [8] F. Englert, R. Brout, *Broken Symmetry and the Mass of Gauge Vector Mesons*. [Phys.Rev.Lett. 13 (1964), doi:10.1103/PhysRevLett.13.321]
- [9] P.W. Higgs, *Broken Symmetries and the Masses of Gauge Bosons*. [Phys.Rev.Lett. 13 (1964), doi:10.1103/PhysRevLett.13.508]
- [10] I. van Vulpen, A. Castelli, *Lecture on Particle Physics, The Standard Model Higgs Boson*. [Lectures at the University of Amsterdam]
- [11] D. J. Gross, *Twenty Five Years of Asymptotic Freedom*. [Nucl.Phys.Proc.Suppl. 74 (1999), doi:10.1016/S0920-5632(99)00208-X, arXiv:hep-th/9809060]
- [12] R. Alkofer, J. Greensite, *Quark Confinement: The Hard Problem of Hadron Physics*. [J.Phys.G 34 (2007), doi:10.1088/0954-3899/34/7/S02, arXiv:hep-ph/0610365]
- [13] R. Assmann, M. Lamont, S. Myers, *A Brief History of the LEP Collider*. [Nucl.Phys.B 109 (2002), doi:10.1016/S0920-5632(02)90005-8, cds:549223]
- [14] The Belle and BaBar collaborations, *The Physics of the B Factories*. [Eur.Phys.J. C74 (2014), doi:10.1140/epjc/s10052-014-3026-9, arXiv:1406.6311]
- [15] S. Holmes, *Remembering the Tevatron: The Machine(s)*. [arXiv:1109.2937]

- [16] CMS Collaboration, *Observation of a new boson at a mass of 125 GeV with the CMS experiment at the LHC*. [*Phys.Lett.B* 716 (2012), doi:10.1016/j.physletb.2012.08.021, arXiv:1207.7235]
- [17] ATLAS Collaboration, *Observation of a new particle in the search for the Standard Model Higgs boson with the ATLAS detector at the LHC*. [*Phys.Lett.B* 716 (2012), doi:10.1016/j.physletb.2012.08.020, arXiv:1207.7214]
- [18] The GFitter group, *The global electroweak Standard Model fit after the Higgs discovery*. [arXiv:1306.0571]
- [19] P. Labelle, *Supersymmetry DeMYSTiFied*. [ISBN 978-0071636414]
- [20] K. G. Begeman, *HI rotation curves of spiral galaxies*. [*Astron. and Astrophys.* 223 (1989)]
- [21] K. Garrett, G. Duda, *Dark Matter: A Primer*. [*Adv.Astron.* (2011), doi:10.1155/2011/968283, arXiv:1006.2483]
- [22] S. D. M. White, C. S. Frenk, M. Davis, *Clustering in a neutrino-dominated universe*. [*Astrophys.J.* 274 (1983), doi:10.1086/184139]
- [23] J. Edsjo, P. Gondolo, *Neutralino Relic Density including Coannihilations*. [*Phys.Rev.D* 56 (1997), doi:10.1103/PhysRevD.56.1879, arXiv:hep-ph/9704361]
- [24] M. Drees, H. Iminniyaz, M. Kakizaki, *Constraints on the Very Early Universe from Thermal WIMP Dark Matter*. [*Phys.Rev.D* 76 (2007), doi:10.1103/PhysRevD.76.103524 arXiv:0704.1590]
- [25] R. J. Adler, B. Casey, O. C. Jacob, *Vacuum catastrophe: An elementary exposition of the cosmological constant problem*. [*Am. J. Phys.* 63 (1995), doi:10.1119/1.17850]
- [26] A. D. Sakharov, *Violation of CP in variance, C asymmetry, and baryon asymmetry of the universe*. [*Sv. Phys. U.* 34 (1991), doi:10.1070/PU1991v034n05ABEH002497]
- [27] P. Huet, *Electroweak Baryogenesis and the Standard Model*. [arXiv:hep-ph/9406301]
- [28] H. Georgi, S. L. Glashow, *Unity of All Elementary-Particle Forces*. [*Phys.Rev.Lett.* 32 (1975), doi:10.1103/PhysRevLett.32.438]
- [29] R. D. Peccei, H. R. Quinn, *CP Conservation in the Presence of Pseudoparticles*. [*Phys.Rev.Lett.* 38 (1977), doi:10.1103/PhysRevLett.38.1440]
- [30] P. Sikivie, *The emerging case for axion dark matter*. [*Phys.Lett.B* 695 (2011), doi:10.1016/j.physletb.2010.11.027, arXiv:1003.2426]
- [31] N. Arkani-Hamed, S. Dimopoulos, G. Dvali, *The Hierarchy Problem and New Dimensions at a Millimeter*. [*Phys.Lett.B* 429 (1998), doi:10.1016/S0370-2693(98)00466-3, arXiv:hep-ph/9803315]
- [32] L. Randall, R. Sundrum, *A Large Mass Hierarchy from a Small Extra Dimension*. [*Phys.Rev.Lett.* 83 (1999), doi:10.1103/PhysRevLett.83.3370, arXiv:hep-ph/9905221]
- [33] T. Appelquist, H. Cheng, B. A. Dobrescu, *Bounds on Universal Extra Dimensions*. [*Phys.Rev.D* 64 (2001), doi:10.1103/PhysRevD.64.035002, arXiv:hep-ph/0012100]

-
- [34] Particle Data Group, *The number of light neutrino types from collider experiments*. [[Chin.Phys.C 38 \(2014\)](#), doi:10.1088/1674-1137/38/9/090001]
- [35] M. Drewes, *The Phenomenology of Right Handed Neutrinos*. [[Int.J.Mod.Phys.E 22 \(2013\)](#), doi:10.1142/S0218301313300191, arXiv:1303.6912]
- [36] P. F. Perez, M. B. Wise, *On the origin of neutrino masses*. [[Phys.Rev.D. 80 \(2009\)](#), doi:10.1103/PhysRevD.80.053006, arXiv:0906.2950]
- [37] S. Davidson, M. Peskin, *Astrophysical bounds on millicharged particles in models with a paraphoton*. [[Phys.Rev.D 49 \(1994\)](#), doi:10.1103/PhysRevD.49.2114]
- [38] T. Han, H. E. Logan, B. McElrath, L. Wang, *Phenomenology of the Little Higgs Model*. [[Phys.Rev.D 67 \(2003\)](#), doi:10.1103/PhysRevD.67.095004, arXiv:hep-ph/0301040]
- [39] R. Contino, Y. Nomura, A. Pomarol, *Higgs as a Holographic Pseudo-Goldstone Boson*. [[Nucl.Phys.B 671 \(2003\)](#), doi:10.1016/j.nuclphysb.2003.08.027, arXiv:hep-ph/0306259]
- [40] J. D. Barrow, *Cosmology, Life, and the Anthropic Principle*. [[Annals of the New York Academy of Sciences](#), doi:10.1111/j.1749-6632.2001.tb02133.x]
- [41] F. C. Adams, *Stars In Other Universes: Stellar structure with different fundamental constants*. [[arXiv:0807.3697](#)]
- [42] A. Barrau, *Quelques éléments de physique et de philosophie des multivers*. [[Personnal website](#)]
- [43] Y. A. Gol'fand, E. P. Likhtman, *Extension of the Algebra of Poincare Group Generators and Violation of P invariance*. [[JETP Letters 13 \(1971\) 323-326](#)]
- [44] S. Coleman and J. Mandula, *All Possible Symmetries of the S Matrix*. [[Phys.Rev.159 \(1967\)](#), doi:10.1103/PhysRev.159.1251]
- [45] R. Haag, J. T. Lopuszanski, M. Sohnius, *All possible generators of supersymmetries of the S-matrix*. [[Nucl.Phys.88 \(1975\)](#), doi:10.1016/0550-3213(75)90279-5]
- [46] S. P. Martin, *A Supersymmetry Primer*. [[arXiv:hep-ph/9709356](#)]
- [47] S. Dawson, *SUSY and Such*. [[arXiv:hep-ph/9612229](#)]
- [48] S. K. Vempati, *Introduction to MSSM*. [[arXiv:1201.0334](#)]
- [49] J. C. Romao, *The Minimal Supersymmetric Standard Model*. [[Personal page on Porthos website](#)]
- [50] H. Baer, V. Barger, P. Huang, X. Tata, *Natural Supersymmetry: LHC, dark matter and ILC searches*. [[J.Hi.Ener.Phys. \(2012\)](#), doi:10.1007/JHEP05(2012)109, arXiv:1203.5539]
- [51] W. Beenakker, R. Hopker, M. Spira, P.M. Zerwas, *Squark and Gluino Production at Hadron Colliders*. [[Nucl.Phys.B 492 \(1997\)](#), doi:10.1016/S0550-3213(97)00084-9, arXiv:hep-ph/9610490]
- [52] W. Beenakker, M. Krämer, T. Plehn, M. Spira, P.M. Zerwas, *Stop Production at Hadron Colliders*. [[Nucl.Phys.B 515 \(1998\)](#), doi:10.1016/S0550-3213(98)00014-5, arXiv:hep-ph/9710451]
-

- [53] CMS Collaboration, *Exclusion limits on gluino and top-squark pair production in natural SUSY scenarios with inclusive razor and exclusive single-lepton searches at 8 TeV.* [CMS-PAS-SUS-14-011, cds:1745586]
- [54] ATLAS Collaboration, *Summary of the searches for squarks and gluinos using $\sqrt{s} = 8$ TeV pp collisions with the ATLAS experiment at the LHC.* [J.Hi.Ener.Phys. (2015), doi:10.1007/JHEP10(2015)054 arXiv:1507.05525]
- [55] CMS Collaboration, *Searches for electroweak production of charginos, neutralinos, and sleptons decaying to leptons and W , Z , and Higgs bosons in pp collisions at 8 TeV.* [Eur.Phys.J.C 74 (2014), doi:10.1140/epjc/s10052-014-3036-7, arXiv:1405.7570]
- [56] ATLAS Collaboration, *Search for the electroweak production of supersymmetric particles in $\sqrt{s} = 8$ TeV pp collisions with the ATLAS detector.* [arXiv:1509.07152]
- [57] C. Campagnari, M. Franklin, *The discovery of the top quark.* [Rev.Mod.Phys. 69 (1997), doi:10.1103/RevModPhys.69.137, arXiv:hep-ex/9608003]
- [58] A. Arbey, M. Battaglia, F. Mahmoudi, D. Martinez Santos, *Supersymmetry confronts $B_s \rightarrow \mu^+\mu^-$ Present and future status.* [Phys.Rev.D 87 (2013), doi:10.1103/PhysRevD.87.035026, arXiv:1212.4887]
- [59] A. K. Petukhov, G. Pignol, D. Jullien, K. H. Andersen, *Polarized ^3He as a probe for short range spin-dependent interactions.* [Phys.Rev.Lett. 105 (2010), doi:10.1103/PhysRevLett.105.170401, arXiv:1009.3434]
- [60] J. Jaeckel, A. Ringwald, *A Cavity Experiment to Search for Hidden Sector Photons.* [Phys.Lett.B 659 (2008), doi:10.1016/j.physletb.2007.11.071, arXiv:0707.2063]
- [61] L. Evans, P. Bryant, *LHC Machine.* [J.Inst.3 (2008), doi:10.1088/1748-0221/3/08/S08001]
- [62] A. Siemko, *Safeguarding the superconducting magnets.* [CERN Courier, August 19, 2013]
- [63] M. Lamont, *LHC: status and commissioning plans.* [arXiv:0906.0347]
- [64] A. D. Martin, W. J. Stirling, R. S. Thorne, G. Watt, *Parton distribution for the LHC.* [Eur.Phys.J.C 63 (2009), doi:10.1140/epjc/s10052-009-1072-5, arXiv:0901.0002]
- [65] W. J. Stirling, *Parton luminosity and cross section plots.* [Personal webpage]
- [66] CMS Collaboration, *The CMS experiment at the CERN LHC.* [J.Inst.3 (2008), doi:10.1088/1748-0221/3/08/S08004]
- [67] CMS Collaboration, *Description and performance of track and primary-vertex reconstruction with the CMS tracker.* [J.Inst. 9 (2014), doi:10.1088/1748-0221/9/10/P10009, arXiv:1405.6569, cds:1704291]
- [68] CMS Collaboration, *The CMS Trigger.* [CMS Paper TRG-12-001]
- [69] K. Rose, *Deterministic Annealing for Clustering, Compression, Classification, Regression and related Optimisation Problems.* [Proc.IEEE 86 (1998), doi:10.1109/5.726788]
- [70] CMS Collaboration, *Particle-Flow Event Reconstruction in CMS and Performance for Jets, Taus, and E_T^{miss} .* [CMS-PAS-PFT-09-001, cds:1194487]

-
- [71] W. Adam, R. Frühwirth, A. Strandlie, T. Todorov, *Reconstruction of electrons with the Gaussian-sum filter in the CMS tracker at LHC*. [Talk from CHEP03, doi:10.1088/0954-3899/31/9/N01, arXiv:physics/0306087]
- [72] M. Cacciari, G. P. Salam, G. Soyez, *The anti- k_t jet clustering algorithm*. [J.Hi.Ener.Phys. (2008), doi:10.1088/1126-6708/2008/04/063, arXiv:0802.1189]
- [73] Y. L. Dokshitzer, G. D. Leder, S. Moretti, B. R. Webber, *Better Jet Clustering Algorithms*. [J.Hi.Ener.Phys. (1997), doi:10.1088/1126-6708/1997/08/001 arXiv:hep-ph/9707323]
- [74] H. Kirschenmann, *Jet performance in CMS*. [PoS EPS-HEP 2013]
- [75] B. Dorney, *Anatomy of a Jet in CMS*. [Quantum Diaries]
- [76] CMS Collaboration, *Performance of the CMS missing transverse energy reconstruction in pp data at $\sqrt{s} = 8$ TeV*. [J.Inst. 10 (2015), doi:10.1088/1748-0221/10/02/P02006 arXiv:1411.0511]
- [77] M.A. Dobbs et al., *Les Houches Guidebook to Monte Carlo Generators for Hadron Collider Physics*. [arXiv:hep-ph/0403045]
- [78] Particle Data Group, *Monte Carlo Event Generators*. [Chin.Phys.C 38 (2014), doi:10.1088/1674-1137/38/9/090001]
- [79] The GEANT4 Collaboration, *GEANT4: A Simulation toolkit*. [Nucl.Instrum.Meth.A 506 (2003), doi:10.1016/S0168-9002(03)01368-8, cds:602040]
- [80] A. Giammanco, *The Fast Simulation of the CMS Experiment*. [J.Phys.Conf.Ser. 513 (2014), doi:10.1088/1742-6596/513/2/022012]
- [81] CMS Collaboration, *Search for the standard model Higgs boson produced in vector boson fusion, and decaying to bottom quarks*. [CMS-PAS-HIG-13-011, cds:1547579]
- [82] W. Waltenberger, R. Frühwirth and P. Vanlaer, *Adaptive vertex fitting*. [J.Phys.Nucl.Part.Phys. 34 (2007), doi:10.1088/0954-3899/34/12/N01]
- [83] CMS Collaboration, *Identification of b-quark jets with the CMS experiment*. [J.Inst. 8 (2013), doi:10.1088/1748-0221/8/04/P04013, CMS-PAS-BTV-12-001, cds:1494669, arXiv:1211.4462]
- [84] CMS Collaboration, *Performance of b tagging at $\sqrt{s} = 8$ TeV in multijet, $t\bar{t}$ and boosted topology events*. [CMS-PAS-BTV-13-001, cds:1581306]
- [85] CMS Collaboration, *Tagging b-jets with electrons and muons in 8 TeV pp collisions at CMS*. [CMS-AN-2013/142]
- [86] CMS Tracking group, *730 release validation*. [CMS internal report]
- [87] J. Goh, M. Hildreth, *A New Pileup Mixing Framework for CMS*. [Poster from CHEP2015]
- [88] CMS Collaboration, *Technical proposal for the upgrade of the CMS detector through 2020*. [cds:1355706]
- [89] CMS Collaboration, *Technical Proposal for the Phase-II upgrade of the CMS Detector*. [cds:2020886]
-

- [90] A. G. Cohen, D. B. Kaplan and A. E. Nelson, *The More Minimal Supersymmetric Standard Model*. [[Phys.Lett.B 388 \(1996\)](#), [doi:10.1016/S0370-2693\(96\)01183-5](#), [arXiv:hep-ph/9607394](#)]
- [91] M. Papucci, J. T. Ruderman and A. Weiler, *Natural SUSY Endures*. [[J.Hi.Ener.Phys. \(2012\)](#), [doi:10.1007/JHEP09\(2012\)035](#), [arXiv:1110.6926](#)]
- [92] L. J. Hall, D. Pinner and J. T. Ruderman, *A Natural SUSY Higgs Near 125 GeV*. [[J.Hi.Ener.Phys. \(2012\)](#), [doi:10.1007/JHEP04\(2012\)131](#), [arXiv:1112.2703](#)]
- [93] A. Delgado, G. F. Giudice, G. Isidori, M. Pierini, A. Strumia, *The light stop window*. [[Eur.Phys.J.C 73 \(2013\)](#), [doi:10.1140/epjc/s10052-013-2370-5](#), [arXiv:1212.6847](#)]
- [94] J. Ellis, K. A. Olive, *Supersymmetric Dark Matter Candidates*. [ISBN 9780521763684, [arXiv:1001.3651](#)]
- [95] ALEPH Collaboration, *Absolute mass lower limit for the lightest neutralino of the MSSM from $e+e-$ data at \sqrt{s} up to 209 GeV*. [[Phys. Lett. B583 \(2004\) 247](#), [doi:10.1016/j.physletb.2003.12.066](#), [cds:688526](#)]
- [96] LEPSUSYWG, ALEPH, DELPHI, L3 and OPAL experiments, *Combined LEP stop and sbottom Results*. [LEPSUSYWG/04-02.1 (<http://lepsusy.web.cern.ch/lepsusy/Welcome.html>)]
- [97] D0 Collaboration, *Search for pair production of the scalar top quark in the electron-muon final state*. [[Phys. Lett. B696 \(2011\) 321](#), [doi:10.1016/j.physletb.2010.12.052](#), [arXiv:1009.5950](#)]
- [98] CDF Collaboration, *Search for Pair Production of Supersymmetric Top Quarks in Dilepton Events from $p\bar{p}$ Collisions at $\sqrt{s} = 1.96$ TeV*. [[Phys. Rev. Lett. 104 \(2010\) 251801](#), [doi:10.1103/PhysRevLett.104.251801](#), [arXiv:0912.1308](#)]
- [99] S. Liem, *Constraining Supersymmetry using Simplified Models*. [Master thesis, [urn:nbn:se:su:diva-91365](#)]
- [100] S. Kraml et al., *SModelS: a tool for interpreting simplified-model results from the LHC and its application to supersymmetry*. [[Eur.Phys.J.C 74 \(2014\)](#), [doi:10.1140/epjc/s10052-014-2868-5](#), [arXiv:1312.4175](#)]
- [101] CMS Collaboration, *Search for direct top squark pair production in events with a single isolated lepton, jets and missing transverse energy at $\sqrt{s} = 8$ TeV*. [[CMS-PAS-SUS-12-023](#), [cds:1494074](#)]
- [102] CMS Collaboration, *Search for top-squark pair production in the single-lepton final state in pp collisions at $\sqrt{s} = 8$ TeV*. [[Eur.Phys.J.C 73 \(2013\)](#), [doi:10.1140/epjc/s10052-013-2677-2](#), [CMS-PAS-SUS-13-011](#), [cds:1547550](#), [arXiv:1308.1586](#)]
- [103] CMS Collaboration, *Search for direct stop pair production in the single lepton channel at $\sqrt{s} = 8$ TeV*. [[CMS-PAS-SUS-14-015](#)]
- [104] S. Frixione, P. Nason, C. Oleari, *Matching NLO QCD computations with Parton Shower simulations: the POWHEG method*. [[J.Hi.Ener.Phys. \(2007\)](#), [doi:10.1088/1126-6708/2007/11/070](#), [arXiv:0709.2092](#)]

-
- [105] J. Alwall et al., *MadGraph 5 : Going Beyond*. [*J.Hi.Ener.Phys.* (2011), doi:10.1007/JHEP06(2011)128, arXiv:1106.0522]
- [106] T. Sjostrand, S. Mrenna, P. Skands, *Pythia 6.4 Physics and Manual*. [*J.Hi.Ener.Phys.* (2006), doi:10.1088/1126-6708/2006/05/026, arXiv:hep-ph/0603175]
- [107] CMS Collaboration, *Measurement of differential top-quark pair production cross sections in pp collisions at $\sqrt{s} = 7$ TeV*. [*Eur.Phys.J.C* 73 (2013), doi:10.1140/epjc/s10052-013-2339-4, CMS-PAS-TOP-11-013, cds:1493228, arXiv:1211.2220]
- [108] CMS Collaboration, *Hadronic Recoil Studies of Heavy Boosted Systems*. [CMS-AN-2013/059]
- [109] CMS Collaboration, *Single Muon efficiencies in 2012 Data*. [CMS-DP-2013-009, cds:1536406]
- [110] CMS Collaboration, *Electron performance with 19.6 fb^{-1} of data collected at $\sqrt{s} = 8$ TeV with the CMS detector*. [CMS-DP-2013-003, cds:1523273]
- [111] CMS Collaboration, *Tau reconstruction and identification in CMS during LHC run 1*. [CMS-PAS-TAU-14-001]
- [112] CMS Collaboration, *Jet and MET Commissioning Results from 7 TeV Collision Data*. [CMS-DP-2010-014]
- [113] CMS Collaboration, *Pileup Jet Identification*. [CMS-PAS-JME-13-005, cds:1581583]
- [114] N. Mirman, Y. Wang, J. Alexander, *Missing transverse energy significance at CMS*. [LHCP Conference 2014, arXiv:1409.3028]
- [115] Y. Bai, H. Cheng, J. Gallicchio, J. Gu, *Stop the Top Background of the Stop Search*. [*J.Hi.Ener.Phys.* (2012), doi:10.1007/JHEP07(2012)110, arXiv:1203.4813]
- [116] CMS Collaboration, *Search for dark matter, extra dimensions, and unparticles in monojet events in proton-proton collisions at $\sqrt{s} = 8$ TeV*. [*Eur.Phys.J.C* 75 (2015), doi:10.1140/epjc/s10052-015-3451-4, CMS-PAS-EXO-12-048, cds:1750264, arXiv:1408.3583]
- [117] CMS Collaboration, *Search for supersymmetry in events with soft leptons, low jet multiplicity, and missing transverse momentum in proton-proton collisions at $\sqrt{s} = 8$ TeV*. [CMS-PAS-SUS-14-021, cds:2010110]
- [118] J. Alwall et al., *Searching for Directly Decaying Gluinos at the Tevatron*. [*Phys.Lett.B* 666 (2008), doi:10.1016/j.physletb.2008.06.065, arXiv:0803.0019]
- [119] D. Krohn, L. Randall, L. Wang, *On the Feasibility and Utility of ISR Tagging*. [arXiv:1101.0810]
- [120] A. L. Read, *Presentation of search results: the CLs technique*. [*J.Phys.Nucl.Part.Phys.* 28 (2002), doi:10.1088/0954-3899/28/10/313]
- [121] G. Punzi, *Sensitivity of searches for new signals and its optimization*. [Talk from PhyStat2003, arXiv:physics/0308063]
-

- [122] R. D. Cousins, J. T. Linnemann, J. Tucke, *Evaluation of three methods for calculating statistical significance when incorporating a systematic uncertainty into a test of the background-only hypothesis for a Poisson process*. [*Nucl.Inst.Meth.Phys.Res.A* 595 (2008), doi:10.1016/j.nima.2008.07.086, arXiv:physics/0702156]
- [123] J. T. Linnemann, *Measures of Significance in HEP and Astrophysics*. [Talk from PhyStat2003, arXiv:physics/0312059]
- [124] G. Cowan, K. Cranmer, E. Gross, O. Vitells, *Asymptotic formulae for likelihood-based tests of new physics*. [*Eur.Phys.J.C* 71 (2011), doi:10.1140/epjc/s10052-011-1554-0, arXiv:1007.1727]
- [125] CMS Collaboration, *W+jets differential cross section measurement at 8 TeV*. [CMS-AN-2014/114]
- [126] CMS Collaboration, *Search for monotop in the muon channel in proton-proton collisions at $\sqrt{s} = 8$ TeV*. [CMS-AN-2014/279]
- [127] CMS Collaboration, *Search for the production of dark matter in association with top-quark pairs in the single-lepton final state in proton-proton collisions at $\sqrt{s} = 8$ TeV*. [CMS-PAS-B2G-14-004, cds:1749153, arXiv:1504.03198]
- [128] W. Verkerke, D. Kirkby, *The RooFit toolkit for data modeling*. [Talk from CHEP03, arXiv:physics/0306116]
- [129] CMS Collaboration, *Search for Direct Top Squark Pair Production in the Single Lepton Channel with Transverse Mass at 8 TeV*. [CMS-AN-2013/89]
- [130] M. Botje et al., *The PDF4LHC Working Group Interim Recommendations*. [arXiv:1101.0538]
- [131] CMS Collaboration, *Search for scalar top quark pair production in the dilepton final state at $\sqrt{s} = 8$ TeV with the CMS detector*. [CMS-PAS-SUS-13-025]
- [132] M. Perelstein, A. Weiler, *Polarized Tops from Stop Decays at the LHC*. [*J.Hi.Ener.Phys.* (2009), doi:10.1088/1126-6708/2009/03/141, arXiv:0811.1024v2]
- [133] I. Low, *Polarized Charginos (and Tops) in Stop Decays*. [*Phys.Rev.D* 88 (2013), doi:10.1103/PhysRevD.88.095018, arXiv:1304.0491v2]
- [134] CMS Collaboration, *A Search for Scalar Top Quark Production and Decay to All Hadronic Final States in pp Collisions at $\sqrt{s} = 8$ TeV*. [CMS-PAS-SUS-13-023, cds:2044441]
- [135] ATLAS Collaboration, *ATLAS Run 1 searches for direct pair production of third-generation squarks at the Large Hadron Collider*. [arXiv:1506.08616]
- [136] C. Balázs, M. Carena, and C. E. M. Wagner, *Dark matter, light top squarks, and electroweak baryogenesis*. [*Phys. Rev. D* 70, doi:10.1103/PhysRevD.70.015007]
- [137] CMS Collaboration, *Searches for third-generation squark production in fully hadronic final states in proton-proton collisions at $\sqrt{s} = 8$ TeV*. [*J.Hi.Ener.Phys.* (2015), doi:10.1007/JHEP06(2015)116, arXiv:1503.08037, cds:2004846]
- [138] CMS Collaboration, *Search for supersymmetry in events with soft leptons, low jet multiplicity, and missing transverse momentum in proton-proton collisions at $\sqrt{s} = 8$ TeV*. [CMS-PAS-SUS-14-021, cds:2010110]

- [139] CMS Collaboration, *Measurement of the $t\bar{t}$ production cross section in the em channel in pp collisions at 7 and 8 TeV*. [[CMS-PAS-TOP-13-004](#), [cds:2048642](#)]
- [140] Z. Han, A. Katz, D. Krohn, M. Reece, *(Light) Stop Signs*. [[J.Hi.Ener.Phys.](#) (2012), [doi:10.1007/JHEP08\(2012\)083](#), [arXiv:1205.5808](#)]
- [141] ATLAS Collaboration, *Measurement of Spin Correlation in Top-Antitop Quark Events and Search for Top Squark Pair Production in pp Collisions at $\sqrt{s} = 8$ TeV Using the ATLAS Detector*. [[Phys.Rev.Lett.](#) 114 (2015), [doi:10.1103/PhysRevLett.114.142001](#), [arXiv:1205.5808](#)]
- [142] CMS Collaboration, *Search for top-squark pairs decaying into Higgs or Z bosons in pp collisions at $\sqrt{s} = 8$ TeV*. [[Phys. Lett. B](#) 736 (2014), [doi:10.1016/j.physletb.2014.07.053](#), [arXiv:1405.3886](#)]
- [143] CMS Collaboration, *Search for heavy resonances in the W/Z -tagged dijet mass spectrum in pp collisions at 8 TeV*. [[J.Hi.Ener.Phys.](#) (2014), [doi:10.1007/JHEP08\(2014\)173](#), [arXiv:1405.1994](#)]
- [144] G. Salam, *Jets and jet substructure 4 : substructure*. [Lecture in Theoretical Advanced Study Institute in elementary particle physics, University of Colorado]
- [145] S. D. Ellis, C. K. Vermilion, J. R. Walsh, *Techniques for improved heavy particle searches with jet substructure*. [[Phys.Rev.D](#) 80 (2009), [doi:10.1103/PhysRevD.80.051501](#), [arXiv:0903.5081](#)]
- [146] CMS Collaboration, *Identification techniques for highly boosted W bosons that decay into hadrons*. [[J.Hi.Ener.Phys.](#) (2014), [doi:10.1007/JHEP12\(2014\)017](#), [CMS-PAS-JME-13-006](#), [cds:1955546](#), [arXiv:1410.4227](#)]
- [147] Kalanand Mishra et al., *Hands-on Advanced Tutorial Session on Jet Substructure*. [Jet-substructure hands-on tutorial session (HATS) at LPC, 29th May 2013]
- [148] J. Thaler, K. Tilburg, *Identifying Boosted Objects with N -subjettiness*. [[J.Hi.Ener.Phys.](#) (2011), [doi:10.1007/JHEP03\(2011\)015](#), [arXiv:1011.2268](#)]

RÉSUMÉ

La découverte en 2012 par les collaborations CMS et ATLAS d'un boson de Higgs avec une masse de 125 GeV et ayant des propriétés compatibles avec celles prédites par le Modèle Standard renforce la nécessité de répondre au problème de hiérarchie. La supersymétrie propose une solution naturelle à ce problème, privilégiant un partenaire scalaire du quark top, le stop (\tilde{t}_1), ayant une masse en dessous du TeV tandis que le plus léger des neutralinos ($\tilde{\chi}_1^0$), candidat pour la matière noire dans les modèles avec R -parité conservée, est attendu avec une masse de quelques centaines de GeV.

Cette thèse se concentre sur la recherche de production directe de paires de stop se désintégrant suivant $\tilde{t}_1 \rightarrow t\tilde{\chi}_1^0$, ou $\tilde{t}_1 \rightarrow b\tilde{\chi}_1^\pm$ avec $\tilde{\chi}_1^\pm \rightarrow W^\pm\tilde{\chi}_1^0$, en utilisant les données enregistrées par l'expérience CMS pendant le Run I du LHC à $\sqrt{s} = 8$ TeV. Cette recherche se base sur les événements contenant exactement un lepton, au moins quatre jets dont au moins un est étiqueté comme provenant d'un quark b , et une grande quantité d'énergie transverse manquante signant la production de neutrinos et possiblement de neutralinos.

Le travail de cette thèse a d'abord permis d'améliorer la rejection d'un des bruits de fond majeurs de l'analyse. Des régions de signal ont ensuite été définies et optimisées. Une nouvelle méthode d'ajustement des bruits de fond a été intégrée, et une procédure a été développée pour corriger des effets de contamination du signal. À défaut de mettre un signal en évidence, les résultats ont été interprétés en terme de contrainte sur l'espace $(m_{\tilde{t}_1}, m_{\tilde{\chi}_1^0})$, excluant des masses pour le stop et le neutralino jusqu'à 700 GeV et 250 GeV respectivement.

Finalement, une ouverture sur le Run II du LHC est proposée à travers une étude sur l'utilisation de techniques d'étiquetage de W dans le cadre de l'analyse, et une estimation de la sensibilité de l'analyse pour le début de la prise de données. En parallèle de ce travail d'analyse, une activité de validation des algorithmes d'étiquetage de jets b a été poursuivie.

MOT-CLÉS : physique des particules, LHC, CMS, identification des jets de quark beau, recherche de nouvelle physique, supersymétrie

ABSTRACT

The discovery in 2012 by the CMS and ATLAS collaborations of a Standard Model-like Higgs boson with a mass around 125 GeV reinforces the need to address the hierarchy problem. Supersymmetry proposes a natural solution to this problem, favoring a scalar partner of the top quark, the stop (\tilde{t}_1), to be lighter than the TeV scale while the lightest neutralino ($\tilde{\chi}_1^0$), a dark matter candidate in R -parity conserved models, is expected to have a mass of a few hundred GeV.

This thesis focuses on a search for direct stop pair production decaying through $\tilde{t}_1 \rightarrow t\tilde{\chi}_1^0$, or $\tilde{t}_1 \rightarrow b\tilde{\chi}_1^\pm$ with $\tilde{\chi}_1^\pm \rightarrow W^\pm\tilde{\chi}_1^0$, using data recorded by the CMS experiment during the Run I of the LHC at $\sqrt{s} = 8$ TeV. The search is performed in events with exactly one lepton, at least four jets among which at least one is b -tagged, and large missing transverse energy coming from neutrinos and possibly neutralinos.

The work of this thesis first helped to improve the rejection of one of the main backgrounds. Cut-based signal regions have then been designed and optimized. A new approach for the background estimation has been integrated, and a procedure to correct for signal contamination has been developed. No excess has been observed, and the results were interpreted in terms of constraints on the $(m_{\tilde{t}_1}, m_{\tilde{\chi}_1^0})$ space, excluding stop and neutralino masses up to 700 GeV and 250 GeV respectively.

Finally, prospects for the Run II of the LHC have been investigated through the use of W -tagging techniques in the context of the analysis, and a sensitivity estimation for the beginning of data-taking. In parallel of this analysis, an activity consisting in validating the b -tagging algorithms have been pursued.

KEYWORDS: particle physics, LHC, CMS, b -tagging, search for new physics, supersymmetry